



City Research Online

City, University of London Institutional Repository

Citation: Cabrera-Espana, F. (2017). Analysis of the optical properties of texturing patterns for design of Si solar cells. (Unpublished Doctoral thesis, City, University of London)

This is the accepted version of the paper.

This version of the publication may differ from the final published version.

Permanent repository link: <https://openaccess.city.ac.uk/id/eprint/19766/>

Link to published version:

Copyright: City Research Online aims to make research outputs of City, University of London available to a wider audience. Copyright and Moral Rights remain with the author(s) and/or copyright holders. URLs from City Research Online may be freely distributed and linked to.

Reuse: Copies of full items can be used for personal research or study, educational, or not-for-profit purposes without prior permission or charge. Provided that the authors, title and full bibliographic details are credited, a hyperlink and/or URL is given for the original metadata page and the content is not changed in any way.

Analysis of the optical properties of texturing patterns for design of Si solar cells



Francisco José Cabrera España

School of Mathematics, Computer Sciences and Engineering
City, University of London

This thesis is submitted for the degree of
Doctor of Philosophy

April 2017

TABLE OF CONTENTS

TABLE OF CONTENTS	3
LIST OF FIGURES	7
LIST OF TABLES	11
ACKNOWLEDGEMENTS	13
DECLARATION	15
ABSTRACT	17
LIST OF ABBREVIATIONS	19
LIST OF SYMBOLS	21
Chapter 1: Introduction	25
1.1 Importance of solar cells	25
1.2 History of solar cells	26
1.3. Inorganic solar cells	27
1.3.1. Basic P-N junction and single junction solar cells	28
1.3.1.1 Forward biased p-n junction	30
1.3.1.2 Reverse biased p-n junction	31
1.3.1.3 I-V Curve of a p-n junction	31
1.3.1.4 Single junction solar cell	32
1.3.1.5 Shockley-Queisser limit	41
1.3.2 Multijunction solar cells	42
1.3.3 Crystalline Silicon solar cells	44
1.3.4 Thin film solar cells	45
1.3.4.1 Amorphous Silicon (a-Si) solar cells	45
1.3.4.2 Cadmium Telluride (CdTe) solar cells	46
1.3.4.3 Copper Indium Gallium Selenide (CIGS) solar cells	47
1.3.5 Concentrated solar cells	48
1.4 Organic solar cells	49
1.4.1 Inorganic-Organic Perovskite solar cells	51
1.5 Different techniques to lower Reflectance	53
1.5.2 Anti reflection coatings	53
1.5.3 Plasmonic solar cells	54
1.5.4 Surface Texturing of solar cells	56
1.5.4.1 Pyramid solar cells	57
1.5.4.2 Nanowires solar cells	58

1.5.4.3 Nanowall solar cells	59
1.5.4.4 Moth eye solar cells	61
1.5.4.5 Nanocone solar cells	63
1.5.4.6 Micro pillar solar cells	64
1.6 Summary	65
1.7 References	67
Chapter 2: Methodology	83
2.1 Importance of Numerical methods	83
2.2 Maxwell's equations	88
2.3 Finite-Difference-Time-Domain (FDTD) Method	90
2.3.1 Time discretization of the FDTD method (Leap frog approach)	91
2.3.2 Space discretization of the FDTD method	92
2.3.3 Mesh accuracy and stability	94
2.3.4 Finite differences	97
2.3.5 Governing equations of the 3D FDTD method	99
2.3.6 Simulation set up	102
2.3.6.1 Location of the monitor and the source	103
2.3.6.2 Window height	104
2.3.6.3 Mesh parameters	107
2.3.6.4 Number of PML layers	109
2.3.6.5 Representing the different structures under study	111
2.3.6.6 Processing of the results	115
2.3.7 AM 1.5 reference solar spectrum and plane-wave source	116
2.3.8 Boundary conditions	118
2.3.8.1 Perfect Electric Conductor (PEC) and Perfect Magnetic Conductor (PMC)	119
2.3.8.2 Periodic Boundary Conditions (PBC)	121
2.3.8.3 Absorbing Boundary Condition (ABC)	123
2.3.8.3.1 Perfectly Matched Layer (PML)	124
2.4 Summary	126
2.5 References	129
Chapter 3: Silicon solar cell with micro pillar array texture	133
3.1 Introduction	133
3.2 Effect of different array distribution on the reflection from the solar cell	134
3.3 Effect of Height (H) on the reflection from the solar cell	140

3.4 Effect of Diameter on the reflection from the solar cell	145
3.5 Effect of Surface Coverage and space between pillars on the reflection from the solar cell	149
3.6 Impact of H/D ratio on the reflection from the solar cell	157
3.7 Summary	162
3.8 References	165
Chapter 4: Hut-like Si micro pillar array	167
4.1 Introduction	167
4.2 Comparison with other patterns	169
4.3 Effect of θ , SC and Cap on area in between huts	173
4.4 Effect of H on the reflection from the surface of the solar cell	183
4.5 Effect of D on the reflection from the surface of the solar cell	185
4.6 Effect of Cap on the reflection from the surface of the solar cell	187
4.7 Identifying an optimum set of parameters	195
4.8 Proof of concept by experimental results	196
4.9 Summary	200
4.10 References	203
Chapter 5: Conclusions and recommendations for further work	207
5.1 Introduction	207
5.2 Summary of the research	207
5.3 Recommendations for further work	209
Appendix A	211
Appendix B	215
Appendix C	221

LIST OF FIGURES

FIG. 1.1. SCHEMATIC DIAGRAM OF A P-N JUNCTION. A) WITHOUT DEPLETION REGION. B) WITH DEPLETION REGION.	28
FIG. 1.2. 1D DIAGRAMS OF A P-N JUNCTION UNDER EQUILIBRIUM STATE. (A) ELECTRIC FIELD. (B) VOLTAGE.....	29
FIG. 1.3. SCHEMATIC OF A P-N JUNCTION ON FORWARD BIASED OPERATION.....	30
FIG. 1.4. SCHEMATIC OF A P-N JUNCTION ON REVERSE BIASED OPERATION.....	31
FIG. 1.5. TYPICAL I-V CURVE OF P-N JUNCTION DIODE.	32
FIG. 1.6. SCHEMATIC OF A SINGLE JUNCTION SOLAR CELL.	32
FIG. 1.7. REFLECTIVITY VS. WAVELENGTH CURVE FROM THE PLANAR AIR-SILICON INTERFACE. INSET 1 REAL AND IMAGINARY PARTS OF THE REFRACTIVE INDEX OF SI.	34
FIG. 1.8. SCHEMATIC OF ELECTRON TRANSITION FOR A) DIRECT AND B) INDIRECT BAND GAP.	35
FIG. 1.9. EFFICIENCY VS. ENERGY BAND GAP OF THE ACTIVE MATERIAL ACCORDING TO THE DETAILED BALANCED ANALYSIS PRESENTED BY SHOCKLEY AND QUEISSER.	42
FIG. 1.10. TYPICAL CONCENTRATED SOLAR CELL.....	48
FIG. 1.11. SCHEMATIC OF A BULK-HETEROJUNCTION SOLAR CELL.....	50
FIG. 1.12. SCHEMATIC OF PYRAMID TEXTURING PATTERN.	57
FIG. 1.13. SCHEMATIC OF NANOWIRE TEXTURING PATTERN.	58
FIG. 1.14. SCHEMATIC OF THE NANOWALL PATTERN. (A) SIDE VIEW. (B) TOP VIEW.	59
FIG. 1.15. SCHEMATIC OF THE RESULTING TEXTURING PATTERN WHEN COMBINING NANOWALLS AND NANOWIRES.	60
FIG. 1.16. IMAGE OF A MOTH AND THE IMAGE OF THE ZOOMED EYE OF THE MOTH.....	61
FIG. 1.17. SCHEMATIC OF THE MOTH EYE CONED STRUCTURE.	62
FIG. 1.18. (A) SCHEMATIC OF A NANOCONE ARRAY. (B) TOP VIEW OF THE PATTERN.	63
FIG. 2.1. SCHEMATIC ILLUSTRATING THE STAIRCASING ERROR CAUSED BY THE IMPLEMENTATION OF THE MESH IN THE FDTD METHOD.	85
FIG. 2.2. SCHEMATIC SHOWING THE REASON FOR NUMERICAL DISPERSION IN THE CASE OF $\Delta_x=\Delta_y=\Delta_z$. 88	
FIG. 2.3. SCHEMATIC DIAGRAM OF LEAP-FROG APPROACH.....	91
FIG. 2.4. YEE LATTICE.....	93
FIG. 2.5. 2D SCHEMATIC SHOWING MESH PARAMETERS Δ_x AND Δ_y	94
FIG. 2.6. SCHEMATIC EXPLAINING THE YEE NOTATION FOR THE CASE OF "I".	99
FIG. 2.7. SCHEMATIC ILLUSTRATING THE CONSIDERATIONS DURING THE SETTING UP PROCESS.	102
FIG. 2.8. SCHEMATIC OF SIMULATION SET UP.	103
FIG. 2.9. SCHEMATIC FOR THE SELECTION OF WINDOW HEIGHT.....	104
FIG. 2.10 E FIELD INTENSITY VS. TIME AT REFLECTION MONITOR AND BOUNDARY OF WINDOW.	106
FIG. 2.11. E FIELD INTENSITY NEAR THE REFLECTION MONITOR AT A. 20FS AND B.124FS.	106
FIG. 2.12. PERCENTAGE OF THE SIMULATION ERROR OF R PER WAVELENGTH AS VARYING Δ_z WHILE KEEPING CONSTANT Δ_x AND Δ_y AT 0.01 μ M.	108
FIG. 2.13. RINT VS. NUMBER OF PML LAYERS.	110
FIG. 2.14. SCHEMATIC OF MICRO PILLARS.	111
FIG. 2.15. SCHEMATIC OF HEXAGONAL ARRAY CONFIGURATION.	112
FIG. 2.16. SCHEMATIC OF PROPOSED HUT-LIKE MICRO PILLAR ARRAY. INSET 1 TOP VIEW OF HUT-LIKE PATTERN.	113
FIG. 2.17. AM 1.5 REFERENCE SOLAR SPECTRUM.....	117
FIG. 2.18. SCHEMATIC USING SYMMETRY TO REPLICATE A MICRO PILLAR FROM 1 QUARTER OF THE STRUCTURE.....	120
FIG. 2.19. SCHEMATIC SHOWING THE UNIT CELL OF A PERIODIC STRUCTURE.....	121
FIG. 2.20. ILLUSTRATION OF THE MAPPING OF PBC IN X-Y PLANE.	122
FIG. 2.21. SPURIOUS REFLECTION FROM THE TRUNCATED BOUNDARY.....	123
FIG. 2.22. SCHEMATIC SHOWING THE EFFECT OF PML ON AN INCIDENT WAVE.....	126

FIG. 3.1. R VS. WAVELENGTH FOR HEXAGONAL AND SQUARE CONFIGURATIONS WHEN $H=1\mu\text{M}$, $D=1\mu\text{M}$ AND $SC=60\%$	135
FIG. 3.2. RINT VS. SC FOR HEXAGONAL AND SQUARE CONFIGURATIONS.....	136
FIG. 3.3. E FIELD INTENSITY AT A CROSS SECTION FOR THE CASE OF HEXAGONAL CONFIGURATION....	138
FIG. 3.4. E FIELD INTENSITY AT A CROSS SECTION FOR THE CASE OF SQUARE CONFIGURATION.....	138
FIG. 3.5. RINT VS. SC FOR HEXAGONAL AND SQUARE CONFIGURATIONS FOR THE CASE OF $H=1\mu\text{M}$ AND $D=2\mu\text{M}$	139
FIG. 3.6. EFFECT OF VARYING H FOR FIXED D ($=2\mu\text{M}$).....	140
FIG. 3.7. EFFECT OF VARYING H FOR FIXED D ($=1\mu\text{M}$).....	141
FIG. 3.8. E FIELD INTENSITY IN A VERTICAL CROSS SECTION FOR THE CASE OF (A) $H=1\mu\text{M}$, $D=1\mu\text{M}$ AND $SC=40\%$ (B) $H=2\mu\text{M}$, $D=1\mu\text{M}$ AND $SC=40\%$ (C) $H=5\mu\text{M}$, $D=1\mu\text{M}$ AND $SC=40\%$ AT $\lambda=0.363636$	143
FIG. 3.9. E FIELD INTENSITY IN A VERTICAL CROSS SECTION FOR THE CASE OF (A) $H=1\mu\text{M}$, $D=1\mu\text{M}$ AND $SC=50\%$ (B) $H=2\mu\text{M}$, $D=1\mu\text{M}$ AND $SC=50\%$ (C) $H=5\mu\text{M}$, $D=1\mu\text{M}$ AND $SC=50\%$ AT $\lambda=0.363636\mu\text{M}$	144
FIG. 3.10. EFFECT OF VARYING D FOR FIXED H OF $2\mu\text{M}$ WITH RESPECT TO SC (SOLID LINES IN BLUE, RED AND GREEN) AND SPACE BETWEEN PILLARS (DASHED LINES IN BLUE, RED, GREEN AND CYAN). .	146
FIG. 3.11. SCHEMATIC OF THE SET UP FOR STUDYING EFFECT OF VARYING SC.....	149
FIG. 3.12. E FIELD INTENSITY AT MONITORS S, M AND A FOR PILLAR $H=D=2\mu\text{M}$ AND $SC=60\%$	150
FIG. 3.13. E FIELD INTENSITY AT MONITORS S, M AND A FOR PILLAR $H=D=2\mu\text{M}$ AND $SC=80\%$	151
FIG. 3.14. E FIELD INTENSITY AT MONITORS S, M AND A FOR PILLAR $H=D=2\mu\text{M}$ AND $SC=50\%$	152
FIG. 3.15. SIMULATION SET UP TO OBTAIN E FIELD PLOTS AS SC VARIES.	153
FIG. 3.16. E FIELD INTENSITY OF A CROSS SECTION AT $0.2\mu\text{M}$ ABOVE THE SUBSTRATE FOR THE CASE OF $H=1\mu\text{M}$, $D=1\mu\text{M}$ AND $SC=60\%$	153
FIG. 3.17. E FIELD INTENSITY OF A CROSS SECTION AT $0.2\mu\text{M}$ ABOVE THE SUBSTRATE FOR THE CASE OF $H=1\mu\text{M}$, $D=1\mu\text{M}$ AND $SC=80\%$	154
FIG. 3.18. E FIELD INTENSITY OF A CROSS SECTION AT $0.2\mu\text{M}$ ABOVE THE SUBSTRATE FOR THE CASE OF $H=1\mu\text{M}$, $D=1\mu\text{M}$ AND $SC=50\%$	155
FIG. 3.19. RINT WHEN VARYING SPACE BETWEEN PILLARS AND SC, WITH A) $D=3\mu\text{M}$ AND B) $D=1\mu\text{M}$. 156	156
FIG. 3.20. RINT VARIATION WITH H/D RATIO AND KEEPING D FIXED FOR 50% SC.	158
FIG. 3.21. R VARIATION WITH H/D RATIO AND KEEPING D FIXED FOR 40% SC.	159
FIG. 3.22. EFFECT OF LARGE H/D (RATIO=1) ON R VS. WAVELENGTH FOR 40% SC.....	161
FIG. 3.23. EFFECT OF LARGE H/D (RATIO=10) ON R VS. WAVELENGTH FOR 40% SC.....	162
FIG. 4.1. R VS. WAVELENGTH CURVE COMPARISON BETWEEN THE HUT-LIKE STRUCTURE ($D=1\mu\text{M}$, $H=1\mu\text{M}$ AND $\vartheta=115^\circ$) WITH OTHER TEXTURING PATTERNS OF SIMILAR DIMENSIONS.....	171
FIG. 4.2. ANGULAR PERFORMANCE, AREA IN BETWEEN THE HUTS VS ϑ FOR $H=1\mu\text{M}$, $RADIUSTOP=0.5\mu\text{M}$ AND $CAP=0.2\mu\text{M}$ WHERE THE LINE COLOUR REPRESENTS RINT.	175
FIG. 4.3. RINT VS. ϑ FOR THE SC VALUES: 30%, 40% AND 50%.	176
FIG. 4.4. VARIATION OF AREA IN BETWEEN HUTS VS. ϑ FOR SC VALUES: 30%, 40% AND 50%. INSET 1. CHANGE IN EFFH AS AREA IN BETWEEN HUT DECREASES.....	177
FIG 4.5. SCHEMATIC OF AN OVERLAPPED HUT-LIKE PATTERN.....	177
FIG. 4.6. SCHEMATIC OF AN OVERLAPPED HUT-LIKE PATTERN FROM A TOP VIEW.....	178
FIG. 4.7. CROSS SECTION SHOWING E FIELD INTENSITY AT $0.2\mu\text{M}$ ABOVE THE SUBSTRATE FOR STRUCTURE WITH $H=1\mu\text{M}$, $CAP=0.2\mu\text{M}$ AND $SC=30\%$ AT $\lambda\approx0.373\mu\text{M}$ FOR A) $\vartheta=90^\circ$, B) $\vartheta=105^\circ$ AND C): $\vartheta=115^\circ$ (I.E. OPTIMUM).	178
FIG. 4.8. CROSS SECTION SHOWING E FIELD INTENSITY AT VERTICAL CROSS SECTION (X-Z PLANE) OF THE STRUCTURE WITH $H=1\mu\text{M}$, $CAP=0.2\mu\text{M}$ AND $SC=30\%$ AT $\lambda\approx0.373\mu\text{M}$ FOR A) $\vartheta=90^\circ$, B) $\vartheta=105^\circ$, C) $\vartheta=115^\circ$ (I.E. OPTIMUM) AND D) $\vartheta=125^\circ$	179
FIG. 4.9. EFFECT IN ϑ AND THE AREA IN BETWEEN HUTS AS CAP VARIES.....	181
FIG. 4.10. EFFECT OF VARYING CAP ON THE AREA IN BETWEEN HUTS FOR $H=1\mu\text{M}$, WITH A) $SC=30\%$, B) $SC=40\%$ AND C) $SC=50\%$	182

FIG. 4.11. VARIATION IN RINT AS THE AREA IN BETWEEN HUTS CHANGES, FOR DIFFERENT H.	183
FIG. 4.12. EFFECT OF D AT SC= 30% FOR THE CASE OF D= 0.5 μ M, 1 μ M, 1.5 μ M, 2 μ M.	186
FIG. 4.13. RINT VS. ϑ AT SC= 30% VARYING CAP SIZE FOR H=1 μ M.	187
FIG. 4.14. RINT VS. ϑ AT SC=30 % VARYING CAP SIZE FOR H=2 μ M.	189
FIG. 4.15. RINT VS. ϑ AT SC=30 % VARYING CAP SIZE FOR H=2 μ M.	190
FIG 4.16. SCHEMATIC OF INCREASE IN SLOPED PART AS H INCREASES FOR CONSTANT CAP/H RATIO. .	191
FIG. 4.17. RINT VS. SC CURVE WHILE VARYING CAP SIZE FOR H= 1 μ M AND $\vartheta=115^\circ$	192
FIG. 4.18. E FIELD INTENSITY AT A VERTICAL CROSS SECTION AT SC=40% IN THE CASE OF A) CAP= 0.2 μ M AND B) CAP= 0.0 μ M.	193
FIG. 4.19. E FIELD INTENSITY AT A VERTICAL CROSS SECTION AT SC=20% IN THE CASE OF A) CAP= 0.2 μ M AND B) CAP= 0.0 μ M.	194
FIG. 4.20. RINT VS OPTIMUM θ FOR DIFFERENT VALUES OF H AND SC WITH CAP = 0.2 μ M.	195
FIG. 4.21. CROSS-SECTION SEM IMAGE OF AFTER 20 MINS ETCHING SHOWING $\vartheta=124^\circ$	197
FIG. 4.22. PLANAR SEM IMAGE OF AFTER 20 MINS ETCHING.	198
FIG. 4.23. R VS. WAVELENGTH CURVE COMPARISON BETWEEN THE HUT-LIKE STRUCTURE (D= 1 μ M, H= 1 μ M AND $\vartheta=115^\circ$) INCLUDING EXPERIMENTAL RESULTS WITH OTHER TEXTURING PATTERNS OF SIMILAR DIMENSIONS.	199

**THE FOLLOWING PART OF THIS THESIS HAS BEEN REDACTED
FOR COPYRIGHT REASONS:**

Fig. 1.16. Image of a moth and the image of the zoomed eye of the moth [158]..... 61

LIST OF TABLES

TABLE 1.1. SUMMARY OF BEST ELECTRICAL PERFORMANCE FOR EACH SOLAR CELL TYPE.	53
TABLE 2.1. RELATION BETWEEN MESH PARAMETERS AND MEMORY REQUIREMENTS AND SIMULATION TIME.	87
TABLE 2.2. RELATION BETWEEN MESH PARAMETERS AND TIME STEP.	97
TABLE 4.1. COMPARISON OF MEMORY REQUIREMENTS AND SIMULATION TIME IN VERTICAL MICRO PILLAR SIMULATIONS AND HUT-LIKE PATTERN SIMULATIONS.	169
TABLE 4.2. COMPARISON OF THE SURFACE-TO-VOLUME RATIO OF FOUR TEXTURING PATTERNS.	173

ACKNOWLEDGEMENTS

My utmost gratitude goes to City, University of London and the School of Mathematics, Computer Science and Engineering and all the staff involved for allowing me to complete this PhD fully funded.

My most sincere gratitude goes to my first supervisor Dr. Arti Agrawal, who has guided me through this research. She has spent a lot of her time to direct me towards a constant development of this research. I am also grateful to my co-supervisor Prof. Dr. B. M. A. Rahman who has shared his point of view whenever he was asked.

Furthermore, I would like to express my gratitude to Prof. Hari Reehal from London South Bank University for characterizing the samples of the solar cell proposed in this work. Additionally, my gratitude also goes to Dr. Philip Shields from the University of Bath for fabricating the sample of the solar cell proposed in this work.

I would also like to express my gratitude to my colleagues in the Lab where we have spent many hours together. They shared their experiences with me when I was starting my research.

Finally, I would like to thank my family. They have been supporting me and encouraging me in those moments when the difficulties seemed to overtake me. Starting with my grandmother, who gave me a lot of strength since I was little but is no longer with me to witness the finishing of this work. To my wife who has been very understanding, supportive, kind and helpful during this period. To my parents who have always believed in me and provided the education and support to become the person I am today. To my sister and my aunt, who have spent many hours reviewing the spelling and grammar of this thesis. To my little dog who has spent many hours next to me while I was working on the computer.

DECLARATION

I hereby declare that except where specific reference is made to the work of others, the contents of this dissertation are original and have not been submitted in whole or in part for consideration for any other degree or qualification in this, or any other University. This dissertation is the result of my own work and includes nothing which is the outcome of work done in collaboration, except where specifically indicated in the text. This dissertation contains less than 65,000 words including appendices, references, footnotes, tables and equations and has less than 150 figures.

I hereby grant powers of discretion to the University Librarian to allow this thesis to be copied in whole or in part without further reference to the author. This permission covers only single copies made for study purposes, subject to normal conditions of acknowledgement.

ABSTRACT

The pronounced development in the field of solar cells has been driven by the increasing interest in “green” energy generation in recent decades. Nevertheless, to increase the deployment of solar cells the energy conversion efficiency has to be improved further. The highest energy conversion efficiency has been recorded using a Silicon solar cell. However, there are limitations such as the high reflection from the solar cell surface that limits further improvement of the energy conversion efficiency. The large refractive index contrast between air and the material of the solar cell leads to high reflection. As a consequence, reducing the reflection from the solar cell surface is a priority.

This research aims at reducing reflection from the solar cell surface. To achieve this goal, modeling based analysis of a micro pillar array texturing pattern and a new and exciting texturing pattern (the hut-like pattern) are presented. The simulation method used for this study is the Finite Difference Time Domain (FDTD) method. In the discussion, the effect of key structural parameters on the reflection is analyzed to obtain an in-depth understanding of the patterns. Additionally, the inter-dependence between the different structural parameters under study is considered during the discussion.

The analysis shows that the reflection from a micro pillar array solar cell decreases as the Height (H) increases. The H by Diameter (H/D) ratio analysis presented in this work determines that there is a convergence in the reflection when the H/D ratio is high. This can be useful especially for designers with low precision fabrication equipment who can target higher H/D ratio to ensure a low reflection. The high surface-to-volume ratio when the H/D ratio is high can lead to high surface recombination. High surface recombination is a major problem in textured solar cell since it diminishes the electrical performance.

An alternative is to use the hut-like pattern that combines the benefits of lowering the reflection with a low surface-to-volume ratio. The low surface-to-volume ratio is expected to have a positive effect on the surface recombination (i.e. lower surface recombination). The results show excellent optical performance of the pattern. Additionally, the hut-like pattern provides a reflection lower than other texturing patterns such as pyramid, nanowires and micro pillars. Furthermore, the results of a fabricated proof of concept hut-like sample are presented which highlights the excellent optical performance of the pattern.

LIST OF ABBREVIATIONS

Silicon (Si)

Amorphous silicon (a-Si)

Cadmium Telluride (CdTe)

Copper Indium Gallium Selenide (CIGS)

Gallium Arsenide (GaAs)

Gallium Selenide (GaSe)

Germanium (Ge)

Gallium Phosphite (GaP)

Fill Factor (FF)

Open Circuit Volage (Voc)

Short Circuit Current (Isc)

Crystalline Silicon (c-Si)

Copper Phthalocyanine (CuPc)

Anti Reflection Coating (ARC)

Finite Difference Time Domain (FDTD)

Contour Path FDTD (CP FDTD)

Perfectly Matched Layer (PML)

Periodic Boundary Conditions (PBC)

Reflectance (R)

Reflectance integrated overall wavelengths (RInt)

Height (H)

Diameter (D)

Surface Coverage (SC)

Air Mass 1.5 reference solar spectrum (AM 1.5)

Extraterrestrial (Ext)

Perfectly Electric Conductor (PEC)

Absorbing Boundary Condition (ABC)

Perfect Magnetic Conductor (PMC)

Height by Diameter (H/D)

Cap by Height (Cap/H)

Deep Reactive Ion Etching Process (DRIE)

Rapid Thermal Oxidation (RTO)

Plasma-Enhanced Chemical Vapour Deposition (PECVD)

Thermal Oxidation (CTO)

LIST OF SYMBOLS

n	Refractive index of the material
$\hbar \times \mathbf{k}^i$	Initial electron momentum
$\hbar \times \mathbf{k}^f$	Final electron momentum
$\hbar \times \mathbf{q}$	Photon momentum
E^i	Initial associated energy with photon
E^f	Final associated energy with photon
$\hbar \omega$	Associated energy
$h \nu$	Energy of a photon
α	Absorption coefficient
E_{ph}	Photon energy
E_g	Energy band gap
A	Direct band gap material constant
B	Indirect band gap material constant
FF	Fill factor
V_{OC}	Open circuit voltage
I_{SC}	Short circuit current
V_{MP}	Voltage at maximum power
I_{MP}	Current at maximum power
η	Conversion efficiency
P_{IN}	Power of incoming light
B	Magnetic flux density
E	Electric field
$\nabla \times E$	Curl of E
M	Magnetic current density
D	Electric current density
H	Magnetic field
J	Electric current density
ρ	Charge density

ε	Electric permittivity
ε_r	Relative permittivity
ε_0	Free-space permittivity
μ	Magnetic permeability
μ_r	Relative permeability
μ_0	Free-space permeability
Δ_x	Mesh step size on the x direction
Δ_y	Mesh step size on the y direction
Δ_z	Mesh step size on the z direction
Δ_t	Time step
$u(x)$	Function dependent on x
$u'(x)$	First derivative of a function dependent on x
i	Current node in the FDTD scheme in x direction
j	Current node in the FDTD scheme in y direction
k	Current node in the FDTD scheme in z direction
n	Current node in the FDTD scheme in time
i+1	Next node in the FDTD scheme in x direction
i-1	Previous node in the FDTD scheme y direction
E_x	Electric field component on the x direction
E_y	Electric field component on the y direction
E_z	Electric field component on the z direction
H_x	Magnetic field component on the x direction
H_y	Magnetic field component on the y direction
H_z	Magnetic field component on the z direction
M_{source}	Magnetic field source
σ^*	Magnetic loss
σ	Electric conductivity
J_{source}	Electric field source
t_1	Time taken by the electromagnetic wave to travel from the source to the surface

t_2	Time taken by the electromagnetic wave to travel from the surface to the PML
t_3	Time taken by the electromagnetic wave to travel from the PML to the reflection monitor
$t_{\text{simulated}}$	Simulated time
X	Span of the simulation window in the x direction
Y	Span of the simulation window in the y direction
r	Radius of a micro pillar
π	Number pi
ϑ	Angle between the side walls of the hut-like micro pillar and the substrate
T (f)	Transmission frequency dependent
P (f)	Poynting vector
dS	Surface normal
Sourcepower	Electromagnetic waves launched by the source
$I_{\text{AM1.5}}$	Reference solar spectrum AM 1.5
E_T	E field component transversal to the PEC boundary
E_N	E field component normal to the PEC boundary
$e^{-j\psi_y}$	Phase of the wave in y direction
$e^{-j\psi_x}$	Phase of the wave in x direction
E_{zx}	E field component normal to the PML
E_{zy}	E field component transversal to the PML
ϵ_1	Dielectric constant medium 1
ϵ_2	Dielectric constant medium 2
μ_1	Permeability medium 1
μ_2	Permeability medium 2
σ_y	Conductivity medium 1
σ_{my}	Conductivity medium 1
σ_x	Conductivity medium 2
σ_{mx}	Conductivity medium 2
S_x	Term determining exponential of absorbing curve in PML

Chapter 1: Introduction

In this Chapter, background knowledge of solar cells is introduced to pave the way for a discussion on its current stage. The discussion provides the most relevant information in the field of solar cells. This thesis describes: the importance of solar cells, basic history, basic physics for solar cells and different types of solar cells.

1.1 Importance of solar cells

Currently the energy generated for daily consumption in its vast majority comes from fossil fuels [1, 2]. However, the discovery of solar cells and other renewable energies resources have taken some shares of that consumption [3]. Governments and their citizens around the world have realised the environmental implications of our extremely large energy consumption [4, 5]. As of 2011, the energy consumption was equivalent to energy generated with 12 billion tones of oil [6]. Up to 92% of that energy came from oil, coal, natural gas and nuclear energy [7]. The transition from a fossil fuel based energy supply to a renewable based energy supply is not straight forward. A lot of investigations and improvements have been made towards efficient and economic energy generation from renewable sources.

For this purpose Governments around the world have set up ambitious plans for lowering CO₂ emissions. In the U.S.A the government has set the target of reducing climate change emissions 25% from the levels recorded in 2005 by 2025 [8]. In the E.U., the parliament in 2009 agreed to set an ambitious program to generate 20% of its energy consumption from renewable sources by 2020 [9]. The Chinese government set a target in 2010 to improve the energy production from solar cells by 160 times within ten years [10]. In Australia, the government has targeted the energy consumption from renewable resources to rise to 23.5% of the total energy consumption by 2020 [11].

In this matter, renewable energies will play a very important role. For example, the energy of sunlight reaching the earth in a single day is equivalent to 27 years of the energy consumption of World's current population [1]. The sunlight

is free to access and it is an unlimited resource which makes it a very promising technology. However, there are many aspects that need to be taken into account before deploying a solar cell. Not every place in the world has appropriate conditions for solar cells. Wherever solar cells are not appropriate, other types of renewable energies could be adopted as an alternative solution for clean energy generation. Therefore, it is important that each country defines the most suitable renewable energy policy to develop a sustainable energy market [12]. Furthermore, an efficient energy storage device has to be developed to store generated energy for moments when weather conditions do not allow energy generation [13]. This will enhance the installation of solar cells devices on residential areas as well as on industrial areas. Moreover, the price for purchasing and installing solar cells has to be reduced. The solar cell market has developed considerably in recent years partly due to lower prices [14]. In order to achieve lower prices, which make solar cells more accessible, it is necessary to develop further the technology involved in the field of solar cells. In the following section a discussion on the history of solar cells, is presented.

1.2 History of solar cells

The interest on using the energy from the Sun for human being's daily life has arisen for many centuries [15]. With the discovery of electricity, the interest shifted to generating electricity using sunlight. However, this was not achieved until 1839 when Edmond Bequerel first reported the evidence of the photovoltaic effect [16].

Over one century later, in 1954 a good understanding on p-n junctions formed a path to the invention of the first solar cell at Bell labs [16, 17]. This type of solar cells is known as the first generation solar cells and it was a Silicon (Si) single-crystal solar cell with a conversion efficiency of 6% [16]. Within a short time the efficiency was increased up to 15% [16, 17]. Nowadays the highest efficiency for this type of solar cell is 25% [18, 19]. At first the applications for outer space were more numerous than for terrestrial applications due to a large investment from space programmes of different governments [17, 20]. The applications of solar cells expanded in 1973 when the price of petrol increased due to the oil crisis [5, 17]. In this scenario, governments realised the importance of

developing the required technology for cheaper alternative energy resources. Renewable energies were seen as a clear but fairly expensive alternative for energy generation. The costs for the fabrication of solar cells were very high. As a consequence, many researchers focused on new active materials and on lowering manufacturing costs [6]. This led to a new type of solar cells, with high expectations, known as second generation solar cells.

This group includes: amorphous Silicon (a-Si) solar cells, Cadmium Telluride (CdTe) solar cells and Copper Indium Gallium Selenide (CIGS) solar cells. However, the initial expectations were not fully met due to various problems to be discussed in Section 1.3. As a consequence, researchers focused on a new type of solar cells known as third generation solar cells.

In this type of solar cell, the active material is an organic material. It is expected that the manufacturing process will be faster and cheaper for this type of solar cells. More detailed information will be discussed in Section 1.4. The material, from which solar cells are made of, has a large impact on the performance. In term of material, solar cells can be classified as: inorganic or organic solar cells. In the following sections these two are explained in detail; starting the discussion with inorganic solar cells.

1.3. Inorganic solar cells

The first solar cell was made of Silicon which is an inorganic semiconductor. Since then solar cells using inorganic semiconductors have dominated the market. Moreover, the energy payback time (time it takes for the total energy required for fabrication to be generated by the device) associated with inorganic semiconductors has been reduced from about 40 in 1970s to about 0.5 years in 2010 in Southwest United States [21] and 5 years in Central Europe [22]. Moreover, the highest efficiencies achieved thus far have been recorded for inorganic solar cells which is 25% [18, 19]. However, there are still some unresolved challenges which are related to inorganic solar cells requiring further investigation such as: efficiency limit, manufacturing process and costs. There has been great progress carried out to solve these issues. The efficiency limit can be overcome by increasing the number of junctions within the solar cell. In

addition, the cost can be lowered by using thinner layers of active material without affecting in excess the efficiency. In the following subsections, the different types of inorganic solar cells are discussed. The discussion starts with the most basic form of a solar cell: the basic p-n junction.

1.3.1. Basic P-N junction and single junction solar cells

In a p-n junction, there are two different doped types of a semiconductor material involved. There is a p-type semiconductor with an excess of holes, together with an n-type semiconductor with an excess of electrons [20]. In the case of Silicon (the most conventionally used semiconductor material in IC design as well as for solar cells), the excess of electrons and holes in the semiconductor is achieved by adding Boron, Aluminium, Nitrogen, Gallium or Indium for p-type and Phosphorous, Arsenic, Antimony, Bismuth or Lithium for n-type. There are also alternative semiconductor materials that enable the formation of p-n junctions such as Gallium Arsenide or Cadmium Telluride.

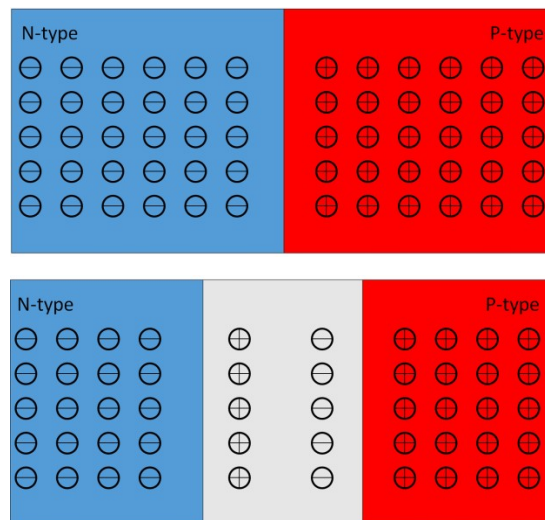


Fig. 1.1. Schematic diagram of a p-n junction. a) without depletion region. b) with depletion region.

Figure 1.1 a shows the p-n junction before the formation of the depletion region. Here, some of the excess electrons and holes from both n and p-types diffuse to the opposite type (i.e. excess electrons from n-type diffuse to the p-type and excess holes from p-type diffuse to the n-type). Hence, the diffused electrons and holes combine with the holes and electrons on the p and n-types

respectively near the interface [23]. The diffusion of electrons and holes leads to the generation of an Electric (E) field that opposes this diffusion as shown in Fig. 1.2 a [23]. As a consequence, the generated E field and the diffusion processes reach the equilibrium state as shown in Fig. 1.1 b [23]. As a result, all the carriers are depleted which means that there are no free carriers available near the interface. For this reason, the region near the interface is called as the depletion region.

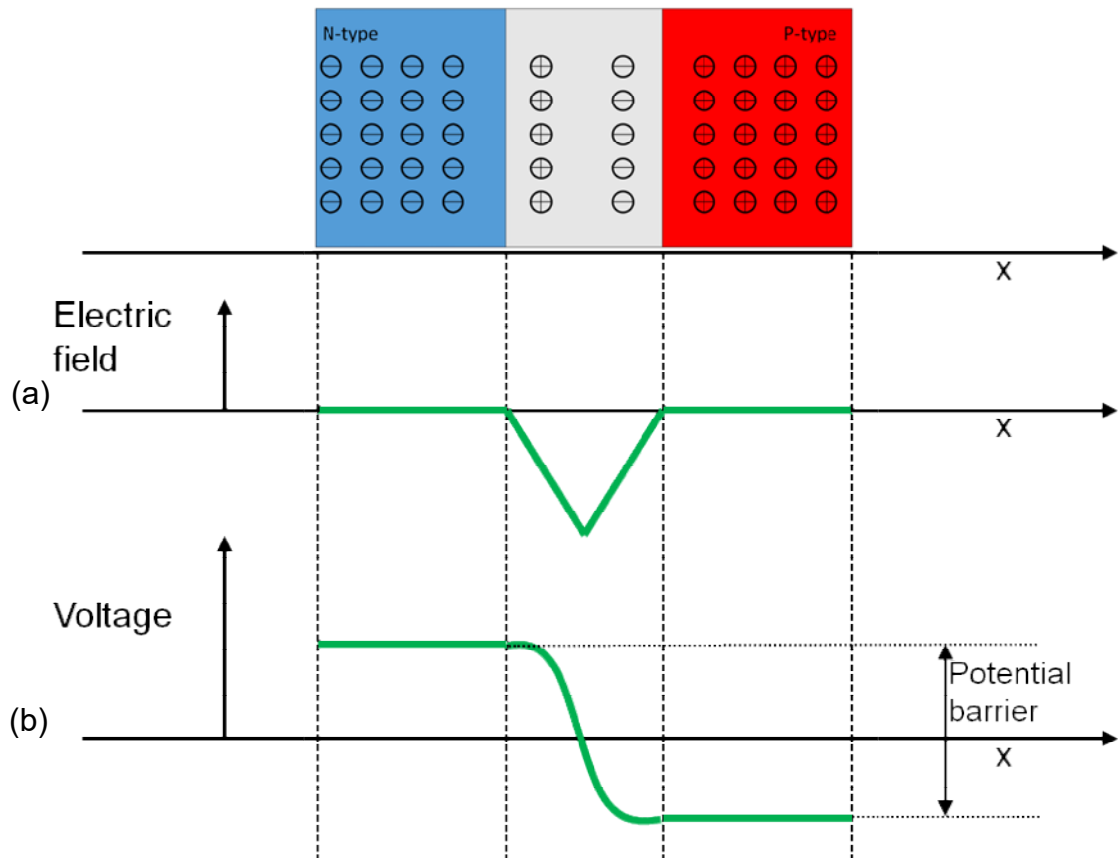


Fig. 1.2. 1D diagrams of a p-n junction under equilibrium state. (a) Electric field. (b) Voltage.

The presence of the depletion region leads to a potential difference across the junction as shown in Fig. 1.2 b. Therefore, the depletion region acts as a potential barrier for the remaining free electrons and holes on the n and p type semiconductor [23]. The selection of the right doping material is very important for the performance of p-n junction. The doping level can adjust how large the width of the depletion region is (which is defined by the semiconductor material) and hence, how high the potential barrier is. Any carrier with a potential which is

lower than the potential barrier at the depletion region cannot diffuse to the opposite type. More information about the p-n junction in the case of solar cells will be provided in the discussion of Section 1.3.1.4.

Figure 1.1 b illustrates the p-n junction after the formation of the depletion region. This scenario is called equilibrium state [23]. However, the equilibrium state can be altered by applying an external voltage across the p-n junction. In this case, the free electrons and holes can diffuse only if its potential is larger than the potential barrier across the junction. The value of the external voltage to be applied may vary with the material used. This value is known as threshold voltage. In the case of Si it is 0.7 V [24]. Moreover, the sign of the external voltage applied can vary the operation of the p-n junction. The p-n junction can operate either in forward or reversed bias which will be discussed in the following sections [20, 23].

1.3.1.1 Forward biased p-n junction

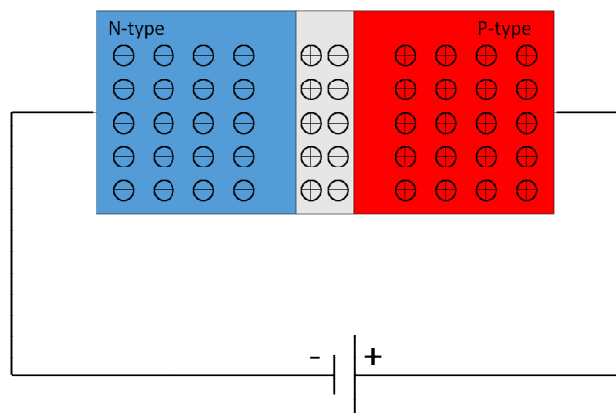


Fig. 1.3. Schematic of a p-n junction on forward biased operation.

Figure 1.3 presents in a schematic the forward biased operation set up of a p-n junction. The p-n junction is considered in forward bias operation when: the positive potential terminal of the external voltage is applied on the p-type semiconductor. In addition, the negative potential terminal of the external voltage is applied on the n-type. Under this condition, the depletion region gets narrower [23]. This is due to the repulsion that the positive and negative terminals have on the positive and negative charges of the p-type and n-type semiconductors respectively [23]. In this way the ability to diffuse increases.

1.3.1.2 Reverse biased p-n junction

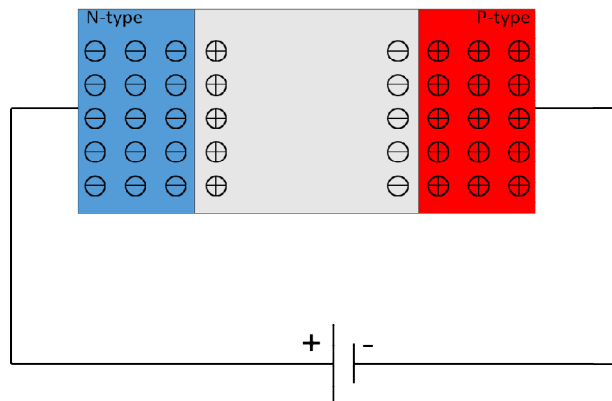


Fig. 1.4. Schematic of a p-n junction on reverse biased operation.

Figure 1.4 presents in a schematic the reverse biased operation set up of a p-n junction. The p-n junction is considered in reversed bias operation when: the positive potential terminal of the external voltage is applied on the n-type semiconductor. In addition, the negative potential terminal of the external voltage is applied on the p-type semiconductor. Under this condition, the depletion region gets wider [23]. This is due to the attraction that the positive and negative have on the positive and negative charges of the p-type and n-type semiconductors respectively [23]. In this way the ability to diffuse decreases.

1.3.1.3 I-V Curve of a p-n junction

The biasing of the p-n junction has a direct effect on the current flowing and on the voltage across the junction. Figure 1.5 shows the current versus voltage curve for a basic p-n junction.

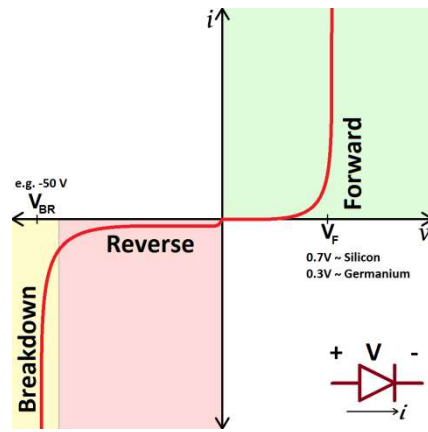


Fig. 1.5. Typical I-V curve of p-n junction diode [25].

When the p-n junction is in reverse bias (i.e. $V < 0$), the potential barrier due to the depletion region is sufficiently large. Hence, the current flowing through the p-n junction is very small as shown on Fig. 1.5. As the voltage across the p-n junction is increased to more than the threshold, the p-n junction is considered to be in forward bias. In this case, the depletion region reduces that leads to a decrease of the potential barrier for free carriers to diffuse. As a consequence, current starts to flow through the p-n junction. Additionally, it is important to highlight that this current is exponentially dependent on the applied voltage.

1.3.1.4 Single junction solar cell

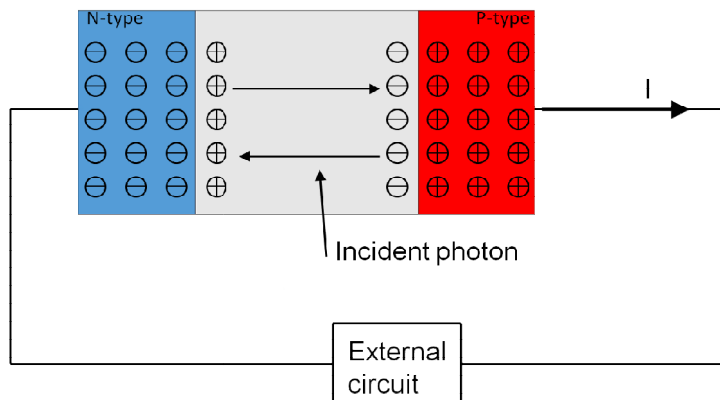


Fig. 1.6. Schematic of a single junction solar cell.

The basic solar cell is a p-n junction as shown in Fig. 1.6. This p-n junction is reversed biased and encapsulated¹ to minimize any performance degradation

¹ The encapsulation process protects the layers of the materials forming the solar cell from rain, dust, extreme temperatures and moisture and it is carried out for all commercial solar cells. The encapsulation process is very important since it may affect the life time of the solar cell.

due to adverse weather conditions. When the light is incident on the surface of a solar cell, part of it penetrates into the solar cell and the rest is reflected back to the air. In the ideal scenario all that light that has penetrated into the solar cell reaches the active layer (depletion region). The creation of electron-hole pairs, via the photovoltaic effect, takes place at this layer. Then, the electrons go to the positive contact and flow through the external circuit. Hence, a photo generated current is produced. However, the ideal case is not possible due to performance limitations caused by material properties such as the band gap of the material (discussed later in this section). As a consequence it is necessary to characterize the solar cell performance. Additionally, there are several quantities that are helpful in understanding whether or not the solar cell performs as required. These parameters can be representative of the optical or of the electrical performance of the device. A brief introduction about the most meaningful parameters is presented below.

Characterization of optical properties:

- Reflection (R) [23]:

This parameter gives the amount of light that the solar cell reflects from the surface. In the case of Si solar cells, at the interface between air and Silicon, there is a large refractive index difference between the two materials [26]. This difference leads to high reflection from the interface of an incident wave [26]. The waves that are reflected can be predicted at normal incidence by Fresnel's equations [27, 28] (given the dispersive refractive index of the material) as follows:

$$\text{Reflectivity} = \frac{(n(\lambda) - 1)^2 + (k(\lambda))^2}{(n(\lambda) + 1)^2 + (k(\lambda))^2} \quad (1.1)$$

The reflectivity versus wavelength resulting from solving Eq. (1.1) for the interface air-Silicon is as shown in Fig. 1.7. The refractive index data (n and k) used to solve Eq. (1.1) are presented in inset 1 for reference [29].

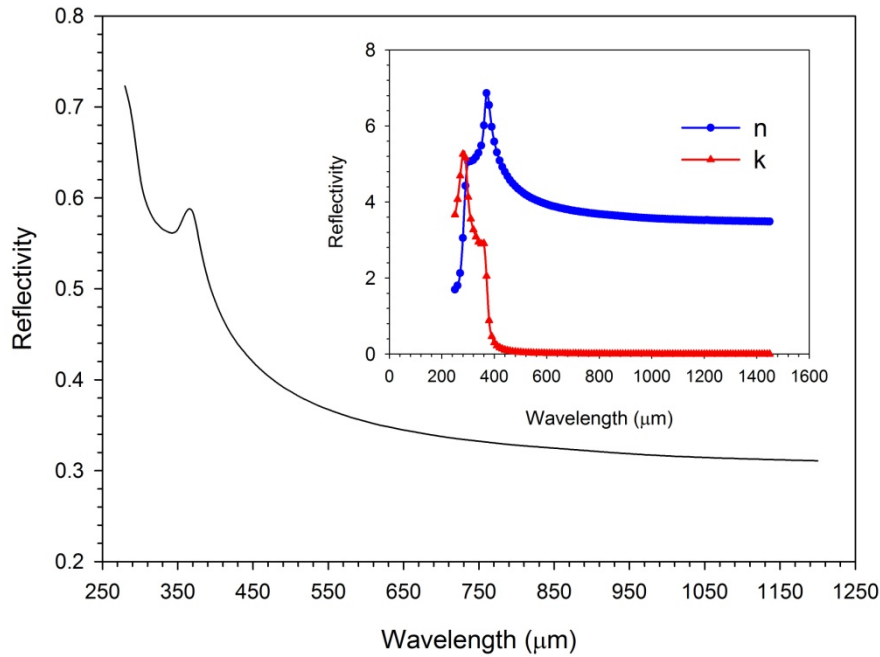


Fig. 1.7. Reflectivity vs. wavelength curve from the planar air-Silicon interface.
Inset 1 real and imaginary parts of the refractive index of Si.

Figure 1.7 shows clearly how large the reflection from the air-Silicon interface is. This means that the amount of light reaching the absorbing layer of a Si solar cell is highly dependent on the refractive index difference at this interface. If the reflection at this interface can be reduced, it would mean that more light reaches the active layer, increasing chances of absorption. There are various means available to increase the transmission into the Si such as: anti reflection coating or trapping the light to increase the light path which will be discussed in Section 1.5. Reducing the reflection from the solar cell is the main target of the work presented in this thesis.

- Absorption (A) [23]:

This parameter gives the amount of light that the solar cell absorbs. For a better performance of a solar cell this parameter needs to be increased as much as possible. This process takes place at the active layer of the solar cell, where electrons transition from the valence to the conduction band. The transfer takes place upon the arrival of a photon with energy equal or larger than the band gap of the material. The process involved, which is in the

photon absorption leading to the transition of electron between energy bands, has to obey the conservation of energy and momentum [30]:

$$\hbar \times k^i + \hbar \times q = \hbar \times k^f \quad (1.2)$$

$$E^i + \hbar\omega = E^f \quad (1.3)$$

where $\hbar k^i$, $\hbar k^f$, E^i and E^f are the initial electron momentum, the electron photon momentum, the initial associated energy with the photon and the final associated energy with the photon respectively. The photon momentum and the associated energy are represented by $\hbar q$ and $\hbar\omega$ respectively. Either direct or indirect band gap semiconductor can be used in this layer. Figure 1.8 presents the transition of an electron upon the arrival of a photon for direct and indirect band gap:

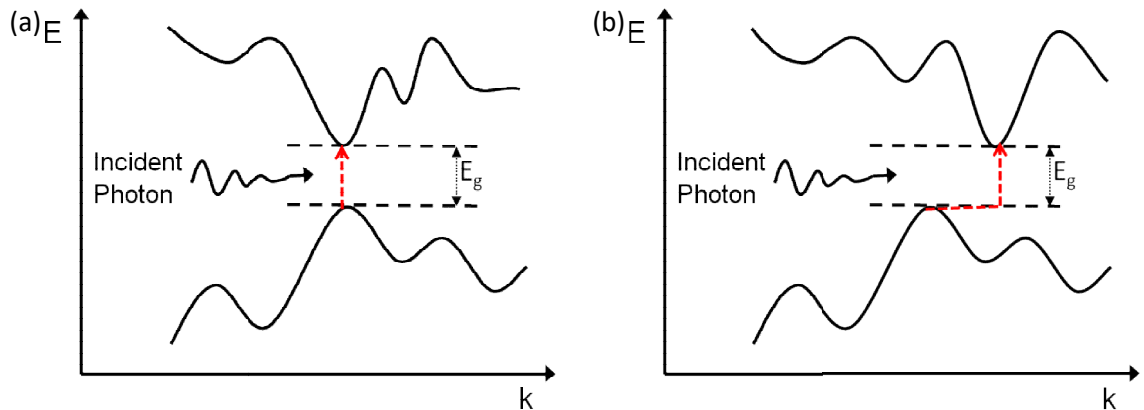


Fig. 1.8. Schematic of electron transition for. a) direct and. b) indirect band gap.

- Direct band gap semiconductor: In this type of material, the transition of electrons from valence to conduction band is direct (i.e. the minimum energy level of the conduction band is aligned with the maximum energy level of the valence band [30]). For the transition to occur, the photon is not required to carry any momentum to conserve the momentum [30]. This leads to high absorption of photons with energy higher than the energy band gap of the device. Gallium Arsenide (GaAs) is one of the most studied direct band gap materials for solar cells [31]. However, there are also reports describing the

properties of other direct band gap materials such as: Gallium Selenide (GaSe) [31].

The absorption coefficient associated with this type of semiconductors is as follows [32]:

$$\alpha(h\nu) = A(E_{ph} - E_g)^{1/2} \quad (1.4)$$

Where α , E_{ph} , E_g and A are absorption coefficient, photon energy, energy band gap and a direct band gap material constant respectively.

- Indirect band gap semiconductor: In this type of material the transition of electrons from valence to conduction band is indirect (i.e. the minimum energy level of the conduction band is not aligned with the maximum energy level of the valence band [30]). Therefore, for the transition of the electron to take place the photon must carry sufficient momentum to satisfy the momentum conservation Eq. (1-2) [30]. This reduces the chances of photon absorption since not all incident photons with energy higher than the energy band gap of Silicon (i.e. 1.1 eV) are absorbed. Nevertheless, photons with energy higher than 3 eV in Silicon can lead to a direct transition. Examples of other indirect band gap materials are: Germanium (Ge) or Gallium Phosphide (GaP).

The absorption coefficient associated with this type of materials is as follows [32]:

$$\alpha(h\nu) = B(E_{ph} - E_g)^2 \quad (1.5)$$

Where α , E_{ph} , E_g and B are absorption coefficient, photon energy, energy band gap and an indirect band gap material constant respectively.

In the solar cells, a direct band gap material is preferred. Devices with direct band gap materials on their active layer are likely to have high conversion efficiencies. However, Silicon which is an indirect band gap material (very abundant on Earth and non-toxic) is the most popular active material in the solar cell industry. This is due to the influence of the IC design industry (Silicon based). This influence led to a strong development of solar cell devices based on Silicon until the limitations of Silicon for photovoltaics were identified. Since then, scientists have tried to improve the performance of devices with direct band gap materials to experimentally compete with those solar cells made of Silicon. The band energy profile needs to match better with the solar spectrum and a direct transition should enable a thinner active layer (reducing costs). A more detailed explanation on the consequences and possible solution will be discussed in Section 1.3.

Characterisation of electrical properties:

- Recombination [23, 33, 34]:

This parameter represents the phenomenon by which electron-hole pairs generated via the photovoltaic effect separate without contributing to the photo current. In a solar cell it is required to control it since it can severely alter the energy conversion. The challenging process of surface passivation can help to reduce the negative effects of recombination on the performance. There are various types of recombination:

- Non-radiative: An electron stays at an energy level which is generated due to defects in the semiconductor material. The non-radiative recombination takes place in the case of a hole from the valence band travelling to the same energy state as the electron. This recombination does not cause the emission of a photon but the energy of the electron-hole pair will be lost. It slows down the process for the carrier density to recover which leads to a lower V_{OC} [35]. A defect can be introduced for example when doping the semiconductor material.

- Auger: It is a type of non-radiative recombination. The difference lies in how the electron is excited to a higher energy state. In this case when an electron-hole pair recombines, there is no emission of a photon or heat as in non-radiative recombination. However, in this case the energy is transferred to an electron which is in the conduction band and then is excited to a higher energy state [20].

- Radiative: An electron from the conduction band bonds with a hole on the valence band. From this combination a photon is emitted with energy similar to the band gap of the material. This process is very frequent in direct band gap materials. In the case of solar cells with indirect active material such as Silicon, it can be neglected.

- Open circuit voltage (V_{oc}) [23]:

This is the voltage across the solar cell when it is not connected to any external circuit. This is the maximum voltage that the solar cell is able to produce. Therefore, the V_{oc} value largely affects the performance of the solar cell.

However, under this condition there is no current flow and hence there is no power delivered. The higher the value of the open circuit voltage the lower radiative recombination is. Hence, V_{oc} is an indicator of the recombination level of the solar cell. Furthermore, V_{oc} is dependent on the photogenerated current density and the saturation current. This is due to the open circuit voltage dependence on the radiative recombination that takes place in the device. Furthermore, the V_{oc} is closely related to the energy band gap of the material since the larger the band gap the higher the V_{oc} .

- Short circuit current (I_{sc}) [23]:

This is the current when the terminals of the solar cell are short circuited. The value of the short circuit current density can vary depending on the flux density incident on the solar cell. For this reason, the measurement of the

short circuit current density, during the developing stage, is done using a standard solar spectrum. The solar spectrum that is conventionally used in the field of solar cells is known as the AM 1.5 solar spectrum [36] (to be discussed in Section 2.3.7). The value obtained from measuring the current, while the terminals are short circuited, is the maximum current the solar cell is able to produce. Similar to V_{OC} there is no power delivered. Under this condition the voltage across the device is minimum. We want to have the short circuit current as high as possible to achieve a high power delivery when in operation.

- Fill factor (FF) [23]:

The information provided by this parameter is how close the performance of the device (delivering maximum power) is to its ideal performance. The maximum power delivered by the solar cell will be achieved when the product of voltage and current delivered are maximum. The maximum value of voltage (V_{OC}) is achieved only when the current is minimum and the maximum current delivered (I_{SC}) is achieved only when the voltage is minimum. In the cases where either voltage or current are prioritised for a specific application, there is a trade-off between current and voltage. This trade-off will have an impact on the maximum power delivered and hence lower the FF value. This is a key factor that shows the ratio between the maximum power available from the solar cell and ideal maximum power of the device. The idea is to have a Fill Factor as close to ideal as possible (i.e. 1).

$$FF = \frac{V_{MP} * I_{MP}}{V_{OC} * I_{SC}} \quad (1.6)$$

Where V_{MP} is the voltage at maximum power and I_{MP} is the current at maximum power.

- Conversion efficiency (η) [23]:

This parameter represents the amount of electricity generated by the solar cell (in percentage) compared with the generated electricity in the ideal

case. This means, in the ideal case where all the incident photons on the solar cell contribute to current generation.

$$\eta = \frac{J_{SC} * V_{OC} * FF}{P_{IN}} \quad (1.7)$$

Where P_{IN} is the power of the incoming light.

These optical and electrical properties may be affected also by external parameters. Some of these parameters and their consequences are introduced as follows:

- Temperature: When there is light incident on the solar cell, part of the energy from the photons, with energy higher than the band gap (please refer to the discussion on basic solar cell), is liberated as heat. Investigations on the effect of increasing operating temperature of solar cells have reported a lower output power as well as lower conversion efficiency [37]. An approach to reduce the unwanted effects is to extract the heat by cooling down the solar cell [38]. This can be done by using photovoltaic thermal collectors [38].
- Partial shading: Since solar cells are deployed outdoors, it is possible that the shadow of some objects (i.e. trees or buildings) may partially block the sunlight from the solar cell. Similarly, it is also unavoidable for particles such as dust or snow to be placed on its surface. The amount of particles on the surface will determine how much it affects the performance [39, 40]. If the amount of particles is small (soft shading) the output voltage remains the same but the output current reduces [39]. In the case of the amount of particles being large (hard shading), light does not reach the solar cell and it affects both output voltage and current [39]. Therefore, it is essential to maintain the solar cell surface free of particles by cleaning it weekly or in some scenarios on a daily basis [40].

- Moisture: As solar cells approach the end of their life time, the probability of moisture inside the solar cell increases. However, this problem can also be present at any moment through the solar cell life time. It is due to the failure of the encapsulation of the solar cell (every commercial solar cells is encapsulated). In this scenario, the mobility of electrons and holes decrease [41]. Furthermore, in some cases there is even a delamination of each individual layer [41]. The best solution to minimise the presence of moisture is to take extra care while encapsulating the solar cell.

In addition to these parameters there are other internal parameters severely affecting the performance of the solar cell. These parameters were reported to limit the efficiency of solar cells. This limit is known as Shockley-Queisser limit [42] which is discussed in the following section.

1.3.1.5 Shockley-Queisser limit

In 1961 a group of researchers led by Shockley and Queisser calculated the theoretical efficiency limit for a single junction Silicon solar cell [42]. To achieve this target, they developed a detailed balance analysis where they used some assumptions. They considered that the solar cell was in equilibrium and at room temperature [23]. There was a perfect absorption which implies that the solar cell was thick enough to successfully absorb all the incoming photons [23]. In addition, each of the absorbed photons generated an electron-hole pair [23]. All recombination processes taking place in the device were limited to radiative recombination. Finally, it was assumed that there was a perfect collection [23]. This implied that each and every electron-hole pair generated was collected.

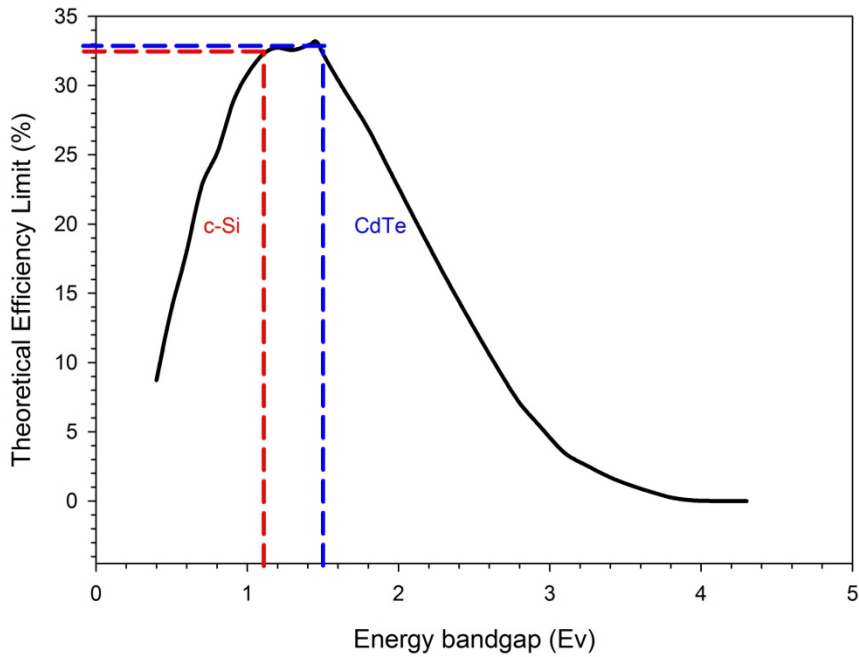


Fig. 1.9. Efficiency vs. Energy band gap of the active material according to the detailed balanced analysis presented by Shockley and Queisser [42].

From Fig. 1.9 it is possible to see the result of the detailed balance. The theoretical maximum efficiency is shown for a range of Energy band gaps. In the case of Si (the most popular active material for solar cells) the 1.1 eV energy band gap leads to an efficiency limit of $\approx 33\%$ as shown in Fig. 1.9. Since this efficiency limit was reported, to overcome it has become the target of many researchers. However, for a single junction Silicon solar cell the conversion efficiency still has not reached the limit. The highest efficiency for this type of solar cell is reported to be 25.6 % [18, 19]. Some researchers have tried to use absorbing materials different from Silicon such as GaAs [43-45]. Others have tried to increase the number of junctions and even concentrate the sunlight onto a multijunction solar cell. In the next section, multijunction solar cells are discussed.

1.3.2 Multijunction solar cells

Multijunction solar cells have the same function as single junction solar cells which is to generate electricity from sunlight [1]. The difference lies in how much of the solar spectrum is used to generate that electricity [46, 47]. In the case of

a single junction solar cell, there is only one absorbing material generating one electron-hole pair per photon absorbed. This happens only when the energy of the incident photon is larger than the energy bandgap of that material. When the energy of the photon is larger than the bandgap, the same number of electron hole pairs is liberated. The excess energy is liberated as heat [48]. Hence, the extra photon energy does not contribute to generate more photocurrent. Alternatively using multijunction solar cells to optimize the solar spectrum can improve the impact of high energy photons. Multijunction solar cells enable different wavelength ranges of the solar spectrum, to be absorbed in different active layers [49].

The idea is to cover the entire spectrum by intelligently placing various absorbing materials [46, 47]. The material to absorb the shorter wavelength range of the solar spectrum is placed on top of the solar cell [49]. Meanwhile the material to absorb the longer wavelengths is placed underneath [49]. In this manner, the energy of the photons is used more efficiently [17]. Only a single electron-hole pair is generated from a single absorbed photon with energy larger than the energy bandgap of the absorbing material. When the photon energy is much larger than the energy bandgap, the excess energy is liberated as heat. In the case of shorter wavelength photons, the energy is larger than in the case of longer wavelength photons. Therefore, with more than one junction it is possible to optimise absorption of the solar spectrum better. High energy photons are absorbed on the top layer avoiding additional heat which could deteriorate performance. Whereas lower energy photons which have a longer wavelength can penetrate to lower layers and can still be absorbed. This concept is not limited to two active layers, it can be applied to a larger number of active layers. Theoretically, the conversion efficiency limit for an infinite number of active layers is 86% [50, 51]. However, the larger the number of active layers the more complex and costly the solar cell becomes. All these together have helped to achieve very high efficiencies such as 37.8% [18, 52]. This high efficiency was achieved using a five junction solar cell. The bandgap for each layer is as follows: top 3 layers had bandgaps 2.2, 1.7 and 1.4 eV and were grown inverted on GaAs substrate. The two bottom layers had bandgap 1.05 and 0.73 eV and were grown upright on InP substrate. The GaAs substrate was removed after bonding the layers together. The V_{oc} , J_{sc} and FF values for

this five junction solar cell were 4.78 V, 12.0 mA/cm² and 83.5 % respectively [18, 52]. These values show how well a multijunction solar cell can perform.

However, even if there are many advantages of using this type of solar cells, their use is limited to specific scenarios. This is due to the higher costs associated with the fabrication techniques required [1]. For example, it is possible to see this type of solar cell in aerospace applications [1]. In terrestrial applications, currently multijunction solar cells are limited in use for concentrated solar cells [53] (to be discussed in Section 1.3.5). The most popular solar cells have crystalline silicon (c-Si) as the active material which are discussed in the following section.

1.3.3 Crystalline Silicon solar cells

Among all solar cell technologies, c-Si solar cells enjoy the largest market share (~90%) [23]. In addition, this type of solar cells is normally known as “traditional” solar cells and first generation solar cells [1]. Silicon is a material widely available on Earth and it is not a contaminating material [54]. The first solar cell in 1950s was made using this technology and there has been a massive development since then [5]. That is partially due to the influence of the integrated circuits industry. The good understanding on Silicon properties for bipolar junction transistors enabled the development of Silicon for solar cells [1]. Currently, this type of solar cell holds the highest conversion efficiency on record for a single junction solar cell 25%, with Voc= 0.740 V, Jsc=41.8 mA/cm² giving FF=82.7% [18, 19]. In addition to this, as of 2013, it enjoyed 90% of the solar cell market share.

Crystalline Silicon solar cells have some limitations associated with them due to the usage of Silicon as the absorbing material. Silicon has an indirect band gap at the wavelength where the solar spectrum has its maximum irradiance [46, 47]. As a consequence, the absorption of photons is not as efficient as expected. This means that the silicon layer needs to be very thick in order to maximize the absorption of the solar spectrum [1]. This leads to higher fabrication costs. In an attempt to reduce the fabrication costs, researchers

have developed new types of solar cells with thinner active layers [55]. In the next section, the most important thin film solar cells are discussed.

1.3.4 Thin film solar cells

Thin film solar cells discussed in this section are grouped as the second generation of solar cells. Many researchers found the development of this type of solar cells for achieving high efficiencies while reducing material costs as an attractive challenge [55]. Different thin film solar cells were tested but the following three types of solar cells were the most promising ones: amorphous Silicon (a-Si) solar cells, Cadmium Telluride (CdTe) solar cells and Copper Indium Gallium Selenide (CIGS) solar cells. In the following sections these types of solar cells are discussed, starting the discussion with a-Si solar cells.

1.3.4.1 Amorphous Silicon (a-Si) solar cells

Among the three types of solar cells mentioned above, a-Si solar cell has been developed faster than the others [1]. It is commonly found in calculators powered by solar power [56]. The active layer is a-Si which means that the active material does not have a crystal structure [55]. As a consequence, the absorption length of a-Si is shorter than that of crystalline Silicon [57]. It results in better photon absorption which enables a thin active layer with energy bandgap 1.75 eV [58]. There are other advantages of using a-Si such as: it is an abundant and non-toxic material, has capability for large scale production and a low temperature growing process [58].

However, the defects that a non-crystalline structure introduces lead to nonradiative recombination lowering the efficiency to about 11% [44]. Moreover, after the first 1000 hours of the solar cell installation, there is a drastic conversion efficiency drop [58]. This is called the photo degradation effect which is known as Staebler-Wronski photodegradation [1, 59]. The reason of this efficiency drop has not been clearly identified yet [59, 60]. The usage of Hydrogen molecules for forming a-Si has been pointed as a possible explanation for the degradation [59]. It is important to indicate that once the efficiency has dropped, it remains at this value [60]. Nevertheless, this issue

has limited the applications of this type of solar cells despite the extensive research on the area [1]. The effect of the photodegradation can be reduced by using a thinner layer. However, a thinner layer reduces absorption requiring optical confinement complicating the process. The highest efficiency recorded for this type of solar cell is 10.2% with $V_{oc}= 0.896$ V, $J_{sc}=16.39$ mA/cm² giving FF=69.8% [58]. The photodegradation and the conversion efficiency, lower than traditional solar cell, made researchers to continue the search for new active materials [58]. In the following section CdTe solar cells are discussed.

1.3.4.2 Cadmium Telluride (CdTe) solar cells

Cadmium Telluride (CdTe) is a material which has a bandgap of 1.5 eV [58]. This is close to the theoretical value considered as ideal for high conversion efficiency [61, 62]. From Fig. 1.9 it is possible to identify that 1.45 eV is the ideal band gap to satisfy the theoretical maximum efficiency of 33% predicted by Schokley and Queisser [62]. The absorption coefficient of this material is $\approx 10^5$ /cm in the visible region [58]. This means that for the active layer thickness to absorb 90% of the arriving photons only few micrometres are required [58]. The theoretical efficiency for this type of solar cells oscillates between 28% and 30% [58, 63-65]. However, the efficiencies achieved are far from this value. In optimum conditions, in an experimental lab, CdTe solar cells have been reported to reach 21% energy conversion efficiency [18, 66]. This optimum solar cell has $V_{oc}= 0.8759$ V, $J_{sc}=30.5$ mA/cm² giving FF=79.4% [66]. The technology involved in the fabrication process of CdTe solar cells is has developed very fast in the last decades [67]. Nowadays the improvement in the field is mainly limited to the improvements recorded by First Solar [68]. Nevertheless, the expectations for further improvements are still high due to the state of the technology involved in the fabrication of CdTe solar cells [68]. It is possible to achieve solar cells with efficiency higher than 10% by applying several manufacturing methods. This is promising for the future of this technology since it indicates low dependence on a single fabrication procedure.

However, there are problems associated with this technology. First of all, Cadmium is a polluting material that affects the environment. What is worse, it

is harmful to the health of human beings [1, 69]. In Europe some countries are concerned about the health and environmental impact [70]. However, there are researches that claim a low risk of environmental impact when CdTe solar cells are placed in residential areas on rooftops [1]. In any case, caution must be taken when recycling all the components of the solar cell [71]. Currently there are companies manufacturing solar cells using this technology. The market share of this type of solar cells is growing but it is small still compared with other technologies. The market share for CdTe solar cell is recorded to be 6% as of 2007 [72]. This is due to lower conversion efficiencies than traditional Silicon solar cells. In the following section CIGS solar cells are discussed.

1.3.4.3 Copper Indium Gallium Selenide (CIGS) solar cells

Copper Indium Gallium Selenide solar cells have the potential of low processing cost. It is a direct bandgap material with energy bandgap 1.53 eV which enables a thin active layer [58]. In addition, there is no polluting component involved in this technology [55]. Further, there is no evidence showing that it is harmful to human beings [55]. Moreover, it offers the possibility of flexible solar cells. This is a very promising characteristic since it enables integrating solar cells into new buildings. In terms of fabrication processes, it introduces the option of the so called roll-to-roll approach. It represents a much simpler manner to mass produce this type of solar cells. The highest energy conversion efficiency reported for this technology is 21% [18, 73]. The Voc of this solar cell is 0.757 V and Jsc is 35.70 mA/cm² giving a fill factor of 77.6% [73].

There are many promising advantages to manufacture CIGS solar cells that have been identified by scientists over last decades [74, 75]. However, up to date it has not been successfully produced CIGS solar cells in large scale [74, 75]. The reason is that, the manufacturing process has not been successfully established in the industry. Commercial CIGS solar cells have not achieved either high efficiencies or low costs as promised [1]. Hence, many companies focusing on this technology had financial difficulties and were forced to close down [1]. In the following section concentrated solar cells are discussed.

1.3.5 Concentrated solar cells

The difference between conventional solar cells and concentrated solar cells lies in a system that focuses the incident sunlight onto a specific point [1, 47]. A small multijunction solar cell is generally placed on this point. The small size compared to non-concentrated solar cells allows the usage of highly efficient and more expensive cells. Figure 1.10 presents a concentrated solar cell with the mirrors focusing the light on the multijunction solar cell [53]. In this way the intensity of the light reaching the solar cell is very high [76]. Since the intensity of the light increases, the chances of absorbing a photon increases as well. Hence, the conversion efficiency of concentrated solar cell increases when compared with non-concentrated solar cells.



Fig. 1.10. Typical concentrated solar cell [77].

However, there are some essential settings and maintenance required to achieve high efficiency [78]: the position of the mirrors with respect to the sun must be optimized, the surface of the multijunction solar cell must be free of dust or dirt and the structure supporting the solar cell must be in good condition. In this way it is ensured that the mirrors concentrate the light on the solar cell throughout the day [78]. Otherwise the focusing mirrors simply would not be as efficient as they are meant to be. For this purpose, it is conventional that concentrated solar cell systems are equipped with a solar tracking system [47,

79]. This device would keep as constant as possible the angle between the solar cell and the sun. Hence, it is ensured that the position of the mirrors would allow for maximum concentration. There are different types of tracking systems:

- Single axis tracking system: This tracking system can only rotate the solar cell in one direction to follow the trajectory of the sun [80].
- Two axes tracking system: This tracking system can rotate in two directions. These directions are normally perpendicular to each other. Hence, it is possible to track the trajectory of the sun more accurately [81].

Up to now, the highest efficiency has been reported for concentrated solar cell systems with a value of 46% [82]. These systems require a high maintenance due to the tracking systems required for optimum operation [47]. This turns into a high cost for installing concentrated solar cells even though the costs have reduced significantly [83]. In 2013, the costs of installing solar cell power plants for 10 MW were within the range of 1400 €/KW and 2200 €/KW [83, 84]. Moreover, the concentration of the sunlight onto the multijunction solar cells leads to overheating the device [1]. This can deteriorate the performance of the solar cell unless cooling systems are deployed to reduce the temperature [85]. In the following section solar cells made of organic materials are discussed.

1.4 Organic solar cells

Organic solar cells are considered to be in the group of third generation solar cells. When researchers started to work on organic solar cell the expectations were: high efficiency, thin solar cell, flexibility, integration on buildings and easy mass production process, etc. [1, 47, 86]. The absorption coefficient of organic materials is larger than the absorption coefficient of inorganic solar cells. In the case of organic materials, usually it is larger than 10^5 cm^{-1} [87]. This enables a high absorption of the solar spectrum even for solar cells as thin as 100 nm [87]. The development of this technology has required new fabrication techniques and new application opportunities [88]. With the development of these techniques, the energy required for fabricating an organic solar cell is less

than the energy required to fabricate a traditional solar cell [86]. Furthermore, flexible organic solar cells can be achieved thanks to the usage of new materials. This can stimulate the integration of solar cells when making new buildings [47]. Furthermore, the fabrication process is simpler than the fabrication process for inorganic solar cells.

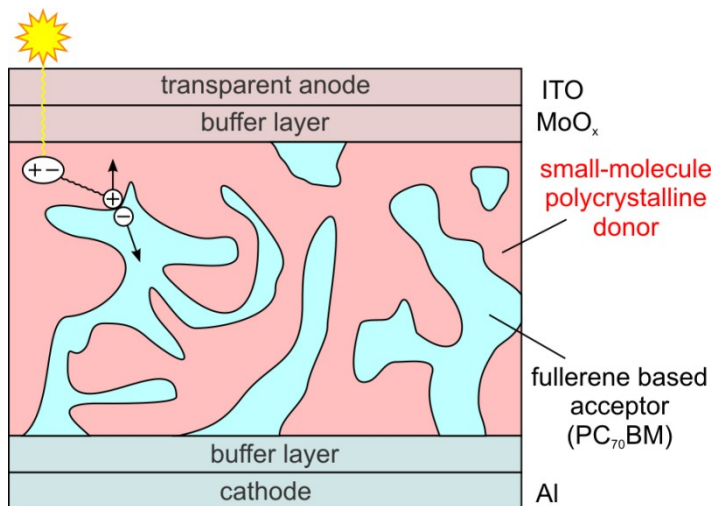


Fig. 1.11. Schematic of a bulk-heterojunction solar cell [89].

At the beginning of the development of organic solar cells, the challenge was how to achieve current flowing through an external circuit. Energy bands are not well defined in organic materials which makes it difficult to transport the generated carriers [86]. In organic solar cells, the photogeneration process is different than for inorganic solar cells [90]. In this case there are no n or p-type materials but photogeneration takes place due to the presence of two types of materials: a donor and an acceptor [91]. An example of a donor material is Copper Phthalocyanine (CuPc) and examples of acceptor materials are Perylene Tetracarboxylic derivatives and Carbon₆₀ (C₆₀) (member of a compound family known as fullerenes). The incident photon is absorbed, the donor material generates an exciton (electron-proton pair) [86]. Then the exciton diffuses towards the acceptor which is where the separation of carriers takes place [86]. When the exciton reaches the acceptor, it splits and the proton returns to the donor. At this moment, the energy from the electron is transferred to the acceptor [86]. This is called a polaron which is dissociated by applying an external voltage. Thereafter, the electron and the hole are delivered to the contacts and flow through the circuit [86], contributing a photocurrent.

This process involves many challenges, such as the diffusion length of the exciton being very short [86]. This implies that while the exciton diffuses towards the acceptor it can recombine; not contributing to the photocurrent [91]. A solution to overcome this is the adoption of the bulk-heterojunction (see Fig. 1.11 for reference) which mixes up both donor and acceptor materials [86]. As a result, the exciton does not need to travel a long distance to reach the acceptor.

Organic solar cells have a great promising feature of flexibility which may enable solar cells to be used in future applications, such as: built-in in new buildings or in clothing, etc. However, the efficiency of organic solar cells is much lower than for inorganic solar cells. The best conversion efficiency achieved for an organic thin film solar cell is 11% with $V_{oc} = 0.739$ V, $J_{sc} = 19.40$ mA/cm² and FF = 71.4 % [92]. Hence, organic solar cells do not have a large market share. Their market share in 2013 was recorded as 1.5% [93]. In recent years the focus has been on new type of solar cells combining both inorganic and organic active layers [94]. They are called perovskite solar cells and are discussed in the following section.

1.4.1 Inorganic-Organic Perovskite solar cells

Perovskite solar cell is a new solar cell type that has emerged in recent years and is developing rapidly. This type of solar cell is an alternative to overcome the difficulties associated with organic and inorganic solar cells. Perovskite solar cells combine inorganic and organic materials into a molecular composite [94]. Taking into account the differences between inorganic and organic materials, it is possible to create new materials by controlling the size of the crystal cell [94, 95]. In terms of the electrical performance of the device, it is not clear whether Perovskite solar cells perform like inorganic solar cells (generating electron-hole pairs) or like organic solar cells (generating excitons). Recent reports suggest that Perovskite solar cells primarily generate electron-hole pairs contributing to photocurrent under sunlight [96]. Therefore, Perovskite solar cells perform similarly to inorganic solar cells. However, there is also evidence of exciton generation that does not contribute to the photocurrent [96].

Independently from the aspects to be clarified, there are some well known advantages associated with Perovskite solar cells such as: easy fabrication process, strong solar spectrum absorption, high carrier mobility and a low level of non-radiative recombination [96]. However, there are still many unknowns associated to this type of solar cell such as: toxicity caused by the usage of lead during the fabrication process and a very fast degradation in the presence of moisture [96].

Perovskite solar cells were first reported in 2009 with a conversion efficiency of 3.5% [97]. This was enough to draw attention from various researchers who considered perovskite solar cell as a technology for the future. The pioneering work on perovskite solar cells presented by Lee et al., 2012, encouraged more investigation on this type of solar cells. This work was based on a perovskite absorber mesoporous TiO₂ as the n-type material and 2,2',7,7'-Tetrakis(N,N-di-p-methoxyphenylamino)-9,9'-spirobifluorene (spiro-OMeTAD) as the p-type material. This solar cell showed an energy conversion efficiency of 7.6% with $J_{sc} = 17.8 \text{ mAcm}^{-2}$, $V_{OC} = 0.80 \text{ V}$ and $FF = 0.53$ [94]. In the same work, Lee and his team proved that replacing TiO₂ with an insulator such as Al₂O₃ with the perovskite coated on top results in a better performance. The electrical performance improved instantly with an energy conversion efficiency of 10.9% [94]. The efficiency improvement is a result of a faster electron transport and an increase of VOC. Short circuit current density becomes $J_{sc} = 17.8 \text{ mAcm}^{-2}$, $V_{OC} = 0.98 \text{ V}$ and $FF = 0.63$ [94].

Since Lee et al., 2012 published their work, a lot of effort has been made to improve perovskite solar cells. Some researchers even attribute to perovskite solar cells the characteristic of self healing in terms of optical and electrical properties [98]. The highest energy conversion efficiency for perovskite solar cells is over 20% [18, 99]. This is still lower than the efficiency for traditional solar cells. However, within only 5 years the efficiency has been improved from 3.1% to 20% which is an indication of the high expectations on perovskite solar cells. Table 1.1 summarises the best electrical performance for various types of solar cells discussed thus far.

Solar cell type	V_{oc} (V)	J_{sc} (mA/cm ²)	FF (%)	Efficiency (%)
Single Junction c-Si [19]	0.74	41.8	82.7	25.6
Multijunction [52]	4.78	12	83.5	37.5
a-Si [58]	0.896	16.39	69.8	10.2
CdTe [66]	0.8759	30.5	79.4	21
CIGS [73]	0.757	35.7	77.6	21
Concentrated [82]				46
Organic [92]	0.739	19.4	71.4	11
Perovskite [99]	1.104	24.67	72.3	19.7

Table 1.1. Summary of best electrical performance for each solar cell type.

In the following section a discussion on the different techniques for reducing the reflection from solar cells is presented. The reflection from the solar cell surface is one of the most fundamental problems in the field of solar cells. When the reflection is high, there is a low percentage of the incident light that is transmitted to the active layer. This implies a decrease in the photon absorption. Therefore, if the reflection from the solar cell surface can be reduced, the chances of absorbing a photon will increase. The discussion starts with the anti reflection coatings technique

1.5 Different techniques to lower Reflectance

1.5.2 Anti reflection coatings

The idea of using an antireflection coating (ARC) is to reduce the reflection from the solar cell surface that arises due to the large refractive index difference between air and silicon. The concept of ARC is achieved by deploying a layer of a material with the refractive index value between that of air and Silicon [47]. As a consequence, the solar cell surface has an average refractive index in between that of air and silicon. Therefore, when the light is incident from air on the ARC coating, the Fresnel reflection is reduced at the interface between air and the ARC [100]. Similarly, the Fresnel reflection at the interface between the ARC and the silicon solar cell is reduced as well [100]. The reduction of the Fresnel equation leads to an increase of the transmission of incident light into

the Si layer of 8% [101]. The conversion efficiency of solar cells is limited by several factors such as contacts, recombination processes [90]. However, it is limited the most by a low transmission of incident light into the active layer [90]. Some of the materials typically used as ARC for solar cells are: SiO, SiO₂, Si₃N₄, TiO₂, Al₂O₃, SiO₂-TiO₂ and ZnS [102-105].

The disadvantage of this technique is the frequency dependence [106]. This is due to the fact that the refractive index of the materials used is not constant over the entire solar spectrum. The ARC is generally optimised at 0.6 µm [23]. The maximum number of photons of the solar spectrum is at this wavelength. However, for other wavelengths the reflection increases. At some wavelengths the reflection may increase as if there were no ARC layers present at all [107].

This concept can be taken further by deploying two layers on top of Silicon. In this case, the benefits of the ARC are expanded to more wavelengths [23]. Moreover, in theory this concept could be taken to the extreme with zero-reflection by an anti reflection coating with smoothly varying refractive index [28]. However, this solution is expensive due to the high precision layer deposition required. This is why researches are looking into alternative techniques that would ensure an effect over a large wavelength range. In the following section plasmonic solar cells are discussed.

1.5.3 Plasmonic solar cells

A different approach to reduce the reflection from a solar cell is to place a metallic nanoparticle either on the top of the solar cell surface or inside the active material of the solar cell [47]. The presence of the metallic particle enhances the transmission of the incident light into the active material. Furthermore, it also increases the light path inside the active material. Conventionally, the size of this metallic particle is in the nano scale. In this case, the wavelength of the incident light is longer than the particle. Hence, the metallic particle experiences an uniform field [47,108]. Hence, it oscillates as the incident wave passes through it, rather than reflecting the incident wave. This is the case only when the incident wavelength is equal to the resonant frequency of the metallic particle [47].

In the first case, the waves, which are incident on the metallic nanoparticle at this frequency, are scattered in many directions [108-110]. This leads to a significant increase in the transmittance into Silicon by about 9% compared with planar Si solar cells [109]. In addition to this, the conversion efficiency increases by up to 8% in an a-Si thin film solar cell by placing Au nanoparticles on top of the solar cell [111, 112]. Moreover, an increase in the photocurrent is achievable when Silver particles are placed on a plane wafer based solar cells [113].

In the second case, the interaction of the incident waves inside the active material and the nanoparticle is different [108, 110]. Since the nanoparticle oscillates with the wave passing through it, it generates a near field in the surroundings [47]. This field then can be absorbed by the active material [114].

When metallic particles are in use, as is the case with plasmonic solar cells, the lossy nature of metal is a characteristic to be taken into account. The metal particles can absorb a portion of the light. This is an unwanted consequence of using plasmonic solar cells [115]. Besides, the dependence of plasmonic solar cells performance on scattering of the light is strongly wavelength dependent due to its resonant nature [116]. Some researchers are trying to control it by engineering the refractive index of the particle or changing its dimensions [117, 118]. As a result, the refractive index of the metallic particle determines at which wavelengths the solar cell performs better [118]. This is a challenging parameter to optimize and in any case it will benefit the performance in a very narrow wavelength range.

However, any improvement on the performance of a solar cell ideally should have an influence in a wavelength range as wide as possible. Nevertheless, there is a solar cell type that allows a benefit over a wider wavelength range. Further, this improvement is achieved by engineering the structure of the solar cell unlike other techniques such as ARC or plasmonics. This is done by texturing on the solar cell a specific pattern. In the following section the most common texturing patterns are introduced.

1.5.4 Surface Texturing of solar cells

The main purpose of texturing the surface is to increase the chances of light absorption by increasing the number of times the light is incident on the solar cell (due to multiple reflections of light within the elements of the pattern) [115, 119-122]. Hence, the chances of absorption increase; reducing the reflection. In some texturing patterns there is an additional phenomenon playing a role: the texturing of the surface is perceived by the incoming light as an averaging effect of the refractive index. The average refractive index in the textured layer is higher than air and lower than Si. Therefore, this intermediate index leads to lowering of the Fresnel reflection. This is in addition to the reduced reflection due to multiple reflections.

Additionally, there is also the possibility of texturing the active layer of the solar cell which is effective but adds complexity. This is done to increase the light path of the light inside the active layer. The wavelength of all incident photons is not the same. Hence, by increasing the light path effectively the chances of photons, with longer wavelengths, contributing to photocurrent increases. This technique is known as light management and it is mainly used with thin-film solar cells. In the remainder of the section the focus is on texturing of the solar cell surface.

There are various options to choose in order to lower the reflection, such as: pyramid [123], nanowire [120] and micro pillar [124] solar cells. However, in the literature there are more exotic texturing patterns available such as: Si branched nanowires [125] or multidiameter nanopillars [126], moth eyes [127], nanowalls [128], nanocones [129] etc. The reported simulation studies of these patterns show a good optical performance that is difficult to replicate in experiments. In the following section the most important advantages and disadvantages for pyramid, nanowire and micro pillar solar cells will be discussed; starting the discussion with pyramid solar cells.

1.5.4.1 Pyramid solar cells

Texturing the surface of the solar cell with pyramids is an effective way to increase the number of times the photon hits the surface of the solar cell [123]. This leads automatically to an improvement in the absorption [119, 130]. Figure 1.12 presents a schematic diagram of a typical pyramid array. In the diagram, it is possible to see the interaction on the light with the pyramids by bouncing from pyramid to pyramid. This leads to higher photon absorption. This is the reason why pyramid texturing became very popular when scientists started to search for improvements on the crystalline silicon solar cell [23]. Baker-Finch et al. (2011) have reported that it is possible to improve the short circuit current density by about $0.39\text{mA}/\text{cm}^2$. A Silicon solar cell with standard pyramid texturing has a conversion efficiency of 18.6% with $V_{OC} = 624\text{ V}$, $J_{sc} = 38.26\text{ mA}/\text{cm}^2$, $FF = 78.1\%$ [131].

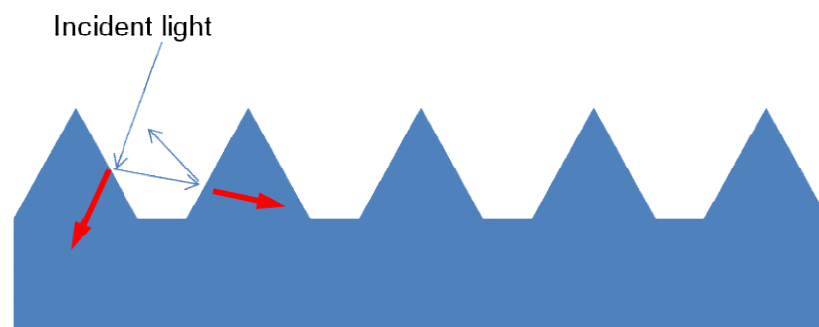


Fig. 1.12. Schematic of Pyramid texturing pattern.

In order to make this technology useful, the pyramid sizes need to be very large, within the range of $10\ \mu\text{m}$ [130, 132, 133]. In some solar cell types, the total thickness can be more than $125\ \mu\text{m}$ [134]. In these cases the texturing of large size pyramids can be neglected from the total thickness. On the contrary, for those types of solar cell where the size of the pyramid is comparable to the total thickness, the pyramid size cannot be neglected [130]. In those cases, texturing the surface with pyramids will lead to increased costs, opposed to the main target of that technology which is to reduce reflection and reduce material costs [130]. Furthermore, the surface recombination increases due to the surface-to-volume ratio [119]. A pattern that is capable of trapping the light with

a low surface-to-volume ratio is the moth eye pattern which is discussed in the following section.

1.5.4.2 Nanowires solar cells

The technology that is capable of lowering the reflection and at the same time not increasing in excess the total thickness is texturing nanowires [120, 128]. The size and configuration of the nanowires determine how well the incident light is absorbed. As with pyramid solar cells, the purpose is to increase the number of times the photon hits on the solar cell. The light path can be enhanced up to a factor of 73 leading to a higher J_{sc} compared to planar solar cells [120]. However, nanowire solar cells also use the principle of resonant trapping to enhance light absorption [135, 136]. In addition to this, there is also a refractive index averaging effect that helps to lower reflection [137]. Furthermore, the highest conversion efficiency achieved by texturing nanowires is 8.2 % [128].

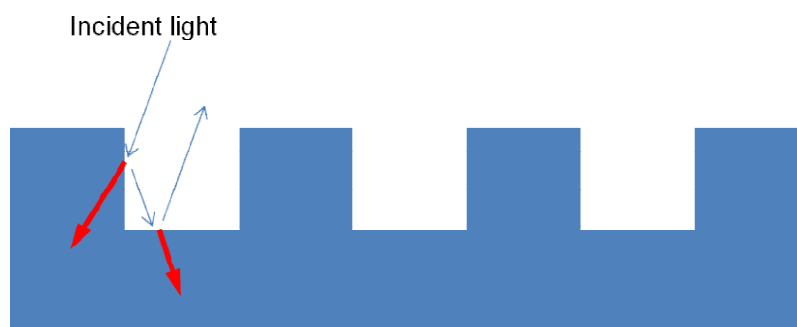


Fig. 1.13. Schematic of nanowire texturing pattern.

Figure 1.13 presents a schematic diagram of a nanowire array. These are circular shaped and grown vertically to have the appearance of a pillar/column. The diagram shows how the absorption of the incident light can be enhanced by bouncing between nanowires. Each time the wave is incident on the surface there is a chance of absorbing a photon as desired. There are parameters that define the optical properties of the pattern such as the diameter or height of the wires.

The problem of the surface recombination in the pyramid solar cell is still present in nanowire solar cells which leads to low charge carrier collection [120, 121, 138, 139]. In addition, for this technique to be useful it is beneficial to implement the radial p-n junction [140-143]. The radial p-n junction provides a low carrier collection path [124]. Besides, theoretical simulations have shown the benefits of using this type of p-n junction [144, 145]. In addition, it enables the usage of low quality Si [144, 145]. However, it is very challenging to make p-n radial junctions due to the small dimensions of the nanowires [121, 138, 139, 1124, 146]. Moreover, the growth process for the radial p-n junction introduces impurities on the interface between the p and n sides of the wires [143]. Therefore, the benefits of better photon absorption are partially reduced by the high surface recombination which translates into lower conversion efficiencies than expected. An alternative approach that delivers reflection reduction is the nanowall solar cell. In the following section the nanowall solar cells are discussed.

1.5.4.3 Nanowall solar cells

The solution of placing a nanowall pattern on top of a solar cell is an effective solution to reduce reflection. The reduction of the reflection can be achieved in a manner similar to the case of nanowire solar cells. The subwavelength nature of the pattern leads to a refractive index averaging effect at shorter wavelengths. Figure 1.14 a and b illustrate in a schematic the side view and the top view of the nanowall pattern. The top view presents the 2D nature of the pattern since it is formed by long nanowalls parallel to each other (nanowires 1D) [147].

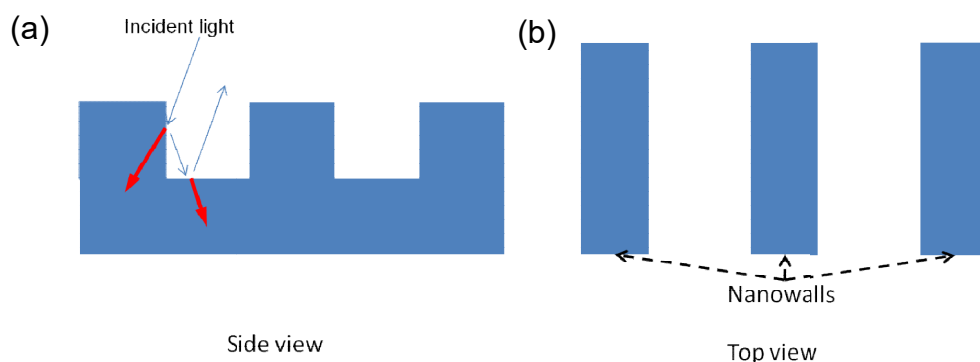


Fig. 1.14. Schematic of the nanowall pattern. (a) Side view. (b) Top view.

The nanowall pattern has some advantages in terms of the open circuit voltage [148]. Additionally, the short circuit current density also experiences an enhancement. The short circuit current density of a nanowall is 7 mA/cm^2 higher than that of a planar Si slab solar cell [149]. Moreover, the nanowall pattern is stronger than nanowires from a mechanical strength point of view [150, 151]. Furthermore, the nanowall pattern is currently being used to achieve a more efficient electron extraction in high efficiency perovskite solar cells [152]. One of the biggest challenges of fabricating nanowall solar cells is the small thickness of the nanowall [150]. Further to this, the current fabrication process (RIE) to create a nanowall pattern when the width of the wall is thinner than 10 nm has an impact on the performance [151]. Therefore, a fabrication method with less impact on the structure should be investigated.

The nanowall texturing pattern for solar cell has been studied over last decades. However, this pattern has not been as extensively investigated as other texturing patterns such as pyramid, nanowires, etc. Since the last decade, it started to draw more attention especially due to combination with other texturing patterns. For example, there are reports presenting a texturing pattern that combines nanowires and nanowalls together [148, 153-155]. Figure 1.15 illustrates the idea of combining nanowires and nanowalls in a schematic.

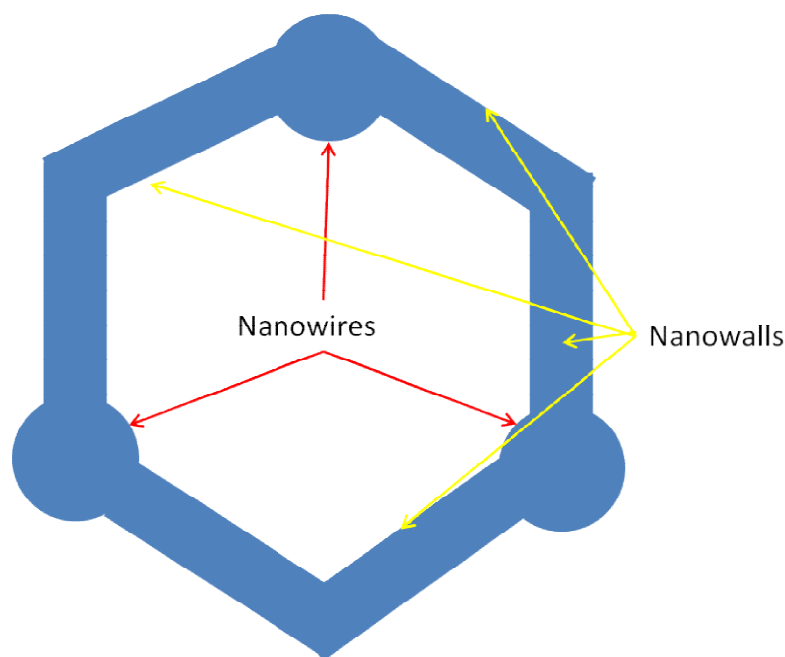


Fig. 1.15. Schematic of the resulting texturing pattern when combining nanowalls and nanowires.

This arrangement to combine nanowires and nanowalls is the one conventionally adapted. However, it should be noted that this is not the only arrangement possible. For example it is possible to arrange the nanowires and nanowalls randomly [154]. In either case the fabrication of such pattern is a challenging task. A texturing pattern that offers an alternative inspired in nature is the moth eye solar cell. In the following section moth eye solar cells are discussed.

1.5.4.4 Moth eye solar cells

There are many occasions when researchers inspire themselves in nature to find a solution to a problem or to discover something new. In the case of night moth's eye solar cells, researchers Bernhard, Mill and Moller inspired themselves on the surface of the eye of a night moth [156, 157]. This insect has its eyes coated by coned structure (hexagonally distributed), which minimize the reflection. In Fig. 1.16 the image of a night moth and the thin structure coating the moth's eye is presented. This special coating enables the night moth to see in darkness but with no reflection. Thus, it is more difficult for their predators to locate them.

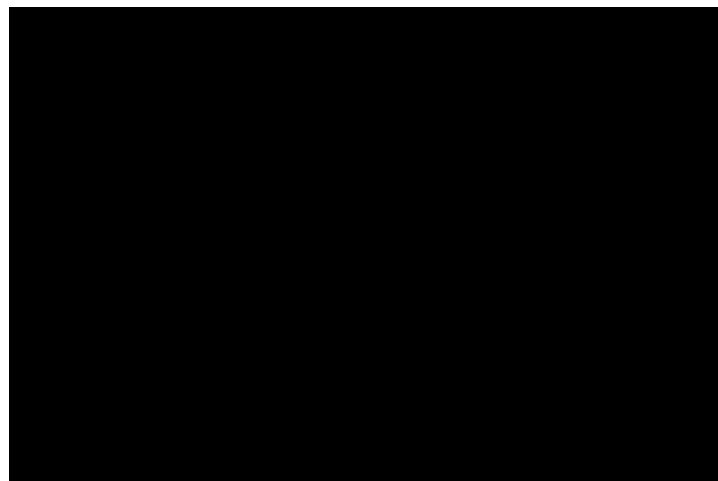


Fig. 1.16. Image of a moth and the image of the zoomed eye of the moth [158].

The key factor of this coating is similar to the one observed in the case of nanowires. The presence of a nanopattern with a period shorter than the wavelength of sunlight leads to a refractive index averaging effect [159]. As a consequence the transmission of any light incident on the surface improves

[159]. Nevertheless, even though the principle is the same, there are differences between moth eye and nanowire solar cells. Figure 1.17 illustrates in a schematic the cross section of the moth eye cone on the surface of a Si solar cell.

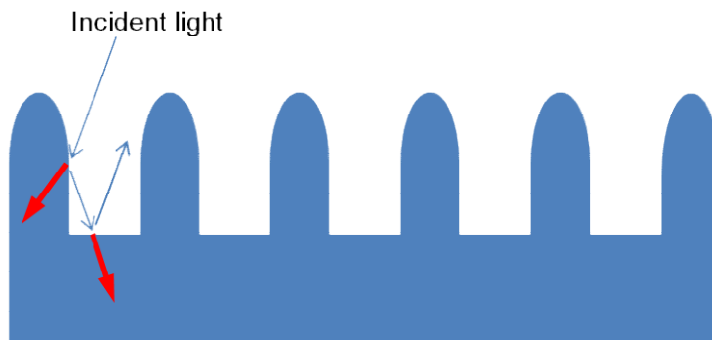


Fig. 1.17. Schematic of the moth eye coned structure.

Placing the moth eye pattern on top of the solar cell surface improves 6% (compared to planar slab Si solar cell) the transmission of sunlight perpendicularly incident onto the solar cell. This improvement is constant for a wide range of angle of incidence [160]. Additionally the improvement on the transmission leads to an improvement in the conversion efficiency of the solar cell. When the sunlight is perpendicularly incident on the solar cell the conversion efficiency is increased by 3.78% compared to the planar Si solar cell [160]. Then as the angle of incidence increases to 80% the improvement in the conversion efficiency compared with the planar Si solar cell case is 23.48% [160]. Therefore, placing the moth eye patterns offers a performance improvement. However, the moth eye pattern has a main drawback such as the lack of suitable coating materials [160]. Additionally, the fabrication process of the moth eye pattern is complex and requires a development to facilitate the reproducibility of the moth eye pattern [160]. Furthermore, similar to the nanowire solar cell the surface recombination may diminish the optical performance due to the surface-to-volume ratio. A different approach to reduce the reflection from the solar cell surface is the nanocone solar cell. In the following section the nanocone solar cells are discussed.

1.5.4.5 Nanocone solar cells

An alternative to the moth eye array is to place an array of nanocones on top of the solar cell. Nanocone solar cells have the advantage of providing excellent light trapping [162]. The highest efficiency obtained when placing nanocones on the surface of a solar cell is 17.1% [163, 164]. The basic physical phenomenon of nanocones is similar to that of nanowires and moth eye [162]. The transmission of incident light on the solar cell is enhanced due to the refractive index averaging effect [162]. However, there are some differences such as the angle of the side wall of the nanocone [163]. Figure 1.18 a presents in a schematic the nanocone pattern and Fig. 1.18 b shows the top view of a single nanocone illustrating its circular nature.

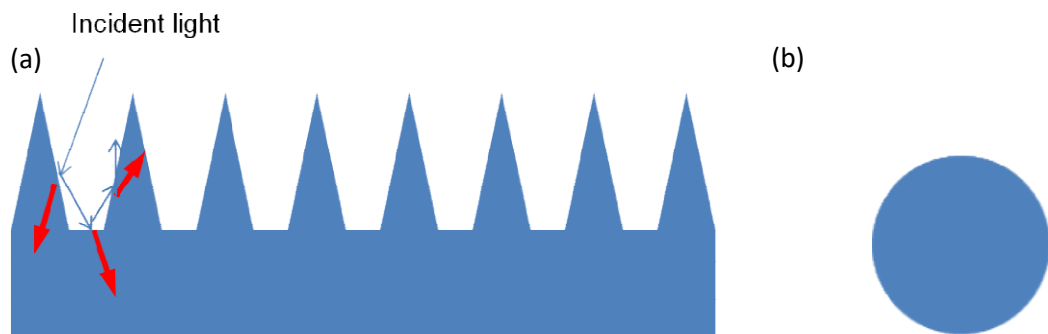


Fig. 1.18. (a) Schematic of a nanocone array. (b) top view of the pattern.

The angle of the side wall of the nanocone has a strong impact on the performance of the nanocone array [163]. Firstly, the effective refractive index of the pattern varies from the top to the bottom of the nanocone [163, 165]. Therefore, refractive index averaging effect is slightly different when compared to nanowires or moth eye. Secondly, when the sunlight is incident on the sidewall of the nanocone it has a different angle of incidence compared to being incident on the nanowire [163]. This difference in the angle of incidence is important due to the amount of reflection but also because it enhances second chance absorption. The second chance absorption enhancement is due to the trajectory of the reflected waves after first hit (first chance absorption) on the pattern [163]. By using this texturing pattern the absorption of sunlight at normal incidence improves by 45% compared to planar Si slab solar cell [165].

Nevertheless, there are also some disadvantages associated with nanocone arrays. One of the disadvantages is the electrical performance of the nanocone array compared to nanowires [163]. This difference is especially noticeable when considering radial p-n junctions [163]. Additionally, the wavelength dependent of the refractive index averaging effect leads to good absorption at shorter wavelengths [163]. However, at longer wavelengths the absorption reduces drastically reaching levels lower than for the planar Si slab solar cell [165]. This scenario is not ideal for solar cell applications due to the wideband nature of the solar spectrum. Moreover, the size of the nanocone leads to a fabrication process that requires high precision to reproduce the pattern [163].

There is another alternative texturing pattern called micro pillar array solar cells. This texturing pattern has proven to be effective when reducing the reflection. Additionally, the electrical performance of the device is better than other patterns. Furthermore, the dimensions of this texturing pattern enable an easier growing process to make a radial p-n junction. In the following section micro pillar array solar cells are discussed.

1.5.4.6 Micro pillar solar cells

An alternative technique to reduce reflection is micro pillar solar cells [124, 166-168]. To achieve the reduction of the reflection similar principles apply in micro pillar and nanowire solar cells. However, the size of the micro pillars makes a difference. Since the dimension of the micro pillar is larger, it is easier to make p-n radial junction in micro pillar solar cell [121, 124, 167]. Furthermore, in terms of energy conversion it has been proven that micro pillar array solar cells show a considerable improvement with respect to the levels of nanowire solar cells [169, 170]. For example, values of $V_{oc} = 0.6 \text{ V}$ have been achieved, which is higher than the equivalent nanoscale approach. Moreover, Shin et al. 2012 have reported that by reducing the thickness of the substrate, the electrical properties of the solar cell will improve. In this particular case, the dimensions of the micro pillar were height = $10 \mu\text{m}$ and diameter = $2 \mu\text{m}$, where the substrate reduced from 325 to $40 \mu\text{m}$ [167]. This difference is attributed to recombination processes together with no contribution to the efficiency of all

photogenerated carriers in the case of thicker substrates [171, 172]. In addition to this Shin et al. 2012 also found that J_{sc} increases with the diameter [167]. This increase reaches values larger than theoretical predictions [172]. However, a large diameter value means that the surface-to-volume ratio is very high. Hence, the surface recombination can increase as well. The highest efficiency obtained using this technique is 8.7 % [166].

In this thesis, a study on how to optimize optical properties of micro pillar arrays is introduced in Chapter 3. In particular, the focus is on the ratio between the height and the diameter. The results indicate that the best performance is achieved for high value of this ratio. In fact, there is a convergence of the optical performance for all values of diameters analysed. Nevertheless, the surface-to-volume ratio can become very large. This can affect the surface recombination and lower the energy conversion efficiency [33]. Surface recombination needs to be a concern for researchers on this area to achieve high efficiency.

In this thesis, the concept of micro pillar arrays has been taken further by trying to reduce surface recombination. A new design where the sizes of the pillars are tilted rather than vertical is presented. The results are very promising since the new design improves the light trapping properties and hence reduces the reflection. Furthermore, the surface-to-volume ratio, required for best performance, is much lower than for traditional vertical micro pillars. Therefore, this design is expected to provide a lower surface recombination. A low surface recombination together with low reflection are very promising features which will be presented in Chapter 4.

1.6 Summary

In the current energy generation scenario, solar cells are gaining importance. There are various reasons for that: environmental benefits, government policies and a very large development of the technology involved. So far the solar cell technology with largest market share is crystalline silicon solar cells with up to 90% of market share. However, there are issues associated with this technology such as costs and efficiency limits.

In this Chapter, a summary of the current status of the solar cell field has been presented. The advantages and disadvantages of the basic and most promising technologies have been explained. Nowadays, there are new types of solar cells under development and their market share will increase soon, such as: CdTe, organic solar cells or perovskite solar cells.

However, to achieve this, it is essential to reduce the reflection from the air-solar cell interface. This is a common issue for any type of solar cells. There are various ways of achieving this such as deploying an ARC layer or including metallic particles on the solar cell (i.e. plasmonic solar cell). However, the most promising thus far in terms of reducing the reflection is texturing the surface of the solar cell since it has been reported to be very effective. Among the different texturing techniques discussed, micro pillar is the most interesting texturing pattern. It is effective and less frequency dependent than other techniques. Among the different texturing patterns in the literature, such as: pyramid, nanowire or micro pillar array, the latter one is the pattern that provides more benefits. It has very good light trapping properties which help to reduce reflection from the surface. Moreover, the electrical performance associated to this type is better than for other texturing patterns.

It is important to have a clear relation between the pillars dimensions (i.e. height, diameter) and the solar cell performance. Besides, it is known that the percentage of the pillars occupying the solar cell affects performance. However, there has not been any study focusing on how this percentage affects performance. The work presented in this thesis, aims to answer some of these questions in a detailed manner. This work also targets the development of a new texturing technique. This technique should be able to lower the reflection from the cell and to facilitate an electrical performance with low surface recombination. To achieve it, the chosen methodology is modelling via the Finite Time Difference Domain (FDTD) technique. In the following Chapter, the methodology used is introduced.

1.7 References

1. Bahger, A. M., Vahid, M. M. A., and Mohsen, M., (2015), "*Types of Solar Cells and Application*", American Journal of Optics and Photonics, Vol. 3, No. 5, pp. 94-113.
2. Krebs, F. C., (2008), "*Polymer photovoltaics: a practical approach*", SPIE press, Washington.
3. International Energy Agency, (2014), "*Renewable energy medium-term market report 2014: market analysis and forecasts to 2020*", International Energy Agency, Paris.
4. Solangi, K. H., Islam, M. R., Saidur, R., Rahim, N. A., and Fayaz, H., (2011), "*A review on global solar energy policy*", Renewable and Sustainable Energy Reviews, Vol. 15, No. 4, pp. 2149-2163.
5. Khattak, C. P., and Ravi, K., V., (1985), "*Silicon Processing for Photovoltaics*", North-Holland Physics Publishing, Amsterdam.
6. Kreith, F., and Krumdieck, S., (2013), "*Principles of Sustainable Energy Systems*", 2nd Ed., CRC Press, Hoboken.
7. BP global, (2016), "*BP statistical review of world energy*". Available at: <http://www.bp.com/statisticalreview>, (Accessed March 2017).
8. The White House: Office of the Press Secretary, (2012), "*SHEET: U.S. Reports its 2025 Emissions Target to the UNFCCC*", Available at: <https://www.whitehouse.gov/the-press-office/2015/03/31/fact-sheet-us-reports-its-2025-emissions-target-unfccc>, (Accessed March 2017).
9. European Parliament, (2009), "*Directive 2009/28/EC of the European Parliament and of the Council of 23 April 2009 on the promotion of the use of energy from renewable sources and amending and subsequently repealing Directives 2001/77/EC and 2003/30/EC (Text with EEA relevance)*", Available at: <http://eur-lex.europa.eu/legal-content/en/ALL/?uri=CELEX%3A32009L0028>, (Accessed March 2017).
10. National Emblem of the People's Republic of China, (2014), "*National Emblem of the People's Republic of China*", paper No. 000014349/2014-00134.
11. Hunt, G., and Macfarlane, I., (2015), "*Certainty and growth for renewable energy*", Available at:

<http://www.environment.gov.au/minister/hunt/2015/mr20150623.html>,
(Accessed Mar.2017).

12. International Energy Agency, (2011), *"Deploying Renewables: Best and Future Policy Practice"*, OECD Publishing, Paris.
13. Ibrahim, H., Ilinca, A., and Perron, J., (2008), *"Energy storage systems: Characteristics and comparisons"*, Renewable and Sustainable Energy Reviews, Vol. 12, No. 5, pp. 1221-1250.
14. Green, M., (2005), *"Third generation photovoltaics: Advanced solar energy conversion"*, Springer, Amsterdam.
15. Prieto, P. A., and Hall, C. A. S., (2013) *"Spain's photovoltaic revolution: the energy return on investment"*, Springer, New York.
16. Goetzberger, A., and Hoffman, V. U., (2005), *"Photovoltaic solar energy generation"*, Springer, Berlin.
17. Archer, M. D., and Green, M. A., (2015), *"Clean electricity from photovoltaics"*, Imperial College Press, Singapore.
18. Green, M. A., (2016), *"Solar cell efficiency tables (version 49)"*, Progress in photovoltaics, Vol. 24, No. 1, pp. 1062-7995.
19. Masuko, K., Shigematsu, M., Hashiguchi, T., Fujishima D., Kai, M., Yoshimura, N., Yamaguchi, T., Ichihashi, Y., Yamanishi, T., Takahama, T., Taguchi, M., Maruyama, and E., Okamoto, S., (2014), *"Achievement of more than 25% conversion efficiency with crystalline silicon heterojunction solar cell,"* IEEE Journal of Photovoltaics, Vol. 4, pp. 1433–1435.
20. Kitai, A., (2011), *"Principles of solar cells, LEDs and diodes"*, Wiley, Kuala Lumpur.
21. Fthenakis, V. M., (2012), *"How long does it take for photovoltaics to produce the energy used? National Society of Professional Engineers Publication"*, Available at :<http://www.clca.columbia.edu>, (Accessed May 2016).
22. Laleman, R., Albrecht, J., and Dewulf, J., (2011), *"Life cycle analysis to estimate the environmental impact of residential photovoltaic systems in regions with a low solar irradiation"* Vol. 15, No. 1, pp. 267-95.
23. Luque, A., and Hegedus, S., (2011), *"Handbook of Photovoltaic Science and Engineering"*, John Wiley and Sons, Ltd., Chichester.
24. Craig, E. C., (1993), *"Electronics via Waveform Analysis"*, Springer, New York.

25. Sparkfun, (2017), "*Real Diodes Characteristics*", Available at:
<https://cdn.sparkfun.com/assets/4/4/a/5/b/5175b518ce395f2d49000000.png>,
 (Accessed March 2017).
26. Hoskins, P., Martin, K., and Thrush, A., (2010), "*Diagnostic ultrasound: physics and equipment*", 2nd Ed., Cambridge University Press, Cambridge.
27. Flowers, G., (1975), "*Introduction to Modern Optics*", Rinehart and Winston Inc., New York.
28. Kuo, M-L., Poxson, D. J., Kim, Y-S., Mont, F-W., Kim, J-K., Schubert, E-F., and Lin, S-Y., (2008), "*Realization of a near-perfect antireflection coating for silicon solar energy utilization*", *Optics Letters*, Vol. 33, No. 21, pp. 2527–2529.
29. Palik, E. D., Ghosh, G., and Knovel, (1998), "*Handbook of optical constants of solids*", Academic Press, San Diego.
30. Saleh, B. E. A., and Teich, M.C. (2007), "*Fundamentals of photonics*", 2nd Ed., Wiley, Hoboken, N.J.
31. Pode, R., and Diouf, B., (2011), "*Solar Lighting*", 1st Ed., Springer Verlag, London.
32. Ravindra, N. M., Ganapathy, P., and Choi, J., (2007), "*Energy gap refractive index relations in semiconductors: An overview*", *Infrared Physics and Technology*, Vol. 50, No. 1, pp. 21-29.
33. Dan, Y., Seo, K., Takei, K., Meza, J. H., Javey, A., and Crozier, K. B., (2011), "*Dramatic Reduction of Surface Recombination by in Situ Surface Passivation of Silicon Nanowires*", *Nano Letters*, Vol. 11, pp. 2527-2532.
34. Böer, K. W., (2013), "*Handbook of the Physics of Thin-Film Solar Cells*", Springer Berlin Heidelberg, Berlin.
35. Miller, O. D., Yablonovitch, E., and Kurtz, S. R., (2012), "*Intense Internal and External Fluorescence as Solar Cells Approach the Shockley-Queisser Efficiency Limit*", *IEEE Journal of Photovoltaics*, Vol. 2, pp. 303-311.
36. American Society for Testing and Materials (ASTM), (1987), "*Standard Tables for Terrestrial Direct Normal Solar Spectrum Irradiance for Air Mass 1.5*", Standard No. E891-87, American Society for Testing and Materials, Philadelphia.
37. Chander, S., Purohit, A., Sharma, A., Nehra, S. P., and Dhaka, M. S., (2015), "*Impact of temperature on performance of series and parallel*

- connected mono-crystalline silicon solar cells*", Energy Reports, Vol. 1, pp. 175-180.
38. Dubey, S., Sarvaiya, J. N., and Seshadri, B., (2013), "*Temperature Dependent Photovoltaic (PV) Efficiency and Its Effect on PV Production in the World: A Review*", Energy Procedia, Vol. 33, pp. 311-321.
 39. Maghami, M. R., Hizam, H., Gomes, C., Radzi, M. A., Rezadad, M. I., and Hajighorbani, S., (2016), "*Power loss due to soiling on solar panel: A review*", Renewable and Sustainable Energy Reviews, Vol. 59, pp.1307-1316.
 40. Ndiaye, A, Kebe C. M. F., Ndiaye, P. A., Charki, A., Kobi, and A.,Sambou. V., (2013), "*Impact of dust on the photovoltaic modules characteristics after an exposition year in Sahelian environment: the case of Senegal*", International Journal of Physical Sciences, Vol. 8, pp. 1166.
 41. Seethamraju, S., Ramamurthy, P. C., and Madras, G., (2014), "Encapsulation for Improving the Efficiencies of Solar Cells", In Viswanathan, B., Subramanian, V., and Lee J. S., (2014), "*Materials and Processes for Solar Fuel Production*", Springer, New York.
 42. Shockley, W, and Queisser, H. J., (1961), "*Detailed balance limit of efficiency of p–n junction solar cells*", Journal of Applied Physics, Vol. 32, No. 3, pp. 510–519.
 43. Tanabe, K., Atwater, H., and Nakayama, K., (2008), "*Plasmonic nanoparticle enhanced light absorption in GaAs solar cells*", Applied Physics Letters, Vol. 93, No. 12, pp. 121904-121904-3.
 44. Abderrezek, M., Djahli, F., Fathi, M., and Ayad, M., (2013), "*Numerical modeling of GaAs solar cell performances*", Elektronika ir Elektrotechnika, Vol. 19, No. 8, pp. 4
 45. Steiner, M. A., Geisz, J. F., Garcia, I., Friedman, D. J., Duda, A., and Kurtz, S. R., (2013), "*Optical enhancement of the open-circuit voltage in high quality GaAs solar cells*", Journal of Applied Physics, Vol. 113, No. 12, pp. 123109.
 46. Marti, A., and Luque, A., (2004), "*Next generation photovoltaics: high efficiency through full spectrum utilization*", IOP Publishing Ltd, London.
 47. Cristobal, A., Martí Vega, A., and Luque López, A. Eds., (2012), "*Next generation of photovoltaics new concepts*", Springer Series in Optical Sciences, London.

48. Yu, S., (2014), *“Computational Modelling of Opto-electric Properties of Nanowire Array Solar Cells”*, Kassel University Press GmbH, Kassel.
49. Corcoran, C. J., (2014), *“Materials and design strategies for solar microcells”*, PhD Thesis University of Illinois.
50. Vos, A. D., (1980), *“Detailed balance limit of the efficiency of tandem solar cells”*, Journal of Physics D: Applied Physics, Vol. 13, No. 5, pp. 839.
51. Marti, A., and Araujo, G. L., (1996), *“Limiting efficiencies for photovoltaic energy conversion in multigap systems”*, Solar Energy Materials and Solar Cells, Vol. 43, No. 2, pp. 203-222.
52. Chiu, P. T., Law, D. C., Woo, R. L., Singer, S. B., Bhusari, D., Hong, W. D., Zakaria, A., Boisvert, J., Mesropian, S., King, R. R., and Karam, N. H., (2014), *“Direct Semiconductor Bonded 5J Cell for Space and Terrestrial Applications”*, IEEE Journal of Photovoltaics, Vol. 4, No. 1, pp. 493-497.
53. Jones, R. K., Ermer, J. H., Fetzer, C. M., and King, R. R., (2012), *“Evolution of Multijunction Solar Cell Technology for Concentrating Photovoltaics”*, Japan Journal Applied Physics, Vol. 51, No. 10, pp. 10ND01-10ND01-4.
54. Pizzini, S., (2012), *“Advanced silicon materials for photovoltaic applications”*, Wiley, Chichester.
55. Hamakawa, Y., (2010), *“Thin-Film solar cell next generation photovoltaics and its applications”*, Springer, New York.
56. Willardson, A., (1984), *“Semiconductors and Semimetals”*, Academic Press, Burlington.
57. Li, H., (2007), *“Single and multijunction silicon based thin film solar cells on a flexible substrate with absorber layers made by hot-wire CVD”*, PhD Thesis Utrecht University.
58. Chopra, K. L., Paulson, P. D., and Dutta, V., (2004), *“Thin film solar cell: an overview”*, Progress in Photovoltaics, Vol. 12, pp. 69-92.
59. Kolodziej, A., (2004), *“Staebler-Wronski effect in amorphous silicon and its alloys”*, Opto-Electronics Review, Vol. 12, No. 1, pp. 21-34.
60. Leon, A., (2008), *“Hydrogen Technology: Mobile and Portable Applications”*, Springer, Berlin.
61. Zhou, F., Wang, X. C., Wu, H. C., and Zhao, C. Z., (2011), *“Achievements and Challenges of CdS/CdTe Solar Cells,”* International Journal of Photoenergy, Vol. 2011, pp. 1-8.

62. Zhao, H., (2008), *"Impurity and back contact effects on cadmium telluride/cadmium sulfide thin film solar cells"*, PhD Thesis University of South Florida.
63. De Vos, A., Parrot, J. E., Baruch, P., and Landsberg, P. T., (1944), *"Bandgap effects in thin-film heterojunction solar cells"*, Proceedings of the 12th European Photovoltaic Solar Energy Conference, pp. 1315–1318.
64. Sze, S. M., (1981), *"Physics of semiconductor devices"*, 3rd Ed., Wiley-Interscience, New York.
65. Bosio, A., Romeo, N., Mazzamuto, S., and Canevari, V., (2006), *"Polycrystalline CdTe thin films for photovoltaic applications,"* Progress in Crystal Growth and Characterization of Materials, Vol. 52, No. 4, pp. 247–279.
66. Krum, S., Brady, D., and Haymore, S., (2014), *"First Solar builds the highest efficiency thin film PV cell on record"*, Available at: <http://investor.firstsolar.com/releasedetail.cfm?ReleaseID=864426>, (Accessed March 2017).
67. Li, Y., Li, Z., Wang, Y., Compaan, A., Ren, T., and Dong, W., (2013), *"Increasing the power output of a CdTe solar cell via luminescent down shifting molecules with intramolecular charge transfer and aggregation-induced emission characteristics"*, Energy and Environmental Science, Vol. 6, No. 10, pp. 2907-2911.
68. Major, J. D., (2016), *"Grain boundaries in CdTe thin film solar cells: a review"*, Semiconductor Science and Technology, Vol. 31, No. 9, pp. 093001.
69. Fthenakis, V. M., (2003), *"Overview of Potential Hazards"*, in Markvart, T., and Castaner, L., (2003), *"Practical Handbook of Photovoltaics: Fundamentals and Applications"*, Elsevier, Amsterdam.
70. Fthenakis, V. M., (2002), *"End-of-life management and recycling of PV modules"*, Energy Policy, Vol. 28, pp. 1051–1058.
71. Bravi, M., Parisi, M. L., Tiezzi, E., and Basosi, R. (2010), *"Life cycle assessment of advanced technologies for photovoltaic panels production"*, International Journal of Heat and Technology, Vol. 28, No. 2, pp. 133-139.
72. Mints, P., (2010), *"The commercialization of thin film technologies: Past, present and future"*, In the proceedings of the 35th IEEE Photovoltaic Specialists Conference (PVSC), pp. 002400.

73. Solibro Press Release, (2014), "*Solibro beats world record for solar cells*", Available at: <http://solibro-solar.com/en/news-downloads/news/>, (Accessed June 2014).
74. Powalla, M., and Dimmler, B., (2001), "*CIGS solar cells on the way to mass production: Process statistics of a 30 cm×30 cm module line*", *Solar Energy Materials and Solar Cells*, Vol. 67, No. 1, pp. 337-344.
75. Tang, Y., (2017), "*Copper Indium Gallium Selenide Thin Film Solar Cells*", In Das, N. (Ed.), (2017), "*Nanostructured Solar Cells*", Intech, Rijeka.
76. Wang, Z. L., Zhang, H., Zhao, W., Zhou, Z. G., and Chen, M. X., (2015), "*Effect of Concentrated Light Intensity on Temperature Coefficient of the InGaP/InGaAs/Ge Triple-Junction Solar Cell*", *The Open Fuels and Energy Science Journal*, Vol. 8, pp. 106-111.
77. Ateto, E., (2015), "Can we use fibre optics in solar cells to improve efficiency?", Available at: http://cdn2b.examiner.com/sites/default/files/styles/image_content_width/h/6e/2a/6e2a2d8b7a5a9997c315c0d79f7595b0.jpg?itok=Srw65_C6, (Accessed March 2017).
78. Shanks, K., Senthilarasu, S., and Mallick, T. K., (2016), "*Optics for concentrating photovoltaics: Trends, limits and opportunities for materials and design*", *Renewable and Sustainable Energy Reviews*, Vol. 60, pp. 394-407.
79. Haysom, J. E., Jafarieh, O., Anis, H., Hinzer, K., and Wright, D., (2014), "*Learning curve analysis of concentrated photovoltaic systems*", *Progress in Photovoltaics: Research and Applications*, Vol. 23, No. 11, pp. 1678-1686.
80. Mohr, A., Roth, T., and Glunz, S. W., (2006), "*BICON: high concentration PV using one axis tracking and silicon concentrator cells*", *Progress in Photovoltaics: Research and Applications*, Vol. 14, No. 7, pp. 663-674.
81. Hallas, J. M., Baker, K. A., Karp, J. H., Tremblay, E. J., and Ford, J. E., (2012), "*Two-axis solar tracking accomplished through small lateral translations*", *Applied optics*, Vol. 51, No. 25, pp. 6117.
82. Fraunhofer ISE, (2014), "*New world record for solar cell efficiency at 46%*", Available at: <http://www.ise.fraunhofer.de/en/press-and-media/press-releases/press-releases-2014/new-world-record-for-solar-cell-efficiency-at-46-percent>, (Accessed March 2017).

83. Philipps, S. P., Bett, A. W., Horowitz, K., and Kurtz, S., (2016), "*Current status of concentrator photovoltaic (CPV) technology*", Fraunhofer, Freiburg.
84. Fraunhofer ISE, (2013), "*Levelized Cost of Electricity - Renewable Energy Technologies*", Available at: www.ise.fraunhofer.de/de/veroeffentlichungen/veroeffentlichungen-pdf-dateien/studien-und-konzeptpapiere/studie-stromgestehungskosten-erneuerbare-energien.pdf, (Accessed March 2017).
85. Kermani, E., (2008), "*Manifold micro-channel cooling of photovoltaic cells for high efficiency solar energy conversion systems*", Dissertation University of Maryland.
86. Bora, B., (2013), "*Contemporary research in organic solar cell*", Akshay Urja, Vol. 6, No. 4.
87. Hoppe, H., and Sariciftci, N. S., (2004), "*Organic solar cells: An overview*", Journal of Materials Research, Vol. 19, No. 7, pp. 1924-1945.
88. Søndergaard, R., Hösel, M., Angmo, D., Larsen-Olsen, T. T., and Krebs, F.C., (2012), "*Roll-to-roll fabrication of polymer solar cells*", Materials Today, Vol. 15, No. 1-2, pp. 36-49.
89. Zhugayevych, A., (2017), "Organic semiconductors", Available at: http://zhugayevych.me/research/fig_BHJ.png, (Accessed March 2017).
90. Khuram, A., Sohail, A. K., and Mat Jafri, M. Z., (2014), "*Effect of Double Layer (SiO₂/TiO₂) Anti-reflective Coating on Silicon Solar Cells*", International Journal of Electrochemical Sciences, Vol. 9, pp. 7865 -7874.
91. Clarke, T. M., and Durrant, J. R., (2010), "*Charge photogeneration in organic solar cells*", Chemical Reviews, Vol. 110, No. 11, pp. 6736.
92. Hosoya M., Ooka, H., Nakao, H., Gotanda, T., Mori, S., Shida, N., Hayase, R., Nakano, Y., and Saito, M., (2013), "*Organic thin film photovoltaic modules*", Proceedings of the 93rd Annual Meeting of the Chemical Society of Japan 2013, pp. 21–37.
93. Zervos, H., (2013), "*Organic Photovoltaics (OPV) 2013-2023: Technologies, Markets, Player*", IDTechEx report, 2013, Available at: <http://www.idtechex.com/research/reports/organic-photovoltaics-opv-2013-2023-technologies-markets-players-000349.asp>.
94. Lee, M. M., Teuscher, J., Miyasaka, T., Murakami, T. N., and Snaith, H. J., (2012), "*Efficient Hybrid Solar Cells Based on Meso-Superstructured Organometal Halide Perovskites*", Science, Vol. 338, No. 6107, pp. 643-647.

95. Harrison, W. T. A., Feild, C. A., Mitzi, D. B., and Guloy, A. M., (1994), *“Conducting tin halides with a layered organic-based perovskite structure”*, Nature, Vol. 369, No. 6480, pp. 467-469.
96. Green, M. A., (2014), *“The emergence of perovskite solar cells”*, Nature Photonics, Vol. 8, No. 7, pp. 506.
97. Kojima, A., Teshima, K., Shirai, Y., and Miyasaka, T., (2009), *“Organometal halide perovskites as visible-light sensitizers for photovoltaic cells”*, Journal of the American Chemical Society, Vol. 131, No. 17, pp. 6050.
98. Brenner, T. M., Egger, D. A., Kronik, L., Hodes, G., and Cahen, D., (2015), *“Hybrid organic-inorganic perovskites: low-cost semiconductors with intriguing charge-transport properties”*, Nature Review Materials, Vol. 1, pp. 15007.
99. Yang, W. S., Noh, J. H., Jeon, N. J., Kim, Y. C., Ryu, S., Seo, J., and Seok, S. I., (2015), *“High-performance photovoltaic perovskite layers fabricated through intramolecular exchange”*, Science, Vol. 348, No. 6240, pp.1234-1237.
100. Yan, X., Poxson, D. X., Cho, J., Welser, R. E., Sood, A. K., Kim, J. K., and Schubert, E. F. (2013), *“Enhanced omnidirectional photovoltaic performance of solar cells using multiple-discrete-layer tailored-and low-refractive index anti-reflection coatings”*, Advanced Functional Materials, Vol. 23, No. 5, pp. 583-590.
101. Yang, C.-H., Lien, S.-Y., Chu, C.-H., Kung, C.-Y., Cheng, T.-F., and Chen, P.-T., (2013), *“Effectively improved SiO₂-TiO₂ composite films applied in commercial multicrystalline silicon solar cells”*, International Journal of Photoenergy, Vol. 2013, pp. 823254.
102. Kesmez, O., Çamurlu, H. E., Burunkaya, E., and Arpaç, E., (2010), *“Sol-gel preparation and characterization of anti-reflective and self-cleaning SiO₂-TiO₂ double-layer nanometric films”*, Solar Energy Materials and Solar Cells, Vol. 93, No. 10, pp. 1833–1839.
103. Hocine, D., Belkaid, M. S., Pasquinelli, M., Escoubas, L., Simon, J. J., Riviere, G. A., and Moussi, A., (2013), *“Improved efficiency of multicrystalline silicon solar cells by TiO₂ antireflection coatings derived by APCVD process”*, Materials Science in Semiconductor Processing, Vol. 16, No. 1, pp. 113-117.

104. Lee, B. G., Sarp, J., Malinen, V., Shuo, L., Sukgeun, C., and Branz, H. M., (2012) "*Excellent passivation and low reflectivity Al₂O₃/TiO₂ bilayer coating for n-wafer silicon solar cells*", Presented at the 38th IEEE Photovoltaic Specialists Conference (PVSC), pp. 001066-001068.
105. Ahmed, N., Singh, C. B., Bhattacharya, S., Dhara, S., and Bhargav, P. B., (2013) "*Ammonia-Free Amorphous Silicon Nitride Thin Films for Photovoltaic Applications*", Spectroscopy Letters, Vol. 46, No. 7.
106. Luo, B., Wu, L., Chen, J., and Lu, Y., (1993), "*Determination of wavelength dependence of the reflectivity at AR coated diode facets*", IEEE Photonics Technology Letters, Vol. 5, No. 11, pp.1279-1281.
107. Born, M., and Wolf, E., (1999), "*Principles of Optics*", 7th Ed., Cambridge University Press, Cambridge.
108. Burak, U. K., (2010), "*Nanoparticle Enhanced Thin Film Solar Cells*", PhD Thesis Wake Forest University.
109. Spinelli, P., Ferry, V. E., Van de Groep, J., Van Lare, M., Verschuuren, M. A., Atwater, H. A., and Polman, A., (2012), "*Plasmonic light trapping in thin-film Si solar cells*", Journal of Optics, Vol. 14, pp. 024002.
110. Nagel, J., and Scarpulla, M., (2010), "*Enhanced absorption in optically thin solar cells by scattering from embedded dielectric nanoparticles*", Optics Express, Vol. 18, No. S2, pp. A139A146.
111. Catchpole, K. R., and Polman, A., (2008), "*Plasmonic solar cells*", Optics express, Vol. 16, No. 26, pp. 21793-21800.
112. Derkacs, D., Lim, S. H., Matheu, P., Mar, W., and Yu, E. T., (2006), "*Improved performance of amorphous silicon solar cells via scattering from surface plasmon polaritons in nearby metallic nanoparticles*", Applied Physics Letters, Vol. 89, pp. 093103.
113. Pillai, S., Catchpole, K. R., Trupke, T., and Green, M. A., (2007), "*Surface plasmon enhanced silicon solar cells*", Journal of Applied Physics, Vol. 101, pp. 093105.
114. Hong, L., Wang, H., Li, J., Li, R., Yu, H., (2011), "*Surface Plasmon Enhanced Light Absorption For Thin Film Polysilicon Solar Cell With Hybrid Structure And Metal Alloy Nanoparticles*", In Proceedings of the 37th IEEE Photovoltaic Specialists Conference, pp. 870-873.
115. Yun, J., Kozarsky, E., Kim, J., Kojori, H. S., Kim, S.-J., Tong, C., Wang, J., and Anderson, W., A., (2011), "*Silver Nanoparticles Incorporated in*

- Aluminum Doped ZnO for Heterojunction Solar Cells*”, In Proceedings of the 38th IEEE Photovoltaic Specialists Conference (PVSC), pp. 002625-002627.
116. Liu, F., Xie, W., Xu, Q., Liu, Y., Cui, K., Feng, X., Zhang, W., and Huang, Y. (2013), “*Plasmonic Enhanced Optical Absorption in Organic Solar Cells With Metallic Nanoparticles*”, IEEE Photonics Journal, Vol. 5, No. 4, pp. 8400509-8400509.
117. Iyenger, V. (2010), “*Optical Properties of Silicon light trapping structures for photovoltaics*”, Solar Energy Materials and Solar Cells, Vol. 94, No. 12, pp. 2251-2257.
118. Zhang, Y., Ouyang, Z., Stokes, N., Jia, B., Shi, Z., and Gu, M., (2012), “*Low cost and high performance Al nanoparticles for broadband light trapping in Si wafers solar cells*”, Applied Physics Letters, Vol. 100, No. 5, pp. 151101-151104.
119. Baker-Finch, S., and McIntosh, K., (2011), “*Reflection of normally incident light from silicon solar cells with pyramidal texture*”, Progress in Photovoltaics, Vol. 19, pp. 406–416.
120. Garnett, E., and Yang, P., (2010), “*Light trapping in silicon nanowire solar cells*,” Nano Letters, Vol. 10, pp.1082-1087.
121. Mallorqui, A., Eppler, F. M., Fan, D., Demichel, O., Fontcuberta A., and Morral, I., (2012), “*Effect of the pn junction engineering on Si microwire-array solar cells*”, Physica Status Solidi A, Vol. 209, No. 3, pp.1588-1591.
122. Park, K., Guo, Z., Um, H.-D., Jung, J.-Y., Yang, J.-M., Lim, S. K., Kim, Y. S., and Lee, J.-H., (2011), “*Optical Properties of Si microwires combined with nanoneedles for flexible thin film photovoltaics*”, Optics express, Vol. 19, No. 101, pp. A41.
123. Moreno, M., Daineka, D., and Roca i Cabarrocas, P., (2010), “*Plasma texturing for silicon solar cells: From pyramids to inverted pyramids-like structures*”, Solar Energy Materials and Solar Cells, Vol. 94, No. 5, pp. 733-737.
124. Kelzenberg, M. D., Turner-Evans, D. B., Warren, E. L., Lewis, N. S., Boettcher, S. W., Petykiewicz, J. A., Spurgeon, J. M., Briggs, R. M., Putnam, M. C., and Atwater, H. A., (2010), “*Enhanced absorption and carrier collection in Si wire arrays for photovoltaic applications*”, Nature Materials, Vol. 9, No. 3, pp. 239-244.

125. Lundgren, C., Lopez, R., Redwing, J., and Melde, K., (2013), "*FDTD modeling of solar energy absorption in silicon branched nanowires*", Optics express, Vol. 21, No. 3, pp. A392.
126. Hua, B., Wang, B., Yu, M., Leu, P.W., and Fan, Z., (2013), "*Rational geometrical design of multi-diameter nanopillars for efficient light harvesting*", Nano Energy, Vol. 2, No. 5, pp. 951-957.
127. Sun, C., Jiang, P., and Jiang, B., (2008), "*Broadband moth-eye antireflection coatings on silicon*", Applied Physics Letters, Vol. 92, No. 6, pp. 061112-061112-3.
128. Wang, J., Li, Z. Singh, N., and Lee, S., (2011), "*Highly-ordered vertical Si nanowire/nanowall decorated solar cells*," Optics Express, Vol. 19, No. 23, pp. 23078-23084.
129. Wang, K. X., Yu, Z., Liu, V., Cui, Y., and Fan, S., (2012), "*Absorption enhancement in ultrathin crystalline silicon solar cells with antireflection and light-trapping nanocone gratings*", Nano letters, Vol. 12, No. 3, pp. 1616.
130. Mavrokefalos, A., Han, S. E., Yerci, S., Branham, M. S., and Chen, G., (2012), "*Efficient light trapping in inverted Nanopyramid thin Crystalline silicon membranes for solar cell applications*", Nano Letters, Vol. 12, No. 6, pp. 2792-2796.
131. Oh, J., Yuan, H., and Branz, H. M., (2012), "*An 18.2%-efficient black-silicon solar cell achieved through control of carrier recombination in nanostructures*", Nature Nanotechnology, Vol. 7, No. 11, pp. 743.
132. Campbell, P., and Green, M. A., (1987), "*Light trapping properties of pyramidally textured surfaces*," Journal of Applied Physics, Vol. 62, pp. 243.
133. Muller, J., Rech, B., Springer, J., and Vanecek, M., (2004), "*TCO and light trapping in silicon thin film solar cells*", Solar Energy, Vol. 77, pp. 917–930.
134. Al-Amin, M., and Assi, A., (2013), "*Efficiency improvement of crystalline silicon solar cells*" in Mendez-Vila, A., (Eds.) (2013), "*Materials and processes for energy: communicating current research and technological developments*" Formatex research center, Badajoz.
135. Garnett, E.C., Tseng, Y.C., Khanal, D.R., Wu, J., Bokor, J., and Yang, P., (2009), "*Dopant profiling and surface analysis of silicon nanowires using capacitance-voltage measurements*", Nature Nanotechnology, Vol. 4, pp. 311-314.

136. Xie, P., Hu, Y., Fang, Y., Huang, J., and Lieber, C. M., (2009), "*Diameter-dependent dopant location in silicon and germanium nanowires*", Proceedings of the National Academy of Sciences of the United States of America, Vol., 106, No. 36, pp. 15254-15258.
137. Zhu, J., Yu, Z., Burkhard, G. F., Hsu, C., Connor, S. T., Xu, Y., Wang, Q., McGehee, M., Fan, S., and Cui, Y., (2009), "*Optical absorption enhancement in amorphous silicon nanowire and nanocone arrays*", Nano letters, Vol. 9, No. 1, pp. 279-282.
138. Toor, F. Branz, H. M. Page, M. R. Jones, K. M., and Yuan, H-C., (2011), "*Multi-scale surface texture to improve blue response of nanoporous black silicon solar cells*", Applied Physics Letters, Vol. 99, pp. 103501.
139. Li, H., Chen, R. J. C., Xing, X., Ding, W., Meng, Y., Wu, D., Liu, X., and Ye, T., (2011), "*Influence of nanowires length on performance of crystalline silicon solar cell*", Applied Physics Letters, Vol. 98, pp. 151116.
140. Yu, S-Q., Kupec, J., and Witzigmann, B., (2010), "*Electro-optical modeling of InP nanowire solar cells: Core-shell vs. axial structure*", In the Proceedings of the 10th International Conference on Numerical Simulation of Optoelectronic Devices (NUSOD), pp. 57–58.
141. LaPierre., R. R., (2011), "*Numerical model of current-voltage characteristics and efficiency of GaAs nanowire solar cells*", Journal of Applied Physics, Vol., No. 3, pp. 034311.
142. Yao, M-Q., Huang, N-F., Cong, S., Chi, C.-Y., Seyedi, M. A., Lin, Y.-T., Cao, Y., Povinelli, M. L., Dapkus, P. D., and Zhou, C., (2014), "*GaAs Nanowire Array Solar Cells with Axial p-i-n Junctions*", Nano letters, Vol.14, No.6, pp. 3293–3303.
143. Cui, Y-C. Wang, J., Plissard, S. R., Cavalli, A., Vu, T. T. T., Van Veldhoven, R. P. J., Gao, L., Trainor, M., Verheijen, M. A., Haverkort, J. E. M., Bakkers, and E. P. A. A., (2013), "*Efficiency enhancement of InP nanowire solar cells by surface cleaning*", Nano letters, Vol. 13, No. 9, pp.4113–4117.
144. Kayes, B. M., Atwater, H. A., and Lewis, N. S., (2005), "*Comparison of the device physics principles of planar and radial p-n junction nanorod solar cells*," Journal of Applied Physics, Vol. 97, pp. 114302–114312.
145. Kayes, B. M., (2009), "*Radial PN Junction, Wire Array Solar Cells*", PhD Thesis California Institute of Technology Pasadena.

146. Hu, L., and Cheng, G., (2007), "*Analysis of optical absorption in silicon nanowire arrays for photovoltaic applications*", Nano letters, Vol. 7, No. 7, pp. 3249-3252.
147. Pradhan, D., Kumar, M., Ando, Y., and Leung, K. T., (2008), "*Efficient field emission from vertically grown planar ZnO nanowalls on an ITO-glass substrate*", Nanotechnology, Vol. 19, No. 3, pp. 035603.
148. Liang, Z., Gao, R., Lan, J., Wiranwetchayan, O., Zhang, Q., Li, C., and Cao, G., (2013), "*Growth of vertically aligned ZnO nanowalls for inverted polymer solar cells*", Solar Energy Materials and Solar Cells, Vol. 117, pp. 34-40.
149. Wang, J., Li, Z., Singh, N., and Lee, S., (2011), "*Highly-ordered vertical Si nanowire/nanowall decorated solar cells*", Optics express, Vol. 19, No. 23, pp. 23078.
150. Kanematsu, D., Yoshiba, S., Hirai, M., Terakawa, A., Tanaka, M., Ichikawa, Y., Miyajima, S., and Konagai, M., (2016), "*Observation of Quantum Size Effect from Silicon Nanowall*", Nanoscale Research Letters, Vol. 11, No. 1, pp. 1-5.
151. Kanematsu, D., Yoshiba, S., Hirai, M., Terakawa, A., Tanaka, M., Ichikawa, Y., Miyajima, S., and Konagai, M., (2016), "*Measurement of the density of states in a Si nanowall exhibiting the quantum size effect*", *The 43rd IEEE Photovoltaic Specialists Conference (PVSC)*, pp. 2101-2104
152. Tang, J., Tseng, Z., Chen, L., and Chu, S., (2016), "*ZnO nanowalls grown at low-temperature for electron collection in high-efficiency perovskite solar cells*", Solar Energy Materials and Solar Cells, Vol. 154, pp. 18-22.
153. Sankaran, K. J., Hoang, D. Q., Kunuku, S., Korneychuk, S., Turner, S., Pobedinskas, P., Drijkoningen, S., Van Bael, M. K., D' Haen, J., Verbeeck, J., Leou, K., Lin, I., and Haenen, K., (2016), "*Enhanced optoelectronic performances of vertically aligned hexagonal boron nitride nanowalls-nanocrystalline diamond heterostructures*", Scientific reports, Vol. 6, pp. 29444.
154. Kim, D., Lee, S., Kim, K., Park, G., Lee, J., and Kim, S., (2008), "*Free-Standing ZnO Nanorods and Nanowalls by Aqueous Solution Method*", Journal of Nanoscience and Nanotechnology, Vol. 8, No. 9, pp. 4688-4691.

155. Rafique, S., Han, L., and Zhao, H., (2015), "*Density Controlled Growth of ZnO Nanowall–Nanowire 3D Networks*", The Journal of Physical Chemistry C, Vol. 119, No. 21, 12023-12029.
156. Bernhard, C. G., and Miller, W. H., (1962), "A corneal nipple pattern in insect compound eyes", Acta Physiologica Scandinavica, Vol. 56, No. 3-4, pp. 385-386.
157. Rahman, A., Ashraf, A., Xin, H., Tong, X., Sutter, P., Eisaman, M. D., and Black, C. T., (2015), "*Sub-50-nm self-assembled nanotextures for enhanced broadband antireflection in silicon solar cells*", Nature Communications, Vol. 6, pp. 5963.
158. Rick Cowen (2017), "*Inspired by the eyes of a moth, engineers at the High Tech campus in Eindhoven have created a coating for solar cells with a graded refractive*", Available at: http://www.pbase.com/1bald_eagle/image/48638897, (Accessed on 27 June 2017).
159. Leem, J. W., Kim, S., Lee, S. H., Rogers, J. A., Kim, E., and Yu, J.S., (2014), "*Efficiency Enhancement of Organic Solar Cells Using Hydrophobic Antireflective Inverted Moth-Eye Nanopatterned PDMS Films*", Advanced Energy Materials, Vol. 4, No. 8, pp. 1301315.
160. Huh, D., Shin, J.-H., Byun, M., Son, S., Jung, P.-H., Choi, H.-J., Kim, Y.-D., and Lee, H., (2017), "*Analysis of long-term monitoring data of PV module with SiO_x-based anti-reflective patterned protective glass*", Solar Energy Materials and Solar Cells, Vol. 170, pp. 33-38.
161. Burghoorn, M., Roosen-Melsen, D., de Riet, J., Sabik, S., Vroon, Z., Yakimets, I., and Buskens, P., (2013), "*Single Layer Broadband Anti-Reflective Coatings for Plastic Substrates Produced by Full Wafer and Roll-to-Roll Step-and-Flash Nano-Imprint Lithography*", Materials, Vol. 6, No. 9, pp. 3710-3726.
162. Ahmadvand, A., and Pala, N., (2017), "*Absorption Enhancement in Ultrathin Structures Based on Crystalline-Si/Ag Parabola Nanocones Periodic Arrays with Broadband Antireflection Property*", Silicon, Vol. 9, No. 1, pp. 25-29.
163. Li, Y., Li, M., Fu, P., Li, R., Song, D., Shen, C., and Zhao, Y., (2015), "*A comparison of light-harvesting performance of silicon nanocones and nanowires for radial-junction solar cells*", Scientific reports, Vol. 5, pp. 11532.

164. Lin, X., Hua, X., Huang, Z., and Shen, W., *“Realization of high performance silicon nanowire based solar cells with large size”*, Nanotechnology, Vol. 24, pp. 235402.
165. Jia Zhu, Zongfu Yu, George F. Burkhard, Ching-Mei Hsu, Stephen T. Connor, Yueqin Xu, Qi Wang, Michael McGehee, Shanhui Fan, and Yi Cui, *“Optical Absorption Enhancement in Amorphous Silicon Nanowire and Nanocone Arrays”*, Nano Letters, Vol. 9, No. 1, pp. 279-282.
166. Yoon, H. P., Yuwen, Y. A., Shen, H., Podraza, N. J., Malouks, T. E., Dickey, E. C., Redwing, J. A., Wronski, C. R., and Mayer, T. S., (2012), *“Parametric study of micropillar array solar cells”*, In Proceedings of 37th IEEE photovoltaic specialists conference (PVSC), pp. 000303-000306.
167. Shin, J., Chanda, D., Chern, W., Yu, K. J., Rogers, J. A., and Li, X., (2012), *“Experimental study of design parameters in silicon micropillar array solar cells produced by soft lithography and metal-assisted chemical etching”*, IEEE Journal of Photovoltaics, Vol. 2, No. 2, pp. 129-133.
168. Logeeswaran, V., Katzenmeyer, A. M., and Islam, M. S., (2010), *“Harvesting and transferring vertical pillar arrays of single-crystal semiconductor devices to arbitrary substrates”*, IEEE Transactions on Electron Devices, Vol. 57, No .8, pp. 1856-1864.
169. Kim, H., Kim, J., Lee, E., Kim, D-W., Yun, J-H., and Yin, J., (2013), *“Effect of the short collection length in silicon microscal wire solar cells”*, Applied Physics Letters, Vol. 102, pp. 193904.
170. Sinton, R. A., Cuevas, A., and Stuckings, M., (1996), *“Quasi-steady-state photoconductance, a new method for solar cell material and device characterisation”*, In Proceedings of the 25th IEEE photovoltaic specialists conference (PVSC), pp. 457-460.
171. Green, M. A., (1984), *“Limits on the open-circuit voltage and efficiency of silicon solar cells imposed by intrinsic Auger processes”*, IEEE Transactions on Electron Devices, Vol. 31, No. 5, pp. 671–678.
172. Li, J., Yu, H., Wong, S. M., Li, X., Zhang, G., Lo, P. G-Q., and Kwong, D-L., (2009), *“Design guidelines of periodic Si nanowire arrays for solar cell application”*, Applied Physics Letters, Vol. 95, pp. 243113–243115.

Chapter 2: Methodology

This Chapter is dedicated to the methodology which is used to generate all the results presented in this work. The discussion provides a derivation of the Finite Difference Time Domain (FDTD) method from Maxwell's equations. A description of the simulation set up is presented.

2.1 Importance of Numerical methods

The process of developing new solar cell devices consists of four stages: designing a prototype, fabricating a prototype, characterizing parameters and redesigning the prototype [1]. The total time to complete this process can be very long and the associated costs can be very large [1]. The usage of computational modelling can help in reducing the total time and associated costs [1]. The searching of a design offering a good performance is facilitated by the possibility of running as many simulations as required to reduce the trial and error approach to a minimum which reduces the total time. Furthermore, the time required to build each prototype is reduced, since no physical prototype is required for running simulations. Hence, the expenses associated with the materials for the prototype is reduced to the final design (optimized prototype). Additionally, simulation tools can be useful in understanding all physical phenomena involved in the solar cell [1]. For example, in a simulation based study using electrical modelling, it is possible to obtain the electrical parameters such as conversion efficiency, V_{OC} , I_{SC} and FF (electrical modelling is not part of this thesis and the focus is on optical modelling) of an optimized structure. Through the optical modelling it is possible to optimise the structure as well as visualising the field propagation inside the solar cell by obtaining a cross section of the solar cell. However, in an experimental based study, it may not be possible to obtain a visualisation similar to a cross section.

The number of numerical methods available in the literature is large. There are two classes of numerical methods that can be used for electromagnetic problems: frequency domain methods and time domain methods. The selection of the appropriate simulation method is important for accurate solutions [2].

Each analysis requires a different numerical method depending on the characteristics of the problem to be solved.

This work requires a numerical method capable of launching an electromagnetic wave with a wide wavelength spectrum that replicates the solar spectrum. Furthermore, it is also expected that the numerical method can obtain the field propagation in more than one direction (i.e. electromagnetic waves travelling in forward and backward directions simultaneously). The time domain methods meet these requirements. Among the time domain methods available (i.e. Finite Element Time Domain method [3], Finite Volume Time Domain method [4], Finite Difference Time Domain method [5], etc.), Finite Difference Time Domain Method (FDTD) is selected for this work based on the consideration of its advantages. The FDTD method is a widely accepted method with many advantages as listed below:

- It is second order accurate in nature due to the central finite difference approximations [5]. The discretization of space, associated with the FDTD method (Yee lattice), centres the E and H field components to ensure these components are surrounded by four H and four E field components respectively. This approach leads to a second order accuracy in space [5].
- The time schedule approach (leapfrog approach) associated with the FDTD method enables the interaction between the E and H fields in the calculation process and it ensures a second order accuracy in time [5].
- It deals with impulse response. Hence, it enables the launching of an electromagnetic wave with a wideband wavelength spectrum in a single simulation [5].
- It provides solutions in time and frequency domain [5]. This enables the study on the physical effects that an electromagnetic wave undergoes when it interacts with the structure. Additionally, it also enables the study in frequency domain, by applying a Fourier

transform, to analyse the electromagnetic field distribution inside and outside the structure at each individual wavelength.

- It has a simpler formulation than other numerical methods used in electromagnetic applications. This is possible due to the usage of the finite difference approximation that allows the partial differential form of Maxwell's equations to be expressed in terms of differences [6].
- It can simulate non linear behaviour [6].

The FDTD method also has some disadvantages that have to be taken into account such as:

- The staircasing of surfaces in oblique planes to Cartesian coordinates (i.e. x , y and z) may lead to errors in the results [5]. Figure 2.1 illustrates how modifications are introduced on the surface of a simple triangle due to the staircasing effect.

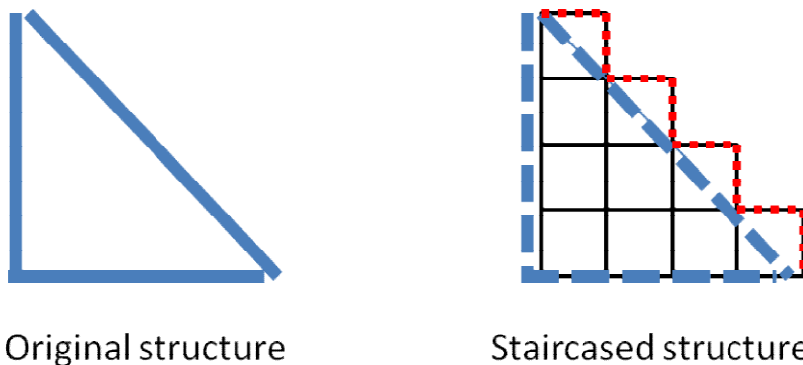


Fig. 2.1. Schematic illustrating the staircasing error caused by the implementation of the mesh in the FDTD method.

The difference between the expected triangle and the final triangle is large. The red dotted line represents the structure for which a hypothetical simulation would be run. This effect is a limitation due to the implementation of the Yee lattice. As a consequence, the results would not be accurate since the interaction of an incident electromagnetic wave with the two different surfaces (expected and

staircased) would be very different. A solution to reduce the staircase effect, is to make the mesh as fine as the computational memory allows. Alternatively, there are codes implementing approximation methods such as the Yu-Mittra method that can help in minimising the staircasing [7]. This type method distorts the mesh surrounding the boundary of the structure in such a way as to conform the surface of the structure. The partial differential form of Maxwell's equations cannot be discretized using finite difference approximation at the distorted nodes. At these nodes the Contour Path (CP) FDTD algorithm is used, which is based on the integral form of Maxwell's equations. This type of an approximation method will not provide accurate results in some cases such as multi stacked layer structures of dispersive materials [8].

- The memory requirements are very high for some of the simulated structures. The high memory requirements lead to large simulation time for each of the simulations as presented in Table 2.1. For example, when the mesh resolution in a 2D simulation of dimensions $5\mu\text{m}\times 5\mu\text{m}$ is increased by 1% (i.e. decreasing Δ_x and Δ_y from $0.01\mu\text{m}$ to $0.0099\mu\text{m}$), the memory requirement and the simulation time increase by approximately 2.3% and 2 seconds respectively, see Table 2.1. When the mesh resolution increases by 10%, the memory requirement and running simulation time increase approximately 18.2% and 16 seconds respectively. In a 3D simulation, the increase in the memory requirements and simulation time is even more noticeable. For the case of a planar Si slab solar cell with a volume $1.00383\mu\text{m}\times 1.73868\mu\text{m}\times 19\mu\text{m}$, when the mesh resolution is increased (i.e. decreasing Δ_x , Δ_y and Δ_z (distance between adjacent nodes or step size in x, y and z coordinates)) by 1%, the memory requirement and simulation time increase by 0.97% and 59 seconds respectively. When the increase is by 10%, the memory requirement and the simulation time increase by 36.6% and 644 seconds respectively.

2D					
Δ_x (μm)	Δ_y (μm)	Memory (MB)	Nodes (Thousands)	Simulation time (s)	
0.0100	0.0100	44	266.256	153	
0.0099	0.0099	45	272.484	155	
0.0095	0.0095	48	294.849	160	
0.0090	0.0090	52	327.184	169	
0.0085	0.0085	56	366.025	170	
0.0080	0.0080	62	410.881	209	
3D					
Δ_x (μm)	Δ_y (μm)	Δ_z (μm)	Memory (GB)	Nodes (Million)	Simulation time (s)
0.0100	0.0100	0.0100	1.536	9.33966	754
0.0099	0.0099	0.0099	1.551	9.54000	813
0.0095	0.0095	0.0095	1.769	10.75360	928
0.0090	0.0090	0.0090	2.098	12.58650	1120
0.0085	0.0085	0.0085	2.434	15.07720	1405
0.0080	0.0080	0.0080	2.989	17.71280	1745

Table 2.1. Relation between mesh parameters and memory requirements and simulation time.

- In the FDTD method it is difficult to implement a specific area where a very fine mesh is located, while the remaining simulation domain has a coarse mesh [5]. Therefore, in those simulations where a very specific area requires finer mesh, there is a dramatic increase in memory requirement in the majority of FDTD packages.
- The location of E and H fields are defined by the Yee lattice in space. At the interface between two materials, there are six different boundaries for each field component. Therefore, it is important to have a fine mesh to ensure the accuracy at these interfaces.

A general problem faced by FDTD users is the numerical dispersion caused by the variation of the speed at which the wave travels in different directions that is dependent on the angle of propagation [5]. This effect is directly related to the mesh in the simulation. When the step size of each coordinate in the mesh is different (i.e. $\Delta_x \neq \Delta_y \neq \Delta_z$), a phase difference on the wave fronts is numerically introduced. However, when the step size is equal in all three directions: x, y and z ($\Delta_x = \Delta_y = \Delta_z$), still

there is numerical dispersion present in the simulation. The reason is illustrated in a schematic in Fig. 2.2 where points A, B, C and D represent FDTD nodes in the same plane. The length of AB, BD, CD and CA is represented as distance “a”. The length of BC and AD corresponds to the diagonal which is represented as “b”. This means that the distance travelled by the wave is direction dependent (since $a \neq b$). In this work, the numerical dispersion is neglected.

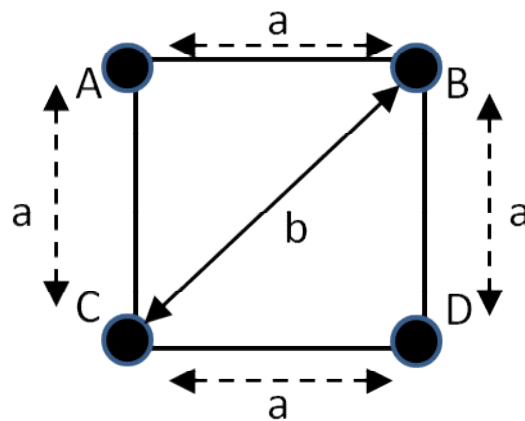


Fig. 2.2. Schematic showing the reason for numerical dispersion in the case of $\Delta_x = \Delta_y = \Delta_z$.

A derivation of the FDTD method starting from Maxwell's equations is presented in Section 2.3. In order to do that in the following section a discussion on Maxwell's equations is introduced.

2.2 Maxwell's equations

The manner in which the electromagnetic fields evolve is defined by solving Maxwell's equations. These equations are coupled, which is an evidence of the strong interrelation between the electric (E) and magnetic (H) fields. These equations are first order differential equations and define the changes in E and H at each point in space in a time-dependent manner. The differential form of Maxwell's equations for a lossless, dielectric medium is as follows:

Faraday's law [5]:

$$\frac{d\vec{B}}{dt} = -\nabla \times \vec{E} - \vec{M} \quad (2.1)$$

Where B is the magnetic flux density, E is the electric field and M is the magnetic current density.

Ampere's law [5]:

$$\frac{d\vec{D}}{dt} = \nabla \times \vec{H} - \vec{J} \quad (2.2)$$

Where D is the electric current density, H is the magnetic field and J is the electric current density.

Gauss's law for electric field [5]:

$$\nabla \cdot \vec{D} = \rho \quad (2.3)$$

where ρ is the volume charge density.

Gauss's law for magnetic field [5]:

$$\nabla \cdot \vec{B} = 0 \quad (2.4)$$

The continuity of the current has the following expression:

$$\nabla \cdot \vec{J} = \frac{-\delta\rho}{\delta t} \quad (2.5)$$

The constitutive relations for the media are as follows [5]:

$$\vec{D} = \epsilon \vec{E} = \epsilon_r \epsilon_0 \vec{E} \quad (2.6)$$

$$\vec{B} = \mu \vec{H} = \mu_r \mu_0 \vec{H} \quad (2.7)$$

where ε is the electric permittivity, ε_r is the relative permittivity, ε_0 is the free-space permittivity, μ is the magnetic permeability, μ_r is the relative permeability and μ_0 is the free-space permeability.

As discussed previously in Section 2.1, there are various numerical methods available to solve Maxwell's equations. In this work, the adopted numerical method is the FDTD method which is discussed in detail in the following section.

2.3 Finite-Difference-Time-Domain (FDTD) Method

The FDTD method solves a partial differential governing equation using finite central difference approximation both in time and space that leads to a second order accuracy [9]. The FDTD method was first introduced in 1966 by Yee [9]. Originally, this method was developed to solve the partial differential form of Maxwell's equations [10]. The first application of the method was to analyse the scattering of electromagnetic waves on infinitely long conducting cylinders in 2 dimensions (2D) [10]. Soon after the publication of Yee's work on FDTD many researchers started to implement it due to the advantages listed in Section 2.2. A consequence of this interest is the expansion to 3 dimensions (3D) of the FDTD method developed by Taflove and Brodwin [10, 11].

Nowadays, the FDTD method is implemented to study a wide range of electromagnetic waves applications such as: microwaves [11], optical fibres [11], metamaterials [11], compact integrated circuits [11] and solar cells [11]. Furthermore, the number of time domain applications based on the FDTD method-like approach is continuously increasing to non electromagnetic wave based problems (varying the governing equation) such as: fluid dynamics [12] and acoustic waves [13]. In all these applications the finite central difference is used to achieve second order accuracy in time and in space. In time, the discretization used is conventionally known as the leap frog approach. In space, the discretization used is conventionally known as the Yee lattice. In the following sections, the discretization in time and space are presented starting the discussion with the time discretization.

2.3.1 Time discretization of the FDTD method (Leap frog approach)

In time, the FDTD method uses the leap frog approach (see Fig. 2.3) to study the evolution of the E and H fields [14]. The calculation of E and H fields is alternated in time steps [14]. In nature, there is a constant interaction between E and H fields. Therefore, the interaction caused by the leapfrog approach between E and H fields (calculating values of E from previous H field values and vice versa) generates more accurate results than calculating the E field and H field individually (i.e. calculating E field values only from previously calculated E field values and the H field only from previously calculated H field values) [14].

Figure 2.3 illustrates in a diagram the calculation steps of the leap-frog approach. The calculation process starts with $\Delta_t = 0$, when all the E field components are calculated at different locations in space. An half time step later (i.e. $\Delta_t = 0.5\Delta t$), all the H field components are calculated based on the E field components which have been calculated in the previous time step. Then, the calculation process repeats with the same time step between calculations. The same logic applies until the number of simulation time steps is equal to the total required simulation time.

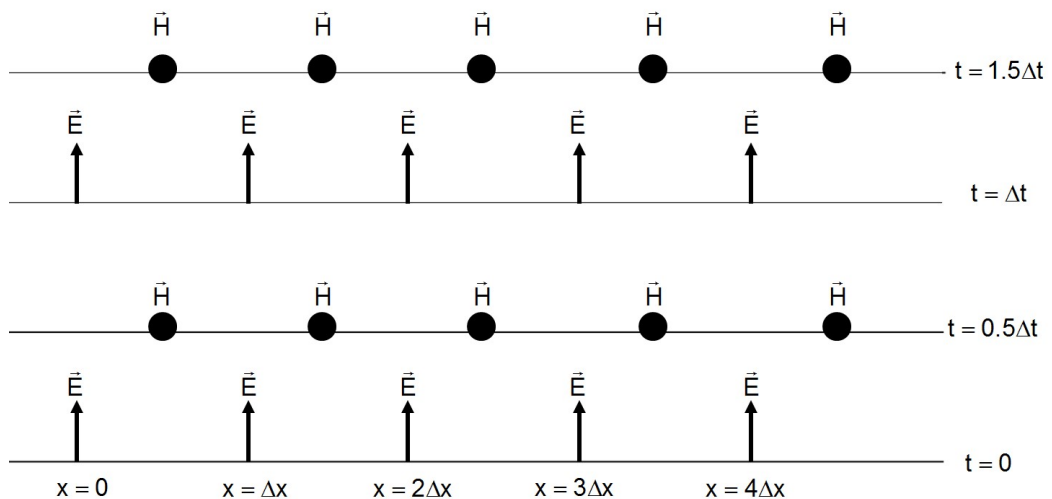


Fig. 2.3. Schematic diagram of leap-frog approach [5].

Applying the leap-frog approach in the calculation process of the FDTD is the key to obtain the second order accuracy in time. This is due to the time step

between successive calculations of E and H fields remaining constant at $0.5\Delta t$ throughout the simulation. The evenly distributed time step of $0.5\Delta t$ enables the usage of finite central difference approximation. The Taylor series expansion of the finite difference approximation can be truncated to give an approximation using two, three, four or more points. In this work the Taylor expansion is truncated to obtain a finite difference approximation using two points (to be discussed in Section 2.3.4). Similar to the leap-frog approach in time, in FDTD the Yee lattice yields second order accuracy in space and is presented in the following section.

2.3.2 Space discretization of the FDTD method

In space, the FDTD method uses the Yee lattice (see Fig. 2.4) to locate each E and H field component [14]. The diagram is drawn in the Cartesian coordinates. The E and H field components are distributed to ensure that the curl operator in Eqs. (2.1) and (2.2) is correctly calculated [14].

For example, in the case of each component of the E field, there are four H field components surrounding it and viceversa. The field component E_x is surrounded by H_z and H_y components. The same principle applies to E_y and E_z which are surrounded by H_x and H_z and H_x and H_y respectively. In Eq. (2.1) the E field is used to calculate H and in Eq. (2.2) the H field is used to calculate E. Additionally, in both Eqs. (2.1) and (2.2) there is a curl operator which represents the rotation of a field as a vector [15]. Therefore, the location of the E and H field components in the Yee lattice satisfies the interaction between fields as well as the curl operator present in Maxwell's equations.

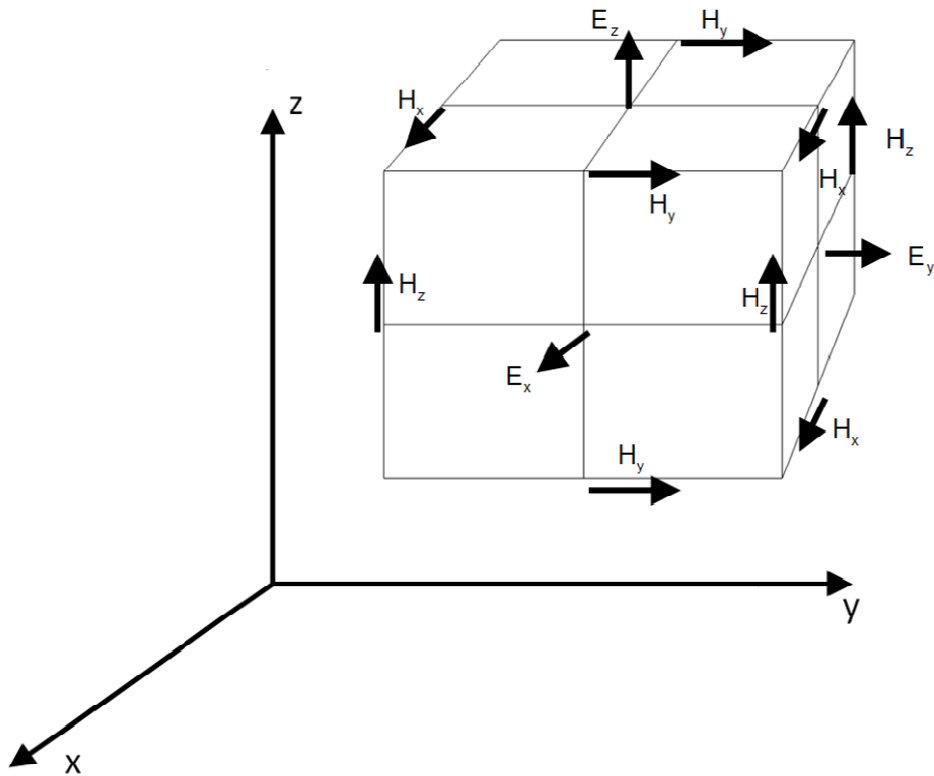


Fig. 2.4. Yee lattice [2].

Furthermore, the location of the different field components not only satisfies the curl operator but also enables usage of the central finite difference approximation. Therefore, the Yee lattice is a key factor for the FDTD method to achieve second order accuracy. This is due to the step size between two locations of the same H or E field component being an integer multiple of step size.

The space and time discretizations enable the calculation of a solution for each partial differential equation to be solved at a node. However, the easier calculation is only possible when certain conditions on the mesh parameters (i.e. Δ_t , Δ_x , Δ_y , Δ_z) are met. Otherwise, the accuracy and stability of the method cannot be secured. In the following section a discussion on the conditions imposed on the mesh to maintain the accuracy and stability of the FDTD is presented.

2.3.3 Mesh accuracy and stability

The mesh is an essential feature of numerical methods since it discretizes the structure of the problem under study. The accuracy of the results highly depends on the mesh parameters. In order to achieve an appropriate mesh accuracy, the parameters Δ_x , Δ_y and Δ_z should be selected with care. Figure 2.5 illustrates in a schematic a top view of a cell introducing the mesh parameters Δ_x and Δ_y (same principle applies with Δ_z).

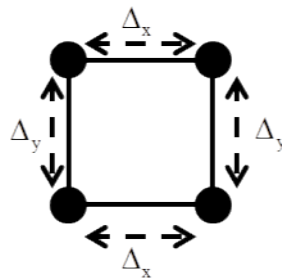


Fig. 2.5. 2D schematic showing mesh parameters Δ_x and Δ_y .

When these parameters are not fine enough (i.e. very large values for Δ_x , Δ_y and Δ_z), the accuracy of the method will be inadequate [14, 16]. The reason for this may be found in the truncation error term in the Taylor expansion of the central difference approximation (Section 2.3.4 and Appendix A). This truncation error is dependent on the square of the step size (i.e. in the order of Δ_x^2) [17]. Hence, the truncation error will increase in a non linear fashion to unacceptable levels (“blow up”) as the mesh is made coarser [17]. In order to maintain the truncation error at a low level, small values of the mesh parameters should be selected. However, the mesh parameters sometimes cannot be chosen fine enough. The memory requirement of a 2D simulation may be approximated as $\text{Area} \times \lambda / \Delta_x^2$ (where Area is the size of the simulation window and $\Delta_x = \Delta_y$). This implies a pronounced increase in the memory requirement with decrease in Δ_x or increase in the number of nodes. In the case of a 3D simulation the increase in the memory requirement $\text{Volume} \times \lambda / \Delta_x^3$ is even more pronounced with increase in the number of nodes [5]. This effect may be seen from Table 2.1, where a small decrease (i.e. 10%) in the value of 3D mesh parameters increases the number of nodes by 3

million. The number of nodes may increase even further depending on the structure being simulated.

In some cases either the structure being simulated or the wavelength spectrum of the simulation is very large. For example in simulations of solar cells a large wavelength spectrum that matches the solar spectrum is required. This leads to very large number of nodes where Maxwell's equations are to be solved. Hence, the memory requirements as well as the simulation time increase. The computational capacity will effectively limit the size (i.e. number of nodes) of the simulation. As a consequence, the mesh parameters should be selected small enough to ensure a low error in the approximation but bearing in mind the computational memory available.

There is another aspect to take into account for an appropriate value of Δ_x , Δ_y and Δ_z . The refractive index of the material under study may also have an impact on the accuracy of the solution. If the refractive index of the material is high and the mesh is not fine enough there would not be sufficient number of points per wavelength to accurately simulate change in the field. The mesh parameters should be chosen in such a way to give a number of points per wavelength large enough for the entire wavelength to achieve accurate results. Empirically this number has been found to be at least 6 points per wavelength for the entire wavelength spectrum. This number of points per wavelength is conventionally considered to provide a good accuracy. Nevertheless, the value may vary depending on the application and simulated materials.

The process to calculate the number of points per wavelength is as follows: the highest value of refractive index in the simulation is divided by the corresponding wavelength. This value gives the effective wavelength. Further to this, the effective wavelength is divided by the largest step size (either Δ_x , Δ_y or Δ_z). The result of this division represents the minimum number of points per wavelength. Any value of Δ_x , Δ_y or Δ_z giving a large number of points increases the mesh accuracy. Normally it is recommended to do a convergence test for simulation studies. Where the initial simulations are run with coarse

mesh (i.e. large values of Δ_x , Δ_y and Δ_z). Then, the mesh is made finer (i.e. smaller values of Δ_x , Δ_y and Δ_z) in a series of simulations until a convergence in the result is obtained. In this manner, the computational power is optimized. However, it should be noted that for a very fine mesh (i.e. very small values for Δ_x , Δ_y and Δ_z) the number of nodes increases cubically [14]. Hence, the computational memory required to solve Maxwell's equations at each node increases drastically as described in Section 2.1 [14]. Therefore, there is usually a compromise between accuracy and computational memory that is available for the simulation. The best approach is a convergence test where the mesh is made finer progressively until no significant change in the fields is recorded. The convergence test carried out for this work is discussed in Section 2.3.6.3.

The finite difference time domain method has also a time step (Δ_t) defining the difference in time between the calculations of E and H field components in the leapfrog approach (Section 2.3.1). The time step and the step size are interrelated and their values have to be chosen appropriately [5]. For this purpose, the values of Δ_x , Δ_y , Δ_z and Δ_t have to meet the Courant condition (also known as Courant, Friedrichs and Lewy criterion) [5]. Otherwise the simulation will be unstable (i.e. as time stepping proceeds the approximation is further apart from the real solution of Maxwell's equations) [5]. The Courant condition is the relation between the space coordinates with the time step to maintain stability of the simulation as follows [5]:

$$\Delta_t \leq \frac{1}{c \sqrt{\frac{1}{\Delta_x^2} + \frac{1}{\Delta_y^2} + \frac{1}{\Delta_z^2}}} \quad (2.8)$$

where c is the speed of light in vacuum. In case of not satisfying Eq. (2.8), the travelling wave could skip one step size when propagating through the medium [18]. In other words, to satisfy Eq. (2.8), the lattice speed (i.e. Δ_x/Δ_t) should be lower than the speed in the travelling medium [17]. Table 2.2 presents the

values of Δ_t in the software used in this work for a range of Δ_x , Δ_y and Δ_z values.

Δ_x (μm)	Δ_y (μm)	Δ_z (μm)	Δ_t (fs)
0.090	0.090	0.090	0.16928000
0.050	0.050	0.050	0.09251200
0.010	0.010	0.010	0.01897990
0.009	0.009	0.009	0.01706640
0.005	0.005	0.005	0.00953056
0.001	0.001	0.001	0.00953056

Table 2.2. Relation between mesh parameters and time step.

When the mesh is coarse such as $\Delta_x = \Delta_y = \Delta_z = 0.09\mu\text{m}$ the corresponding value of Δ_t is 0.16928 fs. As the mesh is made finer, the value of Δ_t to satisfy Eq. (2.8) becomes smaller. For example when the mesh parameters are $\Delta_x = \Delta_y = \Delta_z = 0.009\mu\text{m}$ the value of Δ_t decreases 10% (i.e. $\Delta_t = 0.0170664\text{fs}$). As the mesh is made even finer, the value of Δ_t continues to decrease. Therefore, the increase in the number of nodes is accompanied by a corresponding increase in memory requirements and computational time which can be seen from Table 2.1. However, the increase in the memory requirements is also due to the value of Δ_t . As Δ_t becomes smaller, the number of times Maxwell's equations have to be solved increases as well.

In the following section the approximation, used in the FDTD method to obtain a solution of a partial differential equation is introduced. This technique is called finite differences and it is the key for the second order accuracy of the FDTD method.

2.3.4 Finite differences

The finite difference approximation is a manner of solving the calculation process of derivatives. In the case of very small Δ_x values, any derivative at a specific point (A) can be expressed in terms of a simple difference. This difference should be between the values at two points adjacent to point A (to

achieve first or second order approximation). Conventionally the definition of a derivative is expressed as follows [19]:

$$u'(x) = \lim_{\Delta_x \rightarrow 0} \frac{u(x + \Delta_x) - u(x)}{\Delta_x} \quad (2.9)$$

where $u(x)$ is a function dependent on x , $u'(x)$ is its first derivative and Δ_x is the step size.

There are three types of finite differences: Forward difference (1st order accurate), Backward difference (1st order accurate) and Central difference (2nd order accurate). The equation representing the finite difference is presented below. The Taylor expansion of the three types of finite difference approximation are presented in Appendix A for reference.

- Central difference provides a second order accurate approximation of a derivative. It uses the same number of points as forward and backward differences but with higher level of accuracy. This is the reason why, central difference is selected to implement the FDTD method [5].

$$u'(x_i) \approx \frac{u(x_i + \Delta_x) - u(x_i - \Delta_x)}{2\Delta_x} = \frac{u_{i+1} - u_{i-1}}{2\Delta_x} \quad (2.10)$$

where the symbols i , $i+1$ and $i-1$ represent the current node, the next node and the previous node respectively.

In the following section the governing equations for each of the E and H field components (i.e. E_x , E_y , E_z , H_x , H_y and H_z) of the FDTD method are introduced. Furthermore, the concept of the Yee lattice space distribution and the concept of the leapfrog approach in time are included in the derivation by using the Yee notation.

2.3.5 Governing equations of the 3D FDTD method

The equations presented in this section arise from the derivation of the FDTD method which is shown in Appendix B. The full derivation of the method begins with the 3D form of the Maxwell's equations in the partial differential form (Eq. (2.1)- Eq. (2.7)).

By using the Yee notation the nodes in x, y and z (in the mesh) are given the notation i, j and k as subscripts respectively to indicate their position [5]. Additionally the increase or reduction of half or full step is done by adding/subtracting $\frac{1}{2}$ or 1 from i, j and k [5]. This idea is illustrated in Fig. 2.6. This diagram shows the case of the variable "i" where "i" represents the current step.

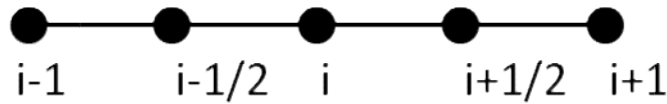


Fig. 2.6. Schematic explaining the Yee notation for the case of "i".

It should be noted that the same principle applies to j and k. Furthermore, the parameter "t" (i.e. time) is represented in the Yee notation as "n" which is represented as a superscript and in similar manner to space coordinates, increment in n by 1/2 or 1 represents time advance by a half or a full step. The governing equation for the E_x field component (Eq. (B.16)) is presented in Eq. (2.11) as follows, after implementing the finite difference scheme:

$$\begin{aligned} \bar{E}_x \Big|_{i,j+1/2,k+1/2}^{n+1/2} = \bar{E}_x \Big|_{i,j+1/2,k+1/2}^{n-1/2} & \left(\frac{1 - \frac{\Delta_t \sigma_{i,j+1/2,k+1/2}}{2\epsilon_{i,j+1/2,k+1/2}}}{1 + \frac{\Delta_t \sigma_{i,j+1/2,k+1/2}}{2\epsilon_{i,j+1/2,k+1/2}}} \right) \\ & + \frac{\Delta_t}{\epsilon_{i,j+1/2,k+1/2}} \left(\frac{\bar{H}_z \Big|_{i,j+1,k+1/2}^n - \bar{H}_z \Big|_{i,j,k+1/2}^n}{\Delta_y} - \frac{\bar{H}_y \Big|_{i,j+1/2,k+1}^n - \bar{H}_y \Big|_{i,j+1/2,k}^n}{\Delta_z} \right) \\ & - \bar{J}_{\text{source}_x} \Big|_{i,j+1/2,k+1/2}^n \end{aligned} \quad (2.11)$$

where σ , ε , Δ_t , Δ_x , Δ_y , Δ_z are the conductivity, dielectric constant, time step and step sizes in x, y and z coordinates respectively. The steps required to

express the partial differential term $\frac{d\bar{H}_z}{dy}$ (Eq. (B.16)) as $\frac{\bar{H}_z|_{i,j+1,k+1/2}^n - \bar{H}_z|_{i,j,k+1/2}^n}{\Delta_y}$

using the finite difference scheme are as follows:

- Identify the variable in the denominator which is dy.
- The variable y is represented by the integer j.
- Identify the variable to be expressed in terms of its difference which is \bar{H}_z .
- Write the first term of the difference considering that j is the variable to experience a change as $\bar{H}_z|_{i,j+1,k+1/2}^n$.
- Write the second term of the difference with a Δ_y step size in variable j as $\bar{H}_z|_{i,j,k+1/2}^n$.
- Then, the term $\frac{d\bar{H}_z}{dy}$ can be expressed in terms of finite differences as

$$\frac{\bar{H}_z|_{i,j+1,k+1/2}^n - \bar{H}_z|_{i,j,k+1/2}^n}{\Delta_y}$$

Using the same approach the governing equations corresponding to H_x , H_y , H_z , E_y and E_z (Eqs. (B.12, B.13, B.14, B.17 and B.18)), can be expressed using the finite difference scheme as shown in Eqs. ((2.12) - (2.16)):

$$\begin{aligned} \bar{E}_y|_{i+1/2,j,k+1/2}^{n+1/2} = & \bar{E}_y|_{i+1/2,j,k+1/2}^{n-1/2} \left(\frac{1 - \frac{\Delta_t \sigma_{i+1/2,j,k+1/2}}{2\varepsilon_{i+1/2,j,k+1/2}}}{1 + \frac{\Delta_t \sigma_{i+1/2,j,k+1/2}}{2\varepsilon_{i+1/2,j,k+1/2}}} \right) \\ & + \frac{\Delta_t}{\varepsilon_{i+1/2,j,k+1/2}} \left(\frac{\bar{H}_x|_{i+1,j,k+1/2}^n - \bar{H}_x|_{i,j,k+1/2}^n}{\Delta_z} - \frac{\bar{H}_z|_{i+1/2,j,k+1}^n - \bar{H}_z|_{i,j+1/2,k}^n}{\Delta_x} \right) \\ & 1 + \frac{\Delta_t \sigma_{i+1/2,j,k+1/2}}{2\varepsilon_{i+1/2,j,k+1/2}} \left(-\bar{J}_{\text{source}_y}|_{i+1/2,j,k+1/2}^n \right) \end{aligned} \quad (2.12)$$

$$\begin{aligned} \bar{E}_z^{n+1/2}{}_{i+1/2,j+1/2,k} &= \bar{E}_z^{n-1/2}{}_{i+1/2,j+1/2,k} \left(\frac{1 - \frac{\Delta_t \sigma_{i+1/2,j+1/2,k}}{2\varepsilon_{i+1/2,j+1/2,k}}}{1 + \frac{\Delta_t \sigma_{i+1/2,j+1/2,k}}{2\varepsilon_{i+1/2,j+1/2,k}}} \right) \\ &+ \frac{\Delta_t}{\varepsilon_{i+1/2,j+1/2,k}} \left(\frac{\bar{H}_y^n{}_{i+1,j+1/2,k} - \bar{H}_y^n{}_{i,j+1/2,k}}{\Delta_x} - \frac{\bar{H}_x^n{}_{i+1/2,j+1,k} - \bar{H}_x^n{}_{i+1/2,j,k}}{\Delta_y} \right) \\ &+ \frac{\Delta_t \sigma_{i+1/2,j+1/2,k}}{2\varepsilon_{i+1/2,j+1/2,k}} \left(-\bar{J}_{\text{source}_z}{}^n{}_{i+1/2,j+1/2,k} \right) \end{aligned} \quad (2.13)$$

$$\begin{aligned} H_x^{n+1/2}{}_{i,j+1/2,k+1/2} &= H_x^{n-1/2}{}_{i,j+1/2,k+1/2} \left(\frac{1 - \frac{\Delta_t \sigma_{i,j+1/2,k+1/2}^*}{2\mu_{i,j+1/2,k+1/2}}}{1 + \frac{\Delta_t \sigma_{i,j+1/2,k+1/2}^*}{2\mu_{i,j+1/2,k+1/2}}} \right) \\ &+ \frac{\Delta_t}{\mu_{i,j+1/2,k+1/2}} \left(\frac{E_z^n{}_{i,j+1,k+1/2} - E_z^n{}_{i,j,k+1/2}}{\Delta_y} - \frac{E_y^n{}_{i,j+1/2,k+1} - E_y^n{}_{i,j+1/2,k}}{\Delta_z} \right) \\ &+ \frac{\Delta_t \sigma_{i,j+1/2,k+1/2}^*}{2\mu_{i,j+1/2,k+1/2}} \left(-M_{\text{source}_x}{}^n{}_{i,j+1/2,k+1/2} \right) \end{aligned} \quad (2.14)$$

$$\begin{aligned} \bar{H}_y^{n+1/2}{}_{i+1/2,j,k+1/2} &= \bar{H}_y^{n-1/2}{}_{i+1/2,j,k+1/2} \left(\frac{1 - \frac{\Delta_t \sigma_{i+1/2,j,k+1/2}^*}{2\mu_{i+1/2,j,k+1/2}}}{1 + \frac{\Delta_t \sigma_{i+1/2,j,k+1/2}^*}{2\mu_{i+1/2,j,k+1/2}}} \right) \\ &+ \frac{\Delta_t}{\mu_{i+1/2,j,k+1/2}} \left(\frac{\bar{E}_x^n{}_{i+1,j,k+1/2} - \bar{E}_x^n{}_{i,j,k+1/2}}{\Delta_z} - \frac{\bar{E}_z^n{}_{i+1/2,j,k+1} - \bar{E}_z^n{}_{i+1/2,j,k}}{\Delta_x} \right) \\ &+ \frac{\Delta_t \sigma_{i+1/2,j,k+1/2}^*}{2\mu_{i+1/2,j,k+1/2}} \left(-\bar{M}_{\text{source}_y}{}^n{}_{i+1/2,j,k+1/2} \right) \end{aligned} \quad (2.15)$$

$$\begin{aligned} \bar{H}_z^{n+1/2}{}_{i+1/2,j+1/2,k} &= \bar{H}_z^{n-1/2}{}_{i+1/2,j+1/2,k} \left(\frac{1 - \frac{\Delta_t \sigma_{i+1/2,j+1/2,k}^*}{2\mu_{i+1/2,j+1/2,k}}}{1 + \frac{\Delta_t \sigma_{i+1/2,j+1/2,k}^*}{2\mu_{i+1/2,j+1/2,k}}} \right) \\ &+ \frac{\Delta_t}{\mu_{i+1/2,j+1/2,k}} \left(\frac{\bar{E}_y^n{}_{i+1,j+1/2,k} - \bar{E}_y^n{}_{i,j+1/2,k}}{\Delta_x} - \frac{\bar{E}_x^n{}_{i+1/2,j+1,k} - \bar{E}_x^n{}_{i+1/2,j,k}}{\Delta_y} \right) \\ &+ \frac{\Delta_t \sigma_{i+1/2,j+1/2,k}^*}{2\mu_{i+1/2,j+1/2,k}} \left(-\bar{M}_{\text{source}_z}{}^n{}_{i+1/2,j+1/2,k} \right) \end{aligned} \quad (2.16)$$

In this work the implementation of the FDTD method is carried out by the commercial package Lumerical FDTD solutions [20]. In the following section the

simulation set up for this work is presented. Furthermore, a rationale of the simulation set up is discussed.

2.3.6 Simulation set up

The simulation set up to obtain the results presented in this work has to be selected carefully. The simulation is set up in a manner to obtain the calculation of the reflection from a surface. The selection of an appropriate mesh is essential for accurate results. Otherwise, the accuracy and stability of the simulation would be compromised (as discussed in Section 2.3.3). A diagram illustrating the parameters that should be considered during the set up process of a simulation is presented in Fig. 2.7.

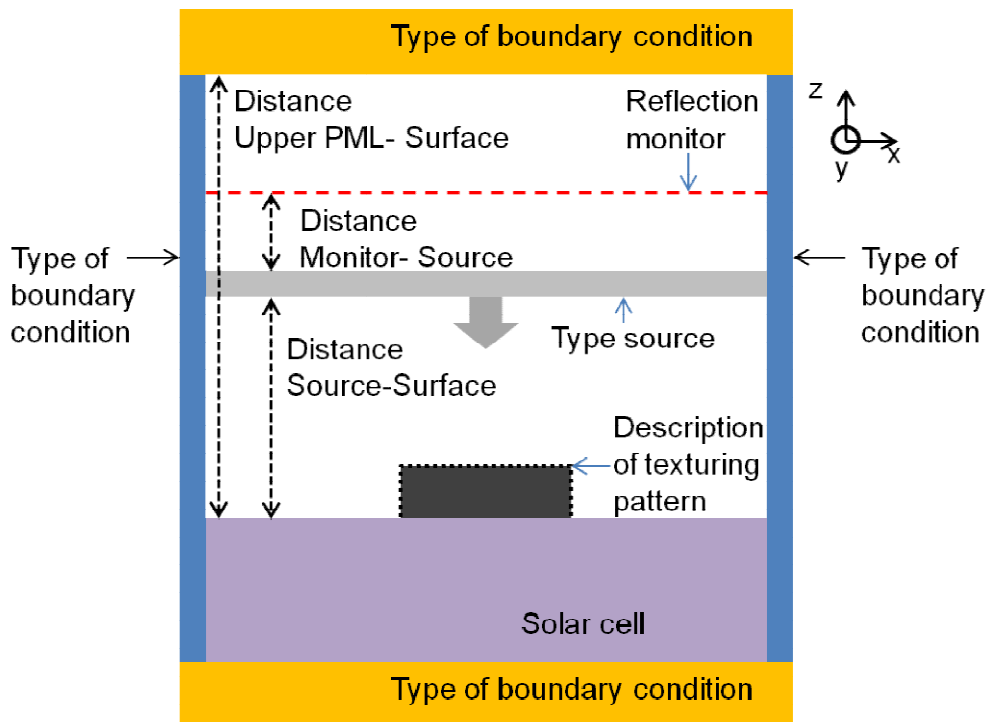


Fig. 2.7. Schematic illustrating the considerations during the setting up process.

In Fig. 2.7 there are various factors that should be considered when setting up a simulation. Among the factors presented in Fig. 2.7 there are some factors fixed beforehand such as the type of source and the type of boundary conditions due to the characteristics of the simulation itself. The type of source is a plane wave source and the boundary conditions are the Perfectly Matched Layer (PML) [5] on the top and bottom boundaries and the Periodic Boundary Conditions (PBC)

[5] on the side boundaries which will be described in more detail in Section 2.3.8. The parameters that require extra definition are: i) locating the monitor and source, ii) defining window height, iii) selecting mesh parameters, iv) choosing the number of PML layers and v) defining the parameters correctly for representing the different structures under study. There are two structures under study in this work (Section 2.3.6.5): a micro pillar array solar cell and a hut-like micro pillar array solar cell. In the following sections the simulation parameters in this work for an appropriate set up are discussed starting with the location of the monitor and source.

2.3.6.1 Location of the monitor and the source

Figure 2.8 shows a Si substrate on top of which the texturing patterns are grown. An electromagnetic wave source and a reflection monitor are placed above the solar cell. The distances between the source and the monitor and the substrate (planar solar cell) or the top of the texturing pattern are defined after a benchmarking study as $1.0 \mu\text{m}$ and $1.3 \mu\text{m}$ respectively. The location of source and monitor are defined. The source required to replicate the electromagnetic waves reaching a solar cell on the Earth is a plane wave-AM 1.5 source. Even though the electromagnetic waves from the sun are of spherical nature, those reaching the Earth can be considered as plane waves.

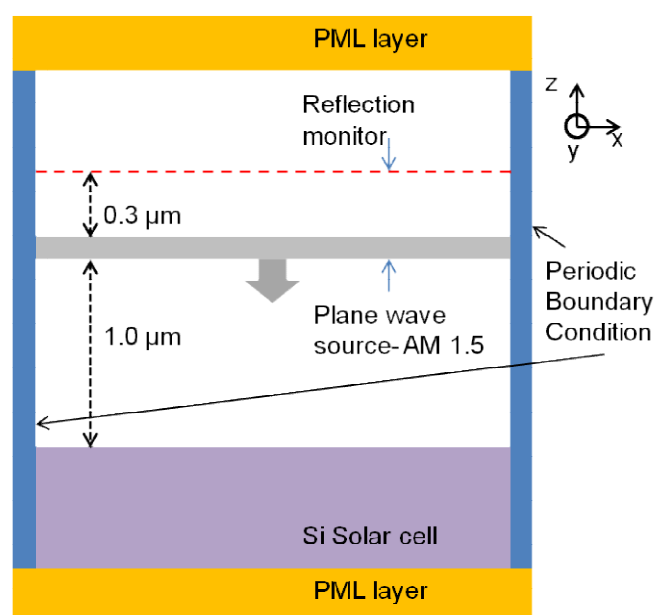


Fig. 2.8. Schematic of simulation set up.

A reflection monitor is placed at $0.3 \mu\text{m}$ above the plane wave source. This monitor measures the electromagnetic waves travelling through it. A Fourier transform is carried out to convert the data to frequency domain for post processing. Then, the frequency (wavelength) dependent transmission at the monitor can be calculated from which the reflection may be obtained.

Periodic Boundary Conditions (PBC) are applied on both sides of the simulation window to repeat the structure periodically in the x-y plane. On the top and bottom end of the simulation window PML (Section 2.3.8.3.1) layers are placed which absorb any waves reaching these boundaries. The absorption of any incident light on the PML is nearly perfect (not 100% of incident waves are absorbed). Therefore, the distance between the reflection monitor and the top PML should be selected carefully. In the following section the window height selection process is discussed.

2.3.6.2 Window height

Figure 2.9 illustrates the factors that should be taken into account when choosing the simulation window height and are discussed below.

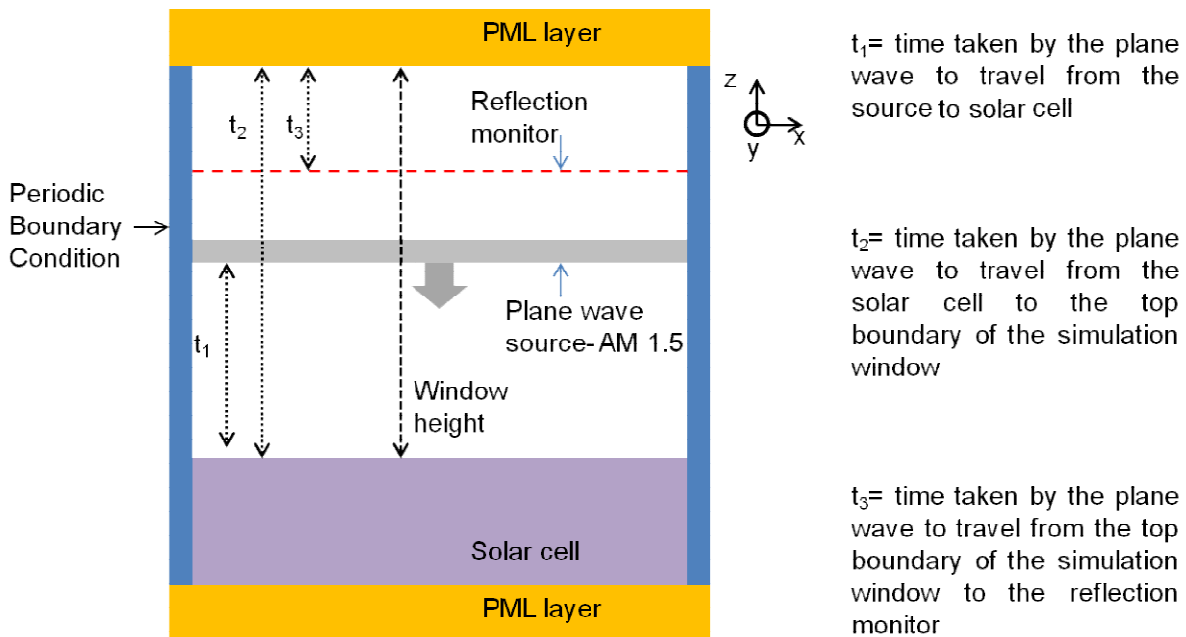


Fig. 2.9. Schematic for the selection of window height.

There are some constraints that should be considered when selecting the height of the simulation window. The top end of the simulation window has to be located at a position higher than the reflection monitor. As can be seen from Fig. 2.9 the boundary selected in this work, at the top boundary, is a PML layer to absorb any electromagnetic wave reaching the top of the simulation window.

The location of the PML (i.e. window height) is very important since there are two conditions that have to be met. One condition is that the simulated time (time indicating the time span of the simulation) should be long enough for the field at the location of the reflection monitor to decay. The other is that the window height should be large enough so that the wave cannot reach the reflection monitor a second time within the simulated time. This means that the total time taken by the electromagnetic wave which is the sum of time taken to travel source-surface (t_1), surface-PML (t_2), PML-reflection monitor (t_3) should be longer than the simulated time.

$$t_{\text{simulated}} < t_1 + t_2 + t_3 \quad (2.17)$$

If the simulated time is longer than $t_1 + t_2 + t_3$ then the data collected by the reflection monitor could have some spurious reflection which would invalidate the results. One possible solution for this is to increase the window height to an extremely large value such as $50\mu\text{m}$ to ensure no contamination of the results. However, this option would imply a high computational cost. Therefore, a more sensible approach is to have a convergence test to find out what window height value is suitable. In addition, the simulation must run for sufficient time to allow the input pulse to travel from the source to the cell surface and the subsequent reflected waves to reach the monitor. The software needs to record sufficient number of time samples of the field to perform a Discrete Fourier Transform (DFT). Therefore, the resultant simulated time, should be longer than $t_1 + t_2$ and shorter than $t_1 + t_2 + t_3$.

For the simulations presented in this work, the height of the simulation window is set to be 12 μm above the solar cell. Figure 2.10 shows the E field intensity² at two different point monitors (time monitors) to show that the fields have decayed at the reflection monitor before the simulation is complete. These time monitors are placed exactly at the centre of the simulation window but at different heights: just above the source (exactly at same height as the reflection monitor) and just below the boundary with the PML region. Additionally, in Fig. 2.11 the data of a 2D time monitor placed normal to the y axis near the reflection monitor are shown.

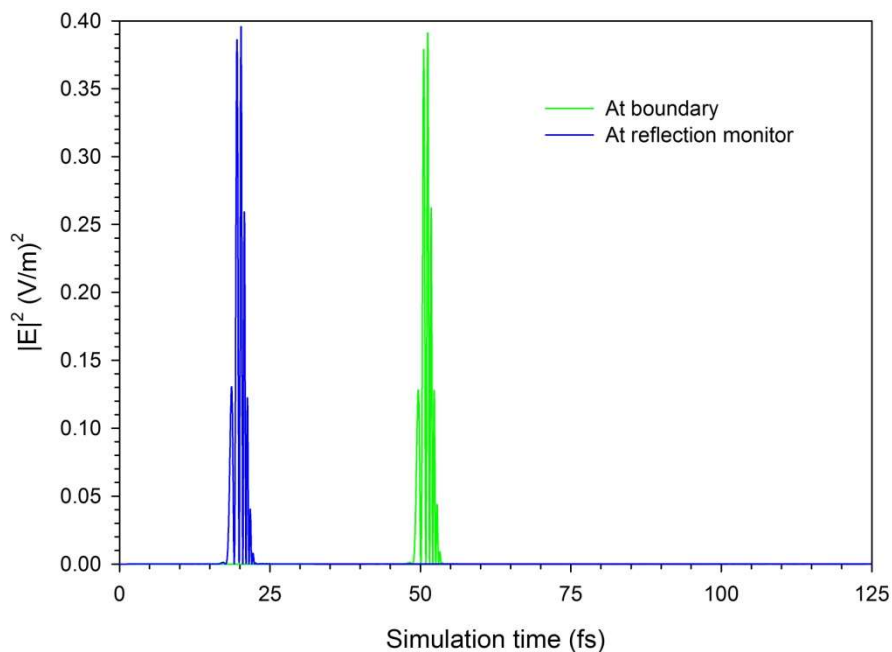


Fig. 2.10 E field intensity vs. time at reflection monitor and boundary of window.

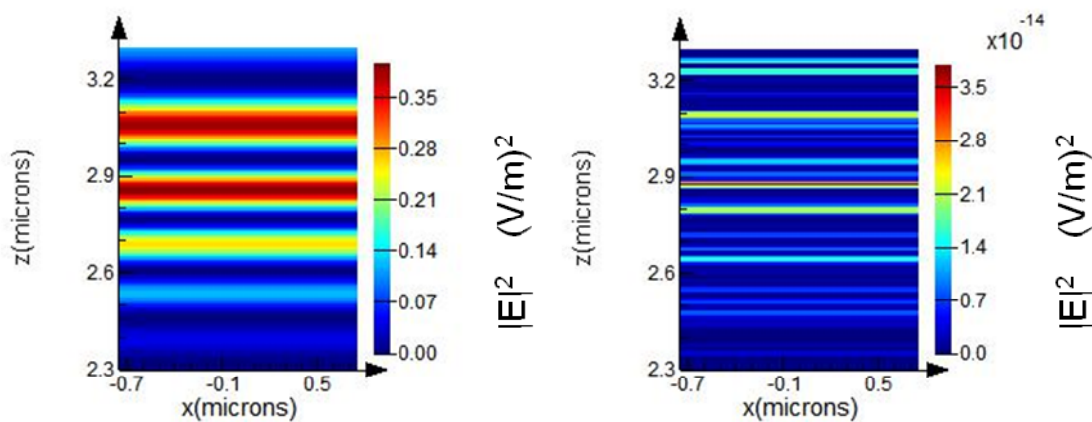


Fig. 2.11. E field intensity near the reflection monitor at a. 20fs and b.124fs.

² In this work the term “E field intensity” stands for $|E|^2$ ($(E/V)^2$).

From Fig. 2.10 it is possible to observe that there is a high E field intensity after 18 fs at the location of the reflection monitor. This corresponds to the electromagnetic wave (reflected at the solar cell surface) when it reaches the location of the reflection monitor. Furthermore, after 48 fs the same pulse is observed near the PML. Then, the electromagnetic waves are absorbed by the PML.

Otherwise in the case of truncating the window without a PML boundary, the wave would be reflected back into the simulation window which would cause corruption of the results. This shows the importance of the PML which will be discussed in more detail in Sections 2.3.6.4 and 2.3.8.3.1.

After approximately 60fs, near the PML and at the reflection monitor before the simulation ends there is no record of any E field intensity. This means that the fields have decayed and that the PML has absorbed the incident wave to avoid any distortion. The latter statement can be confirmed by Fig. 2.11 a and b. After 20 fs the field plot shows a high intensity peak of more than 0.35 V/m at the location of the reflection monitor. However, after 124 fs at the same location the presence of any field intensity is minimum; in the order of 10^{-14} V / m .

Another very important factor in the simulation is the mesh. In the following section how the values of the mesh parameters should be chosen is discussed.

2.3.6.3 Mesh parameters

The mesh parameters are essential for accurate results as discussed in Section 2.3.3. The values of Δ_x , Δ_y and Δ_z have to be small enough for the finite difference approximation to be valid [5]. However, the smaller the values of Δ_x , Δ_y and Δ_z , the larger the computational memory becomes. This is the reason why it is important to do a convergence test.

In the convergence test for the selection of Δ_x , Δ_y and Δ_z , the mesh parameters (i.e. Δ_x , Δ_y and Δ_z) are varied (beginning with large values) for

multiple simulations until an appropriate result is obtained. The test consists of a plane wave which is launched into the simulation domain. This plane wave is incident on a planar slab of Si and the reflected waves are measured by the reflection monitor. Then, the error in the simulation is obtained by comparing the reflection data obtained at the monitor (for each simulation) to the Fresnel reflection data for Si as follows:

$$\text{Error in simulation} = \frac{\text{Predicted reflection} - R}{\text{Predicted reflection}} \times 100 \quad (2.18)$$

where the Error in simulation, Predicted reflection and R are the percentage error, the reflection predicted by Fresnel's equations and the values of R obtained from the simulations respectively.

First Δ_z is kept constant while Δ_x and Δ_y are varied. From these results an appropriate value of Δ_x and Δ_y is selected (fixed) and then Δ_z is varied. This results in error in simulation vs. wavelength curves which are presented in Fig. 2.12 for the case of $\Delta_x = \Delta_y = 0.01\mu\text{m}$. This process is iterated with different values of Δ_x and Δ_y until all the three mesh parameters are chosen.

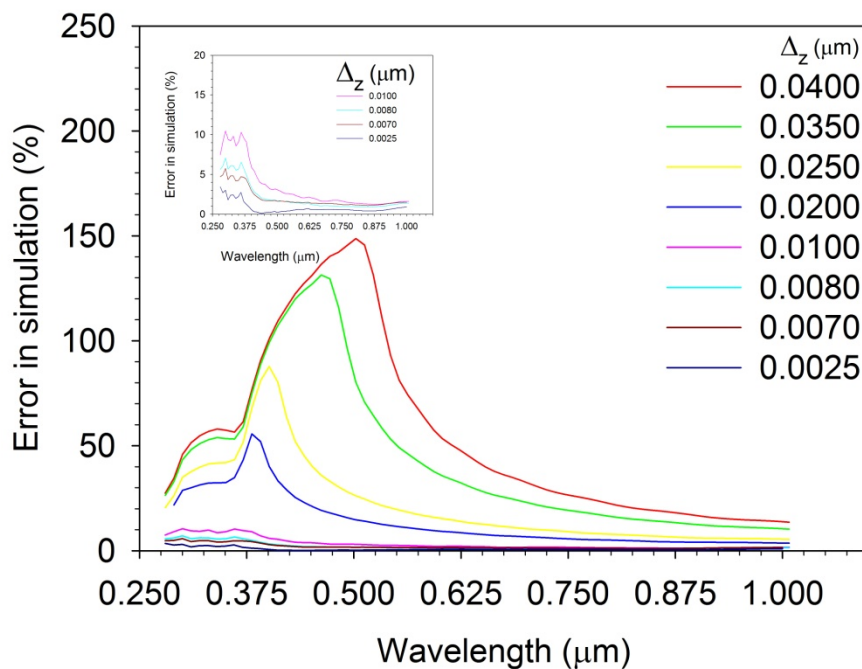


Fig. 2.12. Percentage of the simulation error of R per wavelength as varying Δ_z while keeping constant Δ_x and Δ_y at $0.01\mu\text{m}$.

From Fig. 2.12 the tremendous influence that the mesh parameters have on the measurements can be observed. For a coarse mesh such as $\Delta_x = \Delta_y = 0.01\mu\text{m}$ and $\Delta_z = 0.05\mu\text{m}$ the R measured in the simulation is up to 150% different to the performance predicted by Fresnel. Then, as the values of Δ_z decrease while Δ_x and Δ_y remain constant, the difference between the simulated and the predicted value of reflection reduces considerably. In Fig. 2.12, the simulated reflection with the finest mesh ($\Delta_x = \Delta_y = 0.01\mu\text{m}$ and $\Delta_z = 0.0025\mu\text{m}$) shows less than 2% error. This is a percentage error that ensures high precision of the results. However, the time taken to run the simulation (9530 seconds) was very long for such a simple simulation. Therefore, a different value of Δ_z should be chosen to meet accuracy and simulation time requirements. For accurate results a maximum 5% error is considered as acceptable for this work. The values of Δ_x , Δ_y and Δ_z providing a simulation error of less than 5% and relatively fast simulations (6753 seconds) are $\Delta_x = \Delta_y = 0.01\mu\text{m}$ and $\Delta_z = 0.007\mu\text{m}$. Another parameter related to the mesh is the number of the PML layers. The process to select the number of PML layers for this work is introduced in the following section.

2.3.6.4 Number of PML layers

This section presents the convergence test to define the number of PML layers. A more detailed discussion about the PML itself with its rationale and advantages will be presented in Section 2.3.8.3.1. The number of PML layers effectively determines the amount of incident light to be absorbed by the PML [5]. A larger number of PML layers leads to a larger portion of the incident waves to be absorbed. It is important to emphasize that the process of selecting the number of PML layers should be done once the mesh parameters Δ_x , Δ_y and Δ_z have been selected. The reason is that the value of the mesh parameters directly affects the thickness of the PML independently of the number of PML layers.

The process to select the number of PML layers for this work is as follows. A plane wave is launched normal to a PML with the lowest possible number of PML layers which is two. Then, any reflected wave is measured at a reflection monitor. Then measured data is integrated overall wavelengths (i.e. RInt (refer to Section 2.3.6.6)). Then, the same process is repeated for multiple simulations while increasing the number of PML layers. Figure 2.13 shows the results of this test.

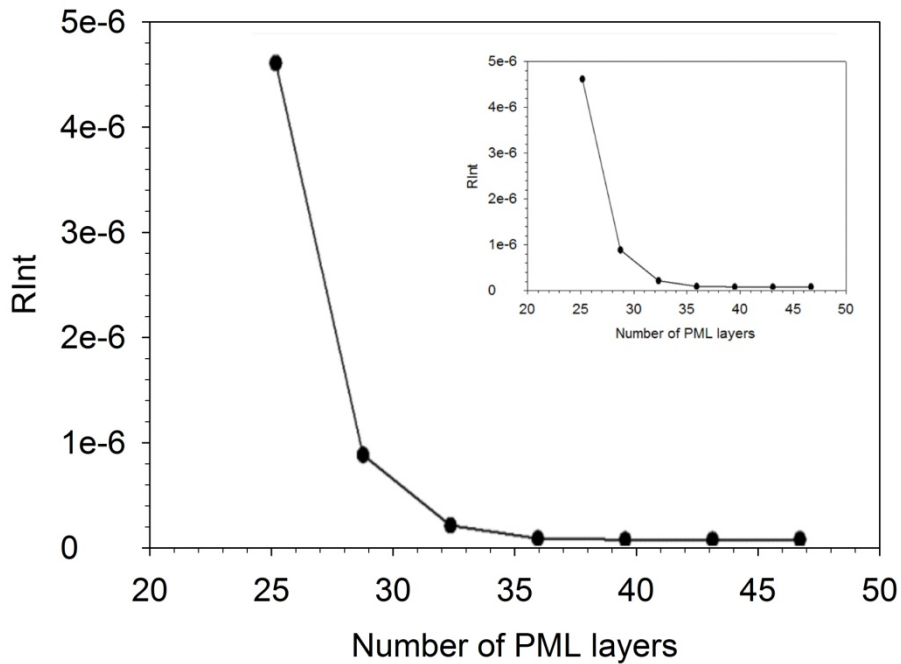


Fig. 2.13. RInt vs. Number of PML layers.

Figure 2.13 shows the RInt values corresponding to a low number of PML layers to be very high. Then as the number of PML layers increases, there is a drastic reduction of the RInt. After a certain number of PML layers, RInt starts to converge. This means that from this specific number of PML layers a good absorption of the PML may be achieved. However, the longer the time the simulation takes to run, the larger the memory requirement. In this work, the number of PML layers chosen is 40.

An appropriate manner to set up the FDTD parameters of a simulation by doing convergence tests has been introduced. These convergence tests define the location of the source, monitor, window height and the number of PML layers. Nevertheless, in the set up of a simulation there are structural parameters that

have to be defined as well. In the following section the parameters defining the structures under study are introduced.

2.3.6.5 Representing the different structures under study

One of the two structures under study in this work is the micro pillar array (results are shown in Chapter 3) presented in Fig. 2.14. The structure consists of texturing cylindrical pillars on the top of the solar cell. The key parameters considered in this study are: Height (H), Diameter (D), Surface Coverage (SC) in hexagonal and square configurations.

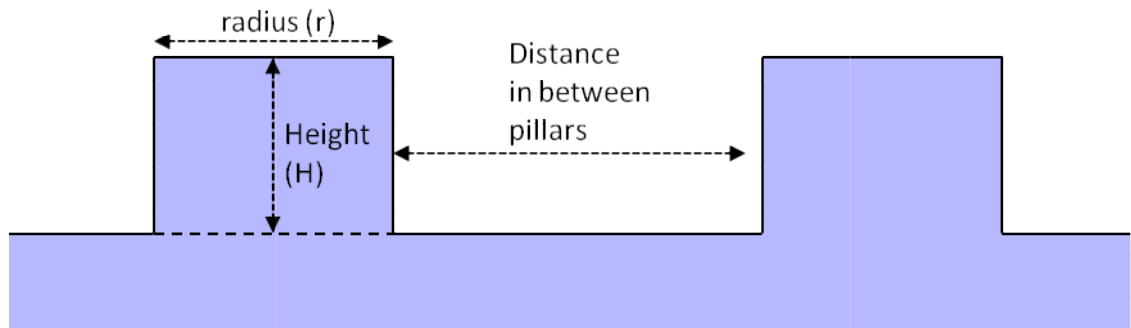


Fig. 2.14. Schematic of micro pillars.

Figure 2.14 illustrates the cross-section of two micro pillars, where the parameters are presented: H, r, distance between huts and SC. Height and radius (r) correspond to the height and radius of the micro pillar. The distance between pillars is the length measured between two adjacent pillars and it is closely related to the simulation window and to the value of SC. The simulation window is the area in the x-y plane of the solar cell being simulated and it may be defined as follows:

$$\text{simulation window} = X \times Y \quad (2.19)$$

where the variables X and Y represent the sides of the simulation window. The SC is the proportion of the solar cell area occupied by micro pillars and it is expressed as a percentage. The SC corresponding to any given simulation may be obtained in terms of the simulation window as follows:

$$SC = \frac{2 \times \pi \times r^2 \times 100}{\text{simulation window}} = \frac{2 \times \pi \times r^2 \times 100}{X \times Y} \quad (2.20)$$

The simulations for this structure were run for two different configurations: square and hexagonal. A schematic diagram showing the top view of a micro pillar array in hexagonal configuration is presented in Figure 2.15, where the parameter A represents the distance between the pillars.

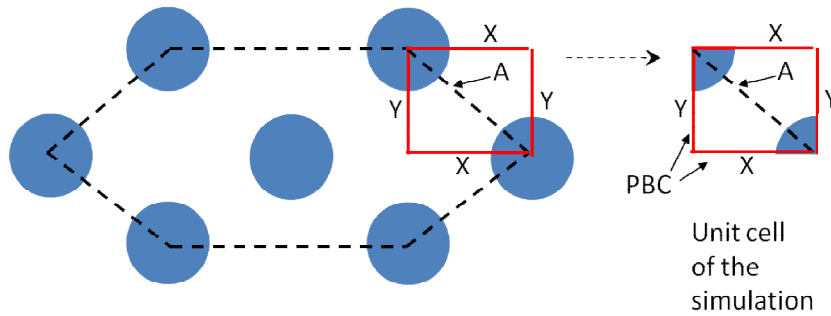


Fig. 2.15. Schematic of hexagonal array configuration.

In both array configurations (i.e. square and hexagonal) the simulation window has the same size for the same SC value. The difference between square and hexagonal configurations is achieved in the set up of the simulation by varying the relation between X and Y. For the square configuration the relation is $X = Y$ and for the hexagonal configuration the relation is $Y = X \times \sqrt{3}$. This difference in Y between the two configurations causes a difference in the location of the micro pillars. This difference leads the hexagonal configuration to have higher array compactness than square configuration for the same SC. Throughout the study the key structural parameters presented above are varied to identify the effect of each of them.

The second structure presented in this thesis is named as hut-like micro pillars arrays (results are shown in Chapter 4). It is a new texturing pattern which is first introduced in this work. It consists in texturing pillars of the solar cell top with an angle (θ) between the solar cell surface and the side walls of the pillar. The arrangement of the pattern for the hut-like micro pillar array for this thesis is the hexagonal configuration.

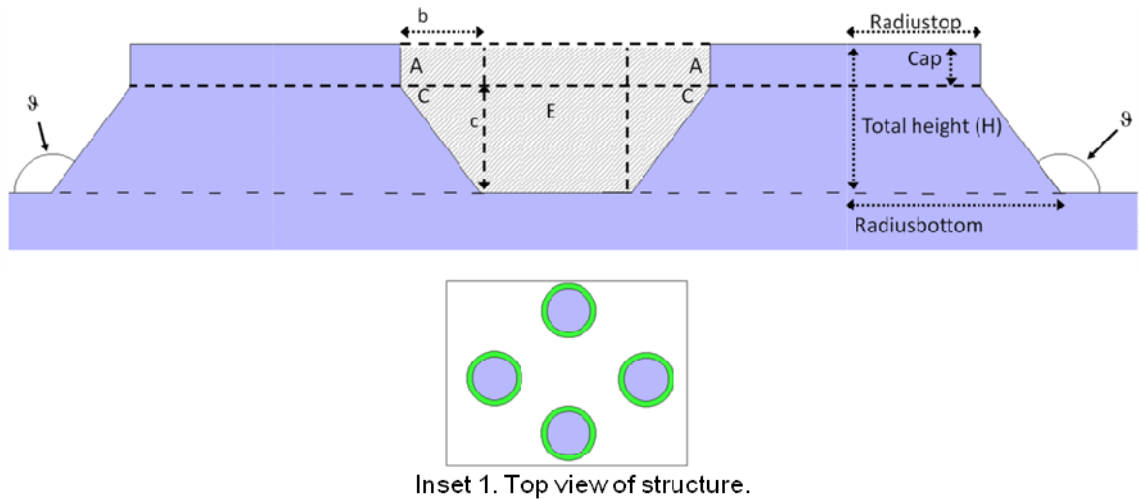


Fig. 2.16. Schematic of proposed hut-like micro pillar array. Inset 1 Top view of hut-like pattern.

A schematic diagram of the hut-like pattern is presented in Fig. 2.16. The purpose of this pattern is to enhance light trapping in-between huts by multiple reflections. This is achieved by an optimization of the air volume between the huts. This is a similar concept to other patterns such as nanowires or micro pillars.

Inset 1 in Fig. 2.16 has a top view of the pattern where we can see the hexagonal configuration of the pattern. The inner circle (i.e. blue) corresponds to the vertical section of the pillar and outer circle (i.e. green) corresponds to the sloped part of the huts that can be seen in Fig. 2.16. This sloped part is considered to be very important for the performance of the pattern. This is due to the changes of the reflection from the surface, predicted by Fresnel's equations, as the angle of incidence of the incoming light changes [21]. Further discussion will be introduced in Chapter 4 where the results are presented.

There are some critical factors to be considered while in the set up stage of the simulation such as: Surface Coverage (SC), Cap, the angle ϑ , and the area in between the huts in cross-section (see Fig. 2.16). Cap is the vertical portion of the hut-like pillar shown. The angle ϑ (in degrees ($^{\circ}$)) is calculated as follows:

$$\vartheta = \frac{180 \times \tan^{-1}\left(\frac{H}{\text{Radiusbottom} - \text{Radiustop}}\right)}{\pi} \quad (2.21)$$

where H is the length measured from the substrate to the top of the hut, Radiustop is the radius corresponding to the top of the hut and Radiusbottom is the radius corresponding to the bottom of the hut. The area in between huts can be easily calculated as the sum of the areas A, C and E which are shaded in grey (area in between the huts) in Fig. 2.16:

$$A = \text{Cap} \times b \quad (2.22)$$

$$C = \frac{1}{2} \times c \times b \quad (2.23)$$

$$E = \text{distance between huts} \times H \quad (2.24)$$

$$\text{Area} = 2A + 2C + E = E + 2(A + C) \quad (2.25)$$

After substituting Eqs. (2.22)-(2.24) into Eq. (2.25) the following expression may be obtained:

$$\text{Area} = \text{distance between huts} \times H + 2 \times b \left(\text{Cap} + \frac{1}{2} \times c \right) \quad (2.26)$$

By rearranging Eqs. (2.22)-(2.26) it is also possible to express the area in between huts in terms of H, Cap, ϑ , SC, Radiustop and Radiusbottom as follows:

$$\text{Area} = H \times \left(\frac{H}{\tan\left(\frac{\vartheta\pi}{180}\right)} \times \left(\frac{\text{Cap}}{H} + 1\right) + \sqrt{12 \times \text{Radiusbottom}^2 - \frac{2\sqrt{3} \times \pi \times \text{Radiustop}^2 \times 100}{\text{SC}}} \right) \quad (2.27)$$

Once the structural parameters required to replicate the structures under study have been introduced, the simulations can be run. In the simulations H, D, SC and ϑ are varied to analyse the optical performance. This leads to a large amount of data being extracted from the simulations. Then, the data obtained from the simulations has to be presented in a clear and meaningful manner. The following section discusses how the results obtained from the monitors are processed.

2.3.6.6 Processing of the results

The presentation style of the simulation results is very important to extract as much information as possible. In this work, the simulation results are obtained from a number of monitors that record the electromagnetic waves travelling through it. In this section the post-processing calculations carried out with the simulation results and the presentation styles used in this work are introduced as follows:

- Plotting the field cross sections at different locations of the simulation domain at different wavelengths (see Fig 3.3).
- Calculating the value of the Reflectance (R) per wavelength (R vs. wavelength). This value may be obtained by calculating the transmission at the reflection monitor and subtracting from unity. The transmission at a monitor may be calculated as follows:

$$T(f) = \frac{\frac{1}{2} \int \text{real}(\vec{P}(f)^{\text{Monitor}}) \cdot dS}{\text{Sourcepower}} \quad (2.28)$$

where $T(f)$, $P(f)$, dS and Sourcepower are the frequency (wavelength) dependent transmission, the Poynting vector (directional flux density of the E field), the normal to the surface and the power of the electromagnetic waves launched by the source respectively. Once T is obtained, it is possible to calculate the value of R, using the transmission data, as follows:

$$R(\lambda) = 1 - T(\lambda) \quad (2.29)$$

Using Eq. (2.29) is possible to obtain R as a function of wavelength and to compare performances across the entire solar spectrum (see Fig. 3.1). However, the performance comparison can become untidy when several patterns with different dimensions are under study.

- Calculating the Reflectance integrated overall wavelength (RInt) as follows [22]:

$$RInt = \frac{\int_{I_{AM1.5}} T(\lambda) * I_{AM1.5}(\lambda) d\lambda}{\int_{I_{AM1.5}} I_{AM1.5}(\lambda) d\lambda} \quad (2.30)$$

where T, $I_{AM1.5}$ and λ represent the transmission through the monitor, reference solar spectrum AM 1.5 and wavelength respectively. This figure of merit can be understood as the area under the Reflectance vs. wavelength curve for each of the structures under study.

The simulation set up that has been introduced in this section is used to obtain the results presented in Chapters 3 and 4 of this thesis. In the following sections, the plane-wave source and boundary conditions are discussed; starting the discussion with the plane-wave source.

2.3.7 AM 1.5 reference solar spectrum and plane-wave source

As explained in Section 2.3.6, in this work the plane-wave source is used since the incident sunlight on the Earth can be approximated as a plane-wave. The AM 1.5 replicates the solar spectrum and is commonly used by other members of the solar cell community. If in every modelling study about solar cells there is a different solar spectrum, it will be difficult to make any comparison between solar cell performances. However, the solar irradiation is different depending on the geographical location. Even at the very same location, the irradiation changes throughout the day and throughout the year (i.e. sunny morning in the summer vs. cloudy afternoon in winter, etc.).

In the majority of the solar cell reports the performance is shown with respect to the AM 1.5 (air mass 1.5) reference solar spectrum [23, 24]. It is accepted by the American Society for Testing and Materials [24] and it can be seen in Fig. 2.17.

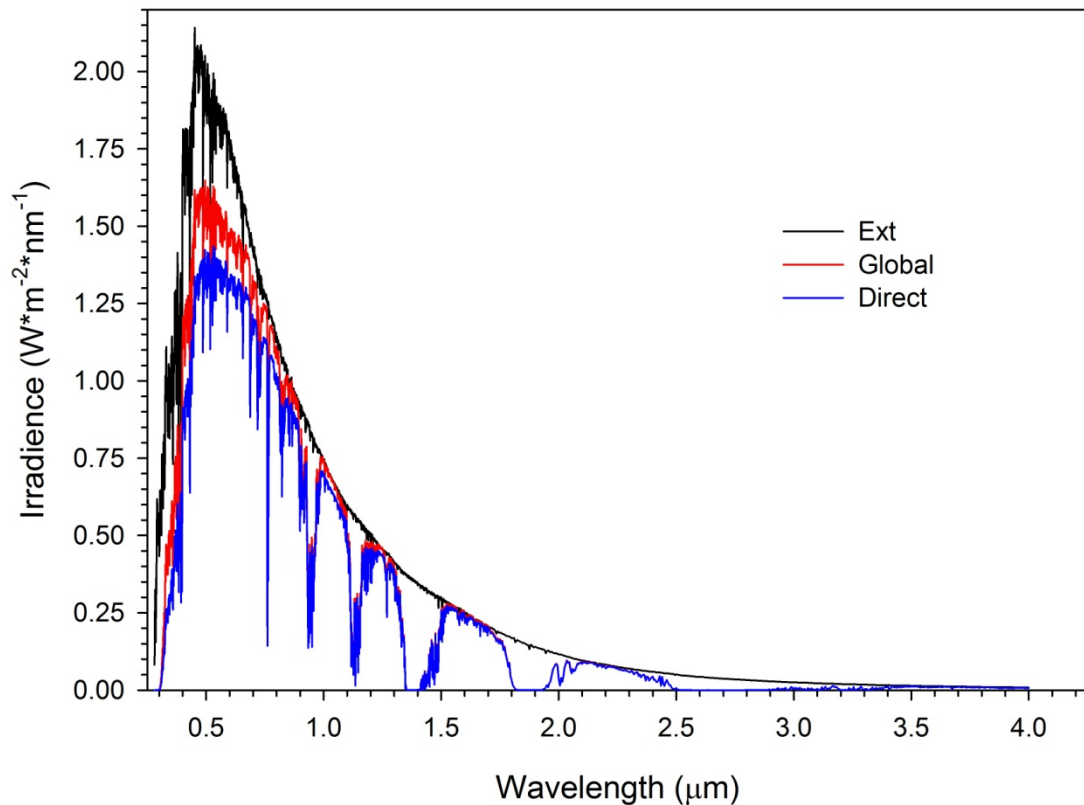


Fig. 2.17. AM 1.5 reference solar spectrum [25].

The AM 1.5 solar spectrum has three set of irradiance values which depend on how the atmosphere interacts with sunlight: Extraterrestrial (Ext), Global and Direct [23]. The atmosphere in the case of the extraterrestrial has no impact on irradiance [23]. This is the reference spectrum for outer space applications and it is commonly known as AM 0. In the case of Global, the atmosphere has an impact on the irradiance [23]. This is the reference spectrum for terrestrial applications. In the case of Direct, the irradiance again is impacted by the atmosphere but the difference in the values arises due to an aperture angle of 5.8° (i.e. acceptance angle of incidence of sunlight on the solar cell from the normal) [23]. Furthermore, in this case the sunlight is considered to be orthogonally incident on the cell [23]. This is ideal for simulating concentrated

solar cells with sun tracking mechanisms since this type of solar cell always has the sunlight incident perpendicular to it [23].

In this work the Global AM 1.5 spectrum has been used as it is the most popular source for terrestrial solar cells and is included in Lumerical FDTD solutions at the set up of the plane wave source. The wavelength range of the source needs to be set between 0.28 to 1.2 μm . Then, the power spectrum of the resulting plane wave is equivalent to the normalized envelope of the Global AM 1.5 solar spectrum. In the following section boundary conditions are discussed.

2.3.8 Boundary conditions

Computational methods require the simulation domain under study to be truncated. Otherwise, the area under study would have to be infinite, requiring an infinite computational memory. The truncation of the mesh can be achieved by including in the simulation domain an artificial boundary to impose a limit to the computational domain. However, the truncation of the domain may disturb the simulation results. The electromagnetic waves reaching the boundaries would reflect and hence contaminate the solutions. To avoid this effect, the nodes at the finite boundary are required to have a modified version of the governing equation than the rest of the mesh. The modified governing equation follows the imposed boundary condition [5].

There is a wide variety of conditions that can be imposed on the simulation boundaries [5, 14, 26]. The most basic boundary condition is the Dirichlet boundary condition (free surface boundary condition). When applying this condition at the boundary the solution of the field is imposed to be zero on the end nodes of the simulation domain [27]. Another basic boundary condition is the Neumann boundary condition (rigid boundary condition). When applying this condition at the boundary a constant value is imposed on the first derivative of the solution on the end nodes of the simulations [27]. The idea is to impose the value on the end node of the simulation to be the same as the first inner node of the simulation window [27]. As a result the flux through that boundary is defined. Dirichlet and Neumann boundary conditions lead to non zero reflection from the boundaries.

There are many applications where this is inappropriate. As a consequence other boundary conditions have to be used in conjunction with Dirichlet or Neumann boundary conditions. In this conjunction, the Dirichlet or the Neumann boundary conditions are placed as the outer boundary of the simulation window. Then, the other boundary conditions would be included between the Dirichlet or Neumann boundary condition and the remainder of the simulation window.

The other boundary conditions can be divided into three cases (A, B and C) depending on the interaction with the waves. In case A, all incident electromagnetic waves reaching the boundaries are reflected from the boundaries [5]. In this scenario a Perfectly Electric Conductor (PEC) is required. In case B, the periodicity of the structure is implemented via a Periodic Boundary Condition (PBC) [25]. In case C, all incident electromagnetic waves reaching the boundaries are absorbed by an absorbing layer (i.e. Absorbing Boundary Condition (ABC) or Perfectly Matched Layer (PML)) [5, 28]. In following sections these boundary conditions are discussed. The discussion starts with PEC boundary conditions.

2.3.8.1 Perfect Electric Conductor (PEC) and Perfect Magnetic Conductor (PMC)

A Perfect Electric Conductor (PEC) boundary condition has the property of reflecting all waves incident on it. This property can be found in nature on metallic surfaces. Therefore, PEC can be considered as placing a metallic plate at the edges of the simulation domain [5]. The incident E field on the boundary is divided into two components: one is tangential to the surface and the other is normal to the surface ($\mathbf{E} = \mathbf{E}_T + \mathbf{E}_N$) [5].

- The tangential E field on the boundary is set equal to zero ($\mathbf{E}_T = 0$)
- The reflected E field intensity is set equal to the normal incident component [5].

In a perfect conductor, the infinite conductivity leads to zero tangential E field. The infinite conductivity in a perfect conductor leads to zero resistance causing

electrons and holes to attract each other. Therefore, any E field tangential to the boundary will automatically generate an E field tangential to the boundary on the opposite direction to cancel it out [5]. As a result, the continuity of the electric field across the boundary is ensured which means [29]:

$$\mathbf{n} \times \mathbf{E} = 0 \quad (2.31)$$

The Perfect Magnetic Conductor (PMC) also reflects every wave incident on it. The PMC boundary condition is defined as follows [30]:

$$\mathbf{n} \times \mathbf{H} = 0 \quad (2.32)$$

However, unlike PEC, there is no material in nature with properties similar to PMC. The tangential magnetic field on the boundary is equal to zero. Additionally, the reflected field intensity is equal to the normal incident component.

Moreover, both PEC and PMC are conventionally used to take advantage of the symmetries of the structures under study. It is possible to simulate only a portion of the structure by applying PEC and/or PMC boundary conditions to ensure continuity of the field components at the boundaries. This would enable using a finer mesh in this smaller portion for better accuracy [31]. For explanatory purposes, an example of how the symmetry can be used in the case of a micro pillar is presented in Fig. 2.18.

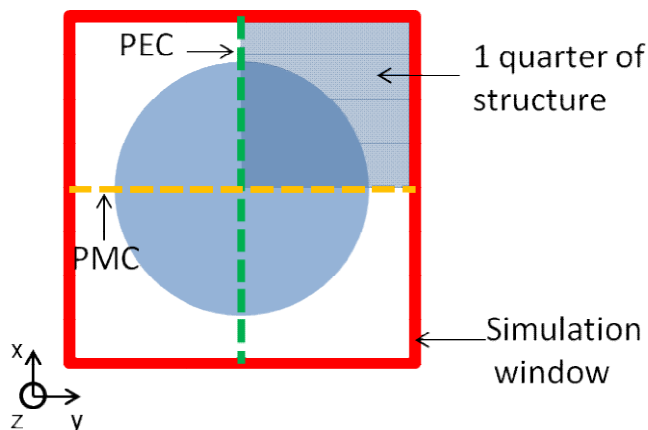


Fig. 2.18. Schematic using symmetry to replicate a micro pillar from 1 quarter of the structure.

Figure 2.18 shows a top view of a single micro pillar which is illustrated as the circle in blue. The red square represents the boundaries of the simulation window. The area shaded dark purple inside the simulation window represents a quarter of the simulation window. The objective of using symmetry on the boundaries is to replicate a full structure from only a part of it [5]. In this case, by simulating only the first quadrant presented in Fig. 2.18 it is possible to obtain the results as if the entire structure is simulated. This scenario is possible only in the case of using PEC and PMC boundary conditions appropriately. In order to do this, the PEC boundary condition is placed in the centre of the simulation window along the x axis. Then, the PMC boundary condition is placed in the centre of the simulation window along the y axis.

In some cases where the structure shows a periodicity, there is an alternative to reduce the memory requirements. In these cases, it is possible to simulate a structure and by applying Periodic Boundary Conditions (PBC) to obtain the results for an infinite structure. In the following section PBC is introduced.

2.3.8.2 Periodic Boundary Conditions (PBC)

Periodic Boundary Conditions (PBC) can be used when the structure under study has a refractive index that changes in a periodic manner in one or more coordinates. Figure 2.19 illustrates with an example a periodic structure where PBC can be applied.

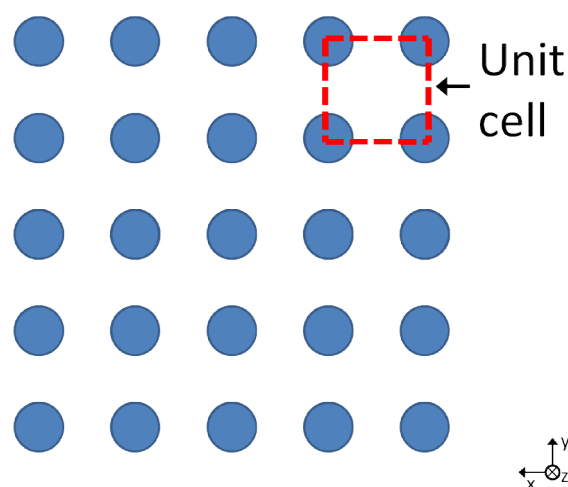


Fig 2.19. Schematic showing the unit cell of a periodic structure.

In this specific case, the periodicity of the structures enables running a simulation for only the unit cell. Then, the solution of the unit cell is replicated in the coordinates determined by the user (i.e. in x and y directions) [1, 26]. Hence, it is possible to run simulations for a single period (i.e. unit cell) rather than for the full structure. When PBC is imposed, the simulation window is truncated and therefore the memory requirement is reduced [5]. Figure 2.20 illustrates, using a diagram, how the mapping takes place when PBC is set on the x-y plane.

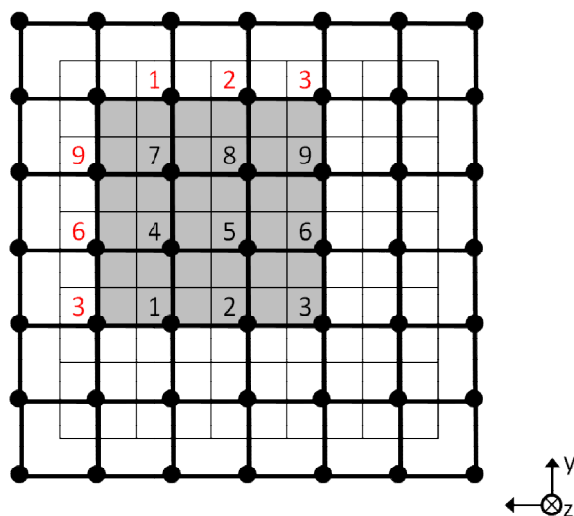


Fig. 2.20. Illustration of the mapping of PBC in x-y plane.

In Fig. 2.20 the black dots represent the FDTD nodes in the mesh on the x-y plane. The unit cell of a simulation with PBC corresponds to the part of a structure (i.e. solar cell) to be replicated on the x-y plane. The unit cell can be identified in Fig. 2.20 as the shaded area with the numbers coloured in black (1-9). Whereas the numbers coloured in red represent the cells that are mapped due to the PBC. For example, the nodes 1, 2 and 3 from the unit cell (i.e. coloured in black) are mapped (i.e. coloured in red) to the cells above nodes 7, 8 and 9. It is important to highlight that the value of the fields corresponding to the mapped nodes remains the same. However, the phase of the fields in these nodes may vary in accordance with the location. The value of the phase can be either $e^{-j\psi_y}$ or $e^{-j\psi_x}$. The generalized governing equation in the case of PBC is as follows [32]:

$$\vec{E}(\vec{r} + \vec{t}_{pqr}) = \vec{E}(\vec{r}) \cdot e^{j\vec{\beta} \cdot \vec{t}_{pqr}} \quad (2.33)$$

where the terms $\vec{E}(\vec{r} + \vec{t}_{pqr})$, $\vec{E}(\vec{r})$ and $e^{j\vec{\beta} \cdot \vec{t}_{pqr}}$ stand for the value of the E field at the node at the new location, the value of the field at the node at the unit cell and the change in phase. In the following section, the Absorbing Boundary Condition (ABC) is discussed.

2.3.8.3 Absorbing Boundary Condition (ABC)

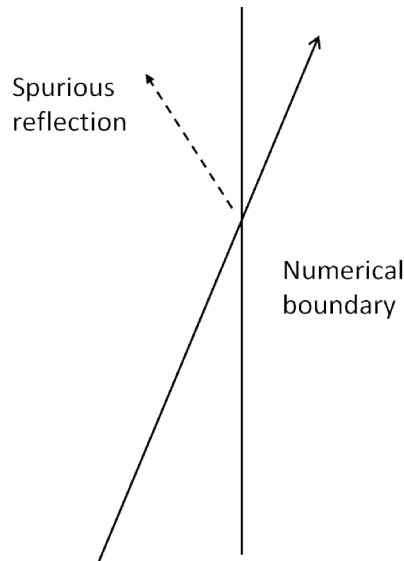


Fig. 2.21. Spurious reflection from the truncated boundary.

As discussed at the beginning of Section 2.3.8, the truncation of the simulation domain leads to unwanted spurious reflection from the domain boundaries [1]. Figure 2.21 illustrates the reflection of an incident electromagnetic wave when it reaches the truncated boundary. The results obtained from such a simulation can be contaminated. To avoid this scenario a boundary condition with the capacity of eliminating these reflections is required [5]. Over recent decades various analytical boundary conditions have been presented [5]. These are known as ABC. Some of the most relevant ABC proposed by researches in the field are: Bayliss-Turkel radiation operators [5, 25], Mur Finite-Difference Scheme [5, 25], Higdon radiation operators [5, 25] and the PML approach [5, 25].

2.3.8.3.1 Perfectly Matched Layer (PML)

Nowadays in computational modelling, the PML is considered as the state of the art to truncate the FDTD simulation domain [1, 5, 25, 28]. Since then it has been used in many different applications in a variety of disciplines [33]. Additionally, it has been adapted to a variety of simulation methods [31]. The most interesting feature of the PML is the zero reflection for all incident angles and all wavelengths [25, 34, 35]. The idea proposed by Bérenger was to split the fields into the sum of two parts (e.g. $E_z = E_{zx} + E_{zy}$) [5]. One field component is normal and the other is tangential to the boundary. The field component which is normal to the propagation direction is absorbed. On the contrary, the tangential component is not absorbed. This idea is possible by including an artificial anisotropic material capable of eliminating reflections [5, 34, 35]. To achieve this, the material must have the appropriate phase velocity and conductivity [5]. This phenomenon is achieved by matching the impedance of the artificial anisotropic material (i.e. PML layer) with that of the non-PML layer.

The list of conditions required to achieve the perfect matching between the PML and the non-PML materials are as follows [26]:

$$\varepsilon_2 = \varepsilon_1 \quad (2.34)$$

$$\mu_2 = \mu_1 \quad (2.35)$$

$$\sigma_y = \sigma_{my} = 0 \quad (2.36)$$

$$\frac{\sigma_x}{\varepsilon_2} = \frac{\sigma_{mx}}{\mu_2} \quad (2.37)$$

where ε_1 , ε_2 , μ_1 , μ_2 , σ_y , σ_{my} , σ_x and σ_{mx} are dielectric constants, permeability and conductivity of medium 1 and medium 2 respectively [26].

When these conditions are satisfied, the propagation inside the PML material is dependent on the phase of the waves and is governed as follows [26]:

$$e^{-jS_x\beta_{1x}x - j\beta_{1y}y} = \exp\left(-j\left(1 + \frac{\sigma}{j\omega\varepsilon_1}\right)\beta_{1x}x - j\beta_{1y}y\right) \quad (2.38)$$

$$e^{-jS_x\beta_{1x}x-j\beta_{1y}y} = \exp\left(-\frac{\beta_{1x}\sigma}{\omega\varepsilon_1}x\right)e^{-j\beta_{1x}x-j\beta_{1y}y} \quad (2.39)$$

where $S_x = 1 + \sigma_x/j\omega\varepsilon_2$, $\beta_{1x} = (\omega^2\mu_1\varepsilon_1 - \beta_{1y}^2)^{1/2}$ and $\beta_{1y} = \sqrt{S_y S_{my}}\beta_{2y}$ (achieving phase matching condition between PML and non PML).

From Eq. (2.39) it can be seen how the field decays exponentially inside the PML. It is important to note the effect that the term S_x has on the absorption. It determines the slope of the exponential curve describing the absorption inside the PML [26]. With the exponential curve becoming steeper, the wave gets more strongly absorbed as it penetrates further in the PML. Figure 2.22 illustrates the effect of the PML on an incident wave.

When the wave reaches point A, the PML artificially splits the incident wave into two components: one normal and the other parallel to the interface [26]. Each of the two components experiences the effect of different conductivity, leading to a difference in the absorption between the two components. The wave normal to the interface gets partially absorbed by the PML. Then, as it penetrates further in the PML the same process repeats [26]. As a result, the wave is absorbed continuously inside the thickness of the PML [26]. This fact shows the importance of the convergence test presented in Section 2.3.6.4. The wave parallel to the interface does not get absorbed by the PML until it reaches point B on the side boundary of the PML [33]. Then, this wave is reflected back at the boundary of the PML.

The corner PML works similarly to the PML with the difference being the absorbing direction. In the case of the corner PML both components of the waves (i.e. normal and tangential) are absorbed. The corner PML is capable of absorbing waves travelling in both directions.

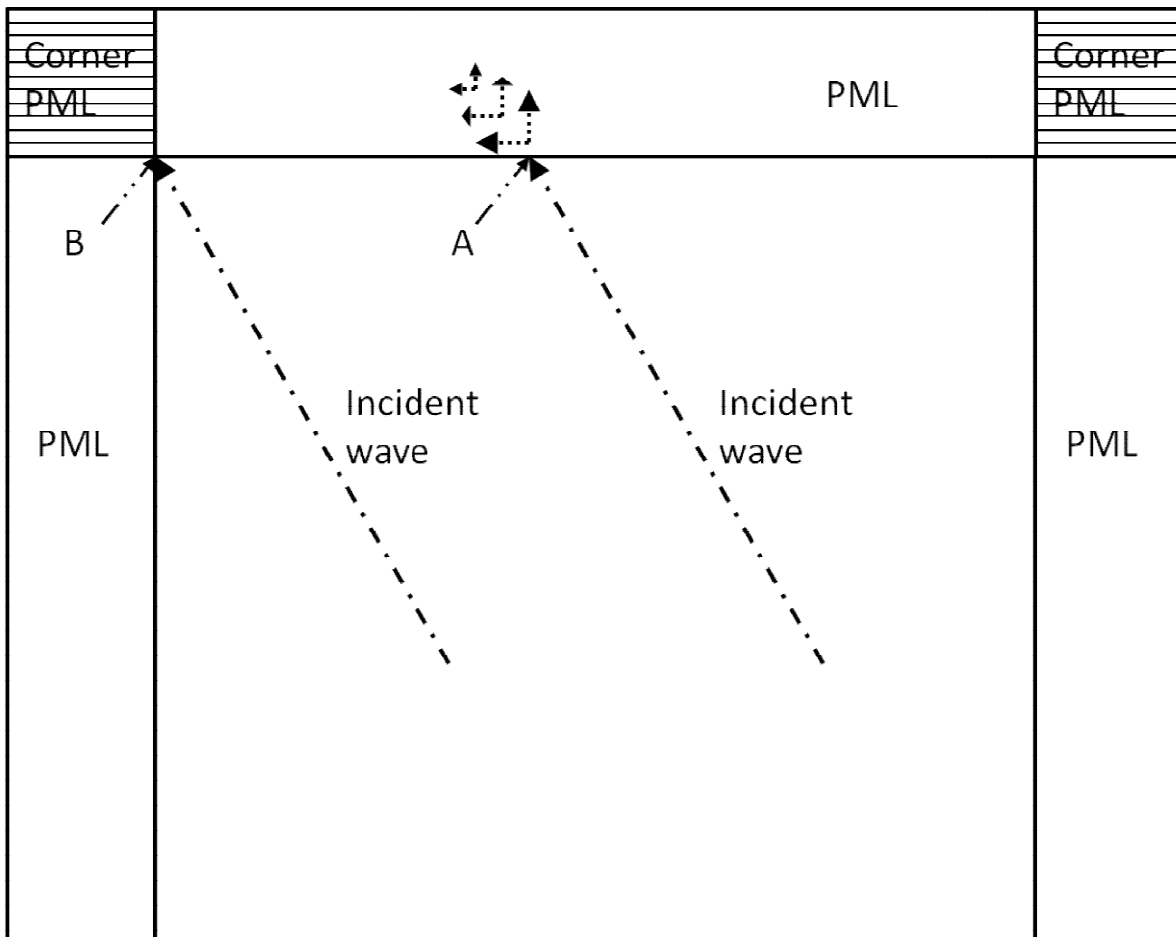


Fig. 2.22. Schematic showing the effect of PML on an incident wave.

The inclusion of the PML has a large impact in the simulation since it eliminates the spurious reflections. However, the thickness of the PML layer has to be selected carefully due to the high memory requirements [33]. Furthermore, the step size for the simulation may influence the PML thickness. For example, the PML thickness required for step size of $\Delta_x = 0.1 \mu\text{m}$ is not the same as in the case of $\Delta_x = 0.01 \mu\text{m}$. Therefore the approach to choose the correct PML thickness should always consider the step size of each simulation. In this work, the appropriate PML layer thickness (i.e. 40) is selected through a convergence test as discussed in Section 2.3.6.4.

2.4 Summary

There are different approaches to analyse a structure. One of the possibilities is to analyse the structure experimentally in a laboratory. The other possibility is to study the structure based on simulations. There is a wide range of simulation

tools available with advantages and disadvantages on the study of solar cells. In this work, the FDTD method is used as a tool to analyse and optimize the performance of two structures. It is second order accurate due to the central finite difference approximation and it can launch broadband pulses into the simulation domain in a single simulation run (required for solar cell simulations).

The mesh parameters used for this work ensure the accuracy of the simulation results presented. In order to achieve this there are some considerations such as: location of the source and the reflection monitor, the number of PML layers and the appropriate size of the simulation window. The appropriate number of PML layers is selected based on a convergence test to ensure absorption of any light incident on it. Additionally, the relation between window height and simulated time is considered to ensure that the field decays and that there is no corruption of the results.

A wide range of parameter values are considered to obtain the best optimization for the structures under study: micro pillar array and hut-like micro pillar array texturing patterns. The analysis focuses on those parameters that show more impact on the performance of the two arrays under study, such as: H, D, distance in between pillars, SC, ϑ and Cap.

To identify the effect of these parameters many simulations have to be run. Many of these simulations take more than 15 hours to complete. This adds complexity to the study since the simulations to be run have to be optimized according to the parameter findings. To identify those parameter findings, the results are analysed in different formats to provide as much information as possible. To achieve this, RInt is a very useful tool to ensure both easy and effective performance comparison. In the case of finding the optimum value of a parameter, especially ϑ , the difference in the R vs. wavelength curve is very small. However, when comparing the RInt values of the corresponding simulations, the best performance can be easily identified.

The methodology and simulation set up introduced in this chapter is used to obtain the results presented in Chapter 3 (micro pillar array) and Chapter 4 (hut-like micro pillar array).

2.5 References

1. Rahman, B. M. A., and Agrawal, A., (2013), "*Finite element modeling methods for photonics*", Artech House, Boston.
2. Griffiths, D. V., and Smith, I. M., (2006), "*Numerical methods for engineers*", 2nd Ed., Chapman and Hall/CRC Press, Boca Raton, London.
3. Li, J., and Huang, Y., (2013), "*Time-Domain Finite Element Methods for Maxwell's Equations in Metamaterials*", Springer Berlin Heidelberg, Berlin.
4. Xuan, L., Jin, G., Gong, J., Zhang, W., and Ming, P., (2014), "*Time domain finite volume method for three-dimensional structural–acoustic coupling analysis*", Applied Acoustics, Vol. 76, pp. 138-149.
5. Taflove, A., (2013), "*Advances in FDTD computational electrodynamics: photonics and nanotechnology*", Artech House, London.
6. Chen, W-K., (2005), "*Electrical engineering handbook*", Elsevier Academic Press, Amsterdam.
7. Yu, W., and R. Mittra, (2000), "*A conformal FDTD software package modeling antennas and microstrip circuit components*", IEEE Antennas Propagation Magazine, Vol. 42, No., 5, pp. 28-39.
8. Josefsson, L., and Persson, P., (2006), "*Conformal array antenna theory and design*", John Wiley and sons Inc., Hoboken, N.J.
9. Yee, K. S., (1966), "*Numerical solution of initial boundary value problems involving Maxwells equations in isotropic media*", IEEE Transactions on Antennas and Propagation, Vol. 14, No. 3, pp. 302-307.
10. Taflove, A., (1980), "*Application of the Finite-Difference Time-Domain Method to Sinusoidal Steady-State Electromagnetic-Penetration Problems*", IEEE Transactions on Electromagnetic Compatibility, Vol. EMC-22, No. 3, pp. 191-202.
11. Chu, S. T., and Chaudhuri, S. K., (1995), "*Finite-difference time-domain method for optical waveguide analysis*", Progress In Electromagnetics Research, Vol. 11, pp. 255-300.
12. Van Renterghem, T., and Botteldooren, D., (2007), "*Prediction-step staggered-in-time FDTD: An efficient numerical scheme to solve the*

- linearised equations of fluid dynamics in outdoor sound propagation*”, Applied Acoustics, Vol. 68, No. 2, pp. 201-216.
13. Van Renterghem, T., (2014), “*Efficient Outdoor Sound Propagation Modeling with the Finite-Difference Time-Domain (FDTD) Method: A Review*”, International journal of Aeroacoustics, Vol. 13, No. 5-6, pp. 385-404.
 14. Sullivan, D. M., (2013), “*Electromagnetic simulation using the FDTD method*”, 2nd edn, Wiley, Hoboken.
 15. Hanson, G. W., and Yakovlev, A. B., (2002), “*Operator Theory for Electromagnetics: An Introduction*”, 1st Ed., Springer, New York.
 16. Gustafsson, B., (2008), “*High Order Difference Methods for Time Dependent PDE*”, Springer, Berlin.
 17. Inan, U. S., and Marshall, R. A., (2011), “*Numerical Electromagnetics: The FDTD Method*”, Cambridge University Press, Cambridge.
 18. Oskooi, A. F., Roundy, D., Ibanescu, M., Bermel, P., Joannopoulos, J. D., and Johnson, S. G., (2010), “*Meep: A flexible free-software package for electromagnetic simulations by the FDTD method*”, Computer Physics Communications, Vol. 181, No. 3, pp. 687-702.
 19. Khan, I. R., and Ohba, R., (2003), “*Taylor series based finite difference approximations of higher-degree derivatives*”, Journal of Computational and Applied Mathematics, Vol. 154, No. 1, pp. 115-124.
 20. Lumerical Solutions, Inc., (2007) Available at: <http://www.lumerical.com>.
 21. Cabrera-España, F. J., and Agrawal, A., (2016), “*Hut-like pillar array Si solar cells*”, Solar Energy, Vol. 132, pp. 357-362.
 22. Zhang, Y., Ouyang, Z., Stokes, N., Jia, B., Shi, Z., and Gu, M., (2012), “*Low cost and high performance Al nanoparticles for broadband light trapping in Si wafers solar cells*”, Applied Physics Letters, Vol. 100, No. 5, 151101-151104.
 23. Riordan, C., and Hulstron, R., (1990), “*What is an air mass 1.5 spectrum? (solar cell performance calculations)*”, In Proceedings of the 21st IEEE Photovoltaic Specialists Conference, Vol. 2, pp.1085-1088.
 24. American Society for Testing and Materials (ASTM), (1987), “*Standard Tables for Terrestrial Direct Normal Solar Spectrum Irradiance for Air Mass 1.5*”, Standard No. E891-87, American Society for Testing and Materials, Philadelphia.

25. Salski, B., (2010), "*Application of semi-analytical algorithms in the finite-difference time-domain modeling of electromagnetic radiation and scattering problems*", PhD Thesis Warsaw University of Technology.
26. Schneider, J. B., (2010), "Understanding the Finite-Difference Time-Domain Method", Available at: www.eecs.wsu.edu/~schneidj/ufdtd.
27. Haeseler, S., Keller, M., Lenz, D., and Wojciechowski, R., (2011), "*Laplacians on infinite graphs: Dirichlet and Neumann boundary conditions*", Journal of Spectral theory, Vol. 2, No. 4, pp. 397-432.
28. Berenger, J., (1996), "*Three-Dimensional Perfectly Matched Layer for the Absorption of Electromagnetic Waves*", Journal of Computational Physics, Vol. 127, No. 2, pp. 363-379.
29. Hussain, A., Naqvi, Q. A., and Abbas, M., (2007), "*Fractional duality and perfect electromagnetic conductor*", Progress In Electromagnetics Research, Vol. 71, pp. 85–94.
30. Hehl, F. W., and Obukhov, Y. N., (2005), "*Linear media in classical electrodynamics and post constraint*," Physics Letters A, Vol. 334, pp. 249–259.
31. Oskooi, A. F., Roundy, D., Ibanescu, M., Bermel, P., Joannopoulos, J. D., and Johnson, S. G., (2010), "*Meep: A flexible free-software package for electromagnetic simulations by the FDTD method*," Computer Physics Communications, Vol. 181, No. 3, pp. 687-702.
32. Gerald, C. F., and Wheatley, P. O., (1989), "*Applied numerical analysis*", 4th Ed., Addison-Wesley Pub. Co, Reading.
33. Agrawal, A., and Sharma, A., (2004), "*Perfectly Matched Layer in Numerical Wave Propagation: Factors that Affect its Performance*", Applied Optics, Vol. 43, No. 21, pp. 4225-4231.
34. Vassallo, C., and Collino, F., (1996), "*Highly efficient absorbing boundary conditions for the beam propagation method*", Journal of Lightwave Technology, Vol. 14, No. 6, pp. 1570-1577.
35. Huang, W-P., Xu, C-L., Lui, W., and Yokoyama, K., (1996), "*The perfectly matched layer PML boundary condition for the beam propagation method*", IEEE Photonics Technology Letters, Vol. 8, No. 5, pp. 649–651.

Chapter 3: Silicon solar cell with micro pillar array texture

3.1 Introduction

This chapter presents an analysis on the effect that key structural parameters have on the performance of a micro pillar texturing pattern on the surface of the solar cell. The main target of the analysis presented in this work is the reduction of the reflection³ from the solar cell surface. Reducing the reflection is important to improve the conversion efficiency of solar cells while reducing fabrication costs [1]. In the last few decades efforts from the solar cell community have been focused on this reduction and remarkable results have been achieved [2]. However, there are still demands for further reduction of the reflection [1]. This work aims at helping designers in the search of new alternatives to reduce reflection.

There are various alternatives available to reduce the reflection, as discussed in Section 1.5.4., such as: i) using ARC layers, ii) using metallic particles to obtain advantage of the surface plasmon polaritons phenomenon using plasmonic solar cells or iii) texturing the solar cell surface. The latter is an alternative with an impact on a wide wavelength range which is a very important factor in solar cell applications (due to the large wavelength range of the solar spectrum). This is the reason why this work focuses on analysing the texturing of the solar cell surface. Nevertheless, there are various types of patterns to texture the solar cell surface such as pyramids, nanowires or micro pillar arrays. The texturing of any of these types helps in reducing the reflection from the solar cell. Micro pillar arrays provide better electrical performance than other patterns, such as nanowires [3]. Additionally, the size of micro pillars in an array is larger than the size of the nanowires. The difference in size leads to an easier fabrication process in the case of micro pillar arrays.

The discussion presented in this chapter introduces an analysis on the performance of the solar cell with different array configuration. This study continues with an examination on the effect that structural parameters have on the performance of textured solar cells. Additionally, the behaviour of the solar

³ The term “reflection” represents the physical phenomenon of an electromagnetic wave being reflected at the solar cell.

cell performance when the Height/Diameter (H/D) ratio varies is discussed to help identify the optimum performance.

The values of the mesh parameters used in the simulations presented in this chapter are $\Delta_x = 0.01 \mu\text{m}$, $\Delta_y = 0.01 \mu\text{m}$, $\Delta_z = 0.007 \mu\text{m}$ and $\Delta_t = 0.0163712 \text{ fs}$. The value of these parameters is obtained through the convergence test presented in Section 2.3.6.3. Therefore, these values ensure both accurate results and acceptable memory requirements. Additionally, it is important to mention that the location of the simulation elements (e.g. source or monitors) is discussed in Section 2.3.6.3.

The chapter is divided into the following sections: the analysis of the results starts with the effect of different array configurations on the reflection in Section 3.2. This is followed by the effect of varying the Height (H) of the micro pillars in Section 3.3. Then, the effect of the Diameter (D) on the reflection is presented in Section 3.4. The discussion continues with the analysis on the behaviour of the reflection while varying Surface Coverage (SC) in Section 3.5. The last part of the discussion is about the evolution of the Reflectance integrated overall wavelengths (RInt)⁴ as the H/D ratio of the micro pillar array is increased in Section 3.6. The discussion starts with the effect of different array configuration on the reflection.

3.2 Effect of different array distribution on the reflection from the solar cell

The pillar distribution inside an array affects the optical performance of a textured solar cell. There is a wide range of possibilities on how to distribute the pillars inside the array. One of these options is to place the pillars randomly inside the array but there is some controversy about how effective non ordered arrays are [4, 5]. An alternative is to place the pillars inside periodic arrays such as square or hexagonal configurations. These distributions are discussed in Section 2.3.6.5 where the key parameters of each of them are presented in a diagram. Additionally, the expressions that define the square and hexagonal configurations are introduced.

⁴ The term "RInt" refers to the Reflectance integrated overall wavelengths introduced in Eq. (2.30). The term RInt will be used to compare solar cell performances in the entire wavelength spectrum.

In the literature a clear comparison between these two configurations (i.e. square and hexagonal) has not been made yet. This work includes a comparison of the performance of a micro pillar array using square and hexagonal configurations. The key structural parameters (Height (H), Diameter (D) and Surface Coverage (SC)) have to be set to the same value in both cases. The first set of results comparing the two configurations are presented in Fig. 3.1. The results correspond to the values of H, D and SC set to $1\mu\text{m}$, $1\mu\text{m}$ and 60% respectively. The value of SC=60% gives the best performance in both array configurations. This is the reason why this value has been selected for comparison. For reference the performance of a planar Si solar cell is also presented.

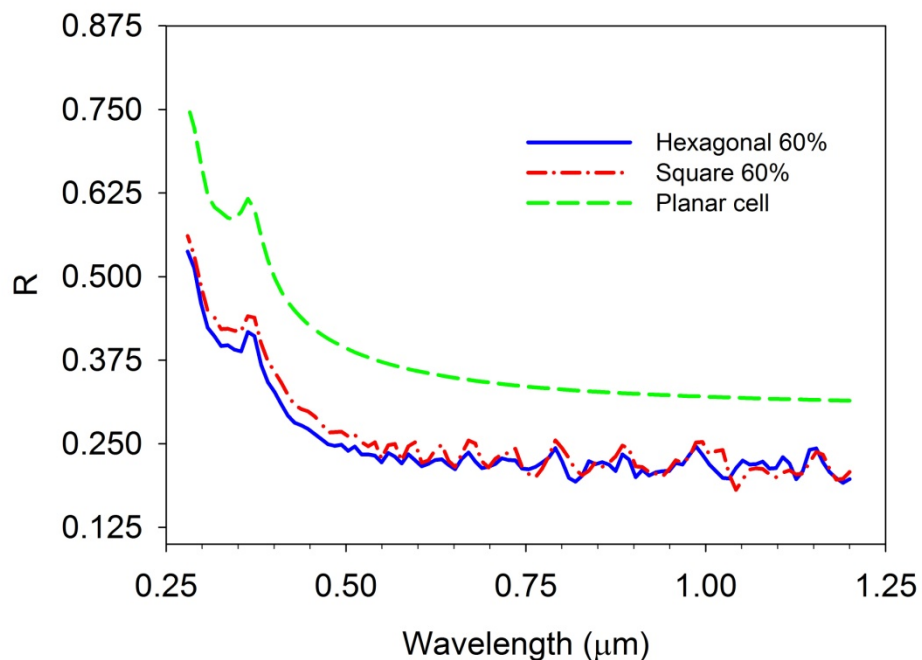


Fig. 3.1. R vs. wavelength for hexagonal and square configurations when $H=1\mu\text{m}$, $D=1\mu\text{m}$ and $SC=60\%$.

From Fig. 3.1, it can be observed that there is a difference in the R performance of the three curves⁵. First of all, there is a clear reduction in R between the planar cell and the textured cells. This finding supports the idea of the benefits of texturing the surface of the solar cell in terms of lowering R. Additionally, it may also be seen that there is a significant difference in the performance of the

⁵ The term "R" refers to the Reflectance which was introduced in Eq. (2.29). The term R will be used to compare solar cell performances in a specific wavelength range.

two array configurations. The array of pillars in the hexagonal configuration gives better performance (i.e. lower R) than the square configuration. This is valid in the case of SC = 60%. To determine whether this trend is applicable to other SC values, the comparison study is extended for a wider range of SC percentages. This is achieved by running simulations for both array configurations where H and D are kept constant at $1\mu\text{m}$ and SC is the only parameter that is varied. The results are presented in Fig. 3.2. To facilitate an easier performance comparison between the performances at a range of SC values, the RInt vs. SC curve (see Chapter 2) for each simulation is shown in Fig. 3.2.

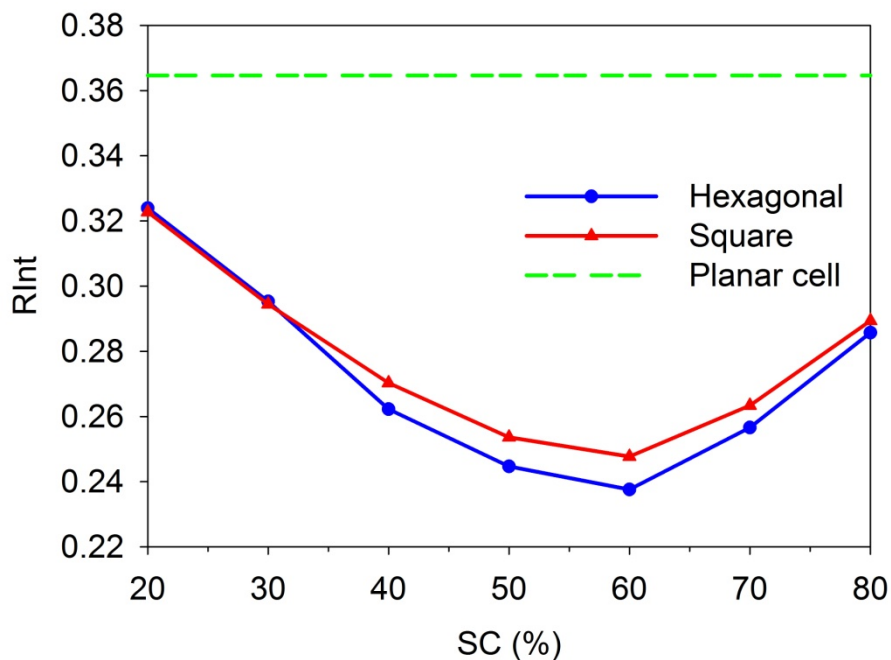


Fig. 3.2. RInt vs. SC for hexagonal and square configurations.

Figure 3.2 shows that the same trend observed in the Fig. 3.1 is repeated in Fig. 3.2 for all the SC values. The hexagonal configuration provides lower RInt than the square configuration. Another important factor to highlight is the impact of SC on the performance. Both configurations are affected similarly by SC. When the SC is low (i.e. SC=20%) the RInt is high, whereas when the value of SC increases, the value of RInt reduces. Then, after reaching a minimum value, the value of RInt starts to increase again for further increase in the value of SC. The effect of SC on the reflection from the surface of the solar cell will be discussed in more detail in Section 3.5.

The cause of the difference in the RInt curves of the two configurations is due to the variation in the surface area available in between pillars. The packing fraction or density in the hexagonal configuration is greater than in the square configuration. Hence, in the case of the same Diameter (D) and SC values, the usage of the hexagonal configuration results in a more compact inter-pillar spacing. This has a direct impact on the number of multiple reflections that was discussed in Section 1.5.4. The term “multiple reflections” refers to the bouncing of the electromagnetic waves inside the area in between the micro pillars. However, the term can be extended to other texturing patterns such as nanowires or pyramids. Hence, an increase in the number of multiple reflections leads to higher chances of photon absorption. In order to confirm the impact of the multiple reflections in the performance of the two configurations in Fig. 3.3 and Fig. 3.4 a field plot is presented for both cases (i.e. hexagonal and square configurations). This helps to compare how the waves interact with the two array distributions. To achieve a fair comparison, the parameters H, D and SC are fixed at $1\mu\text{m}$, $1\mu\text{m}$ and 60% respectively. Additionally, a 2D monitor in the x-y plane is placed at $0.2\mu\text{m}$ above the substrate of the solar cell, measuring the E field intensity at $\lambda = 0.363636\mu\text{m}$. The value of the wavelength is selected because the peak value of the solar spectrum that occurs at this wavelength. This fact makes the comparison between the field plots meaningful. The results are presented in Figs. 3.3 and 3.4 where the black lines represent the edges of the micro pillars⁶.

⁶ In the E field plots presented in the remainder of the Chapter, the black lines represent the edges of the micro pillars.

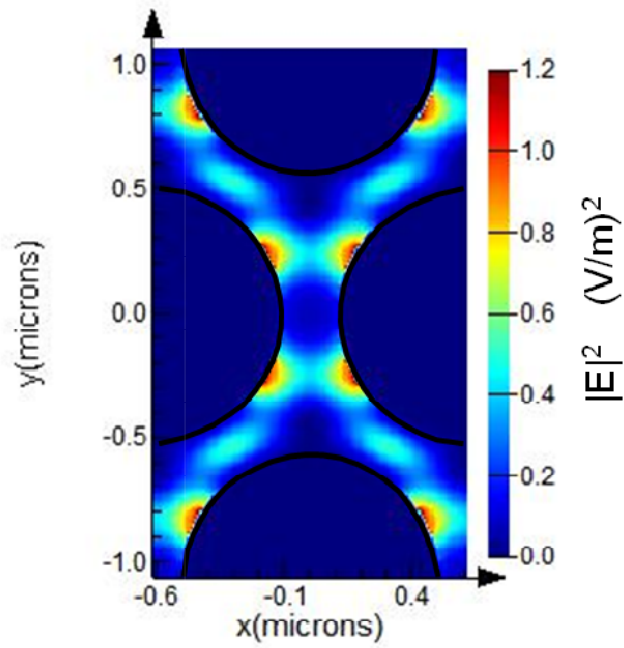


Fig. 3.3. E field intensity at a cross section for the case of hexagonal configuration.

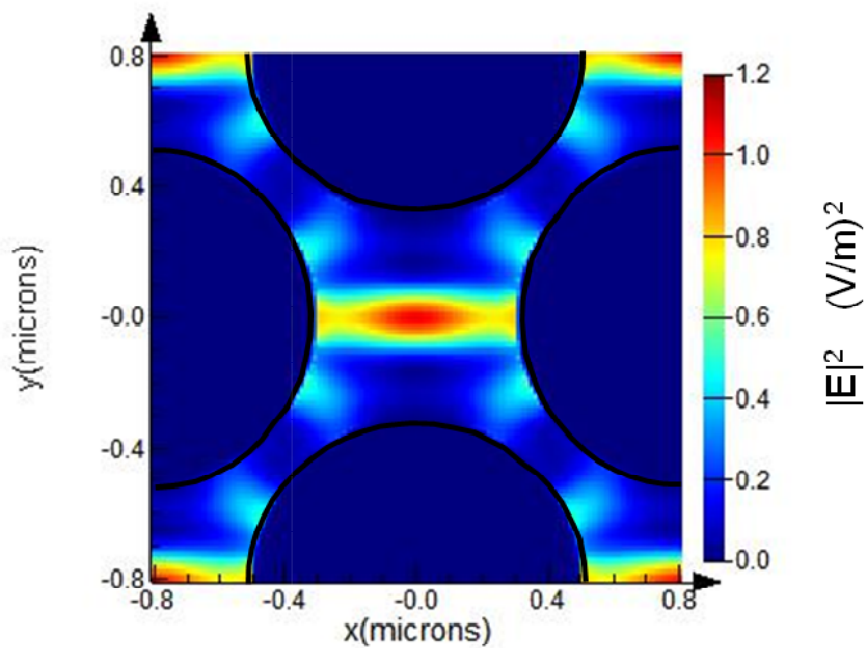


Fig. 3.4. E field intensity at a cross section for the case of square configuration.

By comparing Figs. 3.3 and 3.4, it may be observed that the E field is more compact in the case of the hexagonal configuration. This can be identified by a larger number of peaks in the E field intensity values in the case of hexagonal

configuration. Additionally, the E field intensity peaks in the hexagonal configuration have a higher value than in the square configuration. The large number of peaks and the high values of E field intensity peaks are indications of the strong presence of multiple reflections. As a consequence, the photon absorption in the case of hexagonal configuration is high which reduces the reflection. In order to examine whether or not this trend is applicable to other micro pillar dimensions, the RInt vs. SC curve for both configurations are shown for the case of $H=2\ \mu\text{m}$ and $D=1\ \mu\text{m}$ in Fig. 3.5.

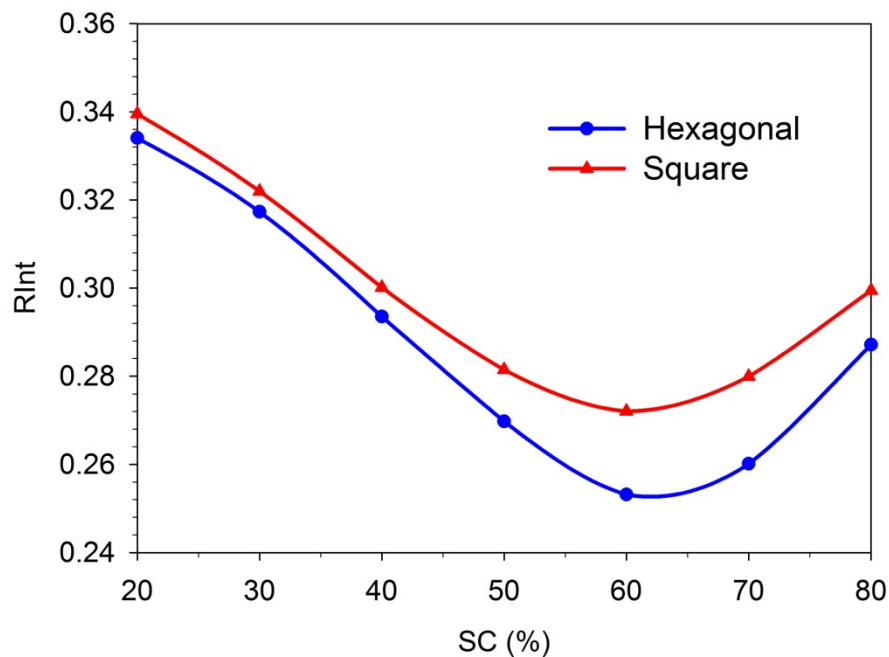


Fig. 3.5. RInt vs. SC for hexagonal and square configurations for the case of $H=1\ \mu\text{m}$ and $D=2\ \mu\text{m}$.

In Fig. 3.5 it can be observed that the hexagonal configuration provides lower RInt than the square configuration for the same SC value. This is the same trend as described in Fig. 3.2. The hexagonal configuration performs better than the square configuration due to the optimization of properties associated with micro pillar arrays as discussed above. Therefore, the hexagonal configuration of arrays is used in the remainder of this work unless specified otherwise. The following sections will focus on the effect of structural parameters on the performance of a micro pillar array solar cell. This discussion starts with a study on the effect of Height (H) on the reflection from the solar cell which is presented in the following section.

3.3 Effect of Height (H) on the reflection from the solar cell

The analysis on the effect of the H is carried out by increasing H while keeping D constant at $2\mu\text{m}$. There are few reports, with limited information, on the effect of H on the reflection from the solar cell. However, these reports do not cover the effect on the optical properties in depth. For example, Garnett *et al.* [6] discussed the effect that H has on short circuit current through experimental studies. In their study, it is found that as the value of H increases, the short circuit current increases [6]. Additionally, in their work Garnett *et al.* found out that the surface recombination increases as the value of H increases as well [6]. However, for the samples analysed ($H=2\mu\text{m}$ and $H=5\mu\text{m}$ are obtained using the Deep Reactive Ion Etching process (DRIE) [6, 7]) they found that the increase in the short circuit current is more dominant than the increase in the surface recombination [6]. In this work the focus is on how the reflection changes as the value of H increases. In order to do this, the R_{Int} vs. SC curves for H values ranging between $H=1\mu\text{m}$ and $H=7\mu\text{m}$ are shown. The R_{Int} value corresponding to the Si slab planar Si solar cell is plotted for reference.

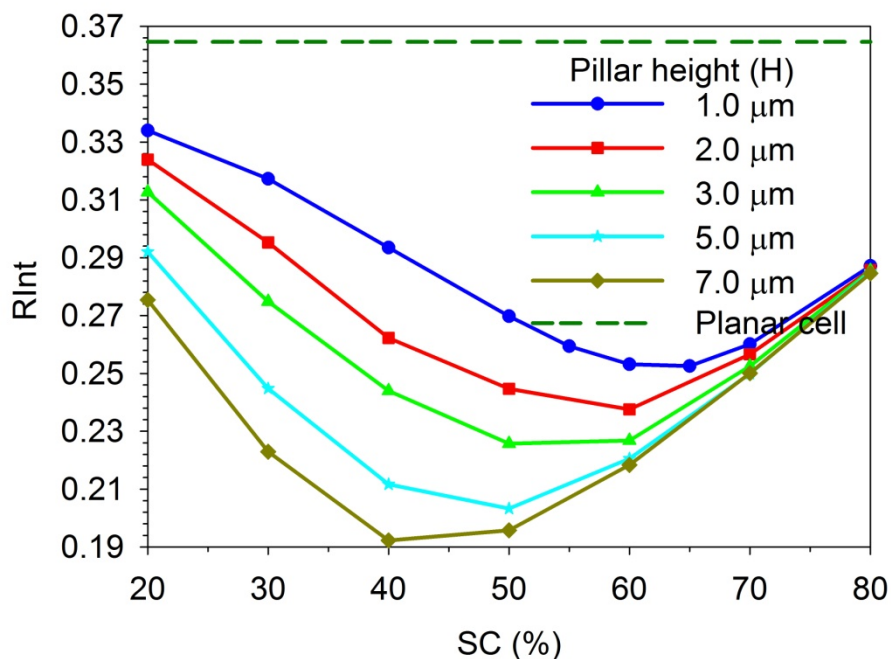


Fig. 3.6. Effect of varying H for fixed D ($=2\mu\text{m}$).

Figure 3.6 shows R_{Int} with respect to SC for the cases of $H=1\mu\text{m}$, $H=2\mu\text{m}$, $H=3.5\mu\text{m}$, $H=5\mu\text{m}$ and $H=7\mu\text{m}$. There is a clear trend. As the pillar height increases, R_{Int} decreases. This trend is valid for all the studied SC and it is due to the increase in area in between pillars. This increase leads to more multiple reflections which enhances the photon absorption (lower R_{Int}). Further to this, it may also be noticed that the optimum SC shifts towards lower SC values when H increases. For a short micro pillar and a value of SC lower than optimum, the area in between pillars is very large. Hence, some of the incident light escapes from the area in between pillars suffering few or no multiple reflections. However, by increasing H , even though D and SC are kept fixed, less incident light could escape with no contribution to multiple reflections. Hence, photon absorption for the higher pillars with the same SC value offers lower R_{Int} in the case of D fixed at $2\mu\text{m}$. In order to find out if this statement can be extended to other D values, additional simulations are run where H is increased while keeping D constant at $1\mu\text{m}$. The results of these simulations are presented in Fig. 3.7.

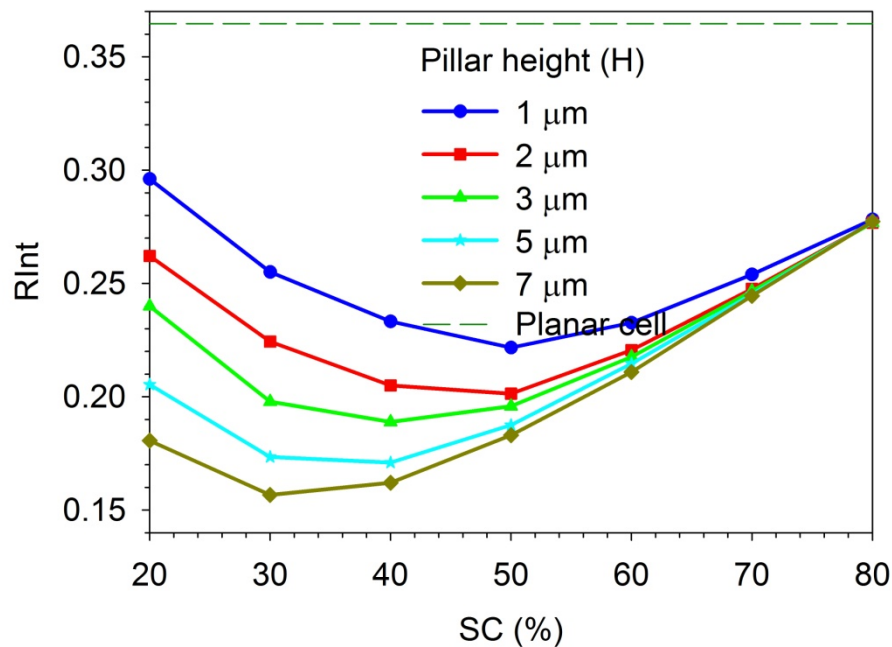


Fig. 3.7. Effect of varying H for fixed $D (=1\mu\text{m})$.

Figure 3.7 presents the R_{Int} vs. SC curve as H is varied for the cases of $H=1\mu\text{m}$, $2\mu\text{m}$ and $5\mu\text{m}$ while keeping D constant at $1\mu\text{m}$. This figure shows the

R_{int} decreasing as the value H increases for every SC value. For high values of SC there is a convergence due to the presence of a low number of multiple reflections. This point will be discussed further in Section 3.5. Then, as the value of SC decreases, there is a more clear difference in the R_{int} behaviour as H increases. Furthermore, it may be noticed how the optimum SC value shifts towards lower values as H increases. This is in line with the findings discussed in Fig. 3.6. Considering all the different factors that impact the performance, it is possible to conclude that the trend of lowering R_{int} as H increases is applicable to other values of D.

Nevertheless, when comparing Figs. 3.6 and 3.7 the shape of the R_{int} vs. SC curves, in the two graphs corresponding to the same H value, are not identical. In the case of Fig. 3.6, the optimum SC is in the higher range of values (specially at shorter pillars (i.e. $H=1\mu\text{m}$)). However, in the case of Fig. 3.7, the optimum SC shifts towards lower SC values. In other words, the performance behaviour changes as the H/D ratio varies due to more light being reflected from the top of the pillars as D increases. Therefore, the optimization of the multiple reflections of the incident light that penetrates in between pillars (i.e. not reflected from the top of the micro pillars) may be achieved by defining a shorter distance in between pillars (i.e. higher SC value) as D increases. More detailed discussion on the effect of D and the H/D ratio on the reflection is presented in Sections 3.4 and 3.6 respectively.

In order to understand how the wave interaction with the texturing pattern varies as H increases, a series of field plots are presented in Figs. 3.8 a, b and c - Fig.3.9 a, b and c. These figures show the E field intensity in a cross section of the pattern in the x-z plane for three values of H ($H=1\mu\text{m}$, $2\mu\text{m}$ and $5\mu\text{m}$) and two values of SC (SC = 40% and 50%) while keeping D constant at $1\mu\text{m}$ at $\lambda=0.363636\mu\text{m}$. These values are selected regarding the results presented in Fig. 3.7 to enable the best comparison. The SC values that provide the lowest R_{int} are: SC=50% for $H=1\mu\text{m}$ and $2\mu\text{m}$; SC=40% for $H=5\mu\text{m}$. The idea is to compare the two factors: i) how the reflection reduces as H increases from $H=1\mu\text{m}$ for two SC values, ii) how the value of H shifts the optimum value of SC.

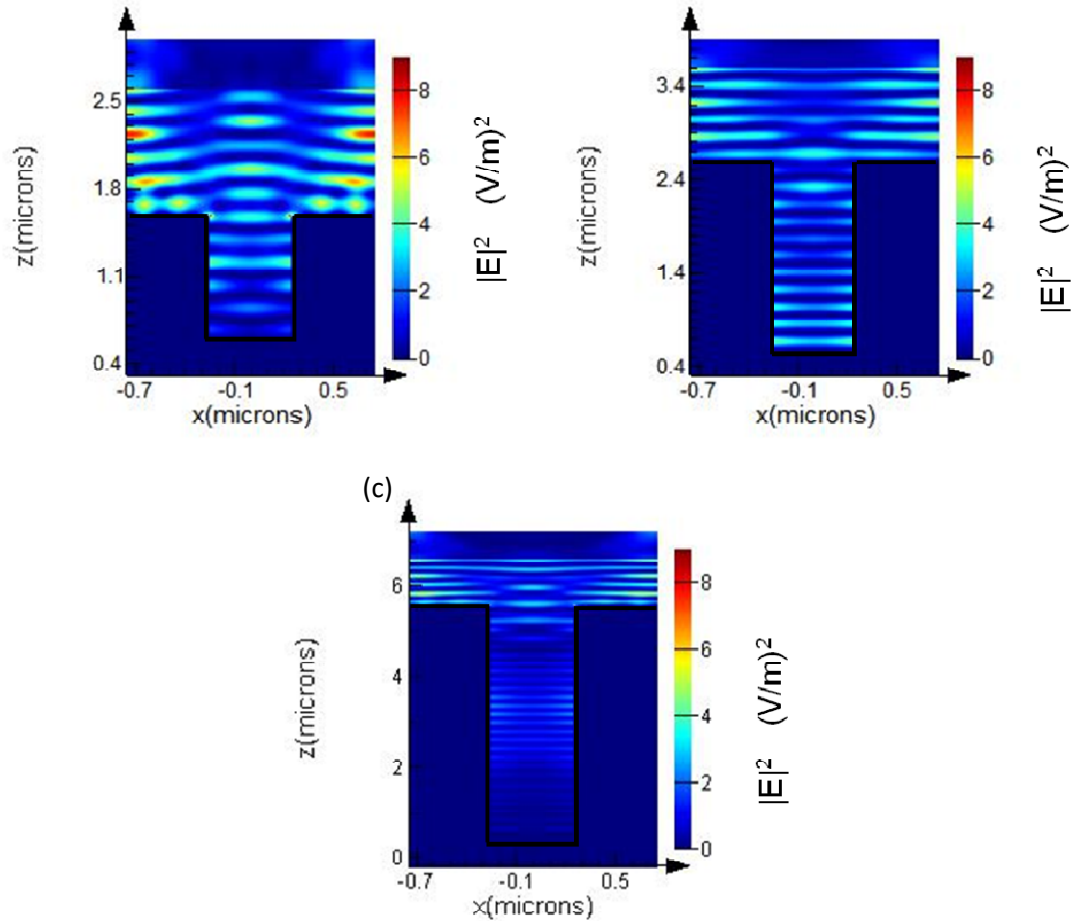


Fig. 3.8. E field intensity in a vertical cross section for the case of (a) $H=1\ \mu\text{m}$, $D=1\ \mu\text{m}$ and $SC=40\%$ (b) $H=2\ \mu\text{m}$, $D=1\ \mu\text{m}$ and $SC=40\%$ (c) $H=5\ \mu\text{m}$, $D=1\ \mu\text{m}$ and $SC=40\%$ at $\lambda=0.363636$.

By comparing Figs. 3.8 a, b and c it may be observed how the E field intensity above the pattern reduces as H increases. Furthermore, the E field intensity above the pattern in Fig. 3.8 c is lower than in the cases of a and b. This is because at $H=5\ \mu\text{m}$ there is a better optimization of the multiple reflections than in the cases of $H=1\ \mu\text{m}$ and $H=2\ \mu\text{m}$. This fact is an indication of an increase in the photon absorption due to multiple reflections as H increases for the same values of SC and D (i.e. the same portion of light penetrating in between pillars). Then as the location inside the area in between pillars becomes higher, the E field intensity peaks become weaker as shown in Fig. 3.8 c. The results for the three values of H when $SC=50\%$ are presented in Fig. 3.9 a, b and c.

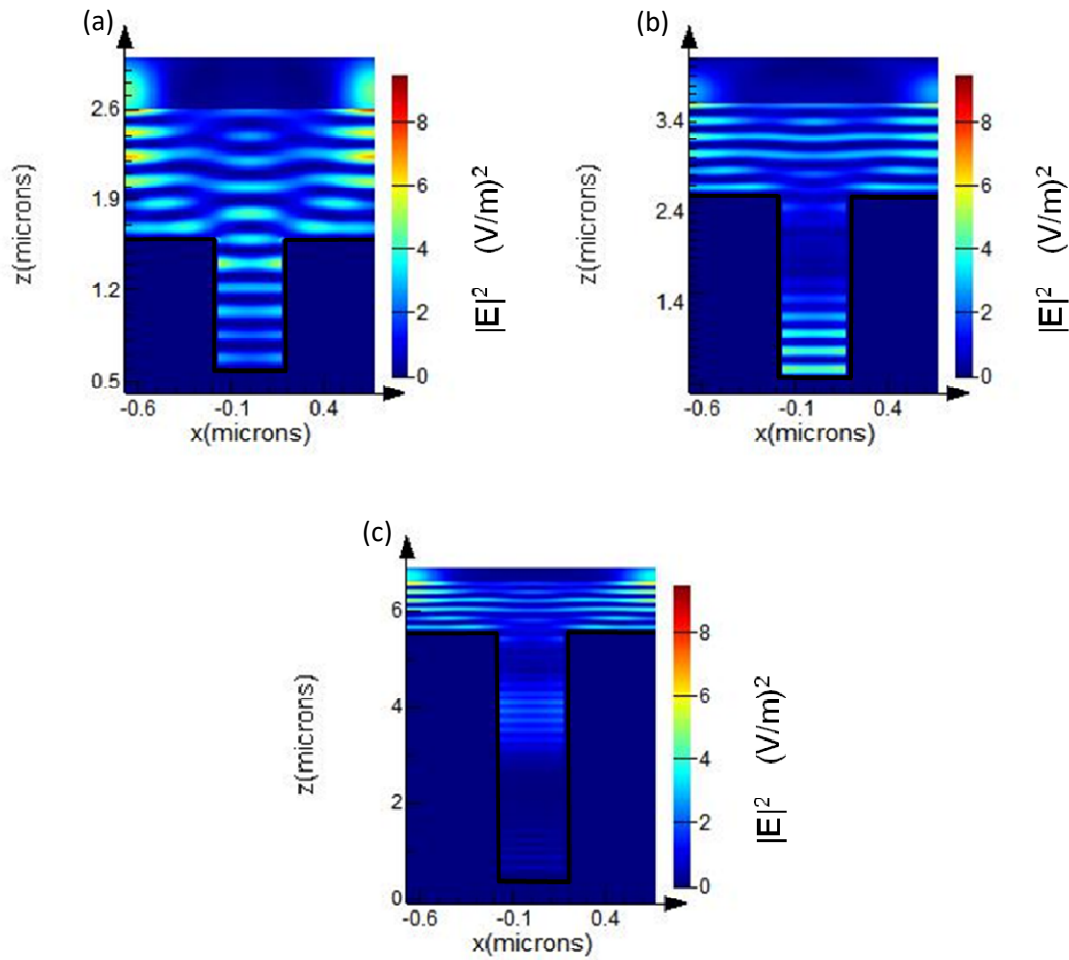


Fig. 3.9. E field intensity in a vertical cross section for the case of (a) $H=1\mu\text{m}$, $D=1\mu\text{m}$ and $SC=50\%$ (b) $H=2\mu\text{m}$, $D=1\mu\text{m}$ and $SC=50\%$ (c) $H=5\mu\text{m}$, $D=1\mu\text{m}$ and $SC=50\%$ at $\lambda=0.363636\mu\text{m}$.

By comparing Figs. 3.9 a, b and c it is possible to see again how the multiple reflections increase while H increases. Nevertheless, there are clear differences when comparing Figs. 3.8 a, b and c with Figs. 3.9 a, b and c. When changing from $SC=40\%$ to $SC=50\%$ the E field intensity above the pattern in the cases of $H=1\mu\text{m}$ and $H=2\mu\text{m}$ decreases. This is an indication of a lower reflection from the pattern as H increases. Additionally, the E field intensity between the pillars increases as well. This is another indication of an increase in the photon absorption that causes a reduction in the reflection. On the contrary in the case of $H=5\mu\text{m}$ the E field intensity above the pattern increases when SC is increased from $SC=40\%$ to 50% . This is due to a larger number of multiple reflections in the case of $SC=40\%$. As H increases, less incident light escapes without providing any contribution to the multiple reflections. This means also

that there is a better usage of the incident light as H increases in the case of lower SC values. This point is applicable to the case of $D=1\mu\text{m}$. In the following section a study to determine whether similar trends are applicable to other D values is presented.

3.4 Effect of Diameter on the reflection from the solar cell

In this section, the effect on the reflection from the surface as the value of D varies is introduced. The value of H is kept constant at $2\mu\text{m}$. Figure 3.10 shows the R_{Int} values for different SC (solid symbols with solid lines) and for space between pillars (transparent symbols with dashed lines) where D varies. The symbol shape (square, circle, etc.) is the same in both sets of curves for the same value of D. The change in the R_{Int} as the value of D varies is substantial. This trend can be observed in the performance of SC values ranging from 20% to 70%. This is in agreement with the results reported by Yoon *et al.* [8] and by Shin *et al.* [9]. They identified a correlation between larger values of D and worse reflection performance. Additionally, Yoon *et al.*, found that the value of short circuit current decreases almost 50% when D increases from $8\mu\text{m}$ ($J_{\text{sc}} = 20\text{mA}/\text{cm}^2$) to $32\mu\text{m}$ ($J_{\text{sc}} \approx 11\text{mA}/\text{cm}^2$) [8]. However, in their studies the performances of a limited set of D values are reported and a deep discussion is not provided [8, 10]. This work intends to provide a deeper insight into the effect of D on the reflection.

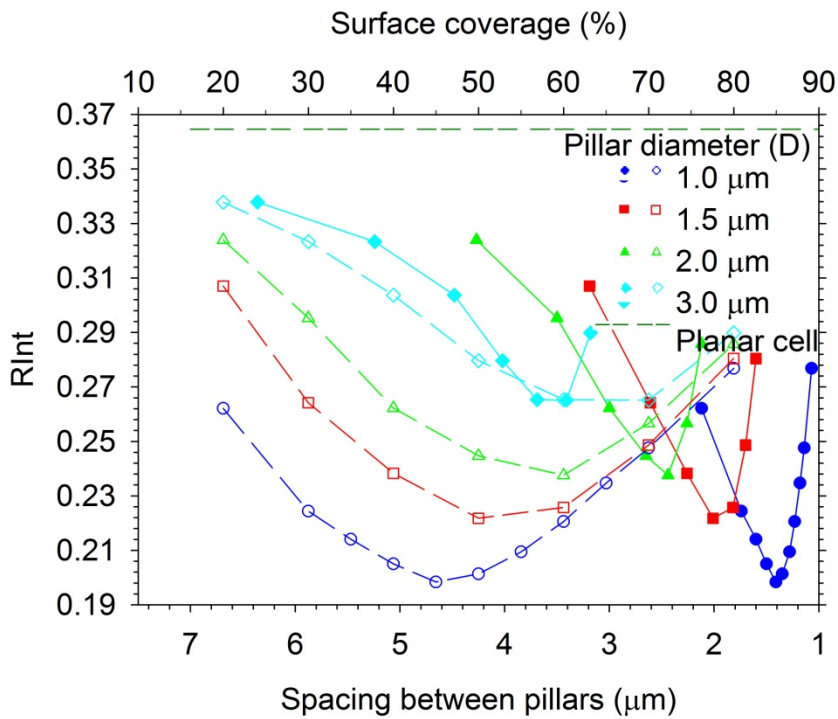


Fig. 3.10. Effect of varying D for fixed H of $2\mu\text{m}$ with respect to SC (solid lines in blue, red and green) and space between pillars (dashed lines in blue, red, green and cyan).

In Fig. 3.10 there are two horizontal scales: one is placed at the bottom x-axis of the figure and the other is at the top x-axis. The scale at the bottom x-axis of the figure corresponds to the spacing between pillars. The scale at the top x-axis of the figure corresponds to the SC. The y-axis represents R_{Int} for both SC and space between pillars. From Fig. 3.10, the trend of R_{Int} as D varies may be observed. When the value of D increases, there is an increase in R_{Int} . This is due to an increase in the surface area on the top of the pillars implying that a larger portion of incident light gets reflected from the top of the pillars. This effect (increase in R_{Int}) is present at all SC values. However, the intensity of R_{Int} increase is not the same at all SC values. For example, in the case of high pillar concentration (i.e. $SC=80\%$) the increase in R_{Int} is not large. Additionally, the R_{Int} value at 80% SC converges for all D values. This convergence indicates that further increase in D does not contribute a significant change. This is due to a small portion of the light penetrating in between pillars contributing to the absorption. As the value of SC reduces, R_{Int} starts to decrease as well. Nevertheless, this behaviour is not valid for all SC values. When the SC value is smaller than an optimum value R_{Int} starts to increase

again. More details on this phenomenon will be introduced in the following section where the effect of SC is discussed in detail.

The R_{Int} behaviour shows a clear improvement in the performance as the value of D decreases. However, even if R_{Int} decreases as D decreases it is not appropriate to assume that by decreasing D to zero it could result in zero R_{Int} . Firstly, when the value of D reaches very small values, the fabrication process can become very challenging. Conventionally, the most powerful fabrication process to achieve non tilted pillars with small value of D is the DRIE process [7]. However, this process has also some limitations when dealing with very small dimensions. The “scalloping” (i.e. oscillations on the side walls of the pillars) can become a major problem [7]. Secondly, the extreme case of $D = 0.0\mu\text{m}$ would be equivalent to a planar cell for which the R_{Int} value has been presented in Fig. 3.2. The R_{Int} of a planar cell is higher than that of a textured cell as discussed in previous sections. This suggests that there is a value of D with minimum R_{Int} . However, Singh *et al.* [10] experimentally identified that the reflection improves as the D value increases from $D = 0.05\mu\text{m}$ to $0.2\mu\text{m}$, for H values ranging between $0.25\mu\text{m}$ and $1\mu\text{m}$. For example at $\lambda = 0.9\mu\text{m}$ the value of R is ≈ 0.35 in the case of $D = 0.05\mu\text{m}$ [10], whereas, in the case of $D = 0.2\mu\text{m}$ the value of R is ≈ 0.05 [10]. Therefore, the optimum value of D should be in the hundreds of nanometre range but larger than $D = 0.2\mu\text{m}$. An analysis to determine this value has not been covered in this work. In future a study on the value of D that offers minimum reflection will be explored. From Fig. 3.10 it can be observed that $D = 1\mu\text{m}$ yields optimum R_{Int} .

When the focus is put on the distance in between pillars equivalent to each of the SC values rather than on the SC value itself, the resulting R_{Int} vs. distance in between pillars curve shows a pronounced change. The distance in between the pillars is the separation between two adjacent pillars as illustrated in Fig. 2.13.

The most important factor to highlight in Fig. 3.10 with respect to distance in between pillars is the smaller distance in between pillars as D decreases. For

example, for the same value of SC=20% the distance in between pillars for the case of $D = 1\mu\text{m}$ is $\approx 2.1\mu\text{m}$ whereas for the case of $D = 3\mu\text{m}$ it is $\approx 6.4\mu\text{m}$. Therefore, as the value of D decreases, this necessitates a fabrication process with higher precision, which would be more costly.

Additionally, there is also a small difference in the distances between two adjacent values. For example, the difference between the distance in between pillars equivalent to SC=20% and the one equivalent to SC=30% is $0.35\mu\text{m}$ ($2.1\mu\text{m} - 1.75\mu\text{m}$) in the case of $D = 1\mu\text{m}$. For this SC gap the difference in the RInt value is ≈ 0.037 ($0.262121 - 0.224384$). However, in the case of $D = 3\mu\text{m}$ the difference in distance becomes $1.15\mu\text{m}$ ($6.4\mu\text{m} - 5.25\mu\text{m}$) with a difference in the RInt value of ≈ 0.014469 ($0.337812 - 0.323343$). Therefore, the decrease in RInt in the case of $D = 1\mu\text{m}$ when SC changes from SC=20% to SC=30% is larger than in the case of $D = 3\mu\text{m}$ for SC=20% to SC=30%. Furthermore, the difference between the RInt values of SC=20% and SC=30% occurs in a shorter distance in the case $D = 1\mu\text{m}$ than in the case of $D = 3\mu\text{m}$. As a consequence, the performance tolerance to any unwanted changes in the distance in between pillars is larger in the case of $D = 3\mu\text{m}$ than in the case of $D = 1\mu\text{m}$. In the case of $D = 1\mu\text{m}$ a small variation in the space in between pillars may severely alter the expected RInt performance. Whereas, in the case of $D = 3\mu\text{m}$ the same variation in the space in between pillars may have a minor impact on the expected RInt performance.

Therefore, the value of D should be taken into account when designing a structure to optimize the performance, the space in between pillars and SC. In the next section, the effect of the space in between pillars and SC on the reflection from the solar cell is discussed.

3.5 Effect of Surface Coverage and space between pillars on the reflection from the solar cell

In order to determine the effect of SC (space between pillars) on the performance there are three analyses carried out. The first analysis uses point monitors at half way between the pillars (i.e. the central point between pillars using the hexagonal configuration). The E field at this location is recorded at three different heights (see Fig. 3.11): $0.2\mu\text{m}$ above the substrate surface (S), half-way up the pillar (M) and at $0.5\mu\text{m}$ above the pillars (A).

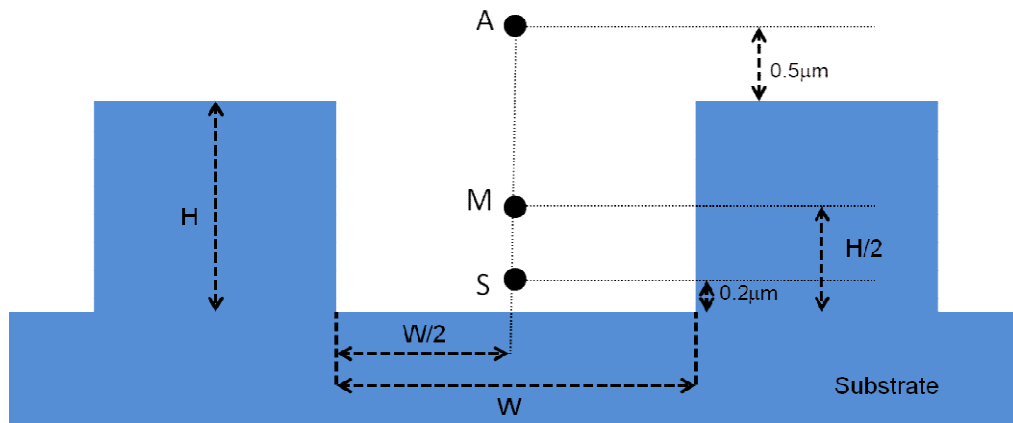


Fig. 3.11. Schematic of the set up for studying effect of varying SC.

Simulations are run using the configuration presented in Fig. 3.11 for three SC values: 50%, 60% and 80% respectively. The values of H and D remain constant at $2\mu\text{m}$ for all three simulations. Previous studies, presented by Yoon *et al.* [8], Shin *et al.* [9] and Park *et al.* [11] have stated the effect of SC on the reflection. They were able to identify a variation in the reflection behaviour as SC varies. For example Yoon *et al.* experimentally varied the SC between SC=20% and 60% for the case of micro pillars with $H=25\mu\text{m}$ and $8\mu\text{m}$ [8]. They found a 40% decrease in R (compared to planar Si solar cell) as SC varies from SC=20% to 50% [8]. Then, the improvement in R saturated when SC varied from SC=50% to 60% [8]. This trend is similar to the results presented in this thesis. However, our study has focused on smaller dimension pillars. The discussion in other studies was primarily focused on the electrical properties. This work intends to provide a deeper insight on the impact of SC on the performance of solar cells and focuses on the optical properties.

The analysis starts with the optimum value of SC (60%) presented in Fig. 3.12. Figure 3.12 shows higher E field intensity in the two monitors within the area in between pillars (monitors S and M). In particular, the monitor S shows higher values of peak E field intensity than any other monitor. This is an indication of incident light penetrating the area in between pillars and getting trapped which would lead to higher absorption. Therefore, higher peak of E field intensity at monitor S indicates a better performance (i.e. lower reflection).

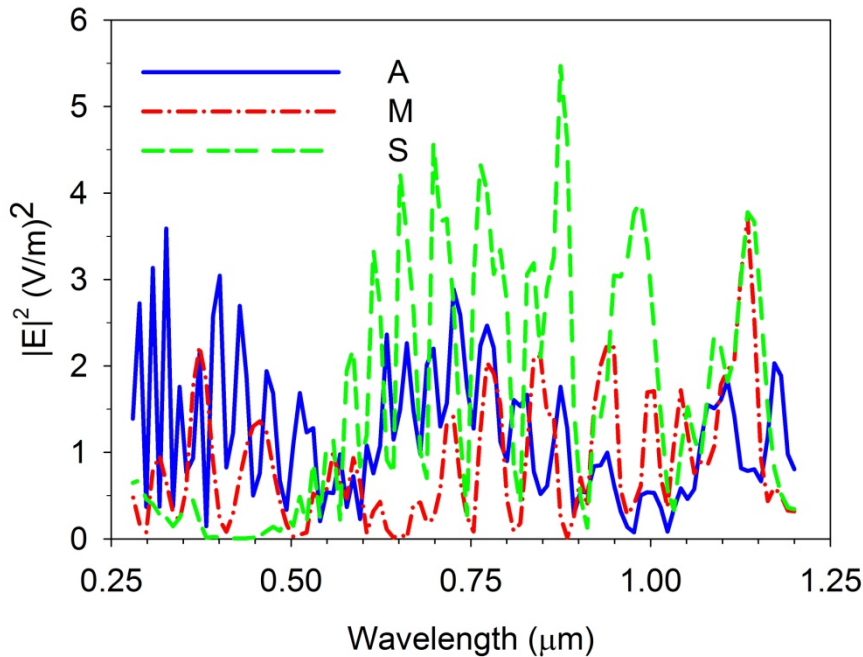


Fig. 3.12. E field intensity at monitors S, M and A for pillar $H= D= 2\mu\text{m}$ and $SC= 60\%$.

Figure 3.13 shows the E field intensity for $SC=80\%$ (i.e. high pillar concentration). Compared to Fig. 3.12, Fig. 3.13 has lower E field intensity in between pillars (i.e. S and M). This is due to the fact that the majority of the light is incident on the top of the pillars. This can be extracted by the recorded high E field intensity at monitor A. This E field intensity values are higher than the ones presented in Fig. 3.12 for the same monitor. Hence, not enough light is penetrating in the area in between pillars. This leads to a low number of multiple reflections in between pillars which reduces the photon absorption; increasing the reflection. This fact can be observed by comparing the E field intensity in point S in Figs. 3.12 and 3.13. Clearly, the E field intensity in the scenario of Fig. 3.13, on average, is much lower than in the scenario of Fig. 3.12.

Therefore, it is possible to state that a consequence of low E field intensity near the substrate is low photon absorption and high reflection.

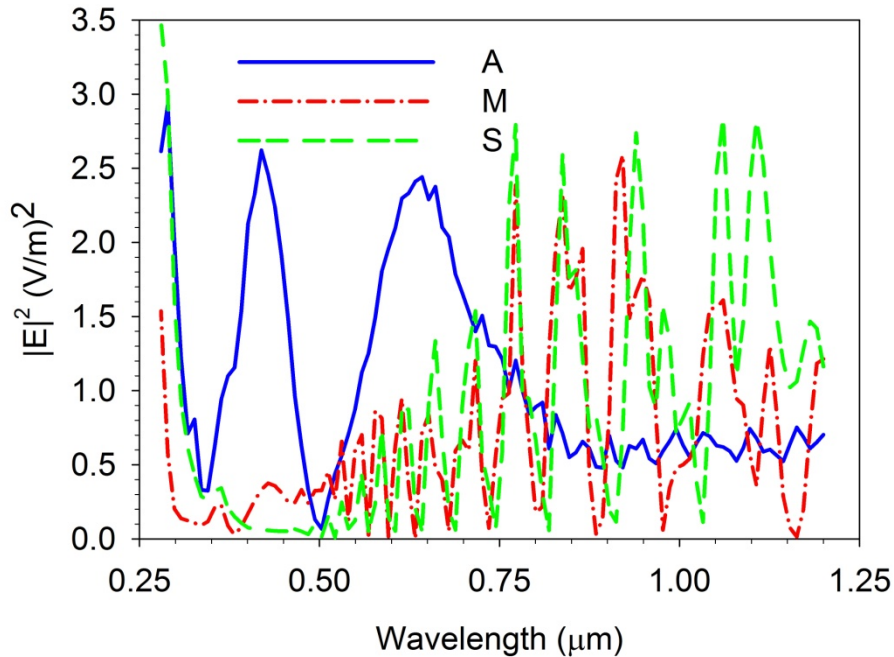


Fig. 3.13. E field intensity at monitors S, M and A for pillar $H = D = 2\mu\text{m}$ and $SC = 80\%$.

Figure 3.14 presents the E field intensity for $SC = 50\%$ (i.e. low pillar concentration). At low SC values the inter pillar spacing is too large to effectively enhance absorption via multiple reflections. The reason is that the light penetrating in between pillars escapes without contributing to the multiple reflections. This is due to the fact that the penetrated light which is incident on and reflected by the substrate is not incident on the side walls of the pillars. This is due to the long distance that separates the micro pillars. As a consequence, the usage of the penetrated light is not optimized in terms of photon absorption due to multiple reflections. In order to maximize (and optimize) the number of multiple reflections, a pillar concentration high enough to enhance photon absorption is required. Meanwhile, the pillar concentration should be low enough to allow the majority of the incident light to penetrate in the area in between pillars. Furthermore, the impact of SC is not limited to the reflection but also on other key parameters. There are reports focusing on the effect of SC on electrical parameters [9, 11]. For example, there are reports indicating that the value of SC has an effect on the short circuit current values. Yoon *et al.*

reported that J_{sc} reduces from 20 to 13.5 mA/cm² when the SC value is reduced from 50% to 20% [8].

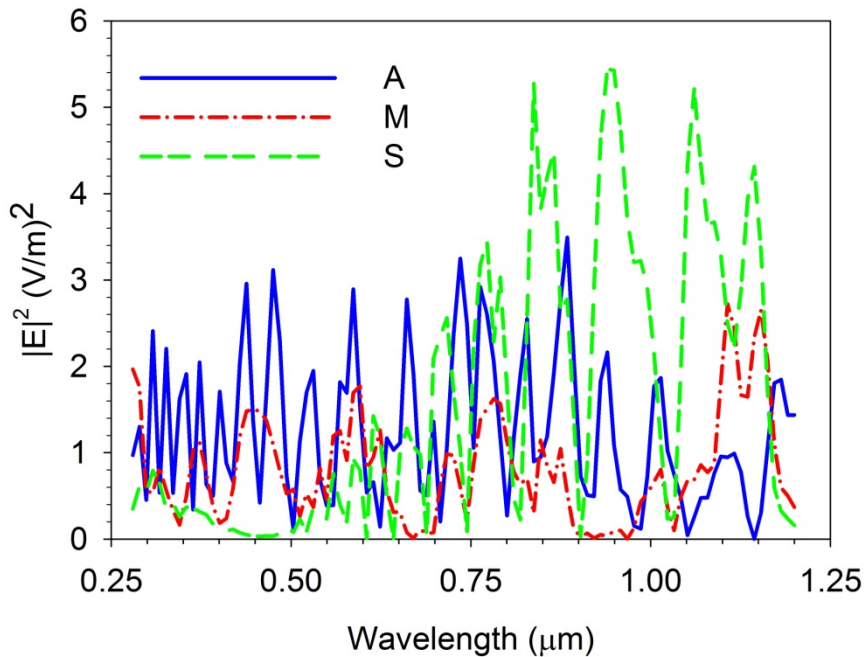


Fig. 3.14. E field intensity at monitors S, M and A for pillar $H = D = 2\mu\text{m}$ and $SC = 50\%$.

Comparing the results presented in Figs. 3.12, 3.13 and 3.14, the optimization of the multiple reflections is achieved by the SC with the highest E field intensity in between pillars. This fact suggests a high importance of the E field intensity level near the substrate.

The main target of the second analysis is to deepen the understanding of the effect of SC on the reflection. To achieve this, the simulation set up is illustrated in Fig. 3.15. Three simulations are run for SC equal to 50%, 60% and 80% respectively. The values of both H and D are set to $1\mu\text{m}$. Then, E field intensity is measured at a 2D monitor placed normal to the z direction (i.e. x-y plane) at $0.2\mu\text{m}$. The results are presented in Figs. 3.16, 3.17 and 3.18. In Fig. 3.16 the E field intensity at a cross section located $0.2\mu\text{m}$ above the substrate is plotted at $\lambda = 0.363636\mu\text{m}$ for the case of $SC = 60\%$.

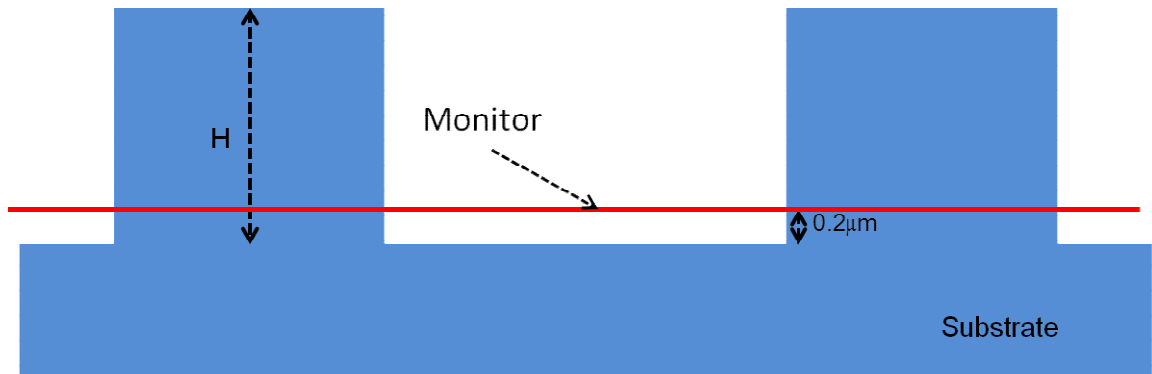


Fig. 3.15. Simulation set up to obtain E field plots as SC varies.

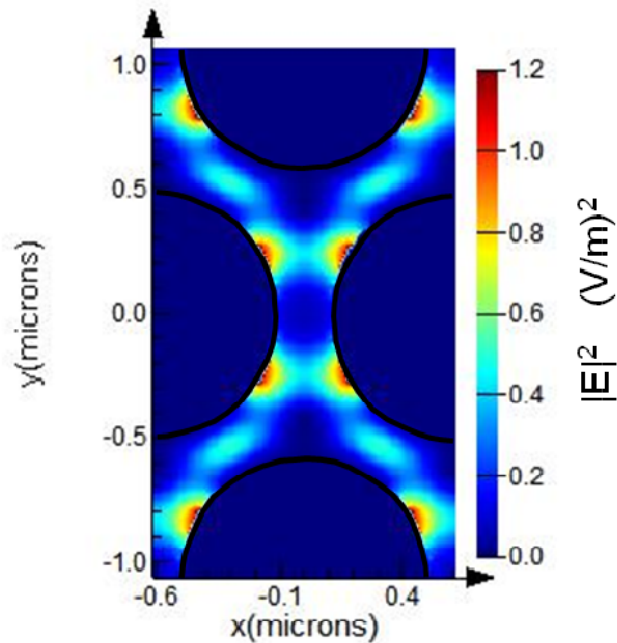


Fig. 3.16. E field intensity of a cross section at $0.2\mu\text{m}$ above the substrate for the case of $H= 1\mu\text{m}$, $D= 1\mu\text{m}$ and $SC= 60\%$.

From Fig. 3.16 the multiple E field intensity peaks that lead to reduction in the reflection may be observed. These peaks are caused by the multiple reflections taking place in the area in between pillars which cause wave interferences. From the discussions of Figs. 3.12, 3.13 and 3.14 it may be recalled that the multiple reflections are maximized when SC is optimum (i.e. $SC=60\%$). In Fig. 3.6 the highest E field intensity peak is $1.2(\text{V/m})^2$. Additionally, the high E field intensity peak values throughout the area in between pillars may be observed. This fact is an indication of the strong presence of the E field near the substrate that leads to improved photon absorption (i.e. reducing reflection). Therefore, the E field intensity in the case of $SC=60\%$ is expected to be the highest. As a

consequence the E field intensity in the case of SC values higher and lower than SC=60% should be expected to be lower due to nonoptimal multiple reflections. In Fig. 3.17 the E field intensity at a cross section located $0.2\mu\text{m}$ above the substrate is plotted at $\lambda=0.363636\mu\text{m}$ for the case of SC=80%.

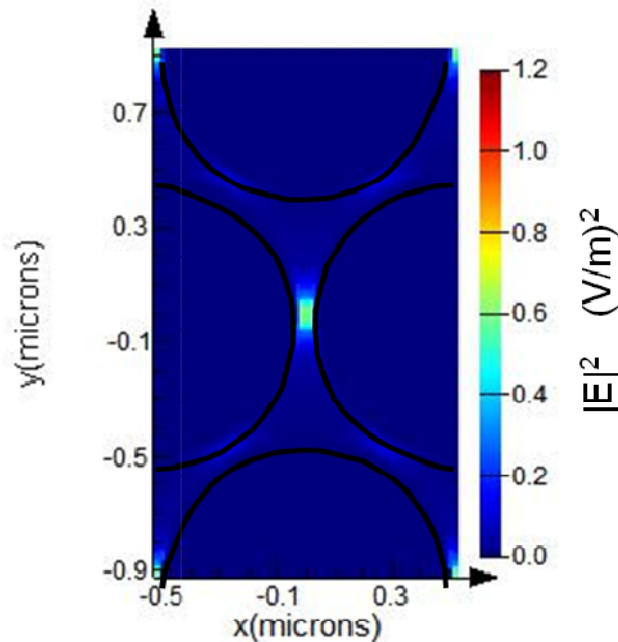


Fig. 3.17. E field intensity of a cross section at $0.2\mu\text{m}$ above the substrate for the case of $H=1\mu\text{m}$, $D=1\mu\text{m}$ and SC=80%.

From Fig. 3.17 a low number of E field intensity peaks may be observed. This corroborates the discussion in Fig. 3.13. The small portion of incident light penetrating into the area in between pillars when SC=80% does not contribute to multiple reflections. As a consequence, the presence of the wave interferences at this SC value is minimum. When comparing Figs. 3.17 and 3.16, a large difference in terms of E field intensity in between pillars may be observed. This fact highlights the importance of multiple reflections to enhance photon absorption and hence to reduce the reflection from the solar cell. In Fig. 3.18 the E field intensity at a cross section $0.2\mu\text{m}$ above the substrate at $\lambda=0.363636\mu\text{m}$ for the case of SC=50% is presented.

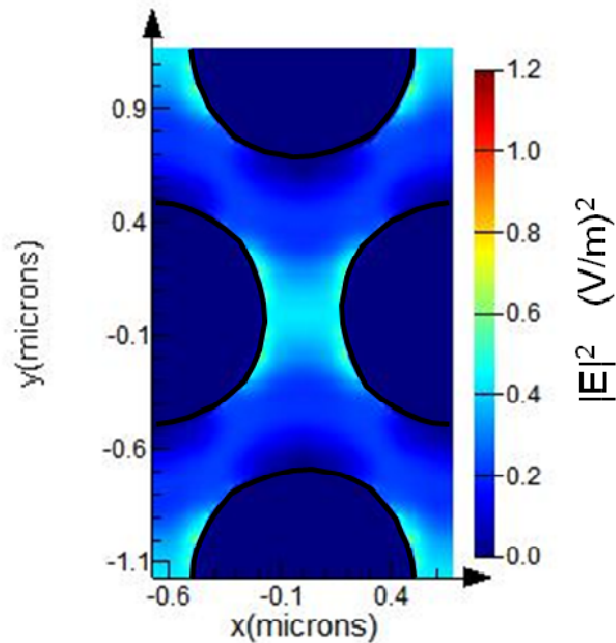


Fig. 3.18. E field intensity of a cross section at $0.2\mu\text{m}$ above the substrate for the case of $H= 1\mu\text{m}$, $D= 1\mu\text{m}$ and $\text{SC}=50\%$.

From Fig. 3.18 E field intensity peaks caused by the presence of multiple reflections may be observed. When comparing Fig. 3.18 with Fig. 3.17 there is a clear improvement in terms of multiple reflections and E field intensity in the case of $\text{SC}=50\%$ (i.e. Fig. 3.18). However, when comparing Fig. 3.18 with Fig. 3.16, the E field intensity is higher in the case of $\text{SC}=60\%$ (i.e. Fig. 3.16). From the discussion on Fig. 3.14, it may be recalled that in the case of $\text{SC}=50\%$ a portion of the light penetrating in between pillars escapes with no contribution to multiple reflections. This concept is supported by a large portion of light that penetrates in between pillars in Fig. 3.18. However, the low number of multiple reflections is an indication of a weak presence of the E field near the substrate. This is the consequence of a large distance in between pillars that leads to a significant portion of light escaping the area with no contribution to multiple reflections. Therefore, the influence of SC is clearly dependent on the distance separating the micro pillars. If this distance is larger, the E field intensity near the substrate is low which is an indication of low photon absorption and high reflection. If this distance is shorter, there is not enough light in between pillars which leads to low E field intensity causing low photon absorption and high reflection. As a consequence, the optimum value of SC leads to a strong

presence of the E field near the substrate thus maximizing multiple reflections. The main purpose of the third analysis is to explore the effect of SC on the reflection.

The third analysis studies the impact of pillar spacing on the reflection by comparing the R_{Int} performance of two values of D ($1\mu\text{m}$ and $3\mu\text{m}$), while the H value is kept constant; and SC and inter pillar spacing are varied for the two diameters. Figures 3.19 a and b present 2D graphs where the x, y and colour bar axes represent SC, inter-pillar spacing and R_{Int} , respectively. The colour bar ranges from blue (i.e. low R_{Int}) to red (i.e. high R_{Int}). Ideally the R_{Int} should be as low as possible (i.e blue) across the majority of the SC and inter-pillar spacing points for any value of D . However, these figures show how R_{Int} depends on pillar spacing as D decreases. In Fig. 3.19 a the blue area covers a wide range of SC and pillar spacing values. Therefore, when $D=3\mu\text{m}$, a small variation in pillar spacing would not affect significantly the performance of the solar cell. However, for smaller D such as $1\mu\text{m}$ (Fig. 3.19 b), the blue area concentrates in a smaller range of SC and pillar spacing values. Therefore, a small variation of pillar spacing would imply a large impact on reflectance. For the pillar with $D=1\mu\text{m}$ even though R_{Int} is the lowest, it is a strongly varying function of inter-pillar spacing.

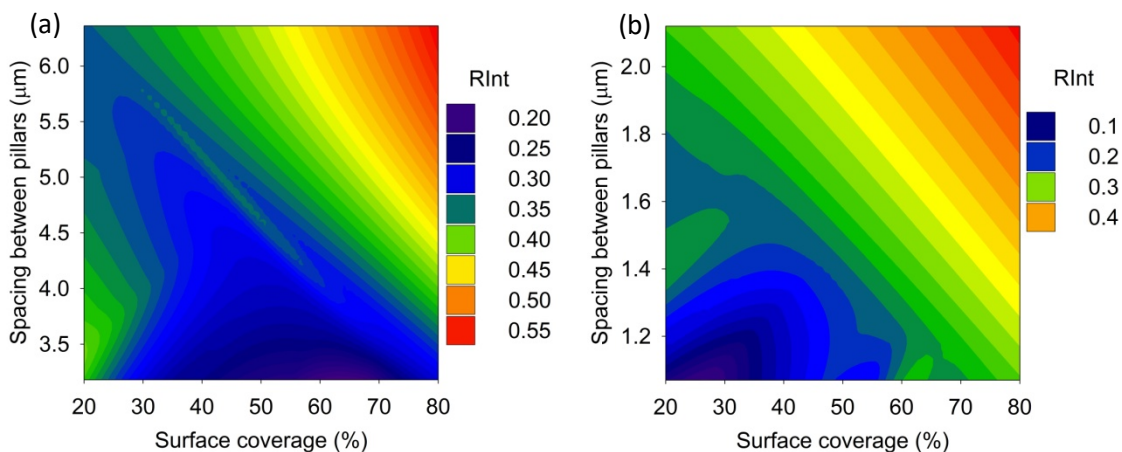


Fig. 3.19. R_{Int} when varying space between pillars and SC, with a) $D= 3\mu\text{m}$ and b) $D= 1\mu\text{m}$.

Hence, for smaller D the fabrication accuracy becomes crucial. Increasing the tolerance is important in bringing down fabrication costs. In the following section an analysis on the H/D ratio providing a new approach to deal with the design tolerance of the micro pillar array is presented.

3.6 Impact of H/D ratio on the reflection from the solar cell

It is possible to choose from a wide range of H and D with tolerance and fabrication costs as critical constraints. What is therefore the method to determine the best set of values? In this section an analysis on the H/D ratio of pillars is presented which can help designers “read off” the best parameters for their given fabrication tolerances. Some researchers such as Shin *et al.* have studied the diameter by pitch (i.e. distance in between pillars) ratio finding that J_{sc} increases as the diameter by pitch ratio remains constant [9]. This increase in J_{sc} was attributed to a lower number of pillars inside the micro pillar array (due to a fixed size of the array) [9]. The authors linked the increase in J_{sc} , as the number of pillars decreased, to the surface recombination caused by the large surface-to-volume ratio [9]. However, to the best of the author’s knowledge an analysis on the H/D ratio is reported for the first time for micro pillars in this work. In the analysis H is varied while D remains constant. The results for SC=50% and SC=40% are presented as representative of the simulation results obtained.

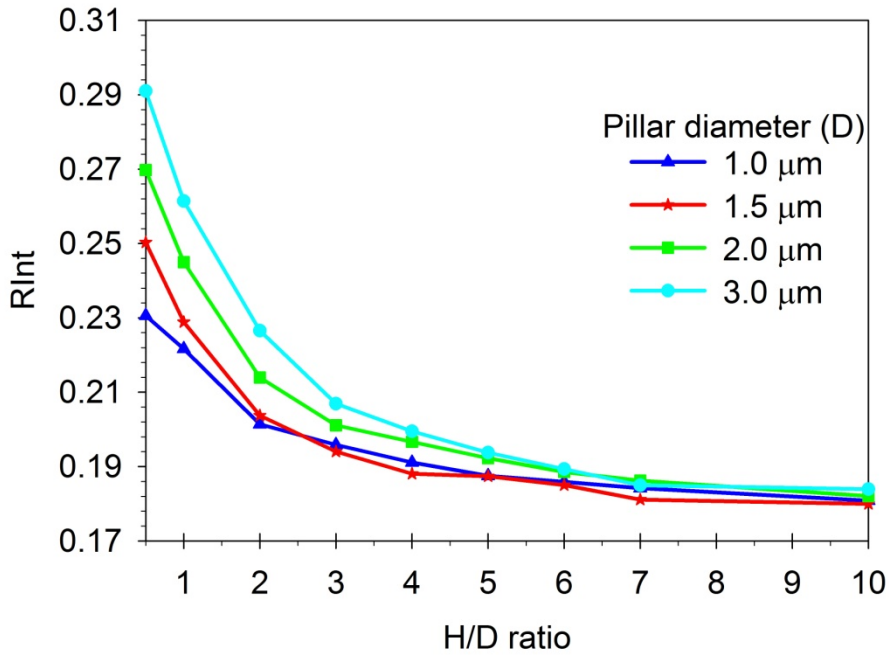


Fig. 3.20. RInt variation with H/D ratio and keeping D fixed for 50% SC.

Figure 3.20 shows RInt against H/D ratio for different D value at 50% SC. In this figure, the value of the RInt is high at low H/D ratio. The RInt decreases rapidly while H/D ratio increases and then it converges slowly for further increase of the ratio. While H/D ratio increases to values higher than 7, the value of RInt converges to ≈ 0.18 .

The difference in the performance between high and low H/D ratio lies in the optimization of the light that penetrates in between pillars. The amount of incident light that penetrates in between pillars does not increase with H/D ratio for constant D and SC and will not contribute to higher absorption. For small values of H/D ratio increase in the ratio (larger H) leads to an increase in multiple reflections resulting in lower values of RInt. This can be seen in Fig. 3.20. However, for a sufficiently large H/D ratio further increase in the value of H does not significantly increase the number of multiple reflections, which is seen in the saturation of the RInt values.

In Section 3.3, the relation between H and the reduction of RInt which is caused by an increase in multiple reflections was discussed. Nevertheless, it was also mentioned that there is a shifting in the optimum value of SC as H increases.

Therefore, in the case of a converged H/D ratio a decrease in the value of SC may lead to a lower reflection. As SC decreases while the H/D ratio remains constant, the amount of incident light penetrating in between pillars increases as well. As a consequence, the number of multiple reflections increases which leads to lower reflection. To support this statement, the RInt vs. H/D ratio curves for different values of D are presented in Fig. 3.21 for the case of SC=40%.

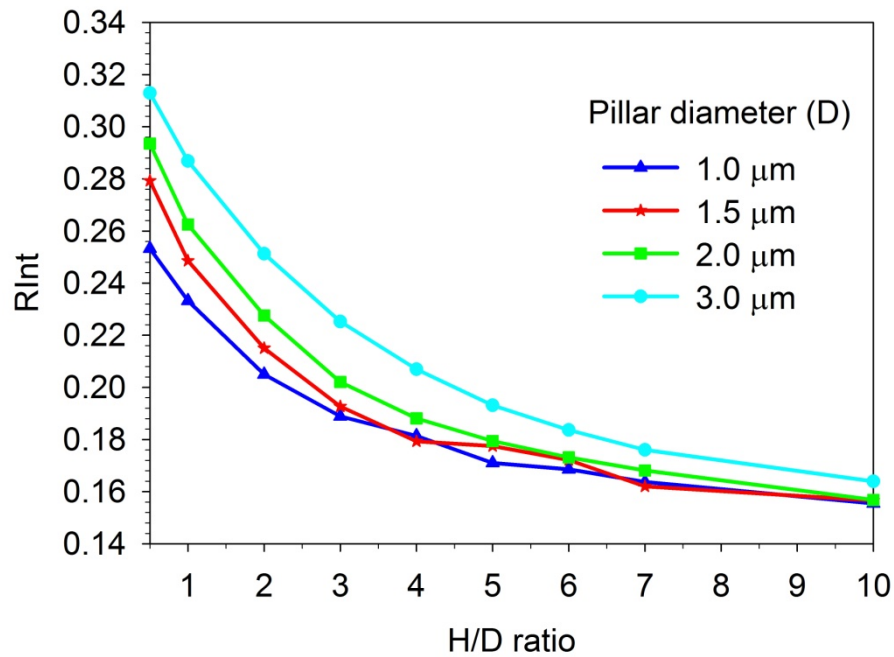


Fig. 3.21. R variation with H/D ratio and keeping D fixed for 40% SC.

From Fig. 3.21, it can be observed that for low H/D ratio, the value of RInt is high. Then, as the value of H/D ratio increases, the value of RInt reduces until it reaches a convergence value after a specific H/D ratio. This means that there is a trend as H/D ratio increases for given SC and D values as shown in Fig. 3.20 and 3.21 that follow the same trend. Nevertheless, there are some differences. In Fig. 3.21 (i.e. SC=40%), the convergence of the curve is reached at higher values of H/D ratio than in the case of Fig. 3.20 (i.e. SC=50%). The explanation lies in the difference between the SC values. As the SC value decreases, the larger area in between pillars facilitates that more incident light penetrates in between pillars. Therefore, the H/D ratio value to maximize the number of multiple reflections increases as SC decreases from 50% (i.e. Fig. 3.20) to 40%

(i.e. Fig. 3.21). Additionally, the converged value of R_{Int} is also lower (i.e. ≈ 0.165) than in Fig. 3.20 (i.e. ≈ 0.18).

Therefore, increasing H when R_{Int} is already converged does not reduce R_{Int} further. However, this fact can be used to benefit designers with low precision fabrication equipments. For example, if it is known that the fabrication may not provide the expected pillar dimensions, it is possible to target a value of H larger than required (\pm tolerance of equipment). Then, the resultant H/D ratio would provide converged R_{Int} . It is clear that in the case of precise fabrication equipments increasing H is not providing any benefit. In such a scenario perhaps it is preferable to reduce the SC value and increase the H/D ratio to obtain lower converged R_{Int} value. This can lead to positive but also to negative outcomes. There are complications associated with the fabrication process of extremely large H/D ratio micro pillars [3].

In such a scenario the probabilities of obtaining micro pillars with a range of complications are higher [12-14]. These complications can be either due to imperfections in the fabrication process (i.e. tilted micro pillars) or due to performance limitations introduced by structural parameters (i.e. high surface recombination) [12-14]. Tilted micro pillars may affect the multiple reflections and therefore may have an impact on the performance of the solar cell. Surface recombination has been reported to be dependent on the surface-to-volume ratio and it can severely diminish the electrical performance of the solar cell [12-14]. When the H/D ratio is large, then the surface-to-volume ratio of the micro pillar array increases. Therefore, the chances of a high surface recombination should be taken into consideration [12-14]. There are some methods available to reduce its effect such as surface passivation which is a challenging task to implement [15-17]. Nevertheless, conventionally the challenging process of surface passivation may be less complex to achieve in the case of micro pillar arrays than in the case of nanowires arrays [3].

By comparing, Figs. 3.20 and 3.21 it may also be observed that as D increases the H/D ratio required to reach convergence is larger. In Section 3.4, the effect of D on the reflection was determined. As D increases, there is a larger portion of the incident light being reflected at the top of the micro pillars. This fact leads

to higher reflection as D increases for any given H and SC . By applying the concept to this analysis, the value of R_{Int} increases as D increases. Then, as the value of D increases, the value of the H/D ratio required to maximize the photon absorption is larger.

To obtain a better understanding of the phenomenon observed, Figs. 3.22 and Fig. 3.23 present the R vs. wavelength curve when $SC=40\%$ for the cases of H/D ratio = 1 (non converged) and for H/D ratio = 10 (converged) respectively. This is done for all D values presented in Fig. 3.21. The R vs. wavelength curve of a planar Si solar cell is presented for reference.

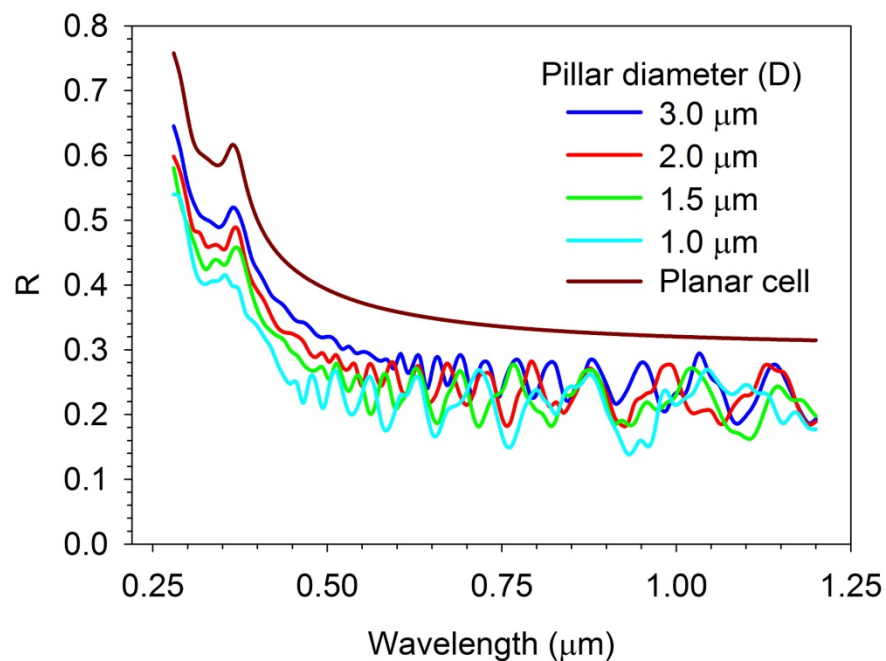


Fig. 3.22. Effect of large H/D (ratio=1) on R vs. wavelength for 40% SC .

From Fig. 3.22, it is possible to see how different the R vs. wavelength curves of four different D values are when a low H/D ratio (i.e. H/D ratio = 1) is selected. This figure supports that the low H/D ratio values do not optimize the multiple reflections. Additionally, any slight mistake during the fabrication process when targeting low D values can lead to a change in performance. Therefore, in such a scenario it is better to target large enough H/D ratio values as presented below in Fig. 3.23.

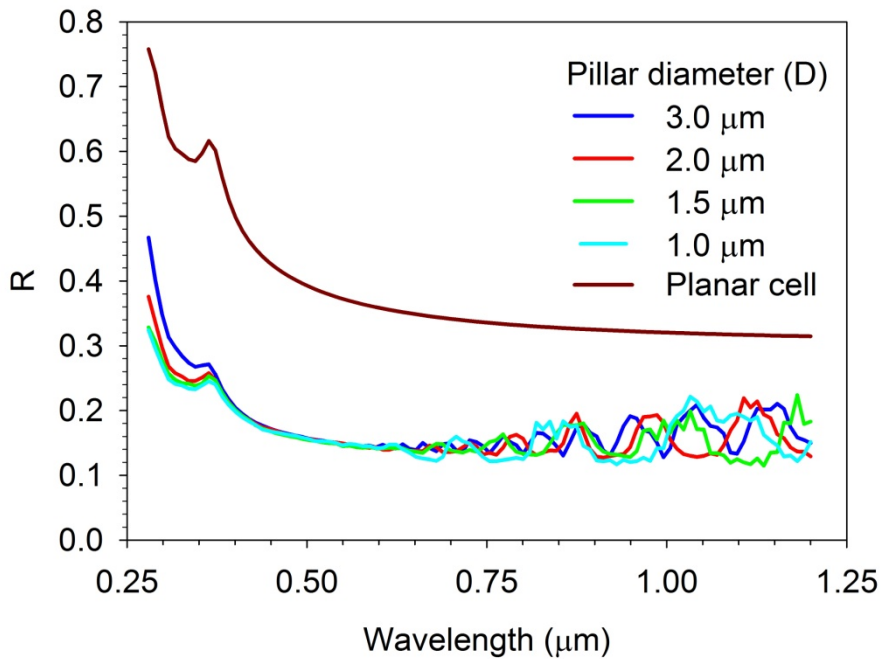


Fig. 3.23. Effect of large H/D (ratio=10) on R vs. wavelength for 40% SC.

From Fig. 3.23, it is possible to see how the R vs. wavelength curves in the cases of four different D values are almost identical. This is possible only in the cases of H/D ratio values large enough to optimize light absorption in between pillars. Additionally, any slight mistake during the fabrication process when targeting low D values would not affect the expected performance.

The importance of Figs. 3.20 and 3.21 and the H/D ratio study is that for any D, it is possible to simply read off the H/D ratio (to calculate H) to obtain a specific reflection. This “normalized” set of curves gives the designers data to use in conjunction with tolerance to design better solar cells with less trial and error.

3.7 Summary

The optical performance of a micro pillar array is dependent on some key material and structural parameters. The simulations presented in this chapter are focused on the effect of the most important structural parameters. Some of the results presented in this chapter have been included in a journal article published by the author [18]. The simulation set up adopted in this chapter was obtained from the convergence test presented in Chapter 2. The memory

requirements of some of the simulations presented throughout this chapter are very large. This fact presented a challenge due to the limitation of the computational memory. In the beginning of the study the computational memory available was of 32 GB (Intel(R) Xeon(R) CPU E31270). Then, the memory capacity was increased by connecting several computers up to 76GB.

When starting the simulation set up process, one of the first factors that should be defined (apart from the mesh parameters) in a texturing pattern is the distribution of the micro pillars inside the array. The hexagonal distribution of pillars inside the array is selected for this work after a detailed comparison with the square configuration due to a better compactness of the array that leads to lower reflection.

Additionally, the value of H has been proven to have an effect on the performance. As H increases more incident light penetrates in between pillars. Hence the number of multiple reflections in the area in between pillars is enhanced which reduces the reflection. The comparison of the electric field intensity as H increases supports this concept. However, the value of H should be selected with care. As the value of H increases to large values, the chances of introducing imperfections during the fabrication process increase.

The worsening of the reflection as D increases causes the preference of smaller values of D . However, the smaller the value of D the more complex the fabrication process becomes. This fact should be considered when there are limitations on the fabrication equipment. For example, targeting small D values can be challenging and errors may be introduced during the fabrication process (especially when low precision equipment is used). In this case, the increase in D can be used to the designer's benefit. As D increases, the difference in the reflection between consecutive SC values decreases. Therefore, when targeting large D values any slight deviation from the optimal design during the fabrication process will have a minor impact in the reflection performance of the sample.

However, in the case of varying the micro pillar concentration (i.e. SC) the portion of incident light in between pillars may vary severely. This is the reason

why it is important to find the SC value providing the best performance. This value clearly depends on how closely the micro pillars are placed to contribute to photon absorption. This value can be easily identified by monitoring the E field intensity inside the area in between pillars. The higher the E field intensity near the substrate the higher the photon absorption (i.e. lower reflection). Therefore, the optimum SC value is the one that optimizes the number of multiple reflections.

Furthermore, the parameter H/D ratio has been first introduced in this work. The discussion shows that the reflection decreases rapidly until it reaches a convergence as the ratio increases. This finding can be useful for designers to select the appropriate ratio and SC values for their application. Then, depending on the accuracy of their equipment, it is possible to tune the value to obtain a result close to the optimum value (i.e. converged RInt).

However, as the H/D ratio increases, the surface-to-volume ratio increases. This has some implications such as higher risk of tilted pillars or high surface recombination. In either of the two cases, the expected benefit on the reflection with the increase in the H/D ratio would be compromised. The multiple reflections inside the area in between pillars may be affected by the presence of tilted pillars. Additionally, the surface recombination is one of the major problems in textured solar cells. When the H/D ratio of a pattern is high the surface recombination is high. Therefore, even though the reflection is improved by increasing the H/D ratio in a micro pillar array the surface recombination is expected to be high. As a consequence, a new texturing pattern capable of both offering low reflection with low surface-to-volume ratio to avoid high surface recombination is required. In the following chapter, a new texturing pattern (hut-like) with these characteristics is presented.

3.8 References

1. Park, H., Iftiqar, S. M., Le, A. H. T., Ahn, S., Kang, J., Kim, Y., Yi, J., Kim, S., and Shin, M., (2016), "*Present Status of Thin Film Solar Cells Using Textured Surfaces: A Brief Review*", Transactions on Electrical and Electronic Materials, Vol. 17, No. 5, pp. 275-279.
2. Zhao, H., (2013), "*Light Trapping for Silicon Solar Cells: Theory and Experiment*", PhD Thesis Syracuse University.
3. Wang, X., and Wang, Z-M., (2014), "*High-Efficiency Solar Cells*", Springer, Heidelberg.
4. Bao, H., and Ruan, X., (2010), "*Optical absorption enhancement in disordered vertical silicon nanowire arrays for photovoltaic applications*", Optics Letters, Vol. 35, No. 20, pp. 3378-3380.
5. Lagos, N., Sigalas, M. M., and Niarchos, D., (2011), "*The optical absorption of nanowire arrays*", Photonics and Nanostructures: Fundamentals and Applications, Vol. 9, No. 2. pp. 163-167.
6. Garnett, E., and Yang, P., (2010), "*Light trapping in silicon nanowire solar cells*", Nano Letters, Vol. 10, pp. 1082-1087.
7. Fu, Y. Q., Colli, A., Fasoli, A., Luo, J. K., Flewitt, A. J., Ferrari, A. C., and Milne, W. I., (2009), "*Deep reactive ion etching as a tool for nanostructure fabrication*", Journal of Vacuum Science and Technology B: Microelectronics and Nanometer Structures, Vol. 27, No. 3, pp. 1520-1526.
8. Yoon, H. P. Yuwen, Y. A. Shen, H. Podraza, N. J. Malouks, T. E. Dickey, E. C. Redwing, J. A. Wronski, C. R., and Mayer, T. S., (2012), "*Parametric study of micropillar array solar cells*", In Proceedings of the 37th IEEE photovoltaic specialists conference (PVSC), pp. 000303-000306.
9. Shin, J., Chanda, D., Chern, W. , Yu, K. J., Rogers, J. A., and Li, X., (2012), "*Experimental study of design parameters in silicon micropillar array solar cells produced by soft lithography and metal-assisted chemical etching*", IEEE Journal of Photovoltaic, Vol. 2, No. 2, pp. 129-133.
10. Singh, N., Wong, S-M., Wang, J., Kwong, D-L., and Yu, H-Y., (2011), "*Structural efficiency boost heralds third-generation solar cells*", SPIE Newsroom, DOI:10.1117/2.1201109.003793.
11. Park, J., Park, J. H., Kim, E., Ahn, C. W., Jang, H. I., Rogers, J. A., and Jeon, S., (2011), "*Conformable solid-index phase masks composed of high-*

- aspect-ratio micropillar arrays and their application to 3D nanopatterning*, Advanced Materials, Vol. 23, pp. 860-864.
12. Baker-Finch, S., and McIntosh, K., (2011), *“Reflection of normally incident light from silicon solar cells with pyramidal texture”*, Progress in Photovoltaics, Vol.19, pp.406–416.
 13. Mallorqui, A., Epple, F. M., Fan, D., Demichel, O., and Fontcuberta i Morral, A. (2012), *“Effect of the pn junction engineering on Si microwire-array solar cells”*, Physica Status Solidi A, Vol. 209, No. 3, pp. 1588-1591.
 14. Dan, Y., Seo, K., Takei, K., Meza, J. H., Javey, A., and Crozier, K. B., (2011), *“Dramatic reduction of surface recombination by in-situ surface passivation of silicon nanowires”*, Nano Letters, Vol. 11, No. 6, pp. 2527-2532.
 15. Dou, B., Jia, R., Sun, Y., Li, H., Chen, C., Jin, Z., and Liu, X., (2013), *“Surface passivation of nano-textured silicon solar cells by atomic layer deposited Al₂O₃ films”*, Journal of Applied Physics, Vol. 114, No. 17, pp. 174301.
 16. Angermann, H., Conrad, E., Korte, L., Rappich, J., Schulze, T. F., and Schmidt, M., (2009), *“Passivation of textured substrates for a-Si:H/ c-Si hetero-junction solar cells: Effect of wet-chemical smoothing and intrinsic a-Si:H interlayer”*, Materials Science and Engineering B, Vol. 159, pp. 219-223.
 17. Kong, E. S. W., (2015), *“Nanomaterials, polymers, and devices: materials functionalization and device fabrication”*, Wiley, Hoboken.
 18. Oates, A., Cabrera-España, F. J., Agrawal, A., and Reehal, H., (2014), *“Fabrication and characterisation of Si micropillar PV structures”*, Material Research Innovations, Vol. 18, No. 7, pp. 500-504.

Chapter 4: Hut-like Si micro pillar array

4.1 Introduction

This chapter presents the results for a new texturing pattern on the surface of the solar cell. The study presented in Chapter 3 has analysed the effect of key parameters on the performance of a micro pillar array solar cell. Additionally, the discussion introduced the advantages of texturing the surface of the solar cell. There is a range of texturing patterns available in the field of solar cells such as nanowires [1], pyramids [2, 3] and micro pillar arrays [4]. There are some advantages present in all these patterns such as reflection⁷ lower than the case of planar Si solar cell [5, 6]. However, micro pillar solar cell offers some advantages that others do not, such as: high photon absorption, low reflection, convergence of R_{Int} ⁸ when H/D ratio is high, controlling the design tolerance, etc.

The discussion has also described the limitations and drawbacks of each of the texturing patterns described above (including micro pillar arrays). Surface recombination is a major challenge to texturing patterns as a whole [5, 6]. This is due to the large impact that surface recombination has on the electrical properties. This negative impact on the electrical performance sometimes can be even more dominant in the overall performance of the solar cell than the positive impact on the reflection [5-8].

Nevertheless, the level of surface recombination is not the same in all texturing patterns. There are factors that lead to higher surface recombination such as the surface-to-volume ratio [9]. The larger the surface-to-volume ratio the higher the surface recombination becomes [6]. In the case of nanowires, the surface-to-volume ratio is very large which leads to high surface recombination. There are reports describing the large impact of this phenomenon [5–9]. Moreover, the case of micro pillar arrays is slightly different due to a smaller surface-to-volume ratio which causes a lower surface recombination. Hence, the electrical

⁷ The term “reflection” represents the physical phenomenon of an electromagnetic wave being reflected at the solar cell.

⁸ The term “ R_{Int} ” refers to the Reflectance integrated over all wavelengths introduced in Eq. (2.30). The term R_{Int} will be used to compare solar cell performances in the entire wavelength spectrum.

performance of the micro pillar array is better than in other texturing patterns [10]. However, in the previous chapter it has been shown how low the reflection is when H/D ratio is large. When the value of the H/D ratio is very high, the surface-to-volume ratio becomes large and hence the surface recombination is expected to be high. Additionally there are other limitations when dealing with micro pillar arrays such as limitations to replicate H/D ratio arrays, etc.

Therefore, in order to minimise the main drawbacks of micro pillar arrays presented in Chapter 3 (i.e. high surface-to-volume ratio, difficulty to replicate large H/D ratio, etc.) while maintaining all the advantages of the pattern (i.e. improved optical performance, expectations of good electrical performance, etc.), the hut-like texturing pattern is developed. The surface-to-volume ratio associated with this pattern is reduced compared to other texturing patterns such as nanowires [1], pyramids [2, 3] or micro pillars [4]. Therefore, the expected surface recombination for the hut-like pattern is lower than for other texturing patterns. Additionally, the optical performance of the hut-like pattern is better than the ones presented in Chapter 3 as will be shown in this chapter.

The appearance of the pattern was presented in Section 2.3.6.5 together with the structural parameters to describe the pattern which are: Radius_{top}, Radius_{bottom}, Diameter (D), Height (H), Cap and θ .

The parameters that define the accuracy and stability of the simulations presented in this chapter are $\Delta_x = 0.005 \mu\text{m}$, $\Delta_y = 0.005 \mu\text{m}$, $\Delta_z = 0.004 \mu\text{m}$ and $\Delta_t = 0.00952674 \text{ fs}$. It can be seen that the mesh used in Chapter 4 is finer than that of Chapter 3. The values of the mesh parameters are selected to ensure an accurate modelling of the hut-like pillars. This means that the memory requirement is very large for each of the presented simulations. As a consequence, the running time of each simulation increases. Table 4.1 presents a comparison of the memory requirements and simulation times for the cases of vertical micro pillar and hut-like pattern. The SC and the distance centre to centre remain constant in both scenarios.

Pattern type	$\Delta_x=\Delta_y$ (μm)	Δz (μm)	SC (%)	Radius or Radiustop (μm)	H (μm)	ϑ ($^\circ$)	Memory (GB)	Simulation time (min)
Vertical micro pillar	0.010	0.007	30	0.5	1	90	5.520	79
Hut-like	0.005	0.004	30	0.5	1	105	11.586	363

Table 4.1. Comparison of memory requirements and simulation time in Vertical micro pillar simulations and Hut-like pattern simulations.

The presentation of the results obtained in the optimisation process of the hut-like texturing pattern is divided into different sections of this chapter. The discussion starts with the performance comparison between different texturing patterns and the hut-like pattern. Then, the optical performance of the hut-like pattern is analysed by studying the effect of the key structural parameters on the reflection. The purpose is to provide a physical insight into the effect that each of the parameters has on the reflection. The first effect of a structural parameter to be discussed is the area in between huts on the reflection, SC and ϑ . The second is the effect of H on the reflection. The third is the effect of D on the reflection. The fourth is the effect of Cap on the reflection. The fifth is a comparison between all the studied parameters to understand the relationship between various parameters and to find an optimum set up. The sixth is a proof of concept by presenting some experimental results. The discussion starts with the comparison of the hut-like pattern with other texturing patterns.

4.2 Comparison with other patterns

The usage of a texturing pattern provides a reduction in the reflection as discussed in Chapter 3. There is a wide range of texturing patterns as discussed in Section 1.5.4. The texturing patterns that are conventionally used are: pyramids [2, 3], nanowires [1] and micro pillars [4]. Each of these texturing patterns offers some benefit on the reflection due to its shape and dimensions. In the case of an array of pyramids, the incoming light is incident on the surface of a pyramid several times. This fact leads to higher photon absorption which reduces the reflection. However, the improvement in the performance is more pronounced only when the height of the pyramids is larger. As a consequence, the amount of material (typically Si) that is needed to fabricate the pyramid solar cell is large (for $H \approx 10\mu\text{m}$) [11, 12]. This fact leads to an increase in the

fabrication costs. Additionally, the surface-to-volume ratio is very large which leads to high surface recombination [13]. This is a disadvantage of the pyramid texturing pattern and other alternatives are discussed below.

A similar phenomenon is experienced in an array of nanowires. However, in the case of an array of nanowires, there is also a refractive index averaging effect that reduces the reflection as predicted by Fresnel's equations [14]. This is possible when there is a periodicity in the pattern and the incident light has a wavelength longer than the pitch of the pattern [14]. Then the incident light interacts with the pattern as if the pattern is a layer composed of a material with refractive index between that of air and the index of the material of the pattern. However, the surface recombination associated with nanowire arrays is high. Additionally, the small dimension of nanowires requires a complex and costly fabrication process.

Some of these problems can be reduced by using an array of micro pillars, as discussed in Chapter 3. Additionally, the dimension of a micro pillar array is larger than the dimension of nanowires which should allow for an easier fabrication process. Furthermore, in the case of low precision fabrication equipment, the structural parameters of the array could be tuned to achieve good optical performance. However, the surface-to-volume ratio of micro pillar arrays will increase with H . As a consequence, the surface recombination will increase with the surface-to-volume ratio.

The implementation of the hut-like pattern allows for low reflection performance. Additionally, the low reflection is achieved with dimensions small enough to expect a low surface recombination. In Fig. 4.1 the R^9 vs. wavelength curve of the optimized hut-like pattern is compared with that of some other available texturing patterns such as: vertical micro pillars [4], nanowires [1] and pyramids [2, 3].

⁹ The term "R" refers to the Reflectance which was introduced in Eq. (2.29). The term R will be used to compare solar cell performances in a specific wavelength range.

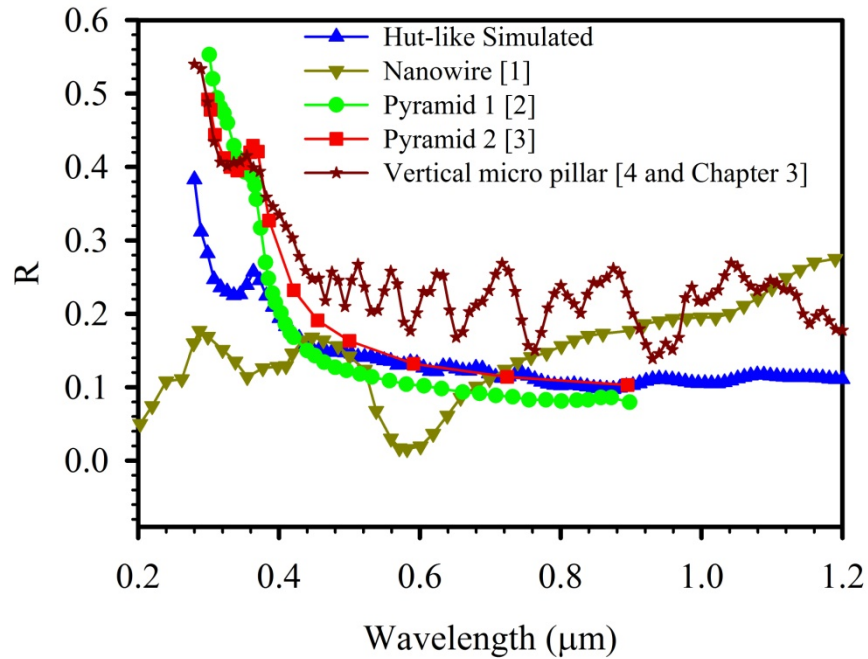


Fig. 4.1. R vs. wavelength curve comparison between the hut-like structure ($D=1\mu\text{m}$, $H=1\mu\text{m}$ and $\theta=115^\circ$) with other texturing patterns of similar dimensions.

From Fig. 4.1, the wavelength dependent performance of the hut-like pattern can be observed. A low R is obtained when the photon absorption and the number of multiple reflections are optimized. The other texturing patterns presented in Fig. 4.1 have similar operating approaches but with different results. The R performance of the hut-like pattern is lower than the micro pillar arrays for the entire solar spectrum. For example in the case of micro pillar arrays the value of R at $\lambda = 0.36\mu\text{m}$ is ≈ 0.42 whereas in the case of the hut-like pattern the value of R is ≈ 0.29 . This is due to the presence of the sloped part on the side walls of each of the hut-like pillars. This sloped part has an effect on the angle of incidence of the incoming light on the hut-like pattern as compared to micro pillar arrays. This point will be discussed in detail in Section 4.3.

In the comparison with the performance of nanowires, the R performance of the hut-like is lower for longer wavelengths. The difference between the performance of the nanowire and the hut-like pattern is due to two reasons. One reason is the presence of the sloped part in the hut-like pattern. The other is the light trapping effect of the nanowires. At shorter wavelengths, the refractive

index averaging produced by the nanoscale dimensions of the nanowires is dominant in the performance. This leads to a reduction of the reflection from the surface (as predicted by Fresnel's equations). This effect is highly dependent on the size of the nanowires as well as on the separation between each nanowire. Therefore, any variation on the design of the distance between the nanowires would have a negative impact on the averaging effect that would reduce efficiency. At the longer wavelengths, the refractive index averaging effect reduces and the multiple reflections become the dominant phenomenon. In this scenario the shape of the hut-like pattern enables better light trapping than nanowires. Therefore, the hut-like pattern optimizes the photon absorption due to multiple reflections. For example in the case of nanowires the value of R at $\lambda = 1.00\mu\text{m}$ is ≈ 0.2 whereas in the case of the hut-like pattern the value of R is ≈ 0.15 .

While, comparing the R performance of the hut-like pattern with that of pyramids, the R performance of the hut-like pattern is lower for shorter wavelengths than in the case of pyramids. The difference between the performance of pyramids and the hut-like pattern is due to two reasons. One reason is the shape of the hut-like pattern where the sloped part of the hut enhances photon absorption. The other reason is the difference in the dimensions [2]. At the shorter wavelengths, the circular nature of the sloped part of the hut-like pattern leads to better photon absorption. For example in the case of pyramids the value of R at $\lambda = 0.36\mu\text{m}$ is ≈ 0.4 whereas in the case of the hut-like pattern the value of R is ≈ 0.29 . At the longer wavelengths there is a difference in the H value between the hut-like pattern ($1\mu\text{m}$) and the pyramid ($6\mu\text{m}$) [2]. This difference leads to a slightly better absorption of the longer wavelengths in the case of the pyramid array. This is due to the improvement in the absorption of longer wavelengths as the height of the pyramids increases [15].

Therefore, the better performance of the hut-like pattern compared to other patterns may be attributed to more effective light trapping. The sloped part of the hut-like pattern is key to obtain this performance. This parameter will be

discussed in detail in Section 4.3. Nevertheless, every parameter is important in the performance as will be discussed in relevant sections of the chapter.

In the field of surface texturing the usage of back reflectors on texturing patterns, to improve the light path inside the structure, is conventional. In the simulations carried out to obtain the results presented in Fig. 4.1, the hut-like pattern is without any back reflector which highlights its effectiveness. Moreover, the size of the hut-like pattern is large compared to other patterns such as nanowires. This fact reduces some degree of difficulty compared with dealing with very small dimensions. Additionally, the surface-to-volume ratio of the hut-like pattern is lower than other texturing patterns such as nanowires, pyramids or micro pillars for the same value of H, as shown in Table 4.2 [13, 16, 17].

Pattern type	Parameter (μm)		Surface-to-volume ratio
Nanowire	radius	0.125	$\frac{22}{25} : \frac{1}{20}$ (= 17.6)
	Height	1.000	
Pyramid	side of base	1.000	$\frac{81}{25} : \frac{33}{100}$ (= 9.8)
	Height	1.000	
Micro pillar	radius	0.500	$\frac{471}{100} : \frac{79}{100}$ (= 5.96)
	Height	1.000	
Hut-like	Radiustop	0.500	$\frac{43}{5} : \frac{5}{2}$ (= 3.44)
	Height	1.000	
	Cap	0.200	

Table 4.2. Comparison of the surface-to-volume ratio of four texturing patterns.

As a consequence, the level of surface recombination of the hut-like pattern should be lower than that of other texturing patterns of similar dimensions [13, 16, 17]. To optimize the hut-like pattern the effect of the key parameters on the performance is analysed in the following section. The discussion starts with the effect of the area in between huts on SC, ϑ and the reflection.

4.3 Effect of ϑ , SC and Cap on area in between huts

Light trapping takes place in the area in between huts. Hence, an appropriate choice of SC and ϑ is important for the best performance. The size of the area in between huts effectively determines the photon absorption due to multiple

reflections. This is in line with the discussion presented in Section 3.5, where the impact of varying SC in a micro pillar array is introduced. An intuitive way of varying this area is to change the distance between huts (i.e. SC).

The hut-like pattern offers an alternative way to vary the area in between huts by changing ϑ . As ϑ increases from vertical micro pillar (i.e. $\vartheta=90^\circ$) to larger values of ϑ , the area in between huts decreases proportionally. It should be noticed that the increase in ϑ (while keeping the rest of the parameters constant) leads to a change in the angle of incidence of the incoming light on the sloped part as well. Hence, there is a variation of the reflection from the sloped in addition to change in multiple reflections.

The discussions starts with the explanation of the behaviour of RInt as a function of area in between huts, SC and ϑ and then examine how the area changes with ϑ and Cap for various SC values separately. Figure 4.2 shows the RInt dependence with variation of the area in between huts and ϑ . The RInt value is represented in Fig. 4.2 as a range of colours according to the colour bar presented. The high end of RInt values are represented by pink whereas the low end values of RInt are represented by red. The values of the area in between huts and ϑ are presented on the y-axis and x-axis respectively. The curves for three different SC values are shown: 30%, 40% and 50%. For all SC the RInt is recorded, as the value of ϑ increases. The optimum range of ϑ is circled in Fig. 4.2 for each of the three SC values. The performance of the vertical micro pillar ($\vartheta=90^\circ$) with $H=1\mu\text{m}$ and $SC=50\%$ has been included for reference.

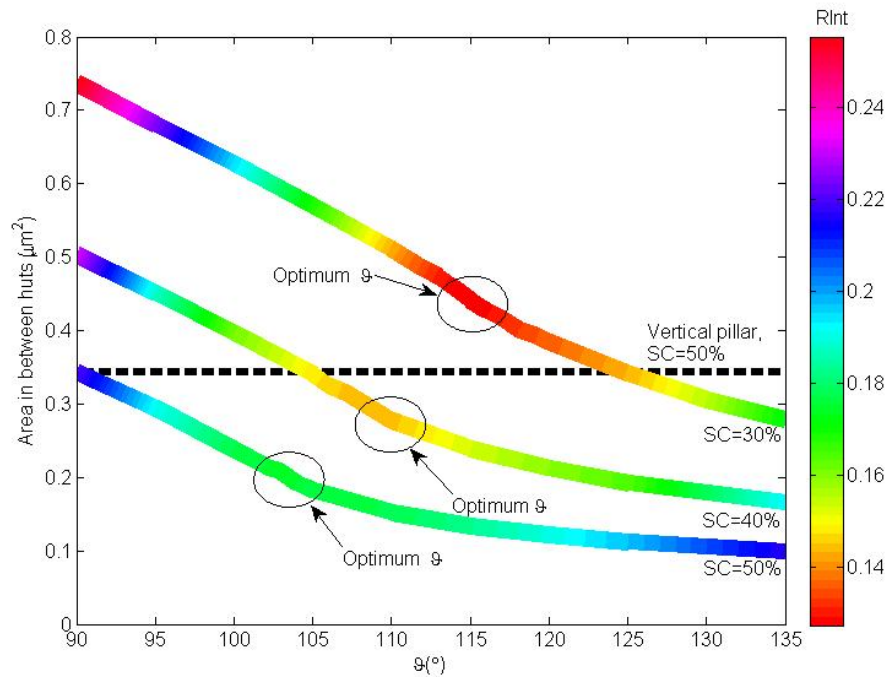


Fig. 4.2. Angular performance, Area in between the huts vs ϑ for $H= 1 \mu\text{m}$, $\text{Radiustop} = 0.5 \mu\text{m}$ and $\text{Cap} = 0.2 \mu\text{m}$ where the line colour represents R_{Int} .

There is a similar trend in all three cases: area in between huts effectively determines the light concentration. As ϑ increases from 90° , first there is a decrease in R_{Int} for all the studied SC values. This can be identified in Fig. 4.2 by the colour of the lines changing towards green (SC= 50%), yellow (SC=40%) and red (SC=30%). For further increase in ϑ , R_{Int} decreases continuously until it reaches a minimum. The minimum value of R_{Int} may be identified in the graph as the optimum range of ϑ . When the value of ϑ increases to higher values than optimum, the colour of the lines changes towards the blue (SC=50%), green (SC=40%) and yellow (SC=30%) end of the spectrum. This means that there is an increase in R_{Int} . Figure 4.2 is a useful tool to compare the performance of different parameters (SC and ϑ) at the same time.

Figure 4.3 presents R_{Int} as a function of ϑ alone (for SC= 30%, 40% and 50%). In all three cases the value of R_{Int} is high when the value of ϑ is 90° (equivalent to micro pillar). Then, as the value of ϑ increases, the value of R_{Int} decreases rapidly with it, until it reaches a minimum value. For increases further than this optimum value, the trend changes since there is an increase in the value of

RInt. This increase is due to an overlap in the pattern and it may be identified as the dotted parts of the lines in Fig. 4.3.

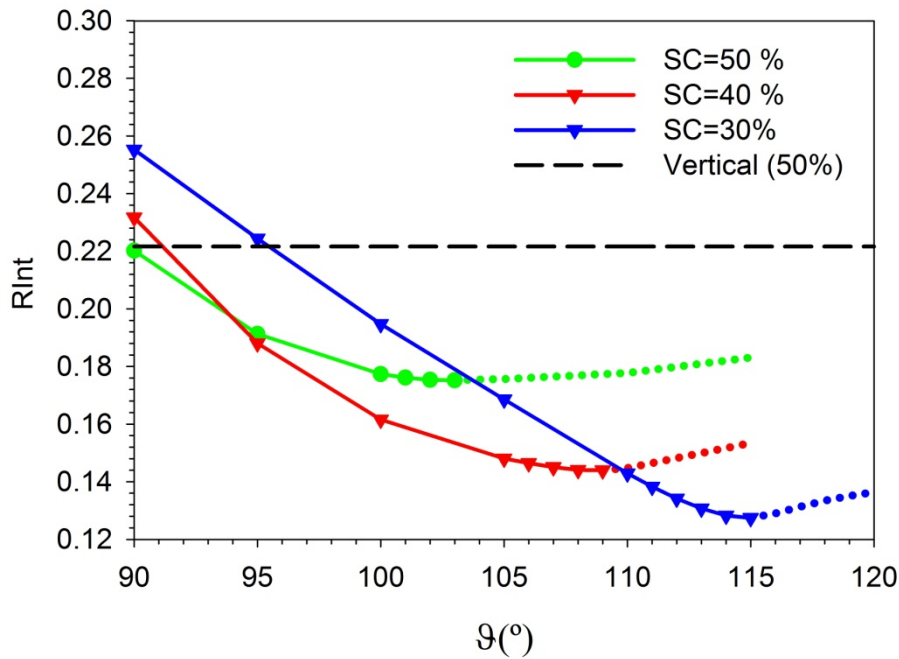


Fig. 4.3. RInt vs. θ for the SC values: 30%, 40% and 50%.

An overlap effectively decreases the height of the huts and as a consequence the area in between huts. Figure 4.4 presents the variation of the area in between huts with θ where the dashed lines indicate the overlapped portion of the pattern. From Fig. 4.4 a constant decrease in the area in between huts as θ increases can be observed. Then, the trend becomes less steep once the pattern overlaps.

The inset 1 in Fig. 4.4 shows that the Effective Height (Eff H) remains at a constant value in the case of the non overlapped pattern. Then, as the pattern becomes overlapped, the value of Eff H decreases sharply. As a consequence, the Fresnel reflection from the sloped part and the subsequent trapping of the reflected light is impacted adversely.

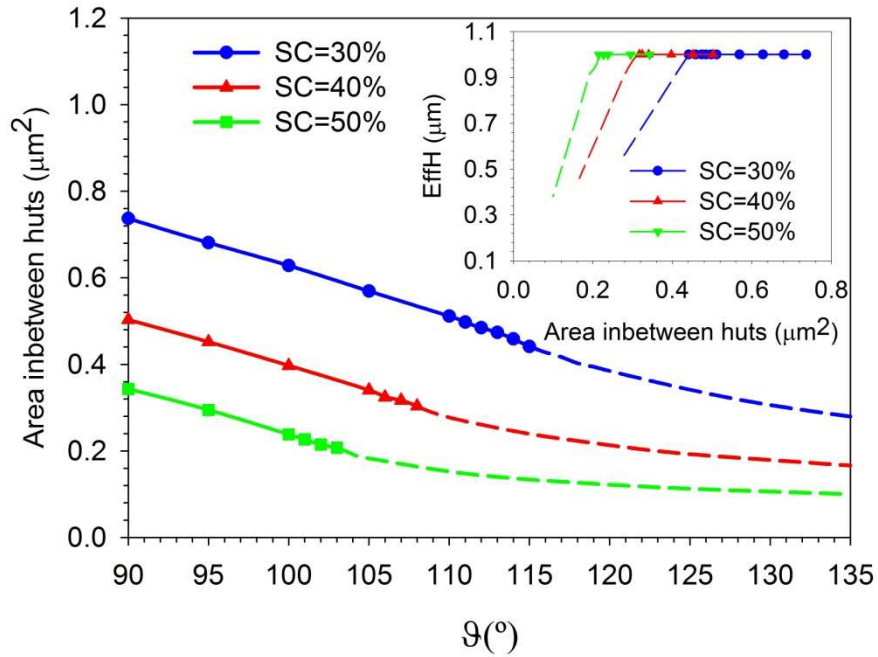


Fig. 4.4. Variation of area in between huts vs. ϑ for SC values: 30%, 40% and 50%. Inset 1. Change in EffH as area in between hut decreases.

Figure 4.5 illustrates in a schematic how the height of the pattern is impacted by the overlap. The difference between the intended H and Eff H after the overlap is $OverH$. Additionally, the value of $OverH$ is dependent on ϑ . This has a direct impact on the performance. The number of multiple reflections taking place in between huts reduces. As a consequence, the photon absorption reduces as well.

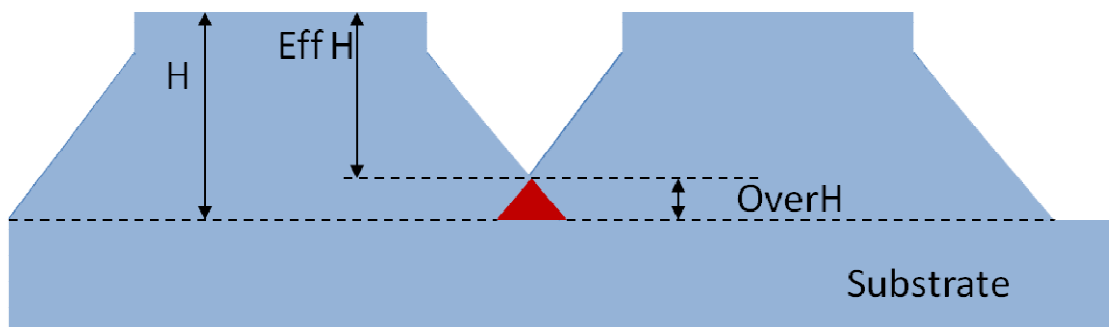


Fig 4.5. Schematic of an overlapped hut-like pattern.

Figure 4.6 shows a top view of an overlapped pattern. This figure shows that the value of $OverH$ is not constant along the outer circumference of the hut. This is due to the circular nature of the huts. When the overlap worsens, caused by an increase in ϑ , there is still photon absorption due to multiple reflections.

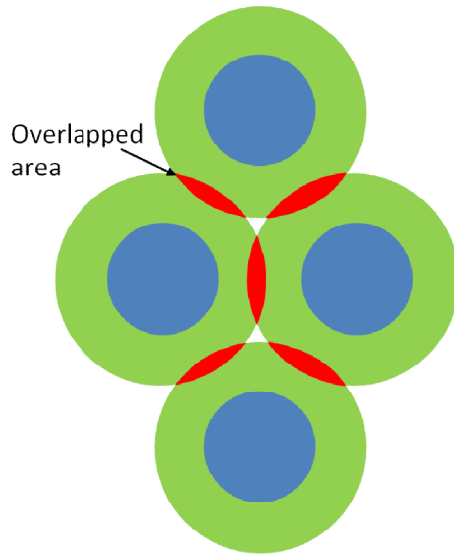


Fig. 4.6. Schematic of an overlapped hut-like pattern from a top view.

Therefore, an appropriate value of ϑ is key for good performance. This is further substantiated by the following figures which show the calculated E field intensity in the pattern for different values of ϑ .

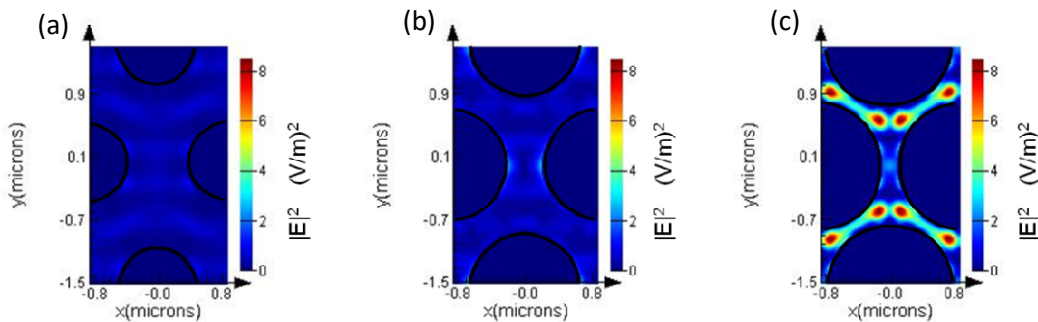


Fig. 4.7. Cross section showing E field intensity at $0.2 \mu\text{m}$ above the substrate for structure with $H = 1 \mu\text{m}$, $\text{Cap} = 0.2 \mu\text{m}$ and $\text{SC} = 30\%$ at $\lambda \approx 0.373 \mu\text{m}$ for a) $\vartheta = 90^\circ$, b) $\vartheta = 105^\circ$ and c): $\vartheta = 115^\circ$ (i.e. optimum).

In Figs. 4.7 (a, b and c), the E field intensity recorded at $0.2 \mu\text{m}$ above the substrate for different values of ϑ ($\vartheta = 90^\circ$, 105° and 115°) for constant $\text{SC} = 30\%$ is presented. The black lines indicate the circumference¹⁰ of the huts. When the value of ϑ is 90° , the E field intensity indicates that there are electromagnetic waves in the area in between huts. Moreover, the multiple maximum and minimum peaks of E field intensity indicate that there are multiple

¹⁰ In the E field plots presented in the remainder of the Chapter, the black lines represent the edges of the micro pillars.

reflections. When the value of ϑ increases from 90° to optimum (i.e. $\vartheta=115^\circ$), the maximum and minimum E field intensity peaks experience a dramatic increase. This increase is due to the optimization of the photon absorption at the sloped and the multiple reflections simultaneously. As a consequence, in the case of optimum ϑ the E field intensity is higher in the area in between huts. In order to have a better understanding of what happens in the area in between huts further analysis should be carried out. Figure 4.8 presents the E field intensity at a vertical cross section (x-z plane) of the pattern for four ϑ values ($\vartheta=90^\circ$, 105° , 115° and 125°) for constant SC=30%.

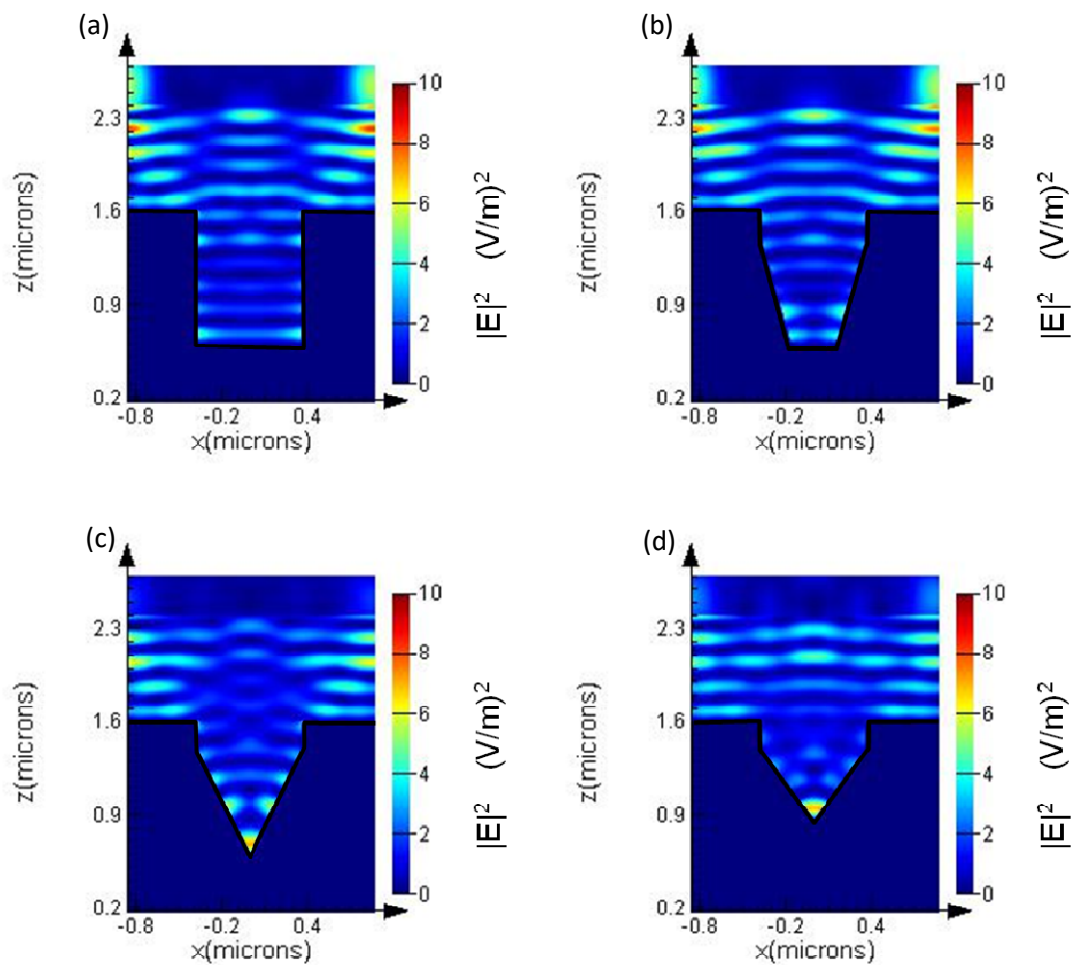


Fig. 4.8. Cross section showing E field intensity at vertical cross section (x-z plane) of the structure with $H=1\ \mu\text{m}$, $\text{Cap}=0.2\ \mu\text{m}$ and $\text{SC}=30\%$ at $\lambda \approx 0.373\ \mu\text{m}$ for a) $\vartheta=90^\circ$, b) $\vartheta=105^\circ$, c) $\vartheta=115^\circ$ (i.e. optimum) and d) $\vartheta=125^\circ$.

From Fig. 4.8 the presence of wave interferences identified by the maximum and minimum peaks in the E field intensity can be observed. This means that there are multiple reflections in the area in between huts. As the value of ϑ

increases from $\vartheta=90^\circ$ to optimum (i.e. $\vartheta=115^\circ$) the value of the E field intensity peaks increases in the area in between huts and decreases above the huts. The highest E field intensity is recorded in the area near the substrate. Therefore, this indicates that for optimum performance, the higher the E field intensity near the substrate the better. This finding is in line with the discussion on SC presented in Section 3.5. Additionally, it is worth highlighting the high E field intensity concentrated on the v-groove like [18] corner in the optimum case presented in Fig. 4.8 c. Then, as ϑ increases further than optimum (i.e. $\vartheta=125^\circ$), the Eff H reduces which causes weaker E field intensity near the substrate. As a consequence, the E field intensity above the pattern is stronger which indicates a higher reflection.

The value of Cap also has an impact on the area in between huts. For a fixed value of H the change in the value of Cap results in change of either ϑ (keeping Radiusbottom and SC constant) or SC and Radiusbottom (keeping ϑ constant). Figure 4.9 b shows how the structure changes when the Cap is increased while keeping constant H, Radiusbottom and SC. This leads to an increase in the value of ϑ (clearly visible from Fig. 4.9 b) and also reduces the length of the sloped portion of the hut. Figure 4.9 b on the other hand shows that for fixed H increasing Cap while keeping ϑ constant leads to change in Radiusbottom and SC. It can be seen that the sloped portion and Radiusbottom decrease. These structural changes lead to a variation in reflection performance.

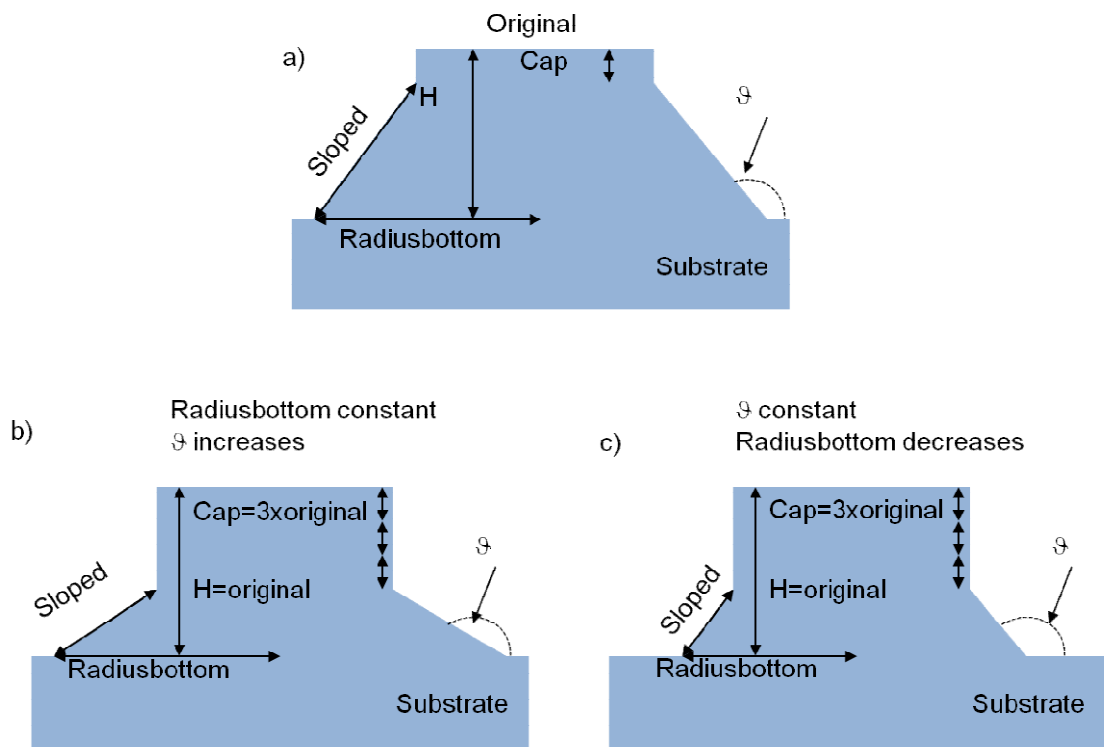


Fig. 4.9. Effect in ϑ and the area in between huts as Cap varies.

In order to clarify the relationship between Cap and the area in between pillars a comparison for different values of Cap and SC is presented in Figs. 4.10 a, b and c.

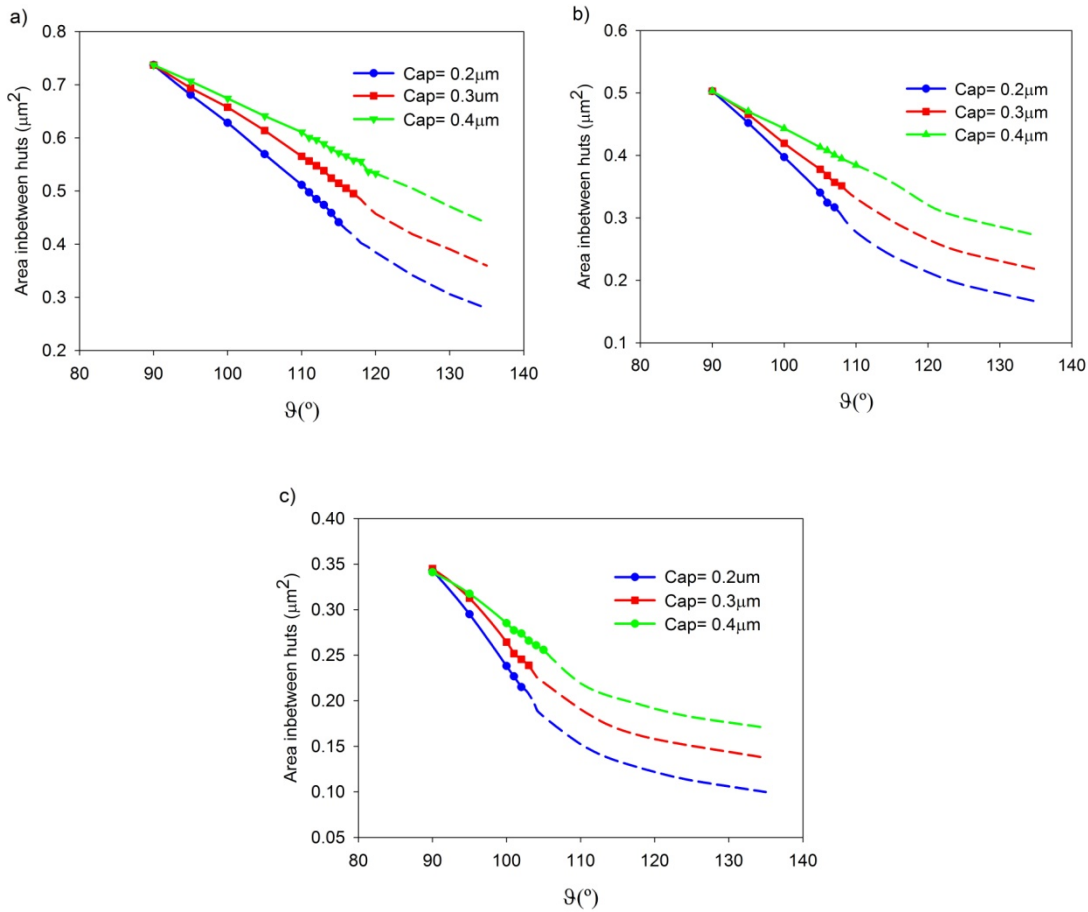


Fig. 4.10. Effect of varying Cap on the area in between huts for $H = 1\mu\text{m}$, with a) $SC=30\%$, b) $SC=40\%$ and c) $SC=50\%$.

In Figs. 4.10 a, b and c there is a variation of the area in between huts vs. ϑ curves as the value of Cap changes at $SC= 30\%$, 40% and 50% respectively. The reason for this variation is the change in the sloped part of the hut as illustrated in Fig. 4.9. For example in Figs. 4.10 a, b and c an increase in the value of ϑ (i.e. keeping SC and Radiusbottom constant) results in a constant decrease in the area in between huts. Additionally, in Fig. 4.10 a, at $\vartheta= 120^\circ$ the pattern is overlapped for the cases of $Cap = 0.2$ and $0.3\mu\text{m}$ but not in the case $Cap = 0.4\mu\text{m}$. This is due to a shorter Radiusbottom in the case of $Cap = 0.4\mu\text{m}$ than in the cases of $Cap= 0.2$ and $0.3\mu\text{m}$. A detailed explanation on the effect of Cap on RInt will be presented in Section 4.6. In the following section the impact of H on the reflection is discussed in detail.

4.4 Effect of H on the reflection from the surface of the solar cell

The effect of H on the reflection can be analysed by recording the R_{Int} while varying H as well as ϑ . Varying the value of ϑ is important to determine whether the performance at some specific ϑ is more affected by H than any other ϑ . This analysis is presented in Fig. 4.11 for $H=1\mu\text{m}$, $2\mu\text{m}$ and $3\mu\text{m}$ and ϑ varying between 90° and 114° . The value of SC is kept constant at $SC=30\%$. As a consequence, in this analysis the area in between huts is varied by H and ϑ . The curve corresponding to the vertical micro pillar for $H=1\mu\text{m}$ is included for reference. It should be recalled that for a fixed Cap an increase in H leads to the sloped portion being larger.

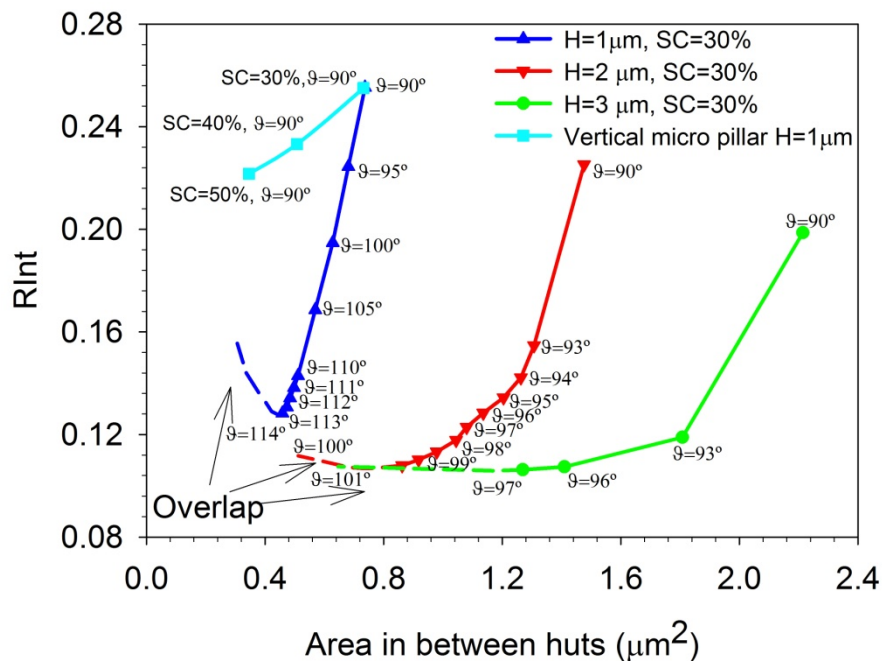


Fig. 4.11. Variation in R_{Int} as the area in between huts changes, for different H.

In Fig. 4.11, it can be observed that for a given ϑ the R_{Int} decreases as H increases. As H increases for a constant value of ϑ and Cap, the length of the sloped part of the hut is longer. This leads to higher photon absorption in the sloped due to the angle of incidence of the incoming light. This is in line with the discussion in Section 4.3 that explains how the light falling on the sloped part of the hut shows lower R_{Int} . Nevertheless, the trend of reducing R_{Int} as H increases is not valid for all studied heights. There is no significant reduction of the R_{Int} when the value of H is increased to large values. This is due to the

impact of H on R_{int} which at first enhances photon absorption. Then, after a certain value of H the photon absorption is not enhanced further. For example, from Fig. 4.11, it may be seen that the difference in R_{int} between $H= 2\mu\text{m}$ and $3\mu\text{m}$ is smaller than the difference between $H= 1\mu\text{m}$ and $2\mu\text{m}$.

Additionally, there is the problem of high surface recombination [1-10]. As discussed in Chapters 1 and 3, the surface recombination can lead to poor electrical performance of solar cells with good optical performance. Unfortunately, in the case of textured solar cells the surface recombination is a factor to be taken into account. Surface recombination tends to be high when surface-to-volume ratio is high [5]. There are various texturing patterns that tend to have a high surface-to-volume ratio such as for example nanowires or pyramids as shown in Table 4.2. These patterns have a good optical performance which means a large number of electron-hole pairs are generated. However, a direct consequence of a high surface recombination is a low carrier collection [1-10]. As a result not all the electron-hole pairs created by texturing the surface to improve the optical performance contribute to the photocurrent. Researchers have developed a technique to minimise the presence of surface recombination which is called surface passivation [10].

The process to successfully achieve surface passivation is complex and costly [19, 20]. There are various techniques available to achieve the surface passivation such as: Rapid Thermal Oxidation (RTO) [21], Plasma-Enhanced Chemical Vapour Deposition (PECVD) [21] and Thermal Oxidation (CTO) [21]. However, the usage of these methods to passivate the surface of textured solar cells such as nanowires or micro pillar array solar cells is not easy [21]. This is the reason why there is a need for an easier surface passivation process for textured surfaces [22]. For example there are new surface passivation techniques, such as the H-passivation that uses Hydrogen atoms to fully passivate the surface of nanowires [22]. In the future, the search for less complex surface passivation processes will help to increase the experimental conversion efficiency of textured solar cells.

An approach to avoid both the surface recombination and the complexity of the surface passivation while achieving a good optical and electrical performance,

is a texturing pattern with low surface recombination. The optical performance of the hut-like pattern is better than other patterns which is an advantage. Additionally, the surface-to-volume ratio is low compared to other texturing patterns such as nanowires [6], see Table 4.2. A high value of the surface-to-volume ratio is reported to increase surface recombination. Therefore, the low surface-to-volume ratio of the hut-like pattern (3.44) is expected to offer an advantage in terms of the electrical performance. The usage of the hut-like pattern helps to optimize the electron-hole pairs and hence the photocurrent. The results obtained for the hut-like pattern indicate that future studies should explore the electrical performance of this pattern. Another parameter related to the performance of the pattern is D which is introduced in the following section.

4.5 Effect of D on the reflection from the surface of the solar cell

The value of D of the hut-like pillars has a large effect on the reflection. An example of this is the effect of the value of D on the reflection presented in Section 3.4 where the value of R_{int} increases as the value of D increases. In some cases the only option is to increase D due to the limitations of the fabrication equipment. In this section a study is presented to understand whether the reflection behaviour of the hut-like pattern is affected in the same manner by the variation in D as the micro pillar array. The value of θ is varied for a range of D values ($0.5\mu\text{m}$, $1\mu\text{m}$, $1.5\mu\text{m}$ and $2\mu\text{m}$) while SC and H are kept constant at 30% and $1\mu\text{m}$ respectively. The R_{int} vs. θ curves are presented in Fig. 4.12.

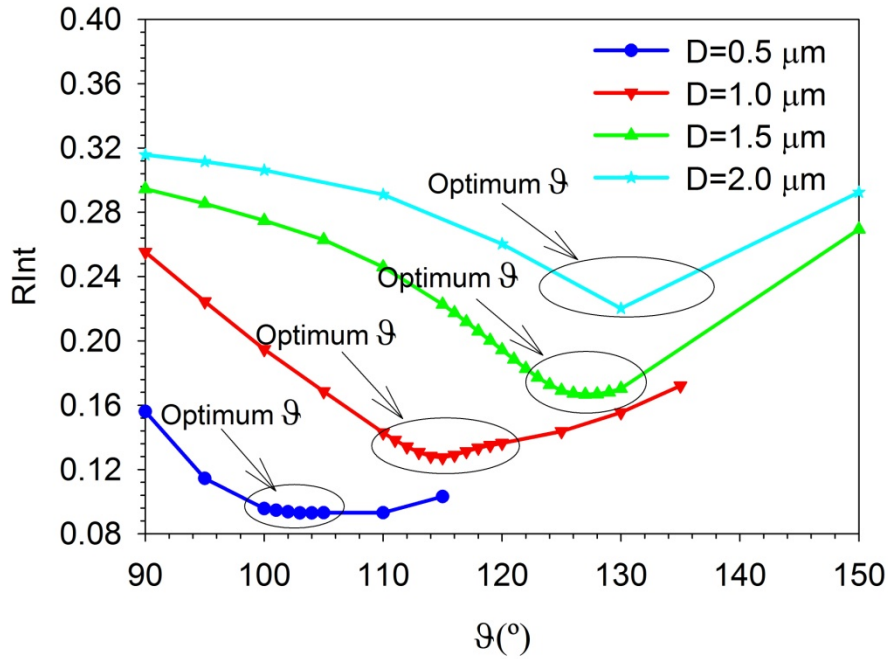


Fig. 4.12. Effect of D at $SC= 30\%$ for the case of $D= 0.5\mu m, 1\mu m, 1.5\mu m, 2\mu m$.

From Fig. 4.12 it may be observed that for small values of D ($0.5\mu m$), the value of R_{Int} remains low even as ϑ increases. Then, as the value of D increases, the value of R_{Int} increases with it. This is in line with the discussion presented in Section 3.4. When $D = 0.5\mu m$, the value of R_{Int} is the lowest among all the D values presented in the figure. Moreover, a change in ϑ , near its optimum value, does not lead to a large difference in the value of R_{Int} . This means that the fabrication tolerance near the optimum value of ϑ is higher which can be useful to designers. As the value of D increases any change in the value of ϑ , near the optimum value, leads to a large variation in R_{Int} . This means that the fabrication tolerance near the optimum value of ϑ is low which can add to the complexity of the design process. Therefore, the lower the value of D the better in terms of fabrication with regards to change in ϑ . The difficulty in fabricating a structure with small D is another issue that merits consideration. There should be an optimum value of D which is worth investigating in the future. Another parameter with an impact on the performance is the Cap which is introduced in the following section.

4.6 Effect of Cap on the reflection from the surface of the solar cell

The Cap in the pattern determines the lengths of the vertical and sloped parts in the structure. In this study the R_{Int} is recorded when the values of Cap and ϑ are increased. Figure 4.13 presents the R_{Int} vs. ϑ curve for three values of Cap (i.e. $0.2\mu\text{m}$, $0.3\mu\text{m}$ and $0.4\mu\text{m}$) while keeping SC and H constant at 30% and $1\mu\text{m}$ respectively. Recall from Fig. 4.10 that as ϑ increases the area in between huts decreases. The R_{Int} for the case of a vertical micro pillar (i.e. $\vartheta=90^\circ$) is presented for reference.

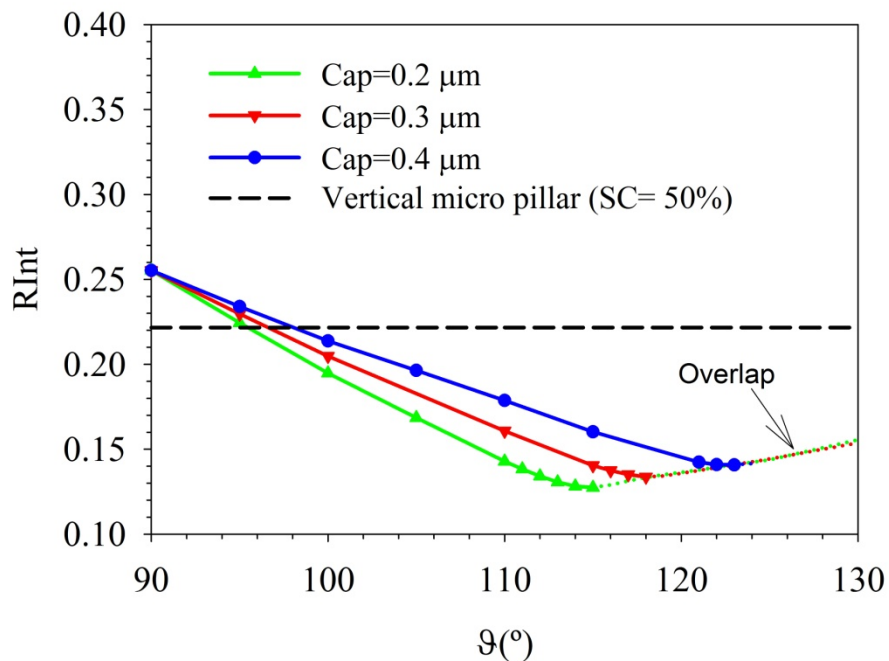


Fig. 4.13. R_{Int} vs. ϑ at SC= 30% varying Cap size for $H=1\mu\text{m}$.

In Fig. 4.13, for the same value of ϑ , the simulated value of R_{Int} increases together with the value of Cap. This increase is due to the larger size of the vertical component of the hut. This means that the portion of the incident light absorbed by the sloped part of the hut reduces. As the value of Cap increases while ϑ remains constant, the Radiusbottom reduces. This reduction leads to a smaller sloped part of the hut. As a consequence, the angle of incidence on the sloped part of the hut does not change. However, the amount of light that is incident on the sloped part of the hut changes. This leads to a change in the Fresnel reflection of the light incident on the sloped part which also affects the

number of multiple reflections. Therefore, for a good performance a low value of Cap is recommended. Nevertheless, it should be highlighted that any Cap value presented in Fig. 4.13 shows a R_{Int} vs. ϑ curve offering better performance than the vertical micro pillar case. This fact supports the importance of the Cap and the sloped part on the hut-like pattern. The Cap provides an additional tool to designers to obtain the required performance.

Furthermore, it is also important to discuss the effect that the value of Cap has on the overlap of the pattern. From Figs. 4.9, 4.10 a, b and c and Eq. (2.27), the relation between Cap , ϑ and the area in between huts may be observed. As a consequence, when the value of Cap is small, the $Radius_{bottom}$ in Eq. (2.27) will be large. This means that there is a large sloped part of the hut which leads to overlapping of the pattern with low values of ϑ . This can be seen in Fig. 4.13. However, when the value of Cap increases while keeping ϑ the same, the corresponding value of $Radius_{bottom}$ reduces. This means that there is a smaller sloped part of the hut which leads to overlapping of the pattern with larger values of ϑ . This can be seen in Fig. 4.13. This means that even though the performance in terms of R_{Int} is worse for larger Cap , there is more room to adjust the value of ϑ . In some cases this can be useful to designers. In the future this idea might be worth exploring.

In order to analyse whether the trend observed when varying Cap in the case of $H=1\mu m$ is applicable to other hut dimensions, the same study is carried out for the case of $H=2\mu m$. The values of SC and Cap are kept constant at 30%, 0.2 μm , 0.3 μm and 0.4 μm respectively. The results are presented in Fig. 4.14 where the case of vertical micro pillar with $H=2\mu m$ and $SC = 50\%$ is presented for reference.

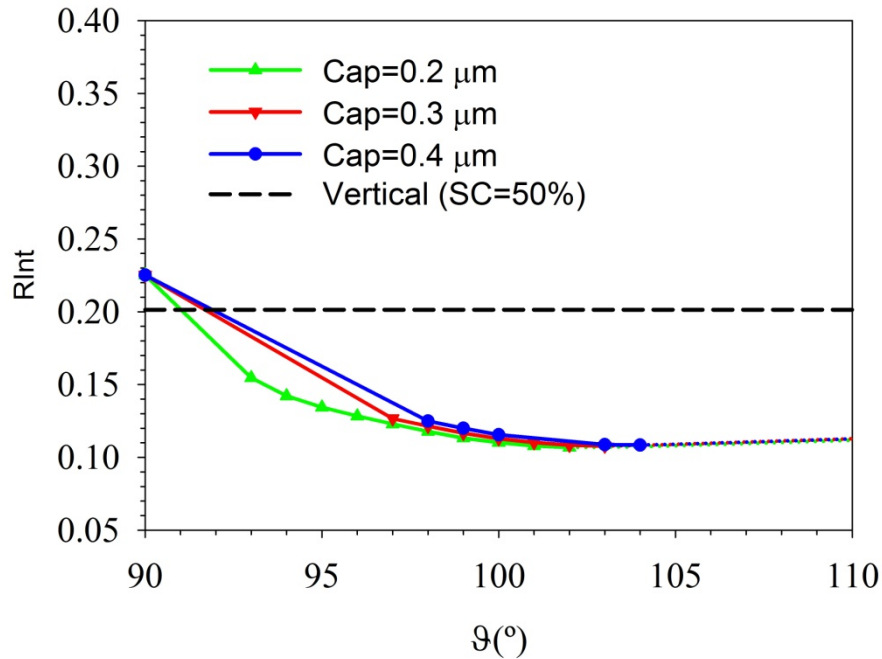


Fig. 4.14. RInt vs. ϑ at SC=30 % varying Cap size for H=2 μm .

From Fig. 4.14, it may be observed that RInt increases as the Cap value increases. Nevertheless, when comparing the RInt values that are presented in Fig. 4.13 with the ones presented in Fig. 4.14, the latter ones are lower. This is due to the impact of H on the performance which was discussed in Section 4.4. The number of multiple reflections increases as H increases which leads to more photon absorption which reduces RInt. Therefore, when H is increased for the same value of Cap the RInt performance is improved.

Additionally, the performance behaviour observed in the case of all Cap values (Cap=0.2 μm , 0.3 μm and 0.4 μm) with H=2 μm , are similar to each other. This similarity is especially pronounced for larger ϑ values when the RInt values for the three lines are close to each other. This similarity is present even when there is no overlap of the pattern. Then, when the pattern is overlapped the performance of the three lines converge. This is a different behaviour than the one observed in the performance for the case of H=1 μm (i.e. Fig. 4.13) where the three lines only converge once the overlap takes place. This distinct RInt behaviour is caused by the difference in the Cap by H (Cap/H)¹¹ ratios. For

¹¹ The Cap/H ratio effectively determines how much of H is occupied by Cap. This ratio may be obtained dividing the value of Cap by the value of H.

example in the case of $H=1\mu\text{m}$, the Cap/H ratios in the cases of $\text{Cap}=0.2\mu\text{m}$ and $0.6\mu\text{m}$ are 20% and 60% respectively. Whereas, in the case of $H=2\mu\text{m}$, the Cap/H ratios in the cases of $\text{Cap}=0.2\mu\text{m}$ and $0.6\mu\text{m}$ are 10% and 30% respectively. Therefore, the Cap/H ratios are not the same and the comparison between Figs. 4.13 and 4.14 is not appropriate, even though similar trend in R_{Int} is observed. Therefore, in order to keep the same Cap/H ratio, the Cap values to be considered for $H=2\mu\text{m}$ are: $\text{Cap}=0.4\mu\text{m}$, $0.6\mu\text{m}$ and $0.8\mu\text{m}$.

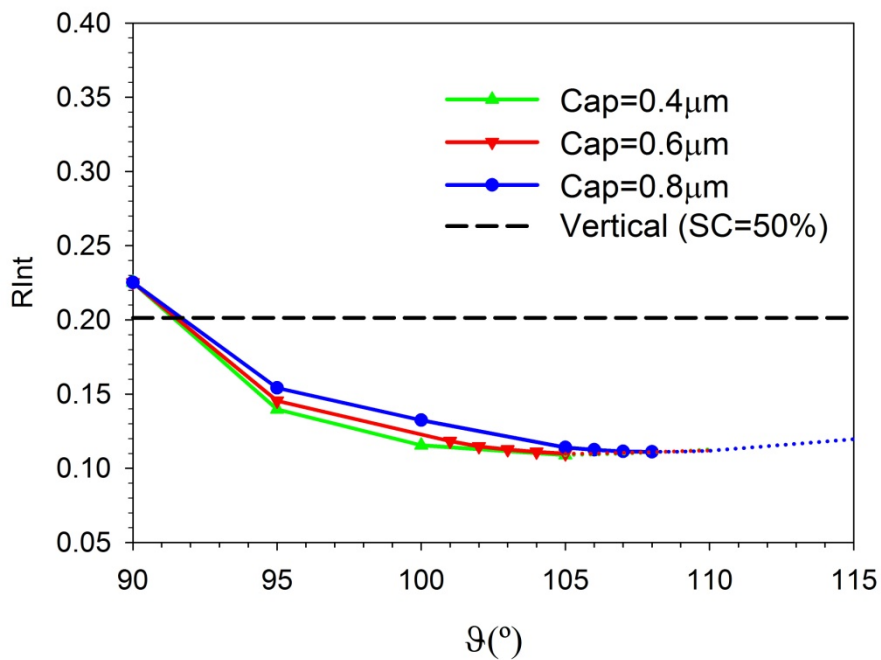


Fig. 4.15. R_{Int} vs. ϑ at $\text{SC}=30\%$ varying Cap size for $H=2\mu\text{m}$.

Figure 4.15 shows the R_{Int} variation with ϑ as Cap varies from $0.4\mu\text{m}$ to $0.8\mu\text{m}$ (Cap/H ratio varies from 20% to 40%) for a fixed value of H ($2\mu\text{m}$) and SC (30%). In Fig. 4.15 the same trend as presented in Figs. 4.13 and 4.14 is followed. Noticeable is the fact that for similar Cap/H ratios (20%, 30% and 40%) Figs. 4.13 and 4.15 are similar in that even before overlap in the pattern the R_{Int} values are quite close.

In Fig. 4.15 the value of R_{Int} reduces as Cap increases. The difference between consecutive R_{Int} values of the three curves is smaller in Fig. 4.15 (i.e. $H=2\mu\text{m}$) than in the case of Fig. 4.13 (i.e. $H=1\mu\text{m}$). Additionally, the convergence of R_{Int} in Fig. 4.15 is achieved for larger values of ϑ than in Fig. 4.13. The reason for

these differences is the sloped part of the hut. For the same value of the Cap/H ratio and ϑ , when H increases there is also an increase in the length of the sloped part of the hut (i.e. increase in $Radius_{bottom}$) as illustrated in Fig. 4.16. This increase affects the area in between huts leading to the difference observed in the R_{Int} performance.

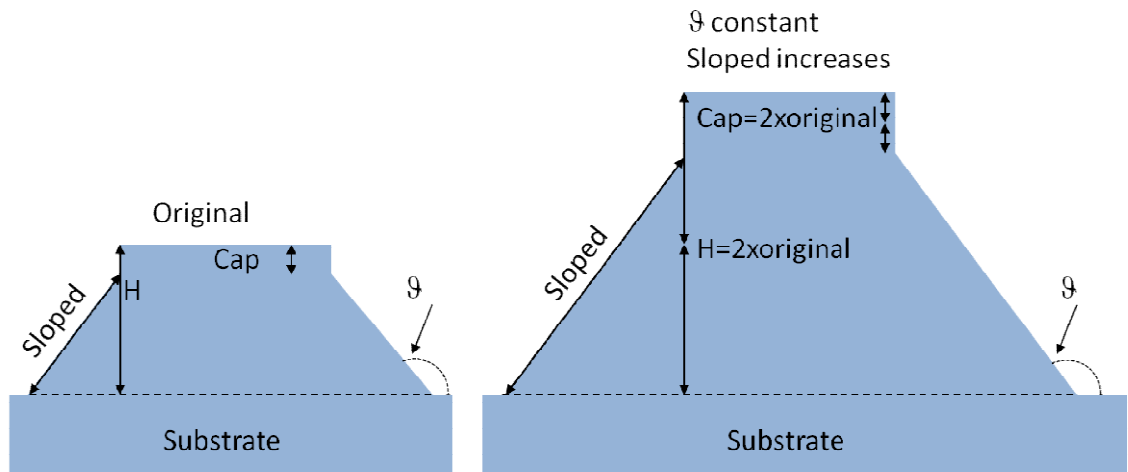


Fig 4.16. Schematic of increase in sloped part as H increases for constant Cap/H ratio.

The discussion about the effect of Cap on the reflection thus far suggests an increase in the reflection, for any given ϑ , as the value of Cap increases. The two cases studied are for $Cap=0.2\mu m$ and $0.0\mu m$ while the remaining structural parameters are kept constant ($Radius_{stop}=0.5\mu m$, $H=1\mu m$, $\vartheta=115^\circ$). The reason for varying SC , rather than ϑ , is to study the effect of varying the area in between huts while keeping constant the angle of incidence on the sloped part of the hut. The results are presented in Fig. 4.17.

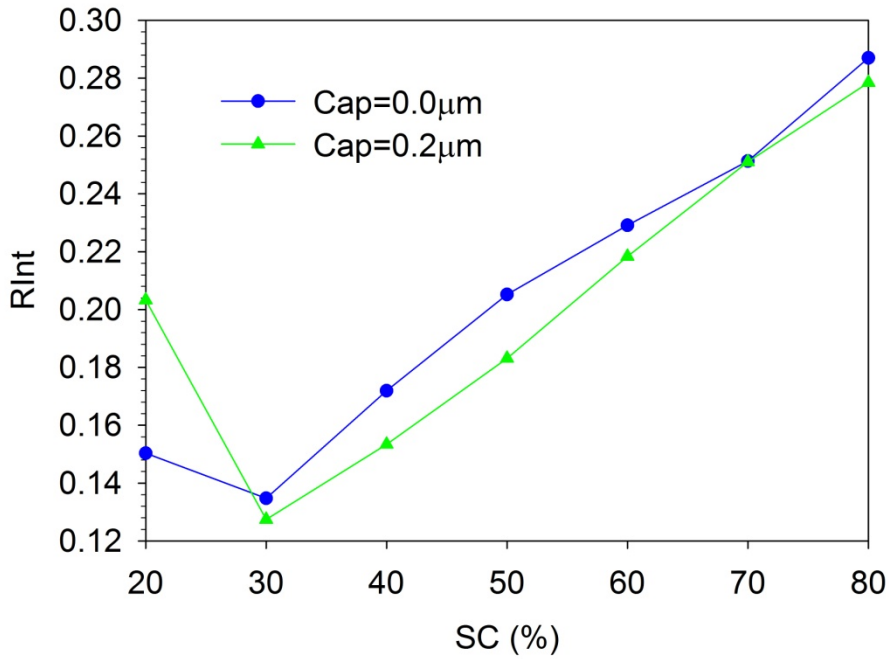


Fig. 4.17. RInt vs. SC curve while varying Cap size for $H=1\mu\text{m}$ and $\vartheta=115^\circ$.

From Fig. 4.17 it may be observed that for SC values larger than 30%, the RInt value is higher in the case of $\text{Cap}=0.0\mu\text{m}$ than in the case of $\text{Cap}=0.2\mu\text{m}$. This finding is not what was expected from the discussion above which indicates that the RInt performance would improve when the value of Cap decreases to zero. However, it is important to recall the discussion about the effect of area in between huts presented in Section 4.3. It was discussed that an optimum range of ϑ provides a lower RInt as the value of SC decreases.

When the value of SC is lower than $\text{SC}=30\%$ the trend changes. Then, the RInt values corresponding to the case of $\text{Cap}=0.2\mu\text{m}$ becomes higher than in the case of $\text{Cap}=0.0\mu\text{m}$. Therefore, the RInt value that can be achieved when the optimum ϑ is found in the case of $\text{Cap}=0.0\mu\text{m}$ and $\text{SC}=20\%$ is lower than in the case of $\text{Cap}=0.2\mu\text{m}$ and $\text{SC}=30\%$. In Figs. 4.18 a, b and 4.19 a, b the E field intensity at a vertical cross section at $\text{SC}=40\%$ and 20% in the cases of $\text{Cap}=0.2\mu\text{m}$, $0.0\mu\text{m}$ are presented to understand the difference in the performance.

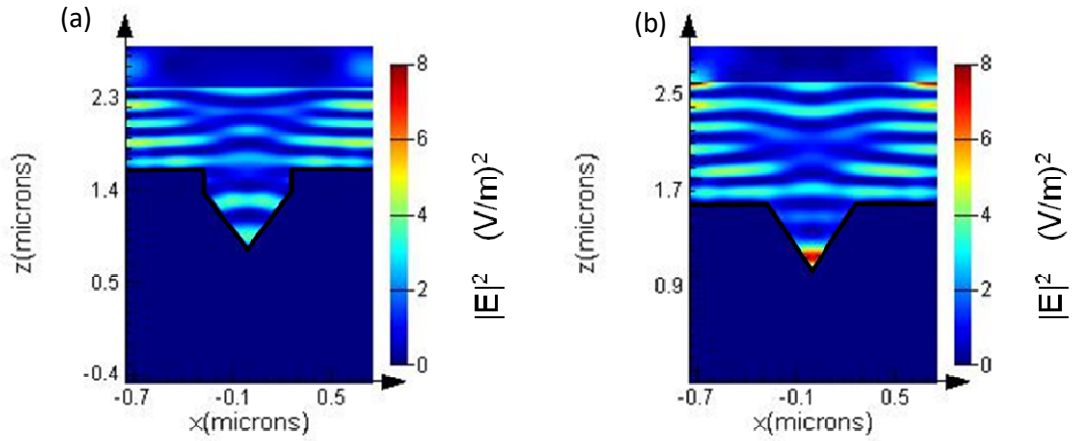


Fig. 4.18. E field intensity at a vertical cross section at SC=40% in the case of a) $Cap = 0.2 \mu m$ and b) $Cap = 0.0 \mu m$.

The comparison of Figs. 4.18 a and b shows that the Eff H of the pattern in the case of $Cap = 0.2 \mu m$ is higher than in the case of $Cap = 0.0 \mu m$ due to an overlap of the pattern. As the value of Cap varies from $Cap = 0.2 \mu m$ to $0.0 \mu m$, for the same value of ϑ , the Radiusbottom in Eq. (2.27) increases. The increase in the value of Radiusbottom for constant distance in between huts leads to an overlap of the pattern. This overlap is the reason why the reflection performance of $Cap = 0.0 \mu m$ is worse than the performance of $Cap = 0.2 \mu m$ for SC=40% in Fig. 4.18 b. The difference in the reflection performance seen in Fig. 4.17 can be identified in Figs. 4.18 b by the stronger E field intensity peaks above the pattern when compared to the Fig. 4.18 a at SC=40%. Additionally, the E field intensity inside the area in between huts is stronger in the case of $Cap = 0.2 \mu m$ than in the case of $Cap = 0.0 \mu m$ at SC=40%. This is a direct consequence of an overlapped pattern.

In Figs. 4.19 a and b the comparison of the E field intensity on the vertical cross section at SC=20% in the cases of $Cap = 0.2 \mu m$ and $0.0 \mu m$ is presented.

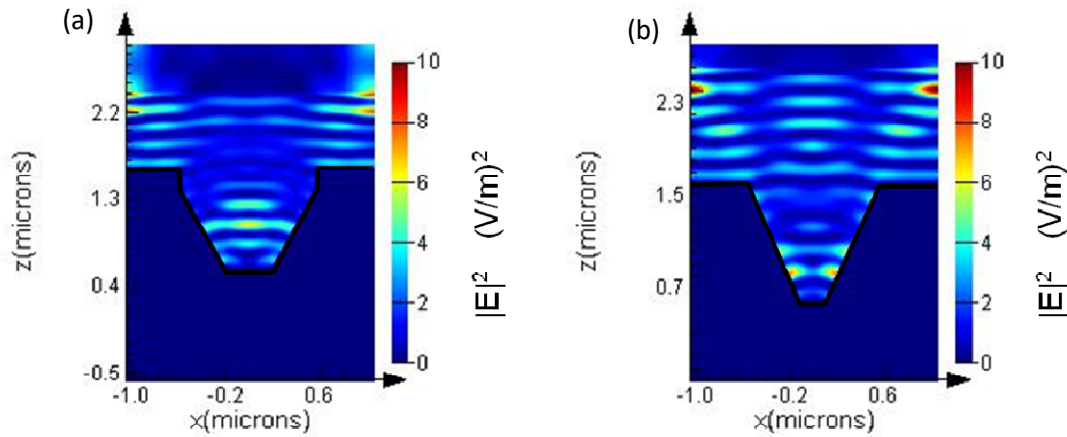


Fig. 4.19. E field intensity at a vertical cross section at SC=20% in the case of
a) Cap= 0.2 μ m and b) Cap= 0.0 μ m.

Figures 4.19 a and b present a different scenario than Figs. 4.18 a and b. Figures 4.19 a and b show that there is no overlap in the two cases. Additionally, the E field intensity above the pattern is lower in the case of Cap = 0.0 μ m than in the case of Cap = 0.2 μ m. This is in line with the discussion presented for Fig. 4.17. Furthermore, the E field intensity inside the area in between huts is higher in the case of Cap = 0.0 μ m than in the case of Cap = 0.2 μ m. As a consequence, when there is no overlap of the pattern, the performance of Cap = 0.0 μ m is better than in the case of Cap = 0.2 μ m.

Therefore, the value of Cap is important when designing the structure: it has a large impact on the performance that can be helpful when adjusting the value of ϑ . As the value of Cap increases, the overlapping of the pattern occurs at larger values of ϑ . This idea should be taken into consideration when designing the pattern with a high SC value. Otherwise, the overlapping of the pattern would minimise any expected benefit in the reflection. However, a larger value of Cap is counter-productive in terms of the reflection. Hence, a low value of Cap is recommended to obtain the best possible reflection performance.

The discussion thus far has explained individually the impact of each of the structural parameters on R_{Int}. There is a large number of parameters impacting the reflection performance. Therefore, it can be difficult to appreciate how best

to choose an optimal set of structural parameters. In the following section a study on the optimum set of ϑ , H, Cap and SC values is presented.

4.7 Identifying an optimum set of parameters

Figure 4.20 shows the R_{Int} as a function of ϑ , SC and Cap. The ϑ value giving the lowest R_{Int} (i.e. optimum value of ϑ) is shown for different SC and H values. Then, the optimum R_{Int} value (y-axis) corresponding to each of the SC and H values is plotted against the optimum value of ϑ (x-axis). The different symbols and colours stand for different H (circle= $1\mu\text{m}$, square= $2\mu\text{m}$ and triangle= $3\mu\text{m}$) and SC (blue= 30%, red= 40% and green= 50%) respectively.

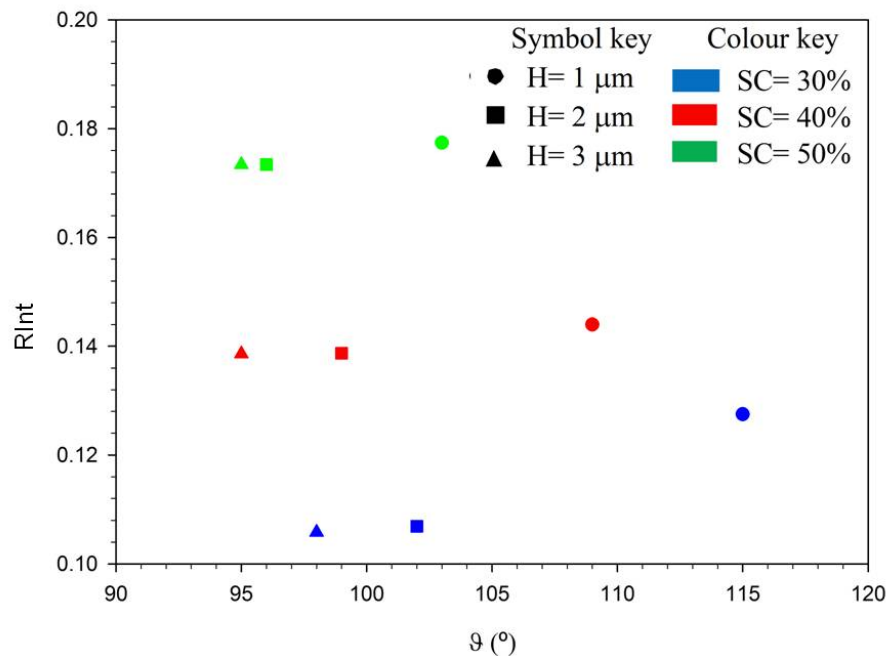


Fig. 4.20. R_{Int} vs Optimum ϑ for different values of H and SC with Cap = $0.2\mu\text{m}$.

In Fig. 4.20, it can be seen how the increase in SC leads to a decrease in the optimum value of ϑ . Further to this, as H increases the difference in the value of optimum ϑ between two consecutive H values reduces. This is applicable to all SC values and it is in line with the discussion presented in Section 4.4. Moreover, for any given height, the optimum ϑ reduces as SC increases. This is in line with the discussion presented in Section 4.3. A useful insight, for fabrication, is the flexibility of the pattern to achieve optimisation for a given H

and Cap. The optimisation can be achieved with two different approaches. One approach is defining an appropriate SC value for the available fabrication equipment and then finding the optimum ϑ . The other approach is defining the ϑ value and then finding the optimum SC value accordingly. Either of these two options will reach the same structure and results.

The optical performance of the hut-like pattern has been extensively discussed through simulation results. The results have shown a very good performance of the pattern. However, sometimes the reproducibility of the texturing patterns designed through simulations is very complicated, if not impossible. This is the reason why it is important to demonstrate the good performance with a fabricated sample of hut-like pattern. In the following section an experimental sample of the hut-like pattern is compared to the equivalent simulated hut-like pattern.

4.8 Proof of concept by experimental results

The fabrication of the hut-like pattern is a challenging task due to its shape. Nevertheless, it is important to compare the simulated performance with the experimental performance as a proof of concept. In the facilities available for the completion of this thesis, there are no fabrication equipments. Therefore, the fabrication and characterization of a sample of this innovative pattern was carried out by our collaborators at University of Bath and the measurement and characterization by another collaborator at London South Bank University.

The fabrication type selected to obtain the sample was dry etching. Dry etching is the process that removes portions from a wafer by applying plasma or etchant gasses. The first step required is to print a mask with the expected pattern. Then, by applying high kinetic energy beams it is possible to etch off the areas not covered by the mask. There is no chemical reaction involved in this process. This means that only the area not covered by the mask will be removed. The dry etching method sometimes offers some disadvantages such as: damaging the substrate [23], contamination [24] and a low throughput for mass production [25].

The resultant experimental sample of the hut-like pattern is shown in Figs. 4.21 and 4.22. The fabrication details to obtain the sample of the hut-like pattern are as follows:

1. The mask is lithographically defined on a Si (100) wafer by the technique of Displacement Talbot Lithography [26].
2. A lift-off process is used to create a regular array of 10-nm thick chrome discs for being used as a mask in the plasma etch process.
3. An SF₆/C₄F₈ is used to create the hut-like using the parameters:
 - 20W RIE
 - 1200 W ICP
 - 5/55 sccm gas ratio
 - Pressure 10 mTorr

The etching rate to obtain the pattern is about 50 nm/min with a 100 V biasing for H=1 μ m hut-like pattern.

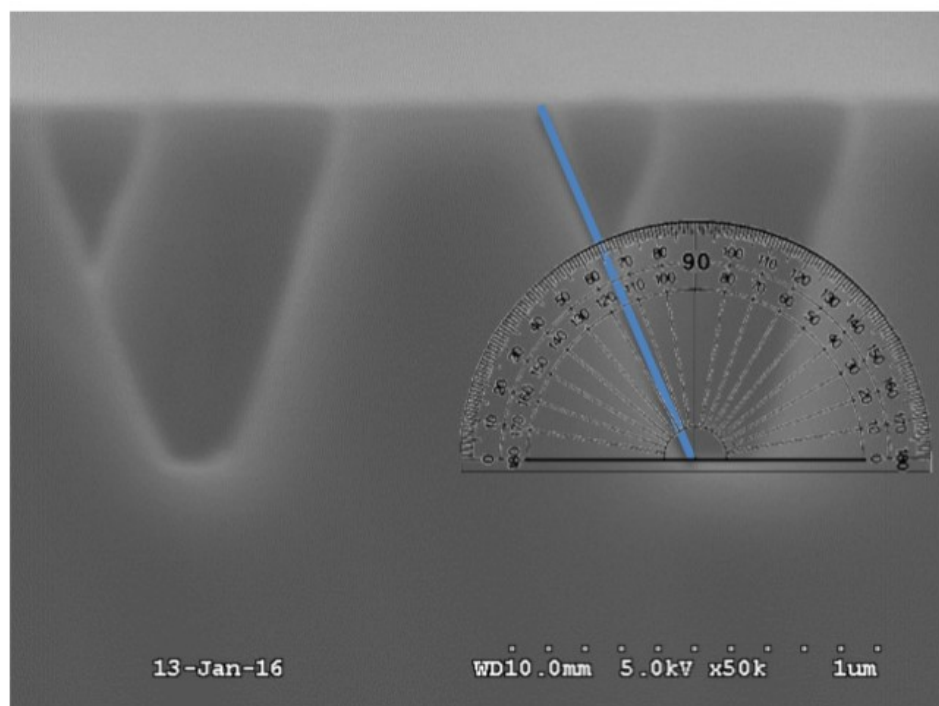


Fig. 4.21. Cross-section SEM image of after 20 mins etching showing $\theta=124^\circ$.

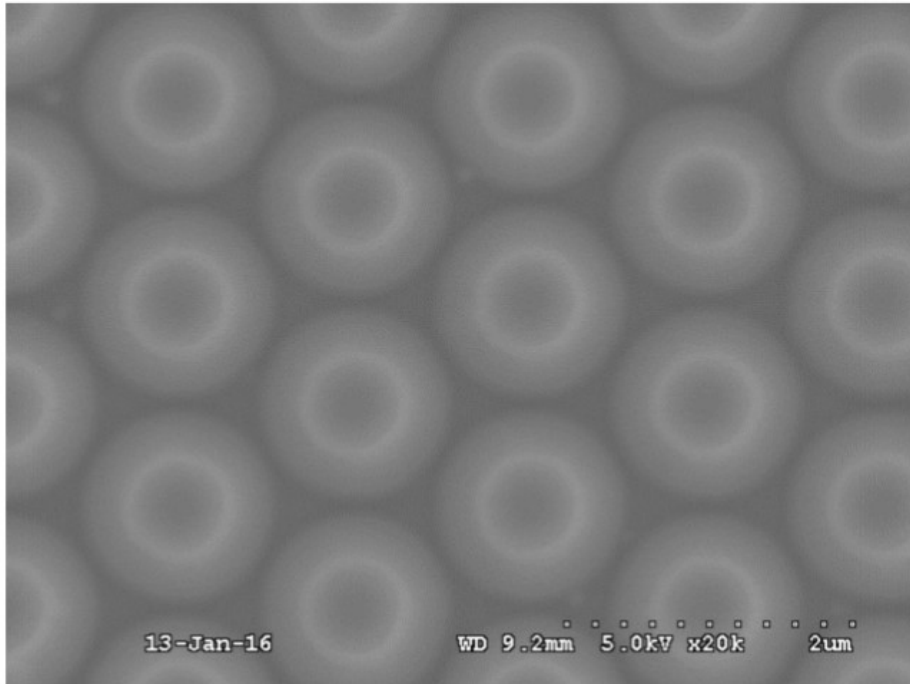


Fig. 4.22. Planar SEM image of after 20 mins etching.

From Figs. 4.21 and 4.22 it may be noticed that no Cap has been included in the pattern. The reason for this is the complexity that it would add to the fabrication process. Additionally, as discussed in Section 4.6, the effect of Cap on the performance is negative. When the value of Cap is minimized or made 0, the performance improves.

In terms of θ , there were some limitations to obtain a range of values. The value of θ was limited to 124° . Then, through simulations, the optimum SC to obtain a good performance was defined as 22.5% and the sample was fabricated accordingly. Additionally, as it may be noticed from Figs. 4.21 and 4.22 there is some level of surface roughness in the vertical cross section of the pattern (i.e. Fig. 4.21). This is due to the dry etching process. Nevertheless, in the horizontal cross section of the pattern (i.e. Fig. 4.22), each of the pillars has a very smooth circular shape. This is considered to be appropriate to achieve a good performance.

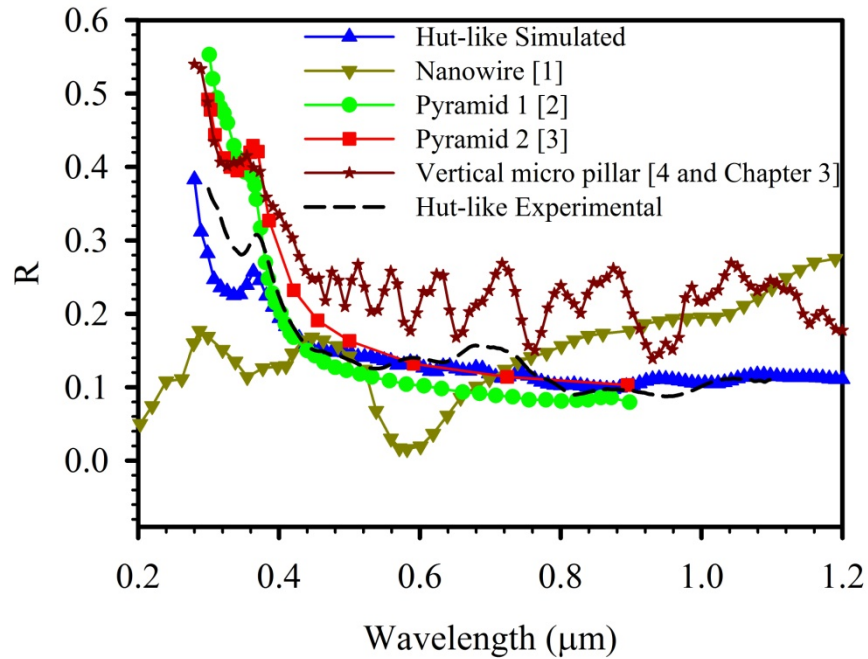


Fig. 4.23. R vs. wavelength curve comparison between the hut-like structure ($D= 1\mu\text{m}$, $H= 1\mu\text{m}$ and $\theta=115^\circ$) including experimental results with other texturing patterns of similar dimensions.

Figure 4.23 presents the comparison of the hut-like pattern with other patterns (i.e. nanowires [1], pyramids [2, 3] and micro pillar array [4]) with the inclusion of measurement of the experimental hut-like pattern. The performance of the experimental hut-like pattern follows the same trend as the simulated performance. This means that its R is lower in the entire spectrum than the micro pillar array. It is important to highlight that it performs better than nanowire and pyramids in the longer and shorter wavelength ranges respectively as discussed in Section 4.2. Additionally, the pattern not only improves the reflection performance but also provides other benefits. For example, the low surface-to-volume ratio predicts a low surface recombination. In texturing patterns the surface recombination worsens the electrical performance of patterns with good optical performance.

The limitations on the fabrication process have not enabled the reproducibility at a large scale. In the future, the fabrication process will be improved together with the collaborators to reach large scale fabrication.

4.9 Summary

The discussion of the optical performance of the hut-like pattern has shown a superior performance compared to other texturing patterns with similar dimensions. To understand the performance of the pattern a study on the effect of some key structural parameters has been carried out. These parameters are: Surface Coverage (SC), θ , area in between huts, Height (H), Diameter (D) and Cap. Some of the results presented in this chapter have been included in a journal article published by the author [27].

The hut-like pattern enables a better reduction of the reflection compared to the micro pillar array. For example, the photon absorption is higher than in the case of a micro pillar array due to two factors. One factor is the higher absorption on the slope part of the hut due to a lower angle of incidence. The other factor is the better optimisation of the photon absorption caused by multiple reflections. The effect of these factors is determined by θ and SC according to which the photon absorption varies.

When the value of θ varies the angle of incidence of the incoming light changes as well. Furthermore, when θ is set to its optimum value for a given SC, D and H, then the reflection is the lowest. Therefore, it is very important to find the optimum value. For the results presented in this work, the optimum value of θ was found by running simulations with a θ step of 1° . This was a challenging task due to the large number of simulations to be run.

When the value of SC varies the angle of incidence of the incoming light does not change. It is the area in between huts that changes which affects the light trapping capacity of the pattern. Furthermore, it is important to highlight the importance of the relationship between the value of SC and θ . For each value of SC there is some θ value that can optimize the photon absorption through multiple reflections.

Another parameter that affects the performance differently from the micro pillar array is H. When the value of H increases the reflection reduces. However,

when the value of H is sufficiently high, the effect of H diminishes significantly. Therefore, to achieve the best performance for given SC , ϑ , and D , the value of H is smaller than in the case of texturing patterns such as micro pillar arrays. This leads to a low surface-to-volume ratio for a given SC , ϑ , and D . A high surface-to-volume ratio is conventionally linked to high surface recombination which is a major limitation of texturing patterns. Therefore, a low surface-to-volume ratio is a very important advantage of the pattern.

The value of D also has an effect on the performance of the pattern. As D increases the reflection increases which indicates that lower D is preferred for better performance. Additionally, the larger D the smaller the difference in the reflection as ϑ increases. However, when ϑ approaches the optimum range of values, the difference in the reflection becomes larger as D increases. Therefore, when targeting the optimum ϑ in the fabrication process, using low precision equipment, any slight mistake in ϑ would lead to a below optimum performance. For small values of D inaccuracy in targeting optimum ϑ would lead to a performance similar to the expected one. Although fabrication tolerance for smaller values of D will also play a part since it may limit the size of the hut-like pillars.

The impact of Cap on the performance is not positive. The analysis of the performance as Cap varies suggests that as Cap decreases to zero, the reflection performance would improve. However, Cap may offer some advantages as well. The larger the value of Cap the wider the range of ϑ values becomes (causing no overlap of the pattern). This means that in the design/fabrication process, it is possible to adjust the value of ϑ with more freedom. This might be useful in some cases where the precision of the equipment is low.

The simulations on the effect of Cap highlighted the difference in the sloped part of the hut-like pattern when Cap is reduced. This difference is a major factor in obtaining a lower reflection as Cap reduces. However, the chance of obtaining an overlapped pattern increases when the value of Cap is very small. As the value of Cap decreases for a constant ϑ and Cap/H ratio the sloped part

increases. As a consequence, the distance in between the huts has to be large enough to avoid the overlap (i.e. low SC).

The fabrication of the hut-like pattern is a challenging task. The nature of this thesis is simulation based. Therefore, the fabrication process and the characterization of the pattern had to be done by a group of collaborators. The hardest part of the fabrication process, encountered by the collaborators, was making a smooth and circular hut-like pattern structure. To achieve this, the dry plasma etching process was implemented successfully. The reproducibility of the hut-like pattern was confirmed with the fabrication of a circular hut-like pillar. The fabricated sample included no Cap due to an easier fabrication process together with simulated results supporting a better performance.

The benefits in the reflection of texturing the hut-like pattern on a solar cell surface have been presented in depth in this chapter. The discussion has analysed results obtained mainly through simulations but also from experiments. Additionally, a comparison with other texturing patterns supports the excellent performance of the pattern. Nevertheless, there are still some unanswered factors regarding the performance of the hut-like pattern such as the electrical performance. Moreover, the confirmation of a low surface recombination and high conversion efficiency would support the establishment of the pattern in the field. These questions could not be part of this thesis due to time constraints. However, these factors should be analysed in further works in the future. A summary of further work is presented in the following chapter.

4.10 References

1. Wang, J., Li, Z., Singh, N., and Lee, S., (2011), "*Highly-ordered vertical Si nanowire/nanowall decorated solar cells*", Optics Express, Vol. 19, pp. 23078-23084.
2. Hou, Y., Abrams, B. L., Vesborg, P. C. K., Bjorketunm, M. E., Herbst, K., Bech, L., Seger, B., Pedersen, T., Hansen, O., Rossmeisl, J., Dahl, S., Norkov, J. K., and Chorkendorff, I., (2012), "*Photoelectrocatalysis and electrocatalysis on silicon electrodes decorated with cubane-like clusters*", Journal of Photonics for Energy, Vol. 2, pp. 026001.
3. Papet, P., Nichiporuk, O., Kaminski, A., Rozier, Y., Kraiem, J., Lelievre, J. F., Chaumartin, A., Fave, A., and Lemiti, M., (2006), "*Pyramidal texturing of silicon solar cell with TMAH chemical anisotropic etching*", Solar Energy Materials and Solar Cells, Vol. 90, pp. 2319-2338.
4. Cabrera-Espana, F. J., Rahman, B. M. A., and Agrawal, A., (2014), "*Study of optical properties of textured Si solar cell with micro pillars*", In Proceedings of Optical Wave and Waveguide Theory and Numerical Modeling workshop, pp. 13.
5. Dan, Y., Seo, K., Takei, K., Meza, J. H., Javey, A., and Crozier, K. B., (2011), "*Dramatic Reduction of Surface Recombination by in Situ Surface Passivation of Silicon Nanowires*", Nano Letters, Vol. 11, pp. 2527-2532.
6. Shin, J., Chanda, D., Chern, W., Yu, K. J., Rogers, J. A., and Li, X., (2012), "*Experimental study of design parameters in silicon micropillar array solar cells produced by soft lithography and metal-assisted chemical etching*", IEEE Journal of Photovoltaics, Vol. 2, No. 2, pp.129-133.
7. Baker-Finch, S., and McIntosh, K., (2011), "*Reflection of normally incident light from silicon solar cells with pyramidal texture*", Progress in Photovoltaics, Vol. 19, No. 4, pp. 406–416.
8. Mallorqui, A., Epple, F. M., Fan, D., Demichel, O., and Fontcuberta i Morral, A., (2012), "*Effect of the pn junction engineering on Si microwire-array solar cells*", Physica Status Solidi A, Vol. 209, No. 3, pp. 1588-1591.
9. Garnett, E., and Yang, P., (2010), "*Light trapping in silicon nanowire solar cells*", Nano Letters, Vol. 10, pp. 1082-1087.
10. Wang, X., and Wang, Z-M., (2014), "*High-Efficiency Solar Cells*", Springer, Heidelberg.

11. Muller, J., Rech, B., Springer, J., and Vanecek, M., (2004), "*TCO and light trapping in silicon thin film solar cells*", Solar Energy, Vol. 77, pp. 917–930.
12. Campbell, P., and Green, M. A., (1987), "*Light trapping properties of pyramidally textured surfaces*", Journal of Applied Physics, Vol. 62, pp. 243.
13. Al-Amin, M., and Assi, A., (2013), "*Efficiency improvement of crystalline silicon solar cells*" in Mendez-Vila, A., (Eds.) "*Materials and processes for energy: communicating current research and technological developments*", Formatex research center, Badajoz.
14. Zhu, J., Yu, Z., Burkhard, G. F., Hsu, C., Connor, S. T., Xu, Y., Wang, Q., McGehee, M., Fan, S., and Cui, Y., (2009), "*Optical absorption enhancement in amorphous silicon nanowire and nanocone arrays*", Nano Letters, Vol. 9, No. 1, pp. 279-282.
15. Sivasubramaniam, S., and Alkaisi, M. M., (2014), "*Inverted nanopyramid texturing for silicon solar cells using interference lithography*", Microelectronic Engineering, Vol. 119, pp. 146-150.
16. Toor, F., Branz, H. M., Page, M. R., Jones, K. M., and Yuan, H-C., (2011), "*Multi-scale surface texture to improve blue response of nanoporous black silicon solar cells*", Applied Physics Letters, Vol. 99, pp.103501.
17. Li, H. F., Jia, R., Chen, C., Xing, Z., Ding, W., Meng, Y., Wu, D., Liu, X., and Ye, T., (2011), "*Influence of nanowires length on performance of crystalline silicon solar cell*," Applied Physics Letters, Vol. 98, pp. 151116.
18. Chappell, T. I., (1979), "*The V-groove multijunction solar cell*," IEEE Transaction on Electron Devices, Vol. 26, No. 7, pp. 1091-1097.
19. Glunz, S. W. Preu, R., and Biro, D., (2012), "*Crystalline silicon solar cells: State-of-the-art and future developments*", Comprehensive Renewable Energy, Elsevier, Vol. 1, pp. 353-387.
20. Kafle, B., Trogus, D., Dresler, B., Köhler, D., Mäder, G., Clochard, L., Duffy, E., Hofmann, M., and Rentsch, J., (2013), "*Industrial screen-printed solar cells with novel atmospheric pressure dry texturing process*", Proceedings of the 28th European Photovoltaic Solar Energy Conference, Paris, pp. 1344-1350.
21. Lee, J-Y., and Lee, S-H., (2004), "*Application of various surface passivation layers in solar cells*", Journal of the Korean Physical Society, Vol. 45, No. 2, pp. 558-563.

22. Lu, N., (2010), "*Theoretical studies of H-passivated silicon nanowires, silicon surface systems and silicon/germanium core/shell nanowires*", PhD Thesis Iowa State University.
23. Yoo, J., Kim, K., Thamilselvan, M., Lakshminarayn, N., Kim, Y-K., Lee, J., Yoo, K-J., and Yi, J., (2008), "*RIE texturing optimization for thin c-Si solar cells in SF₆/O₂ plasma*", Journal of Physics D: Applied Physics, Vol. 41, No. 12, pp. 125205-125211.
24. Tucci, M., Serenelli, L., Iulii, S., De, Salza, E., and Pirozzi L. (2006), "*Dry NF₃/O₂ plasma texturing of multicrystalline silicon*", Proceeding of the 21st European Photovoltaic Solar Energy Conference, pp.1250.
25. Saito, Y., Kubota, A., Iwama, S., and Watanabe, R., (2014), "*Random-Texturing of Phosphorus-Doped Layers for Multi-Crystalline Si Solar Cells by Plasmaless Dry Etching*", Modern Applied Science, Vol. 8, No. 4, pp. 8.
26. Solak, H. H., Dais, C., and Clube, F., (2011), "*Displacement Talbot lithography: a new method for high-resolution patterning of large areas*", Optics Express, Vol. 19, No. 11, pp. 10686.
27. Cabrera-España, F.J., and Agrawal, A., (2016), "*Hut-like pillar array Si solar cells*", Solar Energy, Vol. 132, pp. 357-362.

Chapter 5: Conclusions and recommendations for further work

5.1 Introduction

This study aimed at reducing reflection from the solar cell surface. This aspect is key for the further development of the field which eventually will enhance the deployment of solar cells for residential and commercial purposes. This research has investigated two texturing patterns: micro pillar array and hut-like pattern. In this chapter, the main findings of this research are revisited. Additionally, recommendations for further work are presented.

5.2 Summary of the research

In this work the analysis of two texturing patterns is carried out based on FDTD simulations. The key structural parameters of the micro pillar array discussed in Chapter 3 are as follows:

- Height (H)
- Diameter (D)
- Surface Coverage (SC)
- Height by diameter ratio (H/D ratio)

From the analysis on the micro pillar array texturing pattern it is concluded that the reflection decreases with the value of H increasing. The reflection also increases with the value of D. Therefore, a small value of D is preferred for lower reflection. However, this can have implications for fabrication. Furthermore, I found that variation in SC produces change in the reflection due to change in the amount of incident light penetrating in between pillars and multiple reflections that optimize trapping/absorption of this light. I found that there is an optimum value of SC for a given H and D. This study also examined the impact of H/D ratio on the optical performance. I found that increase in H/D ratio leads to a decrease in reflection and for all D values the reflection converges for sufficiently large H/D.

The key structural parameters of the hut-like pattern discussed in Chapter 4 are as follows:

- Height (H)
- Diameter (D)
- Cap
- ϑ
- Surface Coverage (SC)
- Cap by height ratio (Cap/H ratio)
- Radiusbottom

From the analysis on the hut-like texturing pattern it is concluded that this pattern offers lower reflection than nanowires, pyramids and micro pillar arrays. This occurs due to improved absorption on the sloped part of the hut in addition to optimized multiple reflections/trapping in between the huts. In addition the surface-to-volume ratio of the hut-like structures is lower than the other patterns mentioned. Therefore, I expect a lower surface recombination and better electrical performance from solar cells with this pattern.

The dependence of the reflection on the structural parameters was also examined in detail. I found that the light penetrating in between huts depends on the area in between the huts which is a complex function of ϑ , SC, Cap and Radiusbottom for a given H. Increase in the value of H leads to reduction in reflection. However, further increase of a sufficiently large value of H the improvement in the reflection performance diminishes. For each value of SC there is an optimum ϑ that optimizes the photon absorption through multiple reflections. The reflection increases with D which indicates that lower value of D is preferable. Additionally, for smaller values of D reflection is less dependent in change in ϑ . I found that smaller values of Cap lead to better performance. However, when SC is large Cap can be used to prevent overlap in the pattern over a larger range of ϑ .

In the following section I discuss the scope for future work.

5.3 Recommendations for further work

Based on the results presented, there are some aspects worth exploring to improve the performance of textured solar cells.

To study the effect of D on reflection to identify an optimum range which is compatible with low cost fabrication.

To study the optical and electrical performances of both the micro pillar array and the hut-like pattern. There are examples of texturing patterns that offer good optical performance but the electrical performance needs improvement. It would be useful to determine the electrical performance of these two patterns as a function of H/D ratio.

A detailed understanding of how Cap affects the overlap of the pattern and reflection is needed to identify the parameter range for which fabrication would be feasible. Different crystalline materials would have different refractive indices and each would have specific θ at which the structure would be etched. Therefore, Cap , SC and H could be used to optimize multiple reflections in the hut-like textured array for that material. There would need to be a good understanding of fabrication tolerance on all these parameters.

Our simulations show that the hut-like pattern offers clear advantage in optical performance. We have not studied the electrical performance of this pattern which would be an important future work for comprehensive performance analysis of this pattern.

To show experimentally the electrical convergence efficiency of cells with the hut-like pattern, fabrication of sufficiently large samples from which solar cells can be fabricated is needed. The samples fabricated by our collaborators were not large enough in size to characterize a full solar cell. Furthermore, a detailed understanding of the impact of fabrication tolerance on the performance was not possible.

Appendix A

Finite differences

Conventionally the definition of a derivative is expressed as follows:

$$u'(x) = \lim_{\Delta x \rightarrow 0} \frac{u(x + \Delta x) - u(x)}{\Delta x} \quad (\text{A.1})$$

where $u(x)$ is a function dependent on x , $u'(x)$ is its first derivative and Δx is the step size.

Finite difference approximation is a manner of simplifying the calculation process of derivatives. For very small Δx values, any derivative at a specific point (A) can be expressed in terms of a simple difference. This difference should be between the values at two points adjacent to point A (to achieve first or second order approximation). Depending on what points are selected for the approximation, the order of accuracy will change accordingly. There are three options: Forward difference, Backward difference and Central difference.

Forward difference

The forward finite difference consists in approximating the derivative at a node by calculating the difference between the current and the next step. This can be defined as follows:

$$u'(x_i) \approx \frac{u(x_i + \Delta x) - u(x_i)}{\Delta x} = \frac{u_{i+1} - u_i}{\Delta x} \quad (\text{A.2})$$

The forward finite difference can be expanded as a Taylor series as follows [5]:

$$u(x_i + \Delta x_i) = u(x_i) + \Delta x_i \left. \frac{\partial u}{\partial x} \right|_{x_i} + \frac{\Delta x_i^2}{2!} \left. \frac{\partial^2 u}{\partial x^2} \right|_{x_i} + \frac{\Delta x_i^3}{3!} \left. \frac{\partial^3 u}{\partial x^3} \right|_{x_i} + \dots \quad (\text{A.3})$$

After truncating the Taylor expansion and keeping only the first two terms (up to the term with the first derivative), Eq. (A.3) can be expressed as:

$$\frac{u(x_i + \Delta x_i)}{\Delta x_i} = \frac{u(x_i)}{\Delta x_i} + \left. \frac{\partial u}{\partial x} \right|_{x_i} + O(\zeta) \quad (\text{A.4})$$

where $O(\zeta) = \frac{\Delta x_i}{2!} \left. \frac{\partial^2 u}{\partial x^2} \right|_{\zeta}$ represents the truncation error of approximation which

may be neglected. Therefore, it is possible to say that the approximation is

accurate in $O(\Delta_x)$. This leads to the forward finite difference to be considered as a first order approximation [5]. By rearranging Eq. (A.4) the forward difference approximation (Eq. (A.2)) may be obtained as follows:

$$\left. \frac{\partial u}{\partial x} \right|_{x_i} = \frac{u(x_i + \Delta_{x_i}) - u(x_i)}{\Delta_{x_i}} + O(\zeta) \quad (\text{A.5})$$

This approximation is considered to be more accurate as Δ_x becomes smaller. In the following section the backward difference is discussed.

Backward difference

The backward finite difference consists in approximating the derivative at a node by calculating the difference between the current and the previous step. This is defined as follows:

$$u(x_i) \approx \frac{u(x_i) - u(x_i - \Delta_x)}{\Delta_x} = \frac{u_i - u_{i-1}}{\Delta_x} \quad (\text{A.6})$$

The backward finite difference can be expanded as a Taylor series as follows:

$$u(x_i - \Delta_{x_{i-1}}) = u(x_i) - \Delta_{x_{i-1}} \left. \frac{\partial u}{\partial x} \right|_{x_i} + \frac{\Delta_{x_{i-1}}^2}{2!} \left. \frac{\partial^2 u}{\partial x^2} \right|_{x_i} + \frac{\Delta_{x_{i-1}}^3}{3!} \left. \frac{\partial^3 u}{\partial x^3} \right|_{x_i} + \dots \quad (\text{A.7})$$

After truncating the Taylor expansion and keeping only the first two terms (up to the term with the first derivative), Eq. (A.7) can be expressed as:

$$\frac{u(x_i - \Delta_{x_{i-1}})}{\Delta_{x_{i-1}}} = \frac{u(x_i)}{\Delta_{x_{i-1}}} - \left. \frac{\partial u}{\partial x} \right|_{x_i} + O(\zeta) \quad (\text{A.8})$$

where $O(\zeta) = \frac{\Delta_{x_{i-1}}}{2!} \left. \frac{\partial^2 u}{\partial x^2} \right|_{\zeta}$ represents the truncation error of approximation which

may be neglected. This approximation is accurate in $O(\Delta_x)$. Therefore, the backward difference approximation is considered as first order approximation.

By rearranging Eq. (A.8) the backward difference approximation (Eq. (A.16)) may be obtained as follows:

$$\frac{u(x_i) - u(x_i - \Delta_{x_{i-1}})}{\Delta_{x_{i-1}}} + O(\zeta) = \left. \frac{\partial u}{\partial x} \right|_{x_i} \quad (\text{A.9})$$

In the following section of this appendix the central difference approximation is discussed.

Central finite difference

The central finite difference is a combination of the forward and backward finite difference. It may be obtained from subtracting Eq. (A.6) (backward) from Eq. (A.2) (forward). It consists in approximating the derivative at a node by calculating the difference between half step size before and the half step size after the node. This is defined as follows:

$$u'(x_i) \approx \frac{u(x_i + \Delta_x) - u(x_i - \Delta_x)}{2\Delta_x} = \frac{u_{i+1} - u_{i-1}}{2\Delta_x} \quad (\text{A.10})$$

The central finite difference can be expanded as a Taylor series as follows:

$$\frac{1}{\Delta_{x_i} + \Delta_{x_{i-1}}} \left[\frac{\Delta_{x_{i-1}}}{\Delta_{x_i}} \frac{u(x_i + \Delta_{x_{i+1}}) - u(x_i)}{\Delta_{x_i}} + \frac{\Delta_{x_i}}{\Delta_{x_{i-1}}} \frac{u(x_i) - u(x_i + \Delta_{x_{i-1}})}{\Delta_{x_{i-1}}} \right] - \frac{\partial u}{\partial x} \Big|_{x_i} = \frac{\Delta_{x_{i-1}} \Delta_{x_i}}{3!} \frac{\partial^3 u}{\partial x^3} \Big|_{x_i} + \dots \quad (\text{A.11})$$

If $\Delta_{x_{i-1}} = \Delta_{x_i} = \Delta x$ then Eq. (A.11) simplifies to:

$$\frac{1}{2\Delta x} (u(x_i + \Delta_{x_{i+1}}) - u(x_i + \Delta_{x_{i-1}})) - \frac{\partial u}{\partial x} \Big|_{x_i} = \frac{\Delta_x^2}{3!} \frac{\partial^3 u}{\partial x^3} \Big|_{x_i} + \dots \quad (\text{A.12})$$

By rearranging Eq. (A.12) and keeping the terms up to the first derivative, the central finite difference approximation (Eq. (A.10)) may be obtained:

$$\frac{\partial u}{\partial x} \Big|_{x_i} = \frac{1}{2\Delta_x} (u(x_i + \Delta_{x_{i+1}}) - u(x_i + \Delta_{x_{i-1}})) + O(\zeta) \quad (\text{A.13})$$

where $O(\zeta) = \frac{\Delta_x^2}{3!} \frac{\partial^3 u}{\partial x^3} \Big|_{x_i}$ is the truncation error of the central difference

approximation. This approximation is accurate in $O(\Delta_x^2)$. Hence, the central finite difference approximation is second order accurate.

Appendix B

Derivation of FDTD method

The derivation of the FDTD method presented in this section is in 3D and it uses central finite difference approximation. The calculation begins with the differential form of the Maxwell's equations for a lossless, dielectric medium (Eq. (B.1)-(B.7)) as follows:

Faraday's law:

$$\frac{d\vec{B}}{dt} = -\nabla \times \vec{E} - \vec{M} \quad (\text{B.1})$$

where B is the magnetic flux density, E is the electric field and M is the magnetic current density.

Ampere's law:

$$\frac{d\vec{D}}{dt} = \nabla \times \vec{H} - \vec{J} \quad (\text{B.2})$$

where D is the electric current density, H is the magnetic field and J is the electric current density.

Gauss's law for electric field:

$$\nabla \cdot \vec{D} = \rho \quad (\text{B.3})$$

where ρ is the volume charge density.

Gauss's law for magnetic field:

$$\nabla \cdot \vec{B} = 0 \quad (\text{B.4})$$

The continuity of the current has the following expression:

$$\nabla \cdot \vec{J} = -\frac{\delta \rho}{\delta t} \quad (\text{B.5})$$

The constitutive relations for the media are as follows:

$$\vec{D} = \epsilon \vec{E} = \epsilon_r \epsilon_0 \vec{E} \quad (\text{B.6})$$

$$\vec{B} = \mu \vec{H} = \mu_r \mu_0 \vec{H} \quad (\text{B.7})$$

where ε is the electric permittivity, ε_r is the relative permittivity, ε_0 is the free-space permittivity, μ is the magnetic permeability, μ_r is the relative permeability and μ_0 is the free-space permeability.

To solve the curl of E in Eq. (B.1) the following has to be solved:

$$\begin{aligned} \nabla \times \vec{E} &= \begin{vmatrix} \hat{x} & \hat{y} & \hat{z} \\ \frac{d}{dx} & \frac{d}{dy} & \frac{d}{dz} \\ E_x & E_y & E_z \end{vmatrix} = \\ &= \hat{x} \left(\frac{d\vec{E}_z}{dy} - \frac{d\vec{E}_y}{dz} \right) - \hat{y} \left(\frac{d\vec{E}_z}{dx} - \frac{d\vec{E}_x}{dz} \right) + \hat{z} \left(\frac{d\vec{E}_y}{dx} - \frac{d\vec{E}_x}{dy} \right) \end{aligned} \quad (\text{B.8})$$

Therefore,

$$\frac{d\vec{B}}{dt} = - \left(\hat{x} \left(\frac{d\vec{E}_z}{dy} - \frac{d\vec{E}_y}{dz} \right) - \hat{y} \left(\frac{d\vec{E}_z}{dx} - \frac{d\vec{E}_x}{dz} \right) + \hat{z} \left(\frac{d\vec{E}_y}{dx} - \frac{d\vec{E}_x}{dy} \right) \right) - \vec{M} \quad (\text{B.9})$$

$$\frac{d\vec{H}}{dt} = - \frac{1}{\mu} \left(\hat{x} \left(\frac{d\vec{E}_z}{dy} - \frac{d\vec{E}_y}{dz} \right) - \hat{y} \left(\frac{d\vec{E}_z}{dx} - \frac{d\vec{E}_x}{dz} \right) + \hat{z} \left(\frac{d\vec{E}_y}{dx} - \frac{d\vec{E}_x}{dy} \right) + \vec{M} \right) \quad (\text{B.10})$$

where M is considered to be the magnetic source. However, in order to enable materials with isotropic and nondispersive magnetic losses (causing an attenuation of the magnetic field via conversion to heat energy) the following relation is to be applied:

$$\vec{M} = \vec{M}_{\text{source}} + \sigma^* \vec{H} \quad (\text{B.11})$$

where M is the magnetic current density, M_{source} is the magnetic field source and σ^* is the magnetic loss

Hence, the different field components of the magnetic field can be represented:

$$\begin{aligned} \frac{dH_x}{dt} &= - \frac{1}{\mu} \left(\frac{dE_z}{dy} - \frac{dE_y}{dz} \right) - \frac{1}{\mu} (M_{\text{source}} + \sigma^* H_x) = \\ &= \frac{1}{\mu} \left(\frac{d\vec{E}_y}{dz} - \frac{d\vec{E}_z}{dy} \right) - \frac{1}{\mu} (\vec{M}_{\text{source}} + \sigma^* \vec{H}_x) \end{aligned} \quad (\text{B.12})$$

$$\begin{aligned}\frac{d\vec{H}_y}{dt} &= \frac{1}{\mu} \left(\frac{d\vec{E}_z}{dx} - \frac{d\vec{E}_x}{dz} \right) - \frac{1}{\mu} (\vec{M}_{\text{source}} + \sigma^* \vec{H}_y) = \\ &= \frac{d\vec{H}_y}{dt} = \frac{1}{\mu} \left(\frac{d\vec{E}_z}{dx} - \frac{d\vec{E}_x}{dz} \right) - \frac{1}{\mu} (\vec{M}_{\text{source}} + \sigma^* \vec{H}_y)\end{aligned}\quad (\text{B.13})$$

$$\begin{aligned}\frac{d\vec{H}_x}{dt} &= -\frac{1}{\mu} \left(\frac{d\vec{E}_y}{dx} - \frac{d\vec{E}_x}{dy} \right) - \frac{1}{\mu} (\vec{M}_{\text{source}} + \sigma^* \vec{H}_z) = \\ &= \frac{d\vec{H}_z}{dt} = \frac{1}{\mu} \left(\frac{d\vec{E}_x}{dy} - \frac{d\vec{E}_y}{dx} \right) - \frac{1}{\mu} (\vec{M}_{\text{source}} + \sigma^* \vec{H}_z)\end{aligned}\quad (\text{B.14})$$

Similarly, by following the same procedure with Ampere's law, it is possible to obtain the electric field components. For materials with isotropic, nondispersive electric losses to be enabled (causing the attenuation of the electric field via conversion to heat energy) the following relation is to be applied:

$$\vec{J} = \vec{J}_{\text{source}} + \sigma \vec{E} \quad (\text{B.15})$$

where J is the electric current density, J_{source} is the electric field source and σ is the electric conductivity.

$$\begin{aligned}\frac{d\vec{E}_x}{dt} &= \frac{1}{\varepsilon} \left(\frac{d\vec{H}_z}{dy} - \frac{d\vec{H}_y}{dz} \right) - \frac{1}{\varepsilon} (\vec{J}_{\text{source}} + \sigma \vec{E}_x) = \\ &= \frac{1}{\varepsilon} \left(\frac{d\vec{H}_z}{dy} - \frac{d\vec{H}_y}{dz} \right) - \frac{1}{\varepsilon} (\vec{J}_{\text{source}} + \sigma \vec{E}_x)\end{aligned}\quad (\text{B.16})$$

$$\begin{aligned}\frac{d\vec{E}_y}{dt} &= -\frac{1}{\varepsilon} \left(\frac{d\vec{H}_z}{dx} - \frac{d\vec{H}_x}{dz} \right) - \frac{1}{\varepsilon} (\vec{J}_{\text{source}} + \sigma \vec{E}_y) = \\ &= \frac{1}{\varepsilon} \left(\frac{d\vec{H}_x}{dz} - \frac{d\vec{H}_z}{dx} \right) - \frac{1}{\varepsilon} (\vec{J}_{\text{source}} + \sigma \vec{E}_y)\end{aligned}\quad (\text{B.17})$$

$$\begin{aligned}\frac{d\vec{E}_z}{dt} &= \frac{1}{\varepsilon} \left(\frac{d\vec{H}_y}{dx} - \frac{d\vec{H}_x}{dy} \right) - \frac{1}{\varepsilon} (\vec{J}_{\text{source}} + \sigma \vec{E}_z) = \\ &= \frac{1}{\varepsilon} \left(\frac{d\vec{H}_y}{dx} - \frac{d\vec{H}_x}{dy} \right) - \frac{1}{\varepsilon} (\vec{J}_{\text{source}} + \sigma \vec{E}_z)\end{aligned}\quad (\text{B.18})$$

For the purpose of illustrating the calculation in FDTD of how each field coordinate evolves, the equation to solve for E_x (Eq. (B.16)) is presented in Eq. (B.19) using the Yee notation (the steps corresponding to the coordinates x , y , z and t are represented by i , j , k and n respectively). On the left hand side of the

Eq. (B.16), the derivative is with respect to t. Therefore, the coordinates i, j and k are kept constant whereas n is varied from 1/2 to -1/2 (indicating $\Delta_t = 1$) to calculate the $\frac{d\vec{E}_x}{dt}$. On the right hand side of the equation, the partial differential equations are with respect to coordinates y and z. Therefore, coordinates n and i are kept constant whereas j is varied (from j+1 to j) and k is varied (from k+1 to k).

$$\frac{\vec{E}_x |_{i,j+1/2,k+1/2}^{n+1/2} - \vec{E}_x |_{i,j+1/2,k+1/2}^{n-1/2}}{\Delta_t} = \frac{1}{\epsilon_{i,j+1/2,k+1/2}} \left(\frac{\vec{H}_z |_{i,j+1,k+1/2}^n - \vec{H}_z |_{i,j,k+1/2}^n}{\Delta_y} - \frac{\vec{H}_y |_{i,j+1/2,k+1}^n - \vec{H}_y |_{i,j+1/2,k}^n}{\Delta_z} - \vec{J}_{\text{source}_x} |_{i,j+1/2,k+1/2}^n - \sigma_{i,j+1/2,k+1/2} \vec{E}_x |_{i,j+1/2,k+1/2}^n \right) \quad (\text{B.19})$$

The next step is to shift the Δ_t term from the left hand side to the right hand side. Further, the term $\vec{E}_x |_{i,j+1/2,k+1/2}^n$ is expressed as follows:

$$\frac{\vec{E}_x |_{i,j+1/2,k+1/2}^{n+1/2} - \vec{E}_x |_{i,j+1/2,k+1/2}^{n-1/2}}{\Delta_t} = \frac{1}{\epsilon_{i,j+1/2,k+1/2}} \left(\frac{\vec{H}_z |_{i,j+1,k+1/2}^n - \vec{H}_z |_{i,j,k+1/2}^n}{\Delta_y} - \frac{\vec{H}_y |_{i,j+1/2,k+1}^n - \vec{H}_y |_{i,j+1/2,k}^n}{\Delta_z} - \vec{J}_{\text{source}_x} |_{i,j+1/2,k+1/2}^n - \sigma_{i,j+1/2,k+1/2} \frac{\vec{E}_x |_{i,j+1/2,k+1/2}^{n+1/2} + \vec{E}_x |_{i,j+1/2,k+1/2}^{n-1/2}}{2} \right) \quad (\text{B.20})$$

Then, the term $\sigma_{i,j+1/2,k+1/2} \frac{\vec{E}_x |_{i,j+1/2,k+1/2}^{n+1/2} + \vec{E}_x |_{i,j+1/2,k+1/2}^{n-1/2}}{2}$ is taken outside the parenthesis.

$$\vec{E}_x |_{i,j+1/2,k+1/2}^{n+1/2} - \vec{E}_x |_{i,j+1/2,k+1/2}^{n-1/2} = -\frac{\Delta_t \sigma_{i,j+1/2,k+1/2}}{2\epsilon_{i,j+1/2,k+1/2}} \left(\vec{E}_x |_{i,j+1/2,k+1/2}^{n+1/2} + \vec{E}_x |_{i,j+1/2,k+1/2}^{n-1/2} \right) + \frac{\Delta_t}{\epsilon_{i,j+1/2,k+1/2}} \left(\frac{\vec{H}_z |_{i,j+1,k+1/2}^n - \vec{H}_z |_{i,j,k+1/2}^n}{\Delta_y} - \frac{\vec{H}_y |_{i,j+1/2,k+1}^n - \vec{H}_y |_{i,j+1/2,k}^n}{\Delta_z} - \vec{J}_{\text{source}_x} |_{i,j+1/2,k+1/2}^n \right) \quad (\text{B.21})$$

The next step is to move the term $-\vec{E}_x |_{i,j+1/2,k+1/2}^{n-1/2}$ on the left hand side to the right hand side. Additionally, the term $-\frac{\Delta_t \sigma_{i,j+1/2,k+1/2}}{2\epsilon_{i,j+1/2,k+1/2}} \vec{E}_x |_{i,j+1/2,k+1/2}^{n+1/2}$ on the right hand side is moved to the left hand side. Then, the equation is rearranged by taking the

common factor $\vec{E}_x|_{i,j+1/2,k+1/2}^{n+1/2}$ and $\vec{E}_x|_{i,j+1/2,k+1/2}^{n-1/2}$ on the left and right hand of the equation respectively.

$$\vec{E}_x|_{i,j+1/2,k+1/2}^{n+1/2} \left(1 + \frac{\Delta_t \sigma_{i,j+1/2,k+1/2}}{2\epsilon_{i,j+1/2,k+1/2}} \right) = \vec{E}_x|_{i,j+1/2,k+1/2}^{n-1/2} \left(1 - \frac{\Delta_t \sigma_{i,j+1/2,k+1/2}}{2\epsilon_{i,j+1/2,k+1/2}} \right) \quad (\text{B.22})$$

$$+ \frac{\Delta_t}{\epsilon_{i,j+1/2,k+1/2}} \left(\frac{\vec{H}_z|_{i,j+1,k+1/2}^n - \vec{H}_z|_{i,j,k+1/2}^n}{\Delta_y} - \frac{\vec{H}_y|_{i,j+1/2,k+1}^n - \vec{H}_y|_{i,j+1/2,k}^n}{\Delta_z} \right)$$

$$\left(-\vec{J}_{\text{source}_x}|_{i,j+1/2,k+1/2}^n \right)$$

Then, the term $\left(1 + \frac{\Delta_t \sigma_{i,j+1/2,k+1/2}}{2\epsilon_{i,j+1/2,k+1/2}} \right)$ is taken to the right hand side of the resulting Eq. (B.11) which is the central difference form in the Yee notation for the governing Eq. (B.16) for \vec{E}_x in the Yee notation:

$$\vec{E}_x|_{i,j+1/2,k+1/2}^{n+1/2} = \vec{E}_x|_{i,j+1/2,k+1/2}^{n-1/2} \left(\frac{1 - \frac{\Delta_t \sigma_{i,j+1/2,k+1/2}}{2\epsilon_{i,j+1/2,k+1/2}}}{1 + \frac{\Delta_t \sigma_{i,j+1/2,k+1/2}}{2\epsilon_{i,j+1/2,k+1/2}}} \right) \quad (\text{B.23})$$

$$+ \frac{\Delta_t}{\epsilon_{i,j+1/2,k+1/2}} \left(\frac{\vec{H}_z|_{i,j+1,k+1/2}^n - \vec{H}_z|_{i,j,k+1/2}^n}{\Delta_y} - \frac{\vec{H}_y|_{i,j+1/2,k+1}^n - \vec{H}_y|_{i,j+1/2,k}^n}{\Delta_z} \right)$$

$$\left(-\vec{J}_{\text{source}_x}|_{i,j+1/2,k+1/2}^n \right)$$

In a similar way, the central difference form in Yee notation for the governing equation for the remaining five field components (i.e. \vec{E}_y , \vec{E}_z , \vec{H}_x , \vec{H}_y and \vec{H}_z) may be obtained. In this appendix, only the final equation for each of them is presented in Eqs. (B.24)-(B.28).

$$\vec{E}_y|_{i+1/2,j,k+1/2}^{n+1/2} = \vec{E}_y|_{i+1/2,j,k+1/2}^{n-1/2} \left(\frac{1 - \frac{\Delta_t \sigma_{i+1/2,j,k+1/2}}{2\epsilon_{i+1/2,j,k+1/2}}}{1 + \frac{\Delta_t \sigma_{i+1/2,j,k+1/2}}{2\epsilon_{i+1/2,j,k+1/2}}} \right) \quad (\text{B.24})$$

$$+ \frac{\Delta_t}{\epsilon_{i+1/2,j,k+1/2}} \left(\frac{\vec{H}_x|_{i+1,j,k+1/2}^n - \vec{H}_x|_{i,j,k+1/2}^n}{\Delta_z} - \frac{\vec{H}_z|_{i+1/2,j,k+1}^n - \vec{H}_z|_{i+1/2,j,k}^n}{\Delta_x} \right)$$

$$\left(-\vec{J}_{\text{source}_y}|_{i+1/2,j,k+1/2}^n \right)$$

$$\begin{aligned} \bar{E}_z^{n+1/2} \Big|_{i+1/2,j+1/2,k} &= \bar{E}_z^{n-1/2} \Big|_{i+1/2,j+1/2,k} \left(\frac{1 - \frac{\Delta_t \sigma_{i+1/2,j+1/2,k}}{2\varepsilon_{i+1/2,j+1/2,k}}}{1 + \frac{\Delta_t \sigma_{i+1/2,j+1/2,k}}{2\varepsilon_{i+1/2,j+1/2,k}}} \right) \\ &+ \frac{\Delta_t}{\varepsilon_{i+1/2,j+1/2,k}} \left(\frac{\bar{H}_y \Big|_{i+1,j+1/2,k}^n - \bar{H}_y \Big|_{i,j+1/2,k}^n}{\Delta_x} - \frac{\bar{H}_x \Big|_{i+1/2,j+1,k}^n - \bar{H}_x \Big|_{i+1/2,j,k}^n}{\Delta_y} \right) \\ &+ \frac{\Delta_t \sigma_{i+1/2,j+1/2,k}}{1 + \frac{\Delta_t \sigma_{i+1/2,j+1/2,k}}{2\varepsilon_{i+1/2,j+1/2,k}}} \left(-\bar{J}_{\text{source}_z} \Big|_{i+1/2,j+1/2,k}^n \right) \end{aligned} \quad (\text{B.25})$$

$$\begin{aligned} \bar{H}_x^{n+1/2} \Big|_{i,j+1/2,k+1/2} &= \bar{H}_x^{n-1/2} \Big|_{i,j+1/2,k+1/2} \left(\frac{1 - \frac{\Delta_t \sigma_{i,j+1/2,k+1/2}^*}{2\mu_{i,j+1/2,k+1/2}}}{1 + \frac{\Delta_t \sigma_{i,j+1/2,k+1/2}^*}{2\mu_{i,j+1/2,k+1/2}}} \right) \\ &+ \frac{\Delta_t}{\mu_{i,j+1/2,k+1/2}} \left(\frac{\bar{E}_z \Big|_{i,j+1,k+1/2}^n - \bar{E}_z \Big|_{i,j,k+1/2}^n}{\Delta_y} - \frac{\bar{E}_y \Big|_{i,j+1/2,k+1}^n - \bar{E}_y \Big|_{i,j+1/2,k}^n}{\Delta_z} \right) \\ &+ \frac{\Delta_t \sigma_{i,j+1/2,k+1/2}^*}{1 + \frac{\Delta_t \sigma_{i,j+1/2,k+1/2}^*}{2\mu_{i,j+1/2,k+1/2}}} \left(-\bar{M}_{\text{source}_x} \Big|_{i,j+1/2,k+1/2}^n \right) \end{aligned} \quad (\text{B.26})$$

$$\begin{aligned} \bar{H}_y^{n+1/2} \Big|_{i+1/2,j,k+1/2} &= \bar{H}_y^{n-1/2} \Big|_{i+1/2,j,k+1/2} \left(\frac{1 - \frac{\Delta_t \sigma_{i+1/2,j,k+1/2}^*}{2\mu_{i+1/2,j,k+1/2}}}{1 + \frac{\Delta_t \sigma_{i+1/2,j,k+1/2}^*}{2\mu_{i+1/2,j,k+1/2}}} \right) \\ &+ \frac{\Delta_t}{\mu_{i+1/2,j,k+1/2}} \left(\frac{\bar{E}_x \Big|_{i+1,j,k+1/2}^n - \bar{E}_x \Big|_{i,j,k+1/2}^n}{\Delta_z} - \frac{\bar{E}_z \Big|_{i+1/2,j,k+1}^n - \bar{E}_z \Big|_{i+1/2,j,k}^n}{\Delta_x} \right) \\ &+ \frac{\Delta_t \sigma_{i+1/2,j,k+1/2}^*}{1 + \frac{\Delta_t \sigma_{i+1/2,j,k+1/2}^*}{2\mu_{i+1/2,j,k+1/2}}} \left(-\bar{M}_{\text{source}_y} \Big|_{i+1/2,j,k+1/2}^n \right) \end{aligned} \quad (\text{B.27})$$

$$\begin{aligned} \bar{H}_z^{n+1/2} \Big|_{i+1/2,j+1/2,k} &= \bar{H}_z^{n-1/2} \Big|_{i+1/2,j+1/2,k} \left(\frac{1 - \frac{\Delta_t \sigma_{i+1/2,j+1/2,k}^*}{2\mu_{i+1/2,j+1/2,k}}}{1 + \frac{\Delta_t \sigma_{i+1/2,j+1/2,k}^*}{2\mu_{i+1/2,j+1/2,k}}} \right) \\ &+ \frac{\Delta_t}{\mu_{i+1/2,j+1/2,k}} \left(\frac{\bar{E}_y \Big|_{i+1,j+1/2,k}^n - \bar{E}_y \Big|_{i,j+1/2,k}^n}{\Delta_x} - \frac{\bar{E}_x \Big|_{i+1/2,j+1,k}^n - \bar{E}_x \Big|_{i+1/2,j,k}^n}{\Delta_y} \right) \\ &+ \frac{\Delta_t \sigma_{i+1/2,j+1/2,k}^*}{1 + \frac{\Delta_t \sigma_{i+1/2,j+1/2,k}^*}{2\mu_{i+1/2,j+1/2,k}}} \left(-\bar{M}_{\text{source}_z} \Big|_{i+1/2,j+1/2,k}^n \right) \end{aligned} \quad (\text{B.28})$$

Appendix C

List of Journal papers published by the author

Oates, A., Cabrera-España, F. J., Agrawal, A., and Reehal, H., (2014), "*Fabrication and characterisation of Si micropillar PV structures*", Material Research Innovations, Vol. 18, 7, pp. 500-504.

Cabrera-España, F.J., and Agrawal, A., (2016), "*Hut-like pillar array Si solar cells*", Solar Energy, Vol. 132, pp. 357-362.

List of Conference papers published by the author

Oates, A., Cabrera-España, F. J., Agrawal, A., Reehal, H., (2014), "Fabrication and characterisation of silicon micro pillar PV structures", In Proceedings of the 10th Photovoltaic Science Application and Technology Conference (PVSAT 10). No.10_033.

Cabrera-España, F. J., Rahman, B. A. M., and Agrawal, A., (2014), "*Study of optical properties of textured Si solar cell with micro pillars*", In Proceedings of the 22nd International Workshop on Optical Wave and Waveguide Theory and Numerical Modelling (OWTNM2014),No.P-13.

Cabrera-España, and Agrawal, A., (2014), "FDTD - based study of optical properties of Si solar cells with micro pillars" In Proceedings of Photon 14.

Cabrera-España, F. J., Rahman, B. A. M., and Agrawal, A., (2014), "*Study of the optical properties of a micro pillar array solar cell for different configurations*", In Proceedings of the 14th International Conference on Numerical Simulation of Optoelectronic Devices (NUSOD 2014), No. MP22.

Cabrera-España, F. J., Rahman, B. A. M., and Agrawal, A., (2015), "Optimization of textured Si solar cell with array of hut-like micro pillars", In Proceedings of the Workshop on Optical Wave and Waveguide Theory and Numerical Modelling (OWTNM 2015), No. 20.

Cabrera-España, F. J., Oates, A., Reehal, H., and Agrawal, A., (2016), "Hut-like pillar Si solar cells", In Proceedings of CLEO 2016, No. SF2P.3.